Proceedings

Fani Deligianni and Guang-Zhong Yang (Eds.)

The Hamlyn Symposium
on Medical Robotics

24-27 June 2018, Imperial College London, UK

Published by:
The Hamlyn Centre
Faculty of Engineering
Imperial College London
https://www.imperial.ac.uk/hamlyn-centre/

E-Print, London, United Kingdom — June 2018

Preface

Last year, we celebrated the 10th anniversary of the Hamlyn Symposium and we have just now embarked on a new journey to what we hope to be the next decade of success for medical robotics. The 11th Hamlyn Symposium on Medical Robotics was held at the Royal Geographical Society on 24th to 27th June 2018. The theme for this years symposium was pioneering the next generation of medical robotics with an impressive line-up of leading scientists and engineers in medical robotics and allied technologies.

The keynote lectures were delivered by Dr Frederic Moll, a pioneer and serial entrepreneur in medical robotics, Dr Metin Sitti who is internationally renowned for micro-robotics and bio-inspired materials, and Dr Alberto Arezzo, who chairs the technology committee of the EAES (European Association for Endoscopic Surgery). They provided insightful analysis of the global landscape of interventional robotics, mobile milli/microrobots for medical applications, and the road ahead for endoluminal intervention. This years Storz-Hopkins lecture was delivered by Dr Adrian Park, who provided his vision on surgical visualisation.

A total of 121 papers were submitted from 18 countries, and after systematic peer review, 70 papers were selected for presentation at the Symposium. The topics covered include:

- Miniaturised robots for targeted therapy and drug delivery
- Intraluminal intervention
- Deep learning and surgical vision
- Emerging platforms and clinical applications
- From Brain Computer Intervention to Smart Manipulation

We were delighted to see our workshop programs continue to grow and flourish, held on the days pre- and post- the Symposium. This year, the number of workshops grew significantly and we have 13 workshops in total organised by leaders in the field supported by an enthusiastic team of early career researchers. It is delightful to see them interact and manage to bring together such a wide spectrum of work, addressing some of the emerging trends in medical robotics. A detailed programme of the workshops is listed on http://hamlyn-robotics.org/ and we hope they will seed new collaborations and form new networks.

This year, many of the workshops are supported by the EPSRC NIHR-HTC Network Plus and the Wellcome Trust Translational Partnership. We are very grateful to the EPSRC and Wellcome Trust for their ongoing support and the symposium represents an excellent platform for addressing new robotics technologies from concept to systems, to clinical translation and commercial exploitation.

We were particularly excited to host the 4th Surgical Robot Challenge in partnership with Intuitive Surgical, Kuka Robotics, and Applied Dexterity. The purpose of the Challenge was to foster collaboration, share resources and tackle some of the unmet technical/clinical challenges in robotic surgery. A large number of submissions were received, with 10 finalist teams bringing their kit to London to compete over a 3-day competition, starting in the lab, followed by presentations to an esteemed judging panel and then presented to the Hamlyn Symposiums wider audience.

This year, the Hamlyn Symposium featured for the first time the CEO and Founders Forum from some of the most prominent medical robotics companies. The panellists include Brian Miller of Intuitive Surgical, Frederic Moll of Auris Surgical Robotics, Michael Otto of Kuka, Yulun Wang of InTouch Health, Martin Frost of Cambridge Medical Robotics and Bradley Nelson of Aeon Scientific. They provided unique insights into the medical robotics industry, their journey of bringing new products to market and the importance of integrating engineering, clinical and business innovation.

We would like to thank the International and Local Programme Committees, the Workshop Organising Committees for giving up their valuable time to ensure timely review of the submitted papers, to shape an excellent symposium programme.

We are also grateful to the team who have worked behind the scenes and for their continuous effort in managing all aspects of the Symposium organisation. In particular, thanks to Robert Merrifield, Fani Deligianni, Florent Seichepine, Salzitsa Anastasova, Burak Temelkuran, Alia Talaat Ahmed, Karen Kerr, Jo Seed, Raphaele Raupp, Marianne Knight and Ulrika Wernmark.

Lastly, special thanks go to Lady Hamlyn. This would not be possible without the generous philanthropic support from both the Helen Hamlyn Trust and Lady Hamlyn herself.

It was our great pleasure to welcome attendees to the 11^{th} Hamlyn Symposium in London.

Guang-Zhong Yang, Ara Darzi
June 2018, London

Organisation

General and Programme Co-Chairs

Guang-Zhong Yang
Ara Darzi

Conference Organisers

Fani Deligianni	Conference Proceedings and Programme
Karen Kerr	Sponsorship
Marianne Knight	UK-RAS coordination and Web
Robert Merrifield	Symposium and Robot Challenge
Raphaele Raupp	General organisation
Jo Seed	Social Media and Publicity
Nicky Denovan	Social Media and Publicity
Florent Seichepine	Exhibition and Logistics
Alia Talaat Ahmed	PC Coordination and Workshops
Ulrika Wernmark	Symposium and Logistics
Betty Yue	Symposium and Logistics

International Programme Committee

Darwin Caldwell	IIT, Italy
Philip Chiu	The Chinese University of Hong Kong, China
Howie Choset	Carnegie Mellon University, USA
Kevin Cleary	The Sheikh Zayed Institute, Washington, USA
Paolo Dario	Scuola Superiore Sant'Anna, Pisa, Italy
Simon DiMaio	Intuitive Surgical Inc, USA
Pierre DuPont	Childrens Hospital Boston, USA
Giancarlo Ferrigno	Politecnico Milan, Italy
Gabor Fichtinger	Queen's University, Canada
Paolo Fiorini	University of Verona, Italy
Peer Fischer	University of Stuttgart
Dennis Fowler	Columbia University, USA
Toshio Fukuda	Nagoya University/Meijo University, Japan
Blake Hannaford	University of Washington, USA
Koji Ikuta	University of Tokyo, Japan
Pierre Jannin	INSERM, France
Leo Joskowicz	The Hebrew University of Jerusalem

Peter Kazanzides	Johns Hopkins University, USA
Thomas Looi	Sick Kids, Toronto, Canada
Jacques Marescaux	University Hospital Strasbourg, France
Arianna Menciassi	Scuola Superiore Sant'Anna, Pisa, Italy
Leonardo Mattos	IIT, Italy
Bradley Nelson	ETH Zurich, Switzerland
Rajni Patel	The University of Western Ontario, Canada
Vipul Patel	Global Robotic Institute, USA
Christopher Payne	Harvard University, USA
Cameron Riviere	Carnegie Mellon University, USA
Ichiro Sakuma	University of Tokyo, Japan
Rick Satava	University of Washington, USA
Lee Swanstrom	University of Oregon, USA
Mark Talamini	Stony Brook University, USA
Russ Taylor	Johns Hopkins University, USA
Ashutosh Tewari	Mount Sinai School of Medicine, USA
Chris Thompson	Harvard Medical School
Kirby Vosburgh	Harvard University, USA
Joe Wang	UCSD, USA
Bob Webster	Vanderbilt University, USA
Steve Wexner	Cleveland Clinic Florida, USA

Local Programme Committee

Salzitsa Anastasova	Imperial College London, UK
Kaspar Althoefer	Queen Mary University of London, UK
Thanos Athanasiou	Hammersmith and St Mary's Hospitals, UK
Christos Bergeles	University College London, UK
Colin Bicknell	St Mary's Hospital, UK
Praminda Caleb-Solly	Bristol Robotics Laboratory, UK
Nick Cheshire	Royal Brompton Hospital, UK
Jian Dai	Kings College London, UK
Brian Davies	Imperial College London, UK
Kamal Deep	Glasgow University and Golden Jubilee National Hospital, UK
Jag Dhanda	Queen Victoria Hospital, UK
Sanja Dogramadzi	Bristol robotics Laboratory, UK
Daniel Elson	Imperial College London, UK
Len Fass	GE Healthcare, UK
Stamatia Giannarou	Imperial College London
Daniel Leff	Charing Cross Hospital, UK
Erik Mayer	Royal Marsden Hospital, UK
Andreas Melzer	Dundee University, UK
George Mylonas	Imperial College London, UK
Dinesh Nathwani	Charing Cross Hospital, UK

Philip Pratt	Imperial College London, UK
Kawal Rhode	King's College London, UK
Ferdinando Rodriguez Y Baena	Imperial College London, UK
Andrew Schache	Liverpool University and Aintree University Hospital, UK
Pallav Shah	Royal Brompton Hospital, UK
Paulo Stanga	Manchester Royal Eye Hospital/University of Manchester, UK
Zoltan Takats	Imperial College London, UK
Celia Theodoreli Riga	St Mary's Hospital, UK
Julian Teare	St Mary's Hospital, UK
Neil Tolley	St Mary's Hospital, UK
Pietro Valdastri	University of Leeds, UK
Justin Vale	St Mary's Hospital, UK
Helge Wurdemann	University College London, UK
Shane Xie	University of Leeds, UK

CONFERENCE PROGRAM

Day 1: Monday 25th June 2018

Oral Session 1: Miniaturized Robots for Targeted Therapy and Drug Delivery

Poster Session 1

Oral Session 2: Intraluminal Intervention

Oral Session 3: Deep Learning and Surgical Vision

Poster Session 2

Day 2: Tuesday 26th June 2018

Oral Session 4: Emerging Platforms and Clinical Applications

Oral Session 5: From BCI to Smart Manipulation

Design and development of a miniaturized intra-abdominal flexible HIFU system: a proof of concept

C. Sozer, A. Cafarelli, M. Brancadoro, A. Menciassi

The BioRobotics Institute, Scuola Superiore Sant'Anna, Pisa, Italy,

canberk.sozer@santannapisa.it

INTRODUCTION

HIFU (High Intensity Focused Ultrasound) is the term used to describe the use of high power concentrated ultrasound beams for therapeutic purposes [1]. HIFU is being already efficiently used in clinics, especially for treating prostate, uterus, liver, breast, kidney, malignancies [2]. HIFU is a non-invasive exposure therapy based on non-ionizing energy focused deep into the body without damages to surrounding tissues; on the other hand, there are some challenges that have to be overcome for a wider application of HIFU in the abdominal organs.

Some target areas cannot be reached by ultrasound from the outside due to a not adequate acoustic window. If the acoustic impedance value of the medium changes abruptly in the propagation path of the ultrasound wave, in fact, energy is reflected back and cannot be transmitted to the target. Therefore, areas under the rib cage or air-filled viscera cannot be easily targeted by externally generated HIFU.

The purpose of the study is to present a miniaturized intra-abdominal HIFU device in order to overcome acoustic window problems and anatomical constraints. To achieve this goal, a custom transducer was manufactured and attached to a soft manipulator used as a flexible guide. The transducer was attached to an omnidirectional bendable soft manipulator in order to reach targets which cannot be accessible with externally applied ultrasound, e.g. due to some acoustic barriers.

The robotic disciplines are recently experiencing a paradigmatic revolution. The traditional approach that counts on well-established rules for designing and developing robots based on hard materials has been upset by the presence of soft and flexible structures to cope multiple tasks. Limited triangulation, constrained workspace and impossible navigation around or behind organs are major concerns related to a rigid surgical tool. These disadvantages can be overcome by exploiting the features of soft robotics, especially its intrinsic abilities of maneuverability and compliance [3]. Soft robots are inspired by the observation of the biological agents such as tentacles of the octopus, elephant trunks or snakes, and they are characterized by a continuously deformable structure made of soft, shrinkable and extensible materials (e.g. silicone). These robots are able to perform complex manipulations of objects in a confined environment by allowing curvilinear trajectories. Moreover, a safe interaction with surrounding organs/tissues is guaranteed [4].

In this paper, the authors demonstrate for the first time that a previously presented soft manipulator [5] can be used as a flexible guide for a focused transducer to perform a HIFU treatment in a minimally invasive scenario. The motion abilities of the soft manipulator are used to steer the transducer towards the target in a flexible way in the abdominal workspace. For evaluating the feasibility of the proposed approach, in vitro and ex vivo tests were performed.

MATERIALS AND METHODS

In this study, a custom HIFU transducer was designed and realized. It is composed by a concave piezoelectric ceramic element (diameter of 20.15 mm, radius of curvature of 20 mm), and an ad-hoc case manufactured using a 3D printer (Projet MJP3600, 3D Systems, USA). The back and front surfaces of the ceramic element were soldered to two wires connected to a coaxial BNC cable used for electrically driving the transducer. Thus, the wired ceramic element was placed into the case and fixed using epoxy adhesive glue.

To characterize the realized transducer, the frequency response (i.e. frequency spectrum) and the electric impedance values were measured by using a vector network analyzer (DG8SAQ VNWA V3, SDR-Kits, UK).

Peak frequency and electric impedance resulted to be 2.07 MHz and 49 Ω (@ 2.07 MHz), respectively. Thanks to the fact that the measured value is very close to the output impedance (i.e. 50 Ω) of the electric generation system, composed by a signal generator (Agilent 33220A, Keysight Technologies, USA) and a 50 dB amplifier (240L, Electronics & Innovation, USA), an electric matching circuit is not required.

In parallel, a previously designed soft manipulator [5] was manufactured. The soft manipulator, which can be easily produced at low cost and inherently more compatible with human anatomy than a rigid endoscope, is a bioinspired surgical device and can act as a flexible guide. It is 14.5 mm in diameter, 50 mm in length and presents an inner free central lumen with a diameter of 4.5 mm, within which transducer cables can be passed through. The manipulator consists of three pairs of longitudinal inflatable chambers with the diameter of 3 mm and equally spaced at 120°. Thanks to this geometry, when the chambers are pressurized, the manipulator is able to perform an omnidirectional bending and elongation.

The transducer was fixed at the tip of the soft manipulator by using a silicone glue. The 3D CAD model of the system is represented in Fig. 1-a.
Finally, as shown in Fig. 1-b, a latex balloon was placed at the tip of the transducer to provide the acoustic coupling between the transducer and the target tissue. The balloon was filled with degassed water for transmitting the ultrasound waves with minimum reflections and avoiding cavitation phenomena.

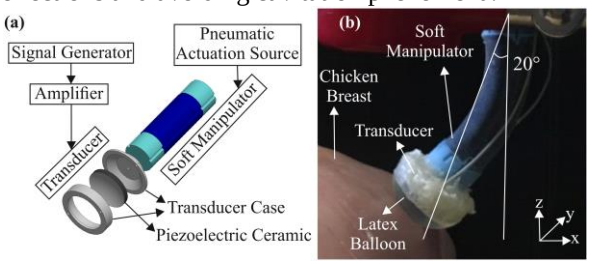

Fig. 1 a) Solid model of the proposed device, characterized by the soft manipulator equipped with the custom HIFU transducer. b) Picture of the bent device in contact with the ex vivo tissue.

The feasibility of the proposed device (HIFU transducer + soft manipulator) was preliminarily assessed by *(i)* evaluating the workspace of the soft manipulator and *(ii)* performing a thermal lesion into an ex vivo tissue (i.e. chicken breast) under an anatomical restriction situation.
The soft manipulator was fixed vertically (rest position) without any pressure at the beginning of the experiment. The workspace of the system was evaluated by assessing the maximum bending angle in the X-Z plane, by ranging the pressure from 0 to 1.2 bars. Then, a piece of chicken breast was placed in proximity of the device into the workspace of the soft manipulator. A coupling ultrasound gel was added to the external surface of the latex balloon in order to enhance the acoustic coupling.
The one pair of chambers of the soft manipulator was pressurized with 0.9 bar to reach the chicken breast with an angle of 20° (see Fig. 1-b). A continuous sine wave signal (2.07 MHz, 28 W, 40 s) was used to induce a thermal lesion 3 mm below the top surface of the chicken breast.

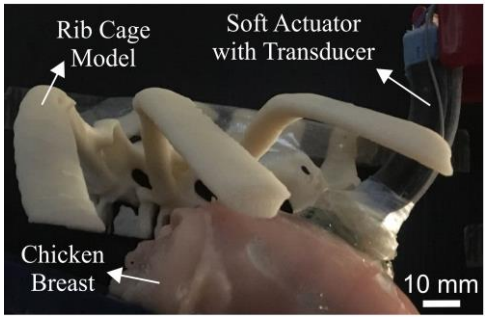

Fig. 2 Interaction between the miniaturized HIFU transducer (on the right) and a soft tissue in a restricted environment scenario.

RESULTS

The workspace of manipulator was a cone of revolution with a cone angle of 30° (the one pair of chambers of the soft manipulator was pressurized with 1.2 bar).

Fig. 3 shows the induced thermal HIFU lesion in proximity of the chicken breast surface. A 6 mm x 7 mm lesion was measured with a calliper, after cutting the tissue perpendicularly in proximity of the white spot.

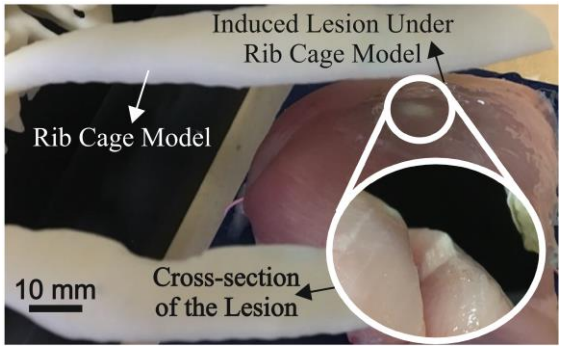

Fig. 3 Induced thermal lesion on the ex vivo chicken breast. (HIFU focus at 3 mm from the surface)

DISCUSSION

This paper reports a successful integration of a miniaturized HIFU transducer and a soft manipulator with the final aim to perform non-invasive intra-abdominal surgical procedures. A dedicated focused transducer was manufactured and integrated with an already developed soft manipulator for minimally invasive procedures (e.g. single port laparoscopy). The feasibility of the proposed system was assessed by inducing a HIFU lesion in an ex vivo tissue under an anatomical scenario restricted by simulated ribs.
In the future, the authors intend to: decrease the diameter of the transducer for covering the entire minimally invasive procedures (i.e. traditional laparoscopy); fully characterize the induced lesions at different stimulation parameters for better tuning HIFU therapy; develop a mechanism for compensating breathing motion of abdominal organs (i.e. liver, kidney, pancreas); add more soft manipulator modules in sequence in order to expand the workspace. A miniaturized camera or a confocal ultrasound imaging probe could be also added in the system in order to enable an image-guided procedure.

ACKNOWLEDGEMENT

The authors would like to thank Dr. Erik Dumont (Image Guided Therapy, Pessac, France) for the support in HIFU transducer development.

REFERENCES

[1] J. E. Kennedy et al. High intensity focused ultrasound: surgery of the future? BJR June 2003; 76(909): 590-9.
[2] J. E. Kennedy. High-intensity focused ultrasound in the treatment of solid tumours. Nature Reviews Cancer March 2005; 5(4): 321.
[3] D. Rus and M. T. Tolley. Design, fabrication and control of soft robots. Nature May 2015; 521: 467-75.
[4] H. Abidi and M. Cianchetti. On intrinsic safety of soft robots. Frontiers in Robotics and AI February 2017; 4: 5.
[5] H. Abidi et al. Highly dexterous 2-module soft robot for intra-organ navigation in minimally invasive surgery. JMRCAS February 2018; 14(1).

A system for in vitro evaluation of magnetic and manual catheter navigation for cardiac ablations

Q. Boehler[1], C. Chautems[1], L. Sabbatini[2], F. Duru[2], B.J. Nelson[1]

[1]*Multi-Scale Robotics Lab, ETH Zurich*

[2]*Department of Cardiology, University Hospital Zurich*
qboehler@ethz.ch

INTRODUCTION

Radiofrequency (RF) cardiac ablation is currently the treatment of choice for many types of cardiac arrhythmias [1]. As an alternative to manually guided catheter used to deliver the RF energy, an emerging technique known as remote magnetic navigation uses a magnetic catheter, which is remotely manipulated by a controlled magnetic field [2]. This approach enables a robotic approach to performing the ablation, with an expected gain in the procedure safety, time-efficiency, and precision. Despite preliminary evidence of the benefits of magnetic manipulation in some difficult ablation cases [3], the advantages of the robotic magnetic approach over the manual one are still to be investigated. In this work, we propose a further step toward this investigation by developing a dedicated setup for an in vitro evaluation of cardiac ablations. We focus on the design of realistic geometries and ablation trajectories in order to assess navigation performance and catheter manipulability. We aim at providing a platform to evaluate and improve the design of magnetic catheters and allow for a comparison with manual catheters for specific navigation tasks. To this extend, we designed and 3D-printed heart models corresponding to common ablations cases. We also developed dedicated control software to perform the magnetic manipulation. We report preliminary results of a user-study to evaluate a magnetic versus a manual manipulation procedure. Since atrial fibrillation (AF) is the most common cardiac arrhythmia, we focus on the pulmonary vein isolation (PVI) procedure that is commonly performed to cure AF [4].

MATERIALS AND METHODS

Our goal is to design a setup to simulate the navigation in one or more of the heart chambers with an ablation tool. We focus on designing geometries that are realistic enough to evaluate the ability of a catheter to follow a realistic trajectory.

In the case of PVI, ablation points are located along a circular trajectory around one or several pulmonary veins located in the left atrium, as depicted in Fig. 1(a). Therefore, we designed a heart model that is 3D-printed in a rigid polymer material and that allows for access with a standard introducer sheath from the inferior vena cava (IVC). The ablation trajectory is represented in our heart model by 19 fiducial marks placed that define a trajectory around the two left pulmonary veins. The points are intended to be touched with the catheter tip as depicted in Fig. 1(b). The model is cut open on the opposite side of the trajectory in order to allow for a visual inspection of the ablation targets.

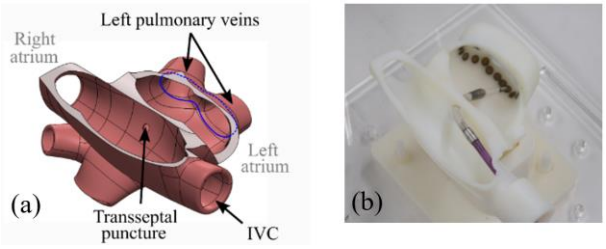

Fig. 1 Heart model for PVI procedure. (a) Anatomy of the atria and trajectory for the PVI in blue, (b) 3D-printed phantom with ablation tool pointing at the target points in black

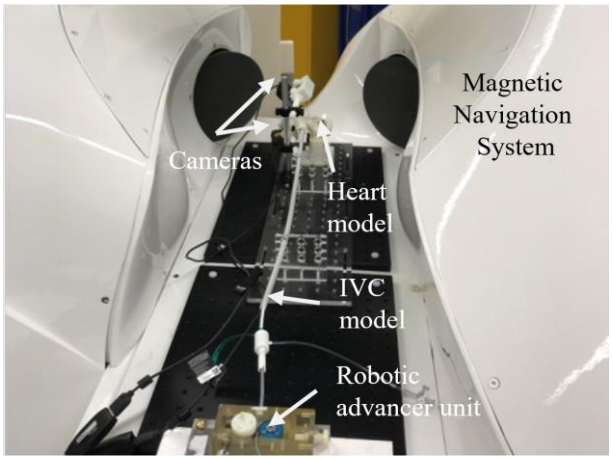

Fig. 2. Configuration of the evaluation setup in the magnetic navigation system

An overview of the setup is provided in Fig. 2. Visual feedback is performed via two cameras whose views are depicted in Fig. 3(b) and (c). The inferior vena cava is modeled as a flexible tube to access the heart model with standard introducer sheaths. A robotic advancer unit that is remotely controlled performs the catheter insertion within the sheath. The entire setup fits into a magnetic navigation system (CardioMag MNS, MSRL, ETH Zurich). This system can generate magnetic fields at a magnitude of 80 mT in any direction using eight current-controlled electromagnets without being affected by its ferromagnetic environment. The system is remotely controlled via a user interface depicted in Fig. 3(a). The interface displays the camera images and

the magnetic field direction with respect to a 3D-CAD model of the phantom geometry. The direction of the magnetic field and the insertion/retraction of the catheter are controlled by a joystick and the buttons of a 3D mouse controller (SpaceNavigator®, 3Dconnexion). The setup is also compatible with manual catheters by removing the robotic advancer unit and displaying camera images on a second screen at the bedside. The ablation task here consists in touching the 19 points of the heart model with the tip of an ablation catheter.

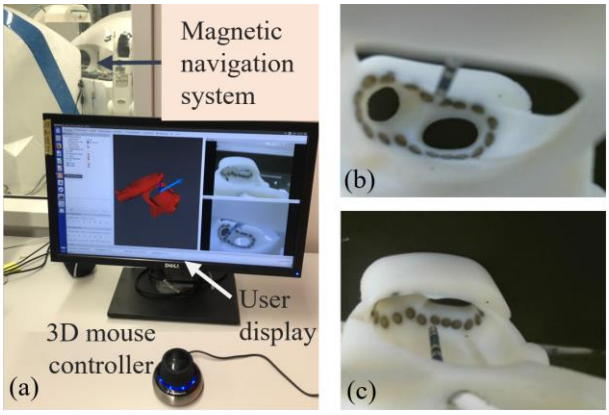

Fig. 3 User interface (a) and camera views (b)-(c)

RESULTS

As a preliminary result, we evaluated the feasibility of reaching the ablation points with both a magnetic and manual commercial catheter (ThermoCool® Navistar RMT and SF NAV, Biosense Webster Inc.). A commercially available standard SL1 introducer sheath is used to guide the ablation catheter up to the transseptal puncture. The time to reach all of the 19 points is considered as the performance criteria. A total of five users were selected for this study. Users include one electrophysiologist, as well as two medical students and two robotic engineers without experience with manual catheter manipulation. After an introduction to the setup and task, each user is given 15 min to test both magnetic and manual navigation on their own. The user is then told to touch all of the points as fast as possible. Each user is performing the magnetic approach first. Both videos and input from the joystick are recorded. The procedure is repeated three times for both magnetic and manual manipulation with 5 minutes break between each trial. The data of 30 trials have thus been collected.

All the 19 points could be reached by the 5 users with both manual and magnetic approaches and with a mean time of 409±110 s for magnetic and 119±55 s for manual procedure. Users reported that the magnetic manipulation is overall much less tiring than the manual one, since the magnetic field holds the tool in position when the controller is at a resting position.

The total time over the 3 trials is reduced by an average of 20% and 30% for the manual and magnetic procedures, which suggests a learning process for both modalities.

DISCUSSION

This study shows the feasibility of simulating the navigation of an ablation catheter along a PVI trajectory with both a magnetic and manual approach. Preliminary results give a first comparison between manual and magnetic catheters. The same test procedure will be repeated in the future to monitor our magnetic navigation system performance as we refined our control algorithms and user interface.

The total time was the only performance criteria used. Other criteria could be considered such as repeatability, accuracy or muscle activity measures, which would require additional sensor-based monitoring. We also noticed the significant influence of the mapping between the 3D mouse controller motion and the magnetic field heading direction on the navigation performance. To this extent, further work could be performed on the analysis of the controller inputs and catheter kinematics to find an optimal mapping. Further improvements for the setup can be considered as well to include more realistic conditions of the real cardiac environment such as blood flow and tissue deformation.

The current setup can already be used as an in vitro training platform for both manual and magnetic navigation. Heart phantoms corresponding to several ablation cases have already been designed, such as for cavotricuspid isthmus ablation in the case of atrial flutter, or treatment of right ventricular outflow tachycardia. Our platform can also be used for the evaluation of new magnetic tools as we proposed in [4], and can lead to the design of the next generation of magnetic ablation catheters.

ACKNOWLEDGEMENT

This work was partially funded by the Swiss National Fund grant 200021_165564. The authors would also like to thank Dr. Chol Jun On and Andrin Bleuler for their participation in the study.

REFERENCES

[1] F. Morady, “Radio-Frequency Ablation as Treatment for Cardiac Arrhythmias,” *N. Engl. J. Med.*, vol. 340, no. 7, pp. 534–544, Feb. 1999.

[2] A. Ali *et al.* “Steerable Catheters in Cardiology: Classifying Steerability and Assessing Future Challenges,” *IEEE Trans. Biomed. Eng.*, vol. 63, no. 4, pp. 1–1, 2016.

[3] M. Kawamura *et al.* “Comparison of remote magnetic navigation ablation and manual ablation of idiopathic ventricular arrhythmia after failed manual ablation,” *J. Interv. Card. Electrophysiol.*, vol. 48, no. 1, pp. 35–42, Jan. 2017.

[4] H. Calkins *et al.*, “2012 HRS/EHRA/ECAS expert consensus statement on catheter and surgical ablation of atrial fibrillation: recommendations for patient selection, procedural techniques, patient management and follow-up, definitions, endpoints, and research trial design,” *J. Interv. Card. Electrophysiol.*, vol. 33, no. 2, pp. 171–257, Mar. 2012.

[5] C. Chautems *et al.* “Design and Evaluation of a Steerable Magnetic Sheath for Cardiac Ablations,” *IEEE Robot. Autom. Lett.*, pp. 1–1, 2018.

Towards an Optimized Path Planner for the EDEN2020 Neurosurgical Steerable Needle

Marlene Pinzi, Stefano Galvan, Wenbo Zhan, Daniele Dini, and Ferdinando Rodriguez y Baena

The Mechatronics in Medicine Laboratory, Mechanical Engineering Department, Imperial College, London,UK - email: f.rodriguez@imperial.ac.uk

INTRODUCTION

Minimally invasive robotic percutaneous treatments are a popular research area in medical robotics due to the clear clinical benefits they deliver [1]. Minimally invasive procedures are a key part of modern surgery; however, they remain a difficult task to carry out, particularly in neurosurgery. Neurosurgeons are required to perform procedures with limited visibility and tool maneuverability, in an environment where the target and tissue surrounding it deform due to the tissue-tool interactions, physiological motion, deliquoration, etc. Percutaneous treatments such as brachytherapy, radio frequency ablation, cryoablation or chemotherapy require the introduction of a needle into a cancerous area; however, minimally invasive neurosurgical instruments are generally constrained to straight line trajectories, which limit the treatment choices available to the surgeon to those requiring a straight insertion.

These are some of the current open issues which fuel the EDEN2020 European project, which aims to develop an innovative neurosurgical tool for application to Convection Enhanced drug Delivery (CED,[2][3]). Based on the concept of a nonholonomic "programmable bevel-tip" (PBN) bio-inspired steerable needle [4], the proposed platform will allow surgeons to plan therapies around delicate tissue structures and will provide a method for direct and precise infusion of drugs in near proximity of tumours.

However, planning for an appropriate three-dimensional (3D) insertion trajectory for the proposed EDEN2020 PBN is particularly challenging with a complete solution yet to be published. This is due to factors like kinematic constraints, the presence of complex anatomical structures such as brain vessels, and constraints on the required start and target poses. First, a predictive brain diffusion model is developed to compute a target pose which optimize the drug transport; subsequently, we propose a new parallelisable 3D path planning approach, codenamed Adaptive Heŕmite Fractal Tree (AHFT), able to generate 3D obstacle-free pre-operative trajectories meeting all of EDEN2020's requirements.

MATERIALS AND METHODS

A Predictive brain diffusion model is developed with the aim to optimize the infusion parameters to achieve homogeneous and efficient drug penetration and accumulation. Incorporating the modules of fluid-tissue interaction and drug transport mechanisms, the numerical framework is designed to predict drug distribution within the tumour based on patient specific geometric and transport properties that are derived from diffusion tensor MR (Magnetic Resonance) images and tractography. The delivery volume and special characteristics of drug distribution serve as the key criteria for determining an appropriate infusion regime and needle tip configuration for each patient.

Once the target pose is calculated, an entry point, with approach angle perpendicular to the patient's skull, is desired in order to facilitate the creation of a suitable burr-hole. To aid in this process, the AHFT highlights an area on the patient's skull (Figure 1) containing multiple possible entry poses, from which it is feasible to reach the required target pose meeting the kinematic constraints of the PBN. However, due to the presence of obstacles (brain arteries and ventricles), the feasibility of a start and target pair does not guarantee the existence of at least one obstacle-free path. Therefore, the AHFT is called recursively for each pair in order to assist the surgeon in identifying a suitable location for the burr-hole, which guarantees a solution. This algorithm combines the efficiency of a parametrised Adaptive Fractal Tree (AFT) [5], able to densely sample the obstacle-free search space with a parallel architecture, with optimised geometric Hérmite (OGH) [6] curves, able to account for heading constraints accurately. This specific property allows us to use OGHs to extend the AFT obstacle-free paths at different positions along candidate trajectories connecting the AFT path to the desired target pose. Finally, an obstacle collision and a maximum curvature check are performed so that only feasible paths are returned.

RESULTS

Results from the predictive diffusion model suggest that CED infusion can effectively enhance the drug convective migration in tumour extracellular space

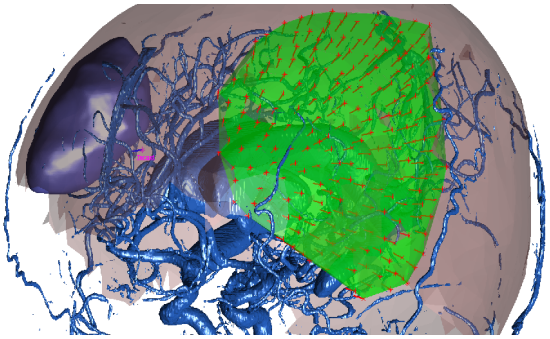

Fig. 1: The skull region containing suitable entry points for a given target pose is highlighted in green. Multiple entry poses (in red), normal to the patient's skull are provided to the surgeon to assist the selection of the insertion point.

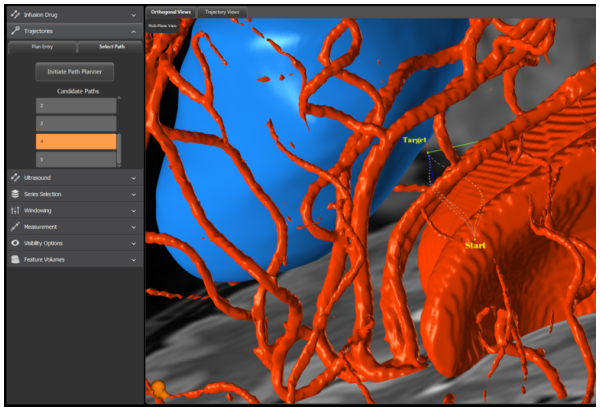

Fig. 2: AHFT trajectories connecting a start pose on the skull of the patient with and target pose in proximity of the tumor. The preoperative selected path is highlighted with a continuous line.

to enlarge the distribution volume. Drug penetration into deep tumour regions is highly dependent on the intratumoural hydraulic environment in which the tissue permeability plays an important role. The targeted pose for infusion needle must be optimized with respect to the original interstitial fluid flow, which is direction dependent and heterogeneous for each patient.

A simulated pre-operative environment, where the infusion pose is optimized by the prediction model is considered to asses the AHFT's ability of generating a pre-operative trajectory for a patient specific case. Each vertex of the skull mesh is considered in turn, where the coordinates represent a possible entry point, and the associated vertex normal represents the corresponding desired start approach vector. All feasible entry points for a given target pose are then identified by executing a feasibility check for each pair based on kinematic constraints of the PBN and the required start and target heading constraints 1. In this specific scenario, 217 entry points out of 1702 skull mesh vertexes are found to be feasible. Each start and target pair is used by the AHFT path planner to look for obstacle-free trajectories. At least one path is found for 18 entry points belonging to a feasible combination. In Figure 2 one of these successful pairs is considered. Multiple solutions are generated, but only the one that better accounts for the PBN preferential path characteristics is selected.

DISCUSSION

The EDEN2020 project will contribute to the wider clinical challenge of extending and enhancing the quality of life of cancer patients through a PBN-based minimally invasive neurosurgical platform, for application to CED. The simulation results demonstrate that the AHFT is able to identify a path planning solution if one can be found, and that the method can be used to identify the complete set of viable skull entry points for a given target pose and set of needle constraints, automatically. In this way, the surgeon can be assisted in identifying a suitable location for the burr-hole, which is both clinically safe and feasible, with full control over both the entry and target needle poses. Further studies will concentrate on the AHFT performances which is currently being reimplemented within a parallel architecture. In addition to the improving on the target approach accuracy and kinematic constraints control with respect to the AFT, we also aim to reach similar AFT computational time to provide quantitatively comparisons with online surgical path planning algorithms.

ACKNOWLEDGMENTS

The research leading to these results has received funding from the European Union's EU Research and Innovation Programme Horizon under grant agreement No 688279.

REFERENCES

[1] Niki Abolhassani, Rajni Patel, and Mehrdad Moallem. Needle insertion into soft tissue: A survey. *Medical Engineering & Physics*, 29(4):413–431, may 2007.

[2] M. A. Vogelbaum and M. K. Aghi. Convection-enhanced delivery for the treatment of glioblastoma. *Neuro-Oncology*, 17(suppl 2):ii3–ii8, mar 2015.

[3] Wenbo Zhan and Chi-Hwa Wang. Convection enhanced delivery of chemotherapeutic drugs into brain tumour. *Journal of Controlled Release*, 271:74–87, feb 2018.

[4] Riccardo Secoli and Ferdinando Rodriguez y Baena. Adaptive path-following control for bio-inspired steerable needles. In *2016 6th IEEE International Conference on Biomedical Robotics and Biomechatronics (BioRob)*, pages 87–93. IEEE, jun 2016.

[5] Fangde Liu, Arnau Garriga-Casanovas, Riccado Secoli, and Ferdinando Rodriguez y Baena. Fast and Adaptive Fractal Tree-Based Path Planning for Programmable Bevel Tip Steerable Needles. *IEEE Robotics and Automation Letters*, 1(2):601–608, jul 2016.

[6] Jun Hai Yong and Fuhua Cheng. Geometric Hermite curves with minimum strain energy. *Computer Aided Geometric Design*, 21(3):281–301, 2004.

Automatic air bubble detection based on bio-impedance for safe drug delivery in retinal veins

L. Schoevaerdts, L. Esteveny, G. Borghesan, M. Ourak, D. Reynaerts, and E. Vander Poorten

Mechanical department KULeuven university, Leuven, Belgium 3001

laurent.schoevaerdts@kuleuven.be

INTRODUCTION

Approximately 16.4 million people live with poor up to no eyesight due to occluded retinal veins. This indication - retinal vein occlusion (RVO) - forms the second most common retinal vascular disorder in the world [1]. Its origin comes from clogged retinal vessels that may lead to leakage of blood underneath the retina. Small vessels may be formed spontaneously (neo-vascularization) to restore the oxygen supply. These unfortunately tend to be brittle and rupture. The blood is then likely to obstruct the photoreceptors, involving black spots within the patient's eyesight. This may even lead to total blindness of the affected eye.

A potential treatment method consists of injecting a thrombolytic agent directly inside the clotted vessel. This procedure requires to introduce a cannula in the patient's sclera. This cannula forms an access point through which a cannulation needle can be inserted in the eyeball. The needle can be maneuvered to target the clogged vessel. Retinal vessel diameters range from 50μm up to 400μm. Surgeons therefore need to maintain the needle steady with a high level of precision for a prolonged period of time while injecting the drug. This may take 10 minutes or more. The feasibility of robot-assisted execution for this procedure was recently demonstrated [2].

While injecting a clot-dissolving agent inside the retinal vessels, air bubbles are likely to make the cannulated vessel explode. Alternatively the bubbles may act as an air cushion, preventing the agent from reaching the clot. On the other hand, releasing air bubbles inside the vitreous body is not harmful. Air bubble detection would allow to stop the vein cannulation, retract the needle and release the air inside the eyeball. Thus, complications could be avoided in such way.

Currently, air bubble sensors in infusion lines rely on three main principles: ultrasonic transducers, optical and impedance measurements. In 2005, Cassidy patented a capacitor-based gas detection where three electrodes were positioned along the IV tubing [3]. By considering the fluid contained in the tubing as a dielectric, a reference capacitor allowed to detect presence of air. In 2009, Erickson patented an optical product detection sensor [4]. An emitter issued radiation towards the fluid and a detector collected the transmitted light spectrum. Later, Wilt developed a sensor for air detection using ultrasonic transducers [5]. Ultrasonics vibrations were transmitted through the IV tubing and the response was transduced by a receptor into an electrical signal.

These technologies need to access the tubing in order to detect upstream air bubbles while micro-air bubbles can come from inaccessible inner cavities in the case of instruments for micro-surgery. To the best of our knowledge, an air bubble detection sensor for vitreoretinal surgery does not yet exist. This paper presents an innovative sensor based on bio-impedance that detects air bubbles that come from the infusion line before they exit the needle tip.

MATERIALS AND METHODS

In order to measure and prevent air bubble injection, an in-house built bio-impedance sensing cannulation needle [6] is used and algorithms have been tailored for automatic detection. Initially, the bio-impedance sensor - schematically shown in Fig. 1 - was meant to detect a puncture when cannulating a retinal vessel. Here it is shown to be also capable of detecting air bubbles. By applying a sinusoidal voltage between the needle's inner and outer probe, the impedance at the level of the needle tip can be measured. The measurement principle relies on the fact that common thrombolytic agents such as tPA (tissue Plasminogen Activator) are made out of electrolytes. This holds also for 0.9% saline solution which was used here as a substitute. When an air bubble - which is effectively an electrical insulator - appears in the needle lumen, the ion flow inside the needle is disrupted. Both the phase and magnitude of the impedance are then affected. To measure the electrical impedance, a Quadra Impedance Spectroscopy (Eliko, Estonia) is connected to the inner probe and outer probe from the instrument. The Quadra measures the impedance for 15 selected excitation frequencies (ranging from 1 kHz to 349 kHz) simultaneously at 1 kHz sampling frequency. The impedance magnitude and phase are sent over USB. In parallel, camera images from a medical-grade stereo-microscope record the scene to visually assess the presence of air bubbles at the needle tip. These can be easily observed while flushing the needle. The instrument was mounted on a co-

manipulation robot to cannulate retinal vessels on open-sky *ex-vivo* pig eyes [7]. The pig eye vitreous was removed and replaced by 0.9% saline solution to simulate the usual condition during eye surgery.

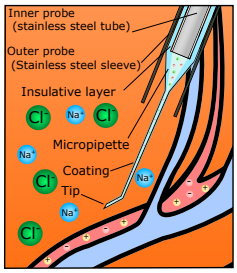

Fig. 1: Sketch of impedance sensor and view upon ions in the vessel vicinity and inside the needle lumen.

RESULTS

Experiments were conducted on 7 *ex-vivo* pig eyes. In total 16 punctures were performed. The needle was flushed with saline solution before and after each puncture to assess the presence of air bubbles in the needle lumen. Bubbles were observed in 4 experiments, releasing the air either inside the eyeball or inside the retinal vessels. The measured phase (Φ) is reported in Fig.2. When air pops up at the inner probe interface, the phase drops at about -90^o, which is the phase of a pure capacitor. Deviation at higher frequencies is due to inaccuracies of the Quadra at higher frequencies. On the other hand, the impedance magnitude ($|Z|$) behaves similarly. From the experiments, more than 134 000 measurements were done respectively with air bubbles at the inner probe interface and 570 000 without such.

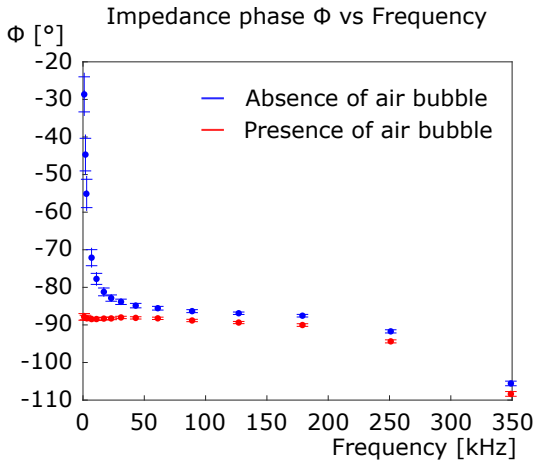

Fig. 2: The impedance phase shows a capacitive behaviour when the air replaces the saline solution.

In order to automatically detect the presence of air from the measured impedance, a classifier is used from the Matlab Classification Learner App over the whole dataset from 1 kHz to 349 kHz. Giving the large dataset, holdout validation is used with 75% of the data to train the classification model. A simple coarse tree model classifier type showed 100% accuracy over the whole dataset, independently of the excitation frequency. Such algorithm has a fast prediction speed, small memory usage and is easy to interpret. Giving the accuracy of this model type, no more complex methods are necessary for air bubble detection.

DISCUSSION

A bio-impedance sensor was used to measure the presence of air bubbles in the lumen of a cannulation needle. This detection was meant to avoid clinical complications during retinal vein cannulation. The impedance magnitude and phase measurements showed that it was possible to reliably detect presence of air inside the lumen. A simple decision tree classifier showed an accuracy of 100% over the whole measurement range. A further step would consist in automatically stopping the injection in a closed loop feedback.

Acknowledgements

This research was funded by a C3-fund (3E160419) from KU Leuven.

REFERENCES

[1] S. Rogers, R. McIntosh, N. Cheung, L. Lim, J. Wang, P. Mitchell, J. Kowalski, H. Nguyen, T. Wong, and International Eye Disease Consortium, The prevalence of retinal vein occlusion: pooled data from population studies from the united states, europe, asia, and australia. Ophthalmology, vol. 140, no. 2, pp. 313319, 2010.

[2] https://nieuws.kuleuven.be/en/content/2017/surgical-eye-robot-performs-precision-injection-in-patient-with-retinal-vein-occlusion.

[3] D. E. Cassidy, E. May, R. Bucchianeri. Capacitor-based gas detection in an intravenous fluid delivery system. Patent US7377148B2. 2005.

[4] J. Erickson, E. Tokhtuev, C. Owen . Optical product detection sensor. Patent US20090262351A1. 2009.

[5] M. J. Wilt, J. M. Sachs. System, Method, and Apparatus for Detecting Air in a Fluid Line Using Active Rectification. Patent US20140165703A1. 2016.

[6] L. Schoevaerdts, L. Esteveny, G. Borghesan, M. Ourak, A. Gijbels, J. Smits, D. Reynaerts and E. Vander Poorten. Innovative bio-impedance sensor towards puncture detection in eye surgery for retinal vein occlusion treatment. International Conference on Robotics and Automation. 2018 May.

[7] A. Gijbels, K. Willekens, L. Esteveny, P. Stalmans, D. Reynaerts, and E. B. Vander Poorten, Towards a clinically applicable robotic assistance system for retinal vein cannulation, in 6th IEEE International Conference on Biomedical Robotics and Biomechatronics, 2016, pp.284291.

AUTOFocus: Reaching a target in the prostate with a 3D-ultrasound image-based control law

R. Chalard[1], D. Reversat[1], G. Morel[1], and M.A. Vitrani [1]

[1]*Sorbonne Université, CNRS UMR 7222, INSERM U1150, Institut des Systèmes Intelligents et Robotique (ISIR), F-75005, Paris, France*

{*chalard,reversat,morel,vitrani*}*@isir.upmc.fr*

INTRODUCTION

Biopsies are the clinical standard routine for prostate cancer diagnosis. Despite a variety of approaches exists to perform this gesture, transrectal sampling is the most widely used. This method consists in inserting a needle through a needle-guide fixed to an endorectal US probe in order to sample the carcinogenic tissue in the prostate. Generally, twelve biopsies are distributed in the prostate volume according to a systematic sextant scheme [1] (Fig.1). However, in some cases, additional targeted samples may be taken in a given area of interest corresponding to a 3D region earlier detected on an MRI image. The partial tissue information provided by the US images makes targeting precision hard. Moreover, pre-operative imaging does not provide information about the deformation and displacements occurring during the biopsy. Thereby, robotic and/or image-guided tools for assisted procedure are being developed [2].

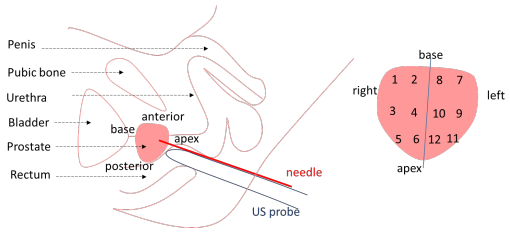

Fig. 1: Conventional sextant scheme.

Attaining a 2 mm-targeting precision[3], can enable the delivery of localized treatments, with reduced collateral impact on the patient's life. In this paper we present the image-based control "AUTOFocus" for high-precision prostate samples targeting. A 6-DoFs robot is coupled to an imaging device for improved needle positioning.

MATERIALS AND METHODS

The robotized probe-holder: "Apollo" (Fig.2) is a 6-DoFs anthropomorphic robot [3], featuring 3 motorized joints and a back-drivable wrist, equipped with breaks for locking purposes. The robot, designed to assist prostate biopsies through co-manipulation, falls into the category of free-wrist robots. Apollo has 3 different modes:

- the FREE mode, characterized by high transparency and gravity compensation [3];
- the LOCKED mode to precisely hold the probe up to a target position [3];
- the AUTONOMOUS mode, to automatically displace the probe toward a desired anatomical location. This control mode is designed to target a desired position T_d inside the prostate by computing the corresponding desired position of the robot wrist center,W_d. Tissues deformations (anus and rectum) are taken into account [2].

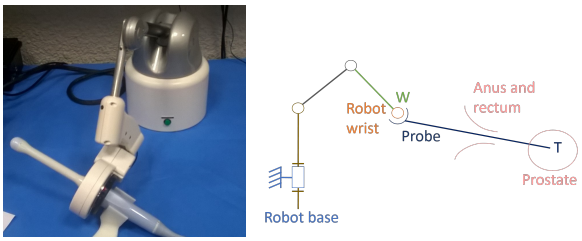

Fig. 2: Apollo robot V2 and kinematics scheme.

Imaging device: The Urostation®, is a commercial device for elastic registration among 3D US images. It is used to measure the current needle and target positions: the urologist first records a set of 3D images to compute a prostate reference 3D volume. They can also define anatomical targets inside this reference. Throughout the examination, intra-procedure 3D images are used to update the current 3D volume with respect to the reference [4].

AUTOFocus Mode: This mode enables to attain a higher precision for anatomical landmark-reaching gestures. As the current needle position can't be measured in real-time, conventional visual servoing control does not apply. However, positioning errors ε_T between the desired target position T_d and the current needle position T are estimated at each new 3D volume acquisition. Therefore, with an iterative process, the robot is able to precisely reach the cancer. The AUTOFocus mode is a semi-automatic closed loop process as it needs the surgeon's supervision to correctly converge toward the target in three steps: at each iteration the surgeon decides, based on the current error, whether to run another acquisition or to sample the tissue, as the precision is deemed satisfactory (step 4). The first trial of the

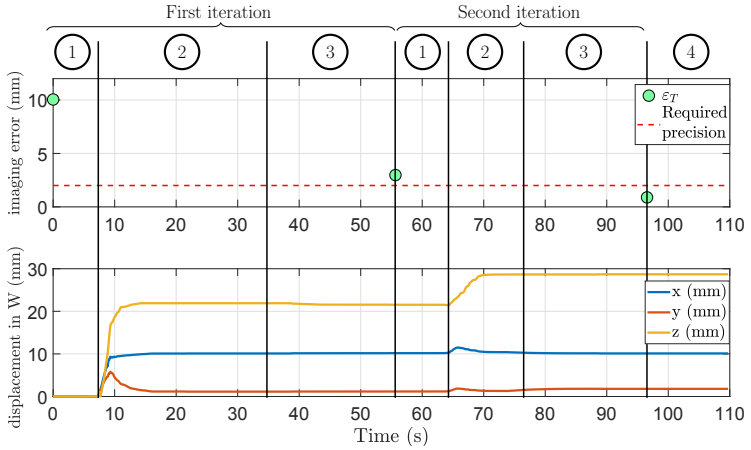

Fig. 3: The error computed by the AUTOFocus mode and the wrist robot displacements in two iterations.

surgeon triggers the AUTOFocus mode, described in four steps (Fig.3):

- step 1: the surgeon's supervision;
- step 2: the robot displacement;
- step 3: the 3D-image acquisition and processing with the definition of a new ε_T;
- step 4: the precision is satisfactory and the surgeon can sample the prostate.

RESULTS

The experimental set-up is described on Fig.4. The probe tip is inserted through a phantom that reproduces both the mechanical and echogenecity of a prostate including the anus and the rectum deformations.

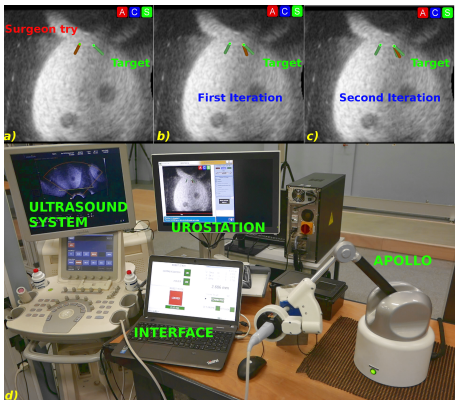

Fig. 4: Convergence to the target by small automatic movements a), b), c), experimental set-up d) and the convergence to the target in two iterations.

As aforementioned, the urologist first acquires the reference 3D volume of the prostate and specifies the target (T_d). During the exploratory exam, the free mode is used. Then, 12 systematic biopsies are sampled and the robot locked mode helps the surgeon in stabilizing the gesture. If targeted biopsies are necessary, the surgeon manually displaces the probe toward the selected target. However, as the patient lies on the side, in a crouched position, a correct matching the US information with the actual prostate position impacts negatively on the targeting precision. The AUTOfocus mode is, then, able to minimize the residual errors by means of a new image acquisition. Fig.3 and Fig.4 highlight the decrease of the pointing error, ε_T: within two iterations, the error decreases from 10mm down to below 2mm. In general, several iterations are needed to ensure convergence to the expected precision level: as we do not have access to the real time needle pose, any prostate deformation occurring in-between two consecutive iterations can't be accounted for; this might lead to unexpected variations of the error. However, the closed loop control ensure a precise and fast convergence (Fig.3).

DISCUSSION

A US-based, closed-loop control for precise probe displacement for prostate biopsies has been presented. Despite the high prostate deformability, a fast and satisfactory alignment of the needle axis with a biopsy target has been attained. Future work will include clinical studies to validate the advantages of robot-based platforms over the conventional routine.

REFERENCES

[1] A. Ouzzane, P. Coloby, JP. Mignard, JP. Allegre, M. Soulié, X. Rébillard, L. Salomon, A. Villers (2011) "*Recommendations for best practice for prostate biopsy.*" Prog Urol 21(1):18.

[2] R. Chalard, D. Reversat, G.Morel, P.Mozer, MA. Vitrani (2018) "*Precisely positioning the tip of an instrument inserted through an orifice with a free wrist robot: application to prostate biopsies,*" IJCARS.

[3] C. Poquet, P. Mozer, MA. Vitrani, and G. Morel (2015) "*An endorectal ultrasound probe comanipulator with hybrid actuation combining brakes and motors,*" IEEE TMECH, pp.20(1)186-196.

[4] M. Baumann, P. Mozer, V. Daanen, and J. Troccaz (2012) "*Prostate biopsy tracking with deformation estimation,*" Medical Image Analysis, pp.16(3)562576.

A Miniature Wirelessly Actuated Magnetic Surgical Tool for Minimally Invasive Grasping

A. Lim[1], S. Salmanipour[2], O. Onaizah[2], C. Forbrigger[2], T. Looi[1], J. M. Drake[1], E. Diller[2]

[1]*Centre for Image Guided Innovation and Therapeutic Intervention (CIGITI), The Hospital for Sick Children, Toronto, Canada*

[2]*Department of Mechanical and Industrial Engineering, University of Toronto*
andrewwilliam.lim@mail.utoronto.ca

INTRODUCTION

The implementation of robotically-assisted surgery has led to improved surgical outcomes in urology, gynecology and general surgery by offering benefits such as reduced surgeon tremor and increased tool precision and dexterity. However, surgical disciplines with narrower workspaces, such as neurosurgery or pediatrics, have yet to see many of these benefits largely due to the lack of small yet dexterous tools. With existing tools, robotically-assisted surgery is ineffective, and adoption into these disciplines is resisted [1-2].

Existing tools typically rely on cable driven actuation. Although reliable and able to generate substantial tool tip forces at large scales, miniaturization remains a challenge. Frictional inconsistencies between moving parts at the tool's tip in cable driven systems become amplified and component fabrication for these intricate mechanisms is difficult at smaller scales. Wireless magnetic actuation avoids these limitations and is an effective actuation method for complex mechanical mechanisms used in various microrobotic applications [3]. Therefore, in this work we present a magnetically-actuated, cable-less strategy for a three-degree-of-freedom (3-DOF) gripper-wrist tool tip with a diameter of 4 mm.

MATERIALS AND METHODS

Gripper-Wrist Design: The gripper-wrist is composed of nitinol and nickel-coated N52 NdFeB permanent magnets (Fig. 1). In the presented design, a single flexural joint is used for the 2-DOF (yaw, pitch) wrist to avoid friction while simultaneously providing axial rigidity. The gripper is composed of two parallel gripping digits connected by a semicircular restoring spring. Permanent magnets are fixed to the proximal ends of the gripping digits and the distal end of the wrist, creating local and global magnetization vectors. The 3x1x1 mm magnets on the gripping digits are responsible for gripper closure and have magnetization vectors oriented inwards. The three 1x1x1 mm magnets located at the distal end of the wrist are responsible for actuating wrist orientation and have proximally-oriented magnetization vectors. The gripper-wrist's orientation and digit tip separation are actuated using an 8-coil electromagnetic system [4] capable of delivering a controlled magnetic field up to 40 mT.

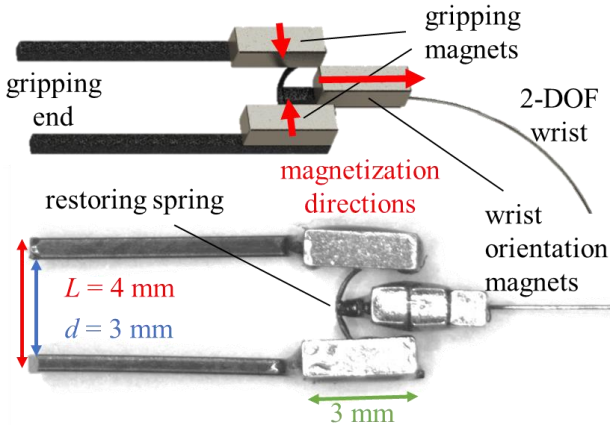

Fig. 1 (Top) 3D render of design with wrist bent. (Bottom) overhead image of the 4mm gripper-wrist prototype.

Gripper-Wrist Fabrication: The gripper-wrist was fabricated in-house. Curved nitinol components were shape set in a high-temperature oven at 550°C for 5 minutes. The gripping digits, restoring spring and 2-DOF wrist were joined using a LaserStar 990 series laser welding system. Permanent magnets were fixed to the gripper using epoxy and left to cure for 24 hours.

Gripper Closure Response: The gripper's digit tip separation, *d*, was measured without wrist deflection using several external magnetic field magnitudes in the direction of the undeflected wrist. Field magnitudes up to 130 mT were generated using two 2.5 cm cube N52 permanent magnets with varying separation distances. A Lake Shore Model 425 gaussmeter was used to measure the applied magnetic field at the proximal tip of the gripping digits.

Wrist Range of Motion Characterization: The wrist's range of motion was characterized using a 75 mT magnetic field, created by two 2.5 cm cube N52 permanent magnets separated by 4.5 cm. The orientation of the wrist's base with respect to the direction of the field was varied, and the gripper's tip orientation was measured.

"Pick and Place" Demonstration: Using the coil system, a time-varying external magnetic field was applied to the gripper-wrist to perform a "pick and place" demonstration on a tissue-mimicking polydimethylsiloxane (PDMS) cargo fabricated such that its density was similar to brain tissue. Kinematic control of the gripper was implemented with a proportional controller and real-time image-tracking

feedback from an overhead camera. The magnitude of the field parallel to the gripper's local orientation controls tip separation while the magnitude and direction of the field vector in the orthogonal plane orients the wrist. The goal of the task was to move the gripper to a position above the cargo, lower its height, grasp the cargo, move to its target position, release the cargo, and finally move back to its initial position.

RESULTS

To determine the potential of this design for use as a surgical grasping mechanism, its ability to close and its total angular range of motion at a constant field magnitude were characterized. Fig. 2 exhibits the gripper's tip separation response to various parallel field magnitudes. Full gripper closure was observed at 75 mT. Fig. 3 shows a maximum wrist yaw deflection of 88° counter-clockwise and 84° clockwise using 75 mT. Our experimental setup was physically limited to maximum wrist deflections of these values and we postulate that further deflection is possible. A similar range of motion is expected for the wrist's pitch DOF. Finally, Fig. 4 shows frames from a "pick and place" video demonstration on a PDMS cargo.

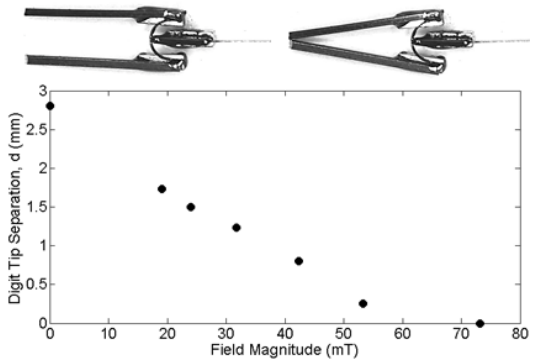

Fig. 2 (Top-left) no field applied; (top-right) gripper under 75 mT of external field pointing left; (bottom) digit tip separation under various magnetic field strengths.

Fig. 3 (Left and right) maximum flexural wrist response to a 75 mT field oriented +/-115° away from the wrist's undeflected position. (Middle) undeflected gripper-wrist under no external magnetic field.

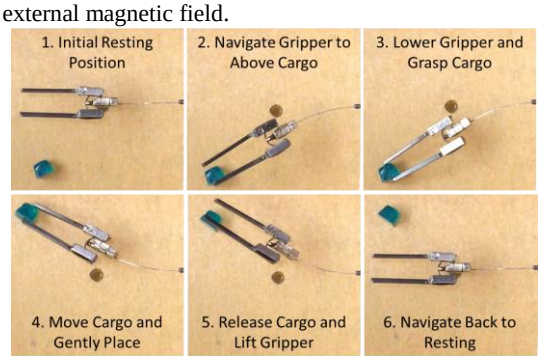

Fig. 4 Frames from the "pick and place" demonstration using the 4mm magnetically actuated gripper-wrist.

DISCUSSION

This work presents a 4 mm magnetically-actuated gripper-wrist tool tip. Early experiments are promising, demonstrating that the wrist has a range of motion of at least 172° and full gripper closure can be achieved using a 75 mT external field. Furthermore, a "pick and place" demonstration was performed on a PDMS cargo using a 40 mT 8-coil electromagnetic system.

The simple design of the proposed mechanism lends itself well to further miniaturization to accommodate more confined surgical workspaces. A more efficient use of space in the mechanism would likely enable miniaturization in future designs while maintaining functionality.

Although this study provides evidence for feasibly grasping and transporting tissue-mimicking cargo, tool tip forces were not characterized. Marcus *et al.* suggested a force exertion of 0.02-0.09 N per digit tip for effective brain tissue retraction on cadavers [5]. Future work will involve characterizing the presented gripper's tip forces.

While this study was limited to a system capable of delivering a maximum of 40 mT, Rahmer *et al.* have developed a clinically scaled coil system that can generate field strengths up to 400 mT and accommodate workspaces over 20 cm [6]. A system with these capabilities would likely be able to actuate our presented gripper-wrist in small surgical workspaces such as the head for neurosurgical applications. It is also probable that fields of this magnitude would increase the range of motion of our flexural wrist and allow for much higher gripping forces to be exerted.

Finally, this magnetically actuated mechanism is not limited exclusively to grasping. Several other tool-tip functions would benefit from this design including magnetically actuated cutting and bipolar electrocautery tips for robotically-assisted surgeries. These functionalities, in addition to grasping, have the potential to feasibly extend the use of surgical robotic systems to neurosurgery and pediatrics, aiming to improve their surgical outcomes.

REFERENCES

[1] Marcus HJ, *et al.* da Vinci robot-assisted keyhole neurosurgery: a cadaver study on feasibility and safety. Neurosurg. Rev. 2015 Apr;38(2):367-71

[2] van Haasteren G, *et al.* Pediatric robotic surgery: early assessment. Pediatrics. 2009 Dec;124(6):1642-9.

[3] Kummer MP, *et al.* OctoMag: An Electromagnetic System for 5-DOF Wireless Micromanipulation. IEEE Trans. on Robot. 2010 Dec;26(6):1006-17.

[4] Salmanipour S, Diller E. Eight-Degrees-of-Freedom Remote Actuation of Small Magnetic Mechanisms. IEEE Int. Conf. Robot. & Autom. Accepted for publication, 2018.

[5] Marcus HJ, *et al.* Forces exerted during microneurosurgery: a cadaver study. Int J Med Robot. 2014 Jun;10(2):251-6.

[6] Rahmer J, Stehning C, Gleich B. Remote magnetic actuation using a clinical scale system. PLoS One. 2018 Mar;13(3):e0193546.

Toward Endobronchial Intervention: A Pre-Curved Continuum Robot with Large Deflection and Linear Elasticity

A. Gao[1], N. Liu[1], Guang-Zhong Yang[1]

[1]Hamlyn Centre for Robotic Surgery, Imperial College London

a.gao@imperial.ac.uk

INTRODUCTION

Endobronchial intervention is now a common clinical practice for managing early-stage lung cancer [1]. However, distal airways are difficult to be reached by normal bronchoscopes due to their size and. Miniaturised continuum robots are preferred for minimally invasive surgeries because of their flexibility, compliance, and ease of distal access [2]. In previous work [3], a miniaturised continuum robot with interlocked joints has been developed to facilitate endobronchial intervention towards distal airways, as shown in Fig. 1. In this paper, we propose an alternative pre-curved continuum robot toward endobronchial intervention using a thin-walled notched nitinol tube as the flexible backbone, and a multi-lumen tube is inserted to provide working channels for miniature probes or other surgical tools. Given the same linear strain range for the same material, the proposed pre-curved continuum robot can generate a larger deflection compared with the straight continuum robot as shown in Fig. 1(b), which is also useful to ensure linear elasticity for online force control avoiding material nonlinearity.

This paper is organized as follows. First, a pre-curved multi-lumen continuum robot is developed. Then finite element analysis is applied for a preliminary quantative evaluation. Finally, a prototype integrating the pre-curved continuum robot, electromagnetic (EM) sensors and a long flexible shaft is built and tested in a silicon lung phantom. Evaluation and experimental results demonstrate that the proposed pre-curved approach can increase the deflection of the continuum robot while ensuring linear elasticity, thereby facilitating the intervention to distal airways in a controllable manner in future. It is also potentially useful for a series of continuum robots with various backbones.

MATERIALS AND METHODS

The notched nitinol tube has been used as the backbone of continuum robots for different applications [4-6]. The pre-curved elastic element has been used for continuum robot to bias the workspace to enhance the curvature [7]. In this paper, we develop a pre-curved continuum robot with multiple lumens by assembling a thin-walled notched nitinol tube with a multi-lumen polymer tube, as shown in Fig. 2. The notched nitinol tube is used to enhance the bending flexibility, torsional stiffness, as well as avoid the bulking of multi-lumen structure. The nitinol tube (O. D. = 2.2 mm and I. D. = 2 mm) was laser cut with asymmetric cutouts, which only allowed it to deform in one direction. Then, a pre-

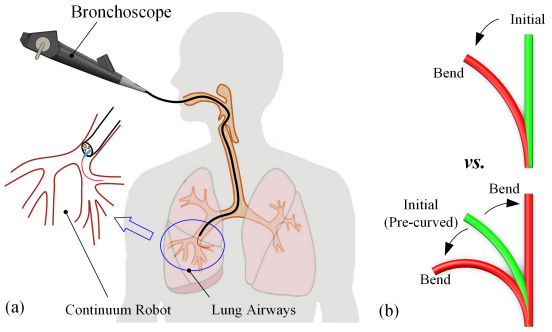

Fig. 1 Endobronchial intervention using the bronchoscope with a miniaturised continuum robot to access the distal airways. (a) shows the clincial applicaiton; (b) shows the comparison of deflection starting from a straight shape and a pre-curved shape.

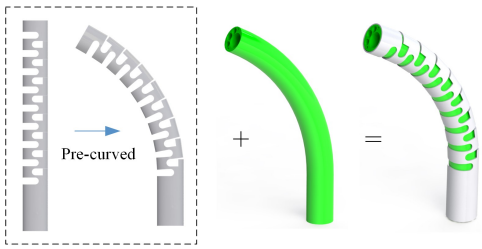

Fig. 2 The concept design of the pre-curved continuum robot consisting of a pre-curved notched nitinol tube and a multi-lumen polymer tube, where the pre-curvature of nitinol tube was formed using heat treament.

curved shape setting for the notched nitinol tube was carried out using heat treatment. After putting the notched tube into a stainless-steel die with a 60° curved fixture, both them were then held in a 500℃ furnace for 15 minutes, followed by a rapid cooling via a water quench. Finally, the multi-lumen polymer tube was inserted into the inner lumen of the notched nitinol tube to provide channels for actuation cables, probes, EM sensors or other surgical tools. It is worth noting that the pre-curvature could have different variations depending on the demands of the maximal bending angle and linear elastic range of the material.

To validate the effectiveness of the proposed pre-curved continuum robot, finite element analysis was applied to simulate the deformation and strain distribution of continuum robot. Ansys workbench 18.2 was used for static structure analysis. Two typical cases were simulated using 60 GPa as Young's Modulus for the nitinol material, where Case I was to bend the original straight notched continuum robot with a rotational angle - 120° as the boundary condition, and

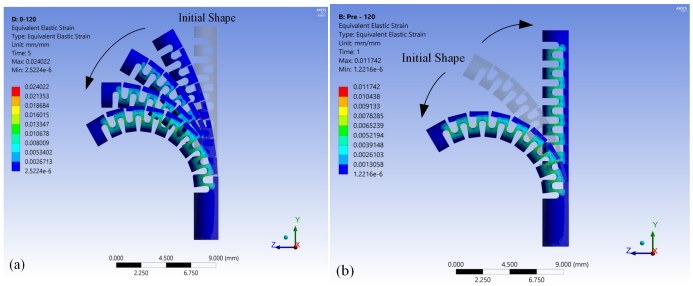

Fig. 3 Deformation and strain distribution. (a) shows the result of straight notched nitinol tube; (b) shows the result of pre-curved notched nitinol tube.

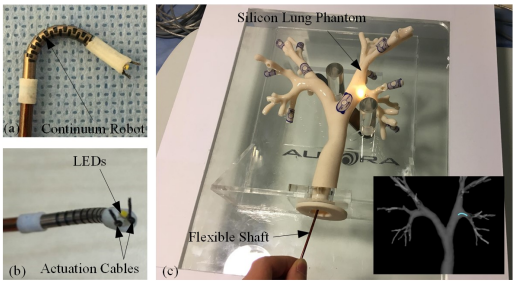

Fig. 4 Phantom study. (a) and (b) show the developed prototype of pre-curved continuum robot; (c) shows the setup and navigation image for the phantom study.

Case II was to bend and recover a 60° pre-curved notched continuum robot with +60° and -60° as the boundary conditions. The maximal strains of two cases were compared. Here, we considered the strain - 1.5% as the maximal linear elastic border for nitinol material.

RESULTS

Fig. 3 shows the deformation and strain distribution of the straight and pre-curved notched nitinol tubes. In (a), when the straight continuum robot was bent to more than 90°, the maximal strain was 2.40%, beyond its linear elastic range; while in (b), given the maximal bending angle as 120° for the pre-curved continuum robot, the maximal strain was only 1.17%, which was within the linear elastic border. Results also indicate that the maximal strain occurs near the centre of each compliant joint, which determines the maximal strain. This is similar to the results in [8]. Modification of compliant joints' parameters could help reduce the maximal strain, therefore increasing the bending angle.

Fig. 4 shows the phantom study of the pre-curved continuum robot integrated with a flexible shaft made of a braided polymer tube (MicroLumen Inc., USA). Two 5DOF EM sensors were placed at the tip and base of the continuum robot to reconstruct its shape using the constant curvature assumption. This shape was displayed together with virtual phantom model in the navigation software. The preliminary endobronchial intervention demonstrated that the proposed continuum robot can reach to the 4th generation successfully, and the increased bending angle can help increase the accessibility to the distal airway with a large bending angle as shown in Fig. 4(c).

DISCUSSION

In this paper, we have shown that the proposed pre-curved continuum robots can potentially enlarge the workspace while ensuring linear elastic property, and multiple lumens are provided for potential tools. The linear characteristics is helpful for online force control, which does not need to consider the hysteresis from the material. Also, the elastic energy stored in the pre-curved continuum robot during the deflection is reduced to around half of that in the straight continuum robot, which is safer during clinical operations. It is worth noting that the deflection range can be enlarged by reducing the height of compliant joints to decrease the maximal strain, but it will make the continuum robot more flexible. Moreover, the pre-curvature can be adjusted for different deflection ranges and shapes. Because of this trade-off between the stiffness and deflection range, there is a potential of optimization in future to look for a best configuration of pre-curvature or notched structure to suit the continuum robot for specific tasks in the confined space. In addition, more sections with different pre-curvatures are worth exploring in terms of the dexterity and adaptability of the continuum robot to the specific anatomy.

REFERENCES

[1] S. Kim, S. Um, *et al.*, "Bronchoscopic features and bronchoscopic intervention for endobronchial hamartoma," *Respirology*, vol. 15, no.1, pp. 150-154, 2010.

[2] R. J. Webster, A. J. Bryan, "Design and kinematic modeling of constant curvature continuum robots: A review," *The International Journal of Robotics Research,* vol. 29, no.13, pp. 1661-1683, 2010.

[3] N. Liu, M. Abdelaziz, M. Shen, G. Z. Yang, "Design and kinematics characterization of a laser-profiled continuum manipulator for the guidance of bronchoscopic instruments," *Proc. IEEE Int. Conf. Robot. Autom.*, 2018, Australia.

[4] M. D. Kutzer, S. M. Segreti, C. Y. Brown, M. Armand, M., R. H. Taylor, S. C. Mears, S. C, "Design of a new cable-driven manipulator with a large open lumen: Preliminary applications in the minimally-invasive removal of osteolysis," *Proc. IEEE Int. Conf. Robot. Autom.*, pp. 2913-2920, 2011.

[5] A. Gao, R. J. Murphy, H. Liu, I. Iordachita, M. Armand, "Mechanical model of dexterous continuum manipulators with compliant joints and tendon/external force interactions," *IEEE/ASME Transactions on Mechatronics*, vol. 22, no. 1, pp. 465-475, 2017.

[6] P. J. Swaney, P. A. York, H. B. Gilbert, J. Burgner-Kahrs, and R. J. Webster III, "Design, fabrication, and testing of a needle-sized wrist for surgical instruments," *ASME Journal of Medical Devices*, vol. 11, no. 1, pp. 014501-9, 2016.

[7] A. A. Remirez and R. J. Webster III, "Endoscopes and robots for tight surgical spaces: use of precurved elastic elements to enhance curvature," *Medical Imaging 2016: Image-Guided Procedures, Robotic Interventions, and Modeling*, vol. 9786, 2016.

[8] A. Gao, R. J. Murphy, H. Liu, I. Iordachita, M. Armand, "Evaluating the deflection of dexterous continuum manipulators with unevenly distributed compliant joints," *Proc. IEEE Int. Engineering in Medicine and Biology Society (EMBC)*, pp. 5099-5102, 2016.

Kinematics and Workspace Analysis of A Contact-Aided Continuum Robot with Laser Profiling

L. Ros-Freixedes[1], A. Gao[1], N. Liu[1], G. Z. Yang[1]

[1]*Hamlyn Centre for Robotic Surgery, Imperial College London*
laura.ros-freixedes17@imperial.ac.uk

INTRODUCTION

Endobronchial intervention is currently a common technique for the diagnosis and therapy toward lung diseases [1]. However, commercial bronchoscopes are usually only able to reach the 3rd or 4th generation of the bronchial tree due to its size and steerability. Although flexible tools can be inserted via the working channel of the bronchoscope, extending its reach to peripheral bronchioles, ergonomic control and lack of direction vision pose major challenges in routine clinical use.

Recently, Liu *et al.* [2] designed a cable-driven continuum robot to address this issue. The proposed continuum robot is constituted of multiple segments with cable-guide disks and interlocking motion-dependent revolute joints. It is actuated by two antagonistic cables that allow bidirectional planar deflection. For in vivo applications, a continuum robot with a constant configuration and no reaction force from tissue is hard to reach all airway segments due to local anatomical variations and confined space of the bronchi, as illustrated in Fig. 1. Collision with the walls can help with the intervention, but result in tissue damage or even penetration if the robot cables are kept being pulled. Nevertheless, there are specific parameters that can be tuned in order to optimize the robot design to access specific regions of the anatomy. These include the number of joints, the length of robot segments and the maximum joint angles. The last one can be tuned by adding constraints to the joints to form contact-aided compliant mechanisms (CCMs). The application of the CCMs allows the robot to adapt its shape to the branching structure, making it easier to access to the target airway with less resistance and fewer risks of damage. The contact-aided approach has previously been investigated with a continuum robot to provide the asymmetric bending shapes for cardiac surgery [3], and a preliminary exploration has been made to accomplish the unidirectional bend for endobronchial intervention in [2].

In this study, we introduce the CCMs to our continuum robot with laser profiling to form asymmetric deflection with non-constant curvature, thereby adjusting the workspace and tip trajectory during endobronchial intervention to adapt to variable bronchi and confined anatomic space. First, the principle of integrating CCMs with our continuum robot with laser profiling is introduced; then kinematics is built and the workspace and profiles of bending angles for all the segments are analysed.

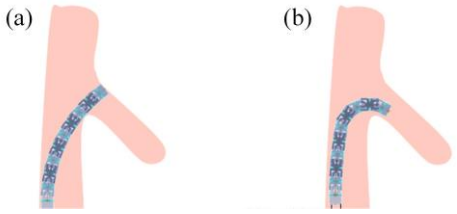

Fig. 1 Comparison of continuum robots with and without CCMs when they are steered inside the airway branches. (a) Without CCMs, collision with anatomy occurs when attempting to go through the bronchus. (b) With CCMs, complete bending with no collision can be achieved.

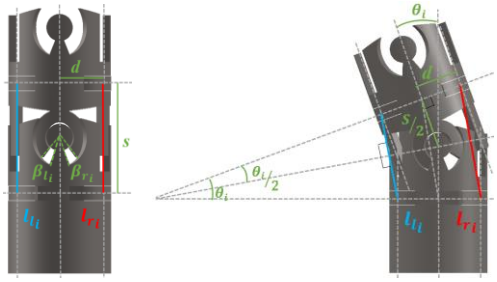

Fig. 2 A schematic illustration of one segment of the proposed continuum robot with a CCM.

MATERIALS AND METHODS

The structure of continuum robot is described in Fig. 2 by showing one segment with double CCMs. They are implemented by adjusting the cutouts with β_l and β_r parameters to limit its maximal bidirectional bending angles. When one driven cable is pulled but a segment reaches its bending limit, the deflection of this segment is fixed and the other segments will increase their bending angles continuously. The parameters of cutouts for each joint can be independently specified, therefore different configurations of CCMs can be set along the continuum robot, which can further improve its deflection to adapt to diverse anatomical structures.

To describe the deflection of the continuum robot, kinematics considering each segment's constraints was built. For each segment in Fig. 2, the relationship between the lengths of left and right cables - l_{l_i} and l_{r_i} - and the joint bending angle θ_i was built as:

$$l_{l_i} = 2 \cdot (s/(2 \cdot \tan(\theta_i/2)) - d) \cdot \sin(\theta_i/2) \quad (1)$$

$$l_{r_i} = 2 \cdot (s/(2 \cdot \tan(\theta_i/2)) + d) \cdot \sin(\theta_i/2) \quad (2)$$

$$\theta_i = 2 \cdot \sin^{-1}((l_{r_i} - l_{l_i})/(4 \cdot d)) \quad (3)$$

where s is the length of the section centreline, d is the distance from the centre of the section of the robot to

the centre of actuation, and $i \in [1,n]$ is the segment number, where n is the number of segments (*see Fig. 2*).

An algorithm was developed to deduce the shape of the robot with CCMs. Given the change of cable length as the input, the segment cable lengths were found. Then, the corresponding segment bending angles were calculated without considering constraints by using Eq. 3. After that, we checked if any segment reached its deflection limit. If so, its bending angle was set to the deflection limit and the angles for the remaining segments were recalculated. Then it was checked again if any of the remaining segment joints reached their limits. The process was repeated until no further constraints were encountered. Finally, forward kinematics was applied to find the final shape of the robot by using the transformation matrices:

$$T_0^i = T_0^1 \cdot T_1^2 \cdot \ldots \cdot T_{i-1}^i \tag{4}$$

$$T_{i-1}^i = \begin{bmatrix} \cos\theta_i & 0 & -\sin\theta_i & -\sin\theta_i \cdot s/2 \\ 0 & 1 & 0 & 0 \\ \sin\theta_i & 0 & \cos\theta_i & \cos\theta_i \cdot s/2 + s/2 \\ 0 & 0 & 0 & 1 \end{bmatrix} \tag{5}$$

where $i \in [1,n]$ is the segment number.

Deflection simulations were performed for both the robots with and without CCMs. The bending limits used are detailed in Table 1 and were set considering that the maximum joint angle range cannot be above 40º for the robot configuration to be feasible. The other robot parameters were set to $n = 9$, $s = 2.28\ mm$ and $d = 0.85\ mm$. Workspaces were obtained by calculating the position of the distal tip, placed at a distance of $1.17\ mm$ from the last disk center, and considering a full revolution along the longitudinal direction.

RESULTS

Fig. 3 (a) and (b) show the shape differences between the robots with and without CCMs. Note that joint contacts do not take place at the same time in both cases given the bending limits. In contrast with the simple arcs that are formed when the robot deflects without the CCMs, more complex shapes are achieved when constraints on multiple segments are applied. The figure also shows that the addition of constraints with CCMs can allow asymmetric bending shapes in comparison to the unconstrained case. The associated workspace of the constrained and unconstrained continuum robots is evident from the changes, as shown in Fig 3 (c) and (d). It shows that smaller volumes could be achieved when CCMs are applied appropriately. This indicates that CCMs could be beneficial to achieve a large bending curvature in confined spaces such as the airways.

Fig. 4 shows the profiles of segment bending angles of the deflections from the continuum robots in Fig 3 (a) and (b). Results show that non-constant curvature can be achieved when CCMs are integrated to the continuum robot.

DISCUSSION

The proposed approach shows that the robot can achieve non-constant curvature shapes and asymmetric deflection by configuring constraints using CCMs at each joint. This facilitates the development of patient specific continuum robots designed to reach unreachable bronchi with increased safety.

Future work will focus on the use of this kinematic model considering constraints on the bending angles to optimize the robot structure given a patient's anatomy. We will establish the best parameter values (i.e. robot length, deflection limits) to navigate through a specific bronchus, without relying on the tissue reaction force and avoid collision with the bronchi walls.

Table 1. Joint deflection limits for the continuum robot

	Without CCMs	Asymmetric CCMs, **left** part	Asymmetric CCMs, **right** part
Joint deflection limits	20º to both directions	First five limited to 2º. Last four limited to 30º	10º

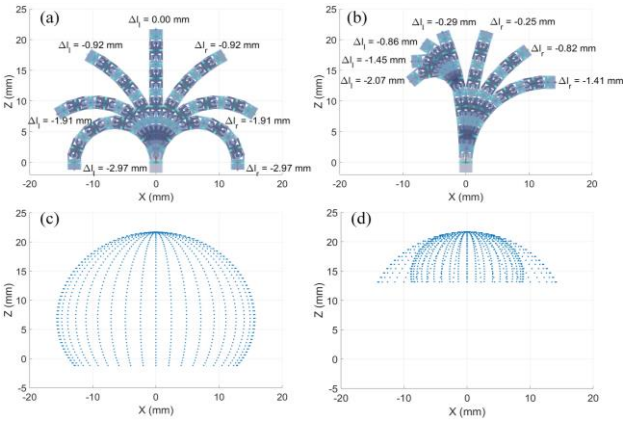

Fig. 3 Different shapes for different change of cable length and workspace of the robot without CCMs (a, c) and with CCMs (b, d). Negative change of length indicates that the cable is being pulled.

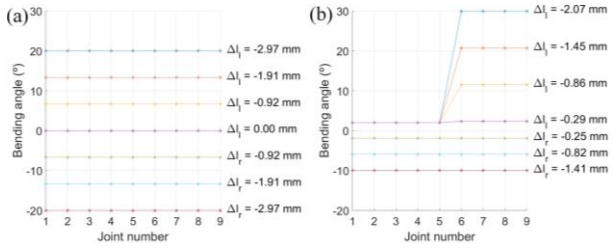

Fig. 4 Segment bending angles for the deflection cases shown in Fig. 3 (a) and (b) for the continuum robot without CCMs (a) and for the continuum robot with CCMs (b).

REFERENCES

[1] Yu DH, Feller-Kopman D. Interventional bronchoscopy in adults. *Expert Rev. Respir. Med.* 2018; 12(3): 239–248.

[2] Liu N, Abdelaziz M, Shen M, Yang GZ. Design and kinematics characterization of a laser-profiled continuum manipulator for the guidance of bronchoscopic instruments. *Proc IEEE Int Conf Robot Autom.* 2018, Australia.

[3] Gao A, Hao L, Zou Y, Wang Z, Liang M, Wang Z. Contact-Aided Asymmetric Steerable Catheter for Atrial Fibrillation Ablation. *IEEE Robot Autom Lett.* 2017; 2(3): 1525-1531.

A Systematic Modelling Approach for Motor-Cable-Joint Kinematics of Coupled Tendon-Driven Surgical Instrument

X. Y. Chu[1], T. Y. Chung[1], and K. W. Samuel Au [1, a]

[1] *Dept. of Mechanical and Automation Engineering, The Chinese University of Hong Kong*

[a] *samuelau@cuhk.edu.hk*

INTRODUCTION

Tendons/cables are widely used to convert motor motion into the joint movement of a surgical instrument. These tendons can couple with the instrument joints and drive motors in many different ways, depending on the geometry and mechanical design. Developing a kinematics model to describe these coupling relationships is not trivial and often is quite time-consuming. [1, 2] built the kinematics for their own designs, however, few efforts have been made to post a systematic modelling method. In this paper, we present a general approach to model the motor-cable-joint kinematics for a class of coupled tendon-driven surgical instrument with the rolling joint. We also implemented the proposed method into our dVRK system to control the articulated wrist joints of our retractor instrument (Figs. 2 a,b). Initial results showed that we can predict the coupling effectively and control a dVRK compatible retractor instrument.

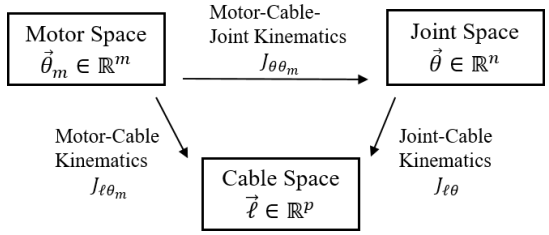

Fig. 1: General kinematics representation for the tendon-driven instrument

Methods

Fig. 1 shows the general representation of the motor-cable-joint kinematics for a coupled tendon-driven instrument. Our method requires to first derive the motor-cable and joint-cable kinematics or Jacobian mappings. We ignore the cable stretch in our derivation. Assume our instrument has multiple rolling joints connected in series and we first consider the k-th joint (Figs. 2 b,c) of an instrument, where $\ell_{k,1}$ and $\ell_{k,2}$ represent the cable length of the first and second cables. Using trigonometry, we have $\delta\ell_{k,1} = 2\lambda\sin(\frac{\theta_k}{2}) = -\delta\ell_{k,2}$, where λ is the moment arm between the center axis and the cable, and $\delta\ell_{k,1}, \delta\ell_{k,2}$ are the cable length variations by rotating the k-th joint to θ_k. $\delta\ell_{k,i}$ is defined to have a positive sign when the i-th cable is being pulled. The joint-cable geometry for the k-th joint is

$$\delta\vec{\ell} = \begin{bmatrix}\delta\ell_{k,1}\\ \delta\ell_{k,2}\end{bmatrix} = \begin{bmatrix}-2\lambda\sin(\frac{\theta_k}{2})\\ 2\lambda\sin(\frac{\theta_k}{2})\end{bmatrix}. \quad (1)$$

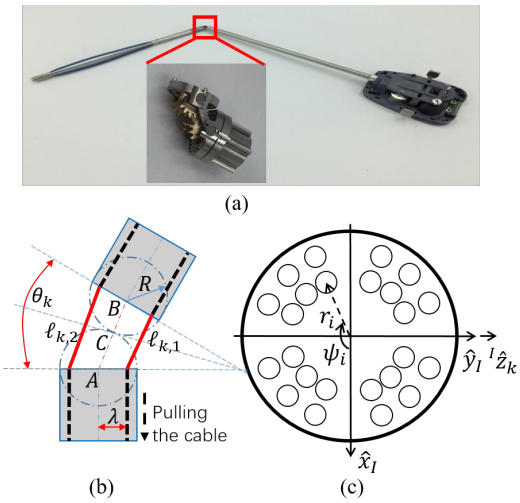

Fig. 2: (a)Prototype of retractor instrument and joint; (b) General geometry of the rolling joint; (c)Cross-section view of a general instrument design.

By linear approximation, we can represent the joint-cable kinematics at the k-th joint by a linear Jacobian matrix as

$$\delta\vec{\ell} = J_{\ell\theta}\delta\theta_k, \quad (2)$$

where $J_{\ell\theta} \in \mathbb{R}^{p\times n}$ is the Jacobian matrix that relates joint angle variation vector $\delta\vec{\theta}_k$ to cable length variation vector $\delta\vec{\ell}$. For a single joint, $J_{\ell\theta} = [-\lambda, \lambda]^T$.

For a general instrument, we may have multiple joints connected in serial configuration, thus multiple cables may pass through the same k-th joint at the same time. Fig. 2c shows a cross-section view of a general instrument design. We define an instrument frame $\{I\}$ and ${}^I\hat{z}_k$ is the z-axis for the k-th joint projected onto the frame $\{I\}$. For illustration purpose, ${}^I\hat{z}_k$ is set to be parallel to $\hat{y}_I$. In fact, ${}^I\hat{z}_k$ can be in any direction on the $\hat{x}_I\hat{y}_I$ plane depending on how the joints are connected serially. ψ_i and r_i are the cable angle and radius of the i-th cable w.r.t the center of the frame $\{I\}$. The effective radius of the i-th cable for the k-th joint w.r.t. the frame $\{I\}$, ${}^I\vec{\lambda}_{k,i}$ can be defined as ${}^I\vec{\lambda}_{k,i} = g(i,k)\begin{bmatrix}r_i\sin\psi_i & -r_i\cos\psi_i & 0\end{bmatrix}^T$, where $g(i,k) = 0$ if the i-th cable does not pass through the k-th joint, i.e., it terminates before the k-th joint, otherwise $g(i,k) = 1$. Once you project the effective radius onto the axis of rotation $({}^I\hat{z}_k)$, the i-th cable length variation at the k-th joint for θ_k is given by $\delta\ell_{k,i} = ({}^I\vec{\lambda}_{k,i} \cdot {}^I\vec{z}_k)\delta\theta_k$, where θ_k is assumed to be small. Adding all the length variation for each joint for the i-th cable, the total cable length

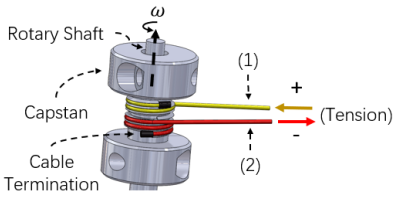

Fig. 3: Cable routing and termination at a capstan of the instrument backend. Assume that w is the rotation direction of the motor. When the motor rotates the capstan in a positive direction, the tension in cable (2) will decrease because the cable (2) was wrapped around the capstan in a counter-clockwise direction, i.e., $S_{wrap}(i) = -1$. On the contrary, as cable (1) was wrapping around the same capstan in a clockwise direction, cable (1)'s tension will increase for the same motor movement, i.e., $S_{wrap}(i) = +1$.

for the i-th cable becomes

$$\delta\ell_i = \sum_{k=1}^{n} \delta\ell_{k,i} = \begin{bmatrix} {}^I\vec{\lambda}_{1,i} \cdot {}^I\vec{z}_1 \\ {}^I\vec{\lambda}_{2,i} \cdot {}^I\vec{z}_2 \\ \vdots \\ {}^I\vec{\lambda}_{n,i} \cdot {}^I\vec{z}_n \end{bmatrix}^T \begin{bmatrix} \delta\theta_1 \\ \delta\theta_2 \\ \vdots \\ \delta\theta_n \end{bmatrix} = J_{(i)}^T \delta\vec{\theta},$$

where $J_{(i)}^T$ and $\delta\vec{\theta}$ are the i-th row of the Jacobian matrix and joint space variable vector, respectively. The joint-cable kinematics for an instrument with n joints and p cables is

$$\delta\vec{\ell} = J_{\ell\theta}\delta\vec{\theta} = \begin{bmatrix} J_{(1)} & J_{(2)} & \dots & J_{(p)} \end{bmatrix}^T \delta\vec{\theta}. \quad (3)$$

On the other end of an instrument, each cable wraps around a capstan in certain direction to convert motor rotation into linear cable displacement (Fig. 3). The motor-cable kinematics for the i-th cable by the g-th motor can be described as $\delta\ell_i = S_{wrap}(i) r_{c,g} \delta\theta_{m,g}$, where $\delta\theta_{m,g}$ and $r_{c,g}$ are the motor position variation and the radius of the capstan for the g-th motor. S_{wrap} is a function to describe the wrapping direction of the cable w.r.t. motor rotation direction. The motor-cable kinematics for a general instrument

$$\delta\vec{\ell} = J_{\ell\theta_m}\delta\vec{\theta}_m, \quad (4)$$

where $J_{\ell\theta_m}$ is the Jacobian matrix that maps motor velocities to cable velocities. For a single joint, $J_{\ell\theta_m} = [r_c, -r_c]^T$, where r_c is the capstan radius.

The motor-cable-joint kinematics between the motor space and the joint space is represented as

$$\delta\vec{\theta} = J_{\theta\theta_m}\delta\vec{\theta}_m, \quad (5)$$

where $J_{\theta\theta_m} \in \mathbb{R}^{n\times m} = J_{\ell\theta}^{\#} J_{\ell\theta_m}$, and $J_{\ell\theta_m}^{\#}$ is the pseudoinverse of $J_{\ell\theta}$.

RESULTS

We used the proposed modelling method to derive the motor-cable-joint kinematics of the retractor instrument with two joints connected serially(Fig. 4a). Substituting instrument parameters, the Jacobian matrix $J_{\ell\theta}$, $J_{\ell\theta_m}$ and $J_{\theta\theta_m}$ can be derived as

$$J_{\ell\theta} = \begin{bmatrix} r_2\sin\psi_2 & -r_2\cos\psi_2 \\ r_6\sin\psi_6 & -r_6\cos\psi_6 \\ r_8\sin\psi_8 & -r_8\cos\psi_8 \\ r_{12}\sin\psi_{12} & -r_{12}\cos\psi_{12} \end{bmatrix} \quad J_{\ell\theta_m} = \begin{bmatrix} r_{c,1} & 0 \\ 0 & -r_{c,2} \\ -r_{c,1} & 0 \\ 0 & r_{c,2} \end{bmatrix}$$

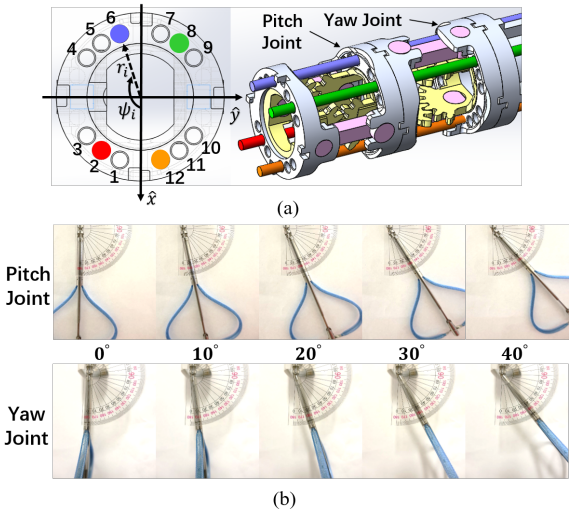

Fig. 4: (a)Schematics of the two coupled joints. All four cables terminate at the end of the distal joint; (b)Validation on the implementation of the motor-cable-joint kinematics. The overall tracking error is about ($\pm 2^\circ$), which is acceptable from a retraction perspective.

$$J_{\theta\theta_m} = \begin{bmatrix} -1.1417 & 0.9717 \\ -0.3782 & -0.7086 \end{bmatrix}.$$

$J_{\theta\theta_m}$ is a non-diagonal constant matrix which creates a strong coupling between the motor and joint positions. We implemented the proposed kinematics mapping into the dVRK and tested with our retractor instrument. We sent different individual joint position commands and measured the actual joint movement through a projector (Fig. 4b). Each joint can track the target position precisely without noticeable movement in the other joint. This implies that the motor-cable-joint kinematics was designed and can effectively address the motor-cable-joint coupling issue. For instance, when the pitch joint was being tested, there was no observable movement in the yaw joint.

DISCUSSION

A systematic motor-cable-joint kinematics modelling method for a class of tendon-driven surgical instrument was developed. With the knowledge of instrument structures and parameters, the kinematics can be obtained systematically. We implemented the proposed model into our dVRK system for the control of a wristed retractor instrument. In the future, we will focus on solving nonlinearity compensation problem to achieve large target position in the joint space.

REFERENCES

[1] N. Evangeliou et al., "Design and Antagonistic Control of a Tendon-Driven Minimally Invasive Surgical Robotic Tool," *Mediterranean Conference on Control and Automation*, pp. 725-730, 2016.

[2] H.Q Sang et al., "Kinematic Analysis of a Class of Multi-DOF Tendon-driven Minimally Invasive Surgical Instruments," *International Conference on Computer Science and Network Technology*, pp. 607-612, 2011.

Impact of Jaw Orientation on Grip Force Estimation for a da Vinci EndoWrist Surgical Tool

T.K. Stephens[1], J.J. O'Neill[2], N.J. Kong[1], T.M. Kowalewski[1]

[1]*Department of Mechanical Engineering, University of Minnesota*

[2]*University College London, London, UK*

steph594@umn.edu

INTRODUCTION

The utlization of accurate grip force estimates during surgical procedures has been widely proposed as a benefit for robotic surgery. Several research publications have proposed varying methods for obtaining this estimate with generally high accuracy [1, 2]. Despite these positive results, many of the proposed methods neglect the impact that the jaw orientation (i.e. roll, pitch, and yaw) has on estimation accuracy. Previous work has shown that grip force in general varies up to three-fold with jaw orientation [3]; we aim to extend upon these raw results by quantifying how accurate our proposed grip force estimation technique is across a wide range of jaw orientations. This work is a further step towards establishing more realistic expectations for applications of grip force estimation in a surgical setting.

MATERIALS AND METHODS

Custom hardware was built and utilized to obtain synchronized data between the distal end (Fig. 1A) and proximal end (Fig. 1B) of a da Vinci EndoWrist Maryland Bipolar Forceps during sinusoidal grasping. Position and torque data were time-synchronously collected on both ends. Details of the hardware setup including the sensors used on the proximal and distal ends are explained in [4] and [5], respectively. For this dataset, the tested range of orientations included the following: pitch angles (-60 to +60°), roll angles (-90 to +90°) and yaw angles (-90 to +30°). The jaw position (θ) is actuated by the same degree of freedom as yaw. For testing, this jaw position performed grasps 45° from the current yaw angle in a sinusoidal trajectory. Resistive torque was applied directly to the distal jaw at a fixed point and ranged from 25 to 100 mNm.

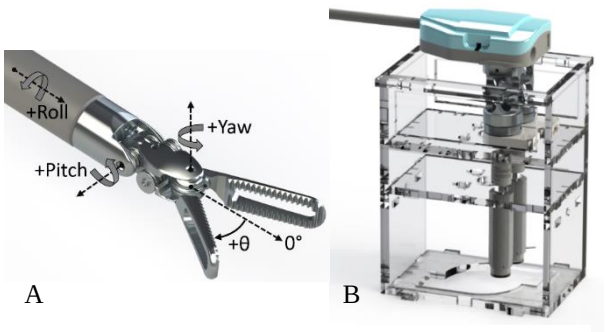

Fig. 1 Renderings of (A) distal-side with coordinate frame notation (B) proximal-side hardware for data collection

The estimation technique utilized in this work is an artificial neural network similar to the one explained in [4]. The neural network architecture consisted of 60 nodes in a single hidden layer, with input features of position, velocity, torque, pitch spindle, and roll spindle all measured on the proximal end. The neural network was trained with torque as the output as measured at the distal end. Training was performed using the scaled conjugate gradient method for back-propagation with a log-sigmoid activation function at the hidden layer and a purely linear activation function at the output layer. The neural network was implemented using the Neural Network Toolbox in MATLAB.

Two separate experiments were conducted. Experiment 1 consisted of fixing pitch and varying the roll and yaw angles; experiment 2 consisted of fixing roll and varying the pitch and yaw angles. For experiment 2, the variations on pitch limited the yaw angles we could test due to physical constraints of the hardware. Therefore, for this experiment a subset of yaws were used from 0 to +30°. A control dataset was used for comparison which consisted of fixing all three degrees of freedom (i.e. fixing roll, pitch, and yaw). In this manner a more diverse (and realistic) subset of jaw orientations were included for experiments 1 and 2 as opposed to traditional approaches of testing in the jaw's neutral orientation (i.e. fixing all three degrees of freedom). For each experiment the respective dataset was binned into five randomized test subsets with the complementary data utilized for training data. This resulted in five different training datasets, and accordingly five-fold cross validation was performed.

The average root-mean-square error (RMSE) and 95th percentile across all five folds was computed for both experiments and the control. Additionally a time series was plotted to visualize the estimation errors in the temporal domain.

RESULTS

The results for RMSE, 95th percentile, as well as number of time samples (N) across all folds for both experiments and the control are included in Table 1.

A sample time series is shown in Figure 3 to give visual context of the estimation in the temporal domain. The time-series is shown in a non-neutral jaw orientation for experiments 1 and 2, and the neutral jaw position for the control.

Tab. 1 Results from each dataset depicting averages from the five-fold validation for RMSE and 95th percentile as well as the number of time samples in the respective dataset.

Dataset	RMSE [mNm]	95th % [mNm]	N [samples]
Control (Varied no DOF)	1.37	1.37	30,691
Experiment 1 (Varied roll, yaw)	2.85	5.22	764,076
Experiment 2 (Varied pitch, yaw)	2.94	4.98	305,681

DISCUSSION

The results from experiments 1 and 2 show that orientations in these datasets. The RMSE for both experiments increases when compared with the control, but is still relatively low at 2.90 mNm, on average.

This estimation technique compares favorably to existing grip force estimation results reported in literature, even with the non-fixed jaw orientations. As an example, the results in [1] report an average error of 0.07 N for grasps with a peak force of roughly 1 N. This was accomplished via Gaussian Process Regression. Our results, when converted to force, resulted in an RMSE of 0.29 N for grasps with a peak force of approximately 10 N. When comparing the error percentage of peak grasping force the results in [1] yield 7% error, while our results yield 3% error. This comparison is not meant to definitively state which estimation techniques is superior, especially considering the multiple factors which differ between experimental setups. However, it is an attempt to suggest that despite the inclusion of varied jaw orientations, estimation of the force at the distal end is realizable.

This work progresses the efforts in grip force estimation by incorporating a wider range of jaw orientations in the training dataset. However, there are some shortcomings within this work which still exist as barriers to transition this work in clinical settings. These shortcomings are recognized and presented here as future work.

Firstly, the experimentation was accomplished by varying two degrees of freedom at a time while keeping one fixed. Although this may accurately represent some surgical scenarios (e.g. fixed roll with varied pitch and yaw), the more generalizable approach would be to allow all degrees of freedom to vary in the training dataset.

Secondly, the impact of grasping frequency was purposefully neglected in this study, but would need to be analyzed prior to clinical adoption. Although many surgical motions occur at relatively slow speeds, the existing estimation technique may suffer if training data across all these speeds is not included.

Additionally, the variations between EndoWrist tools was not analyzed in this work. A single Maryland Bipolar Forceps was used in testing; future work will explore the variations within this specific tool as well as the variations between different types of tools.

Much work remains to translate this for clinical use, but the merely-minor reduction in estimation accuracy when including jaw orientations is encouraging. Previous results in [3] reported three-fold variation in raw grip force, but despite these large variations the estimation technique presented here yields promising results.

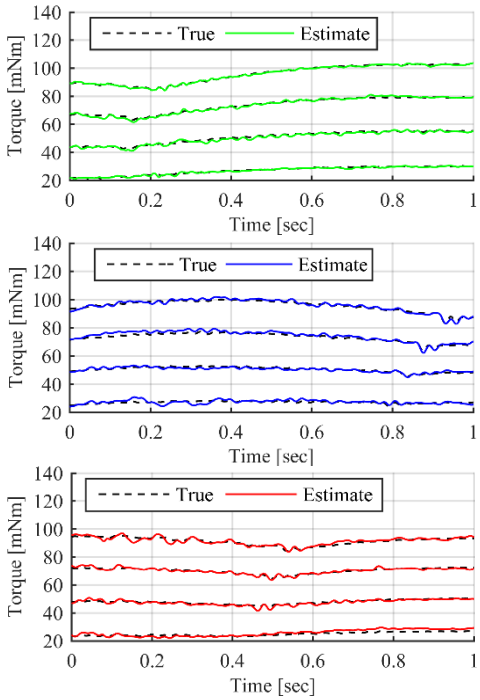

Fig. 3 Time series example data for control (top), experiment 1-varied roll+yaw (middle), and experiment 2-varied pitch+yaw (bottom), for each tested level of torque.

ACKNOWLEDGEMENTS

Research was sponsored in part by the Army Research Laboratory and was accomplished under Cooperative Agreement Number W911NF-14-2-0035. The views and conclusions contained in this document are those of the authors and should not be interpreted as representing the official policies, either expressed or implied, of the Army Research Laboratory or the U.S. Government. The U.S. Government is authorized to reproduce and distribute reprints for Government purposes notwithstanding any copyright notation herein. Additionally, this material is based upon work supported in part by the National Science Foundation Graduate Research Fellowship under Grant No. 00039202. Any opinion, findings, and conclusions or recommendations expressed in this material are those of the authors and do not necessarily reflect the views of the National Science Foundation.

REFERENCES

[1] Li Y, Hannaford B. Gaussian process regression for sensorless grip force estimation of cable-driven elongated surgical instruments. IEEE Robotics and Automation Letters. 2017 Jul;2(3):1312-9.

[2] Anooshahpour F, Polushin IG, Patel RV. Quasi-static modeling of the da Vinci instrument. In IEEE/RSJ International Conference on Intelligent Robots and Systems (IROS 2014), 2014 Sep 14 (pp. 1308-1313).

[3] Lee C, Park YH, Yoon C, Noh S, Lee C, Kim Y, Kim HC, Kim HH, Kim S. A grip force model for the da Vinci end-effector to predict a compensation force. Medical & Biological Engineering & Computing. 2015 Mar 1;53(3):253-61.

[4] Kong NJ, Stephens TK, Kowalewski TM. Da Vinci tool torque mapping over 50,000 grasps and its implications on grip force estimation accuracy. In IEEE Proceedings of the International Symposium on Medical Robotics (ISMR 2018), 2018 Jan 14.

[5] Kong NJ, Stephens TK, O'Neill JJ, Kowalewski TM. Design of a portable dynamic calibration instrument for da Vinci Si tools. In ASME Design of Medical Devices Conference (DMD 2017), 2017 Apr 10 (pp. V001T11A023).

Self-Collision Detection for Dual Arm Concentric Tube Robots

S. Sabetian[1], T. Looi[1], E. Diller[2], J. Drake[1]

[1]Centre for Image-Guided Innovation and Therapeutic Intervention, SickKids Hospital

[2] Department of Mechanical and Industrial Engineering, University of Toronto

saba.sabetian@mail.utoronto.ca

INTRODUCTION

Epilepsy affects more than 50 million people worldwide with 30% of patients require surgical intervention as a primary treatment. The neurosurgical treatment of an epileptic focus involves large skin incisions, extensive bone removal, and excision of brain tissue [1]. One such epilepsy procedure is for hemishperectomy, where the abnormal epileptic hemisphere, is disconnected from the rest of the brain. Currently a major open neurosurgical procedure, it would be technically fesasible to perform the procedure minimally invasively using dexterous tools, working within the cerebral ventricles. Minaturized continuum robots such as Concentric Tube Robots (CTRs) would be well-suited for such an endoscopic minimally invasive approach [2]. Such a procedure requires the use of two tools simultaneously. The challenge for the design and development of a real-time module for dual arm CTR is to detect inter-collision between arms. Self-collision in CTRs can potentially occur due to three main design limitations. First, there is no sensor on the body of each manipulator for localization of arms, with respect to each other. Second, the workspace of the arms overlap. Last, there is no information regarding the shape of each arm in cartesian space since only tip position is controlled.

We have implemented a real-time self-collision detection algorithm for a dual arm CTR system intended to perform epileptic surgery minimally invasively. The algorithm is tested using a 3D model to visualize the arms in varying configurations. The parameters used in the algorithm were modified to measure their impact on performance. The self-collision detection module was also tested in simulation to reach multiple target points in the lateral ventricles in a scenario of minimally invasive epileptic surgery for hemispherectomy.

MATERIALS AND METHODS

A real-time control system has been developed for two 6 Degrees of Freedom (DOF) CTR arms using differential Jacobian-based inverse kinematics with two tasks with different priorities [3]. The first priority task is joint-level constraints that account for unstable configurations. The second task is end-effector tracking.

The self-collision detection module was designed to take the joint values of each arm and descretize the arm body into *n* segments as shown in Fig. 1. Each discretized point is denoted as p_i^j where subscript *i* is referring to the point number and superscript *j* is referring to the arm. The cartesian position of each discretized point along the manipulators is calculated using Forward Kinematics [3]. These cartesian positions are with respect to the proximal end of the corresponding arm. Since the base of Arm 2 is **5mm** apart from the base of Arm 1 in x-direction in trocar channels, the position of points along Arm 2 is mapped to the base of Arm 1. This way both arms are defined in the same coordinate system with the base of Arm 1 to be the origin as illustrated in Fig. 1. To detect self-collision, a set of euclidean distances was computed between a specific discretized points on Arm 1 to all other points on Arm 2 as shown in Fig. 1-a. This is repeated for all points along Arm 1. Then, the minimum distance among all sets of distances was found. The inter-collision is predicted, if the minimum distance between arms for all sets are maintained as a positive value less than a threshold distance, d_{th}. We set the threshold value to be the sum of outer radius of inner tubes with a safety factor.

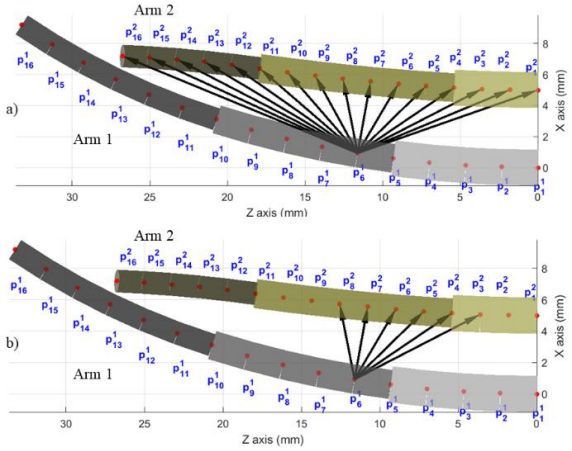

Fig. 1 3D model of CTR used for inter-collision detection. **a)** No pruning; **b)** Pruning to 5 neighbouring points.

To decrease computation time, a pruning approach was implemented [4]. The set of distances was calculated only between active pairs of points instead of all pairs. Active pairs are the neighbouring points as shown in Fig. 1-b with potentially dangerous trajectories. The effect of reducing number of points is evaluated in a test to study the performance of the proposed self-collision algorithm.

RESULTS

A test workspace was generated with **1078** different joint values for outer and middle tube of Arm 2 while Arm 1 remains stationary at specific joint values of *q1=[0;10;0;20;0;45]* where odd joints represent rotation angles and even joints represent translation lengths of outer, middle and inner tube respectively. The inner tube length of Arm 2 was set to 45 mm and rotation angle to π. The tube design parameters were recorded in Table 1

where *OD* and *ID* refer to outer and inner diameter of tubes, *E* is the elastic modulus, *k* is the tube curvature and L_c represents the length of tubes constituted of only curved section.

Table 1 Tube Design Parameters

Tube	outer	middle	inner
OD (mm)	2.31	1.85	1.45
ID (mm)	2.11	1.70	1.32
E (GPa)	56.073	57.9656	61.293
k (mm^{-1})	0.013	0.013	0.0207
L_c (mm)	[0, 20]	[0, 20]	[0, 45]

The accuracy of the proposed collision detection module was evaluated by comparing its results to the number of visually observed collisions using a simulated 3D model of the arms (**859)** shown in Fig. 2. An example of 3D model is shown in Fig. 1. The safety factor was set to 5% of threshold value. The performance of the proposed efficient pruning approach is illustrated in Fig. 3. The computational time reduced **46.04%** on average.

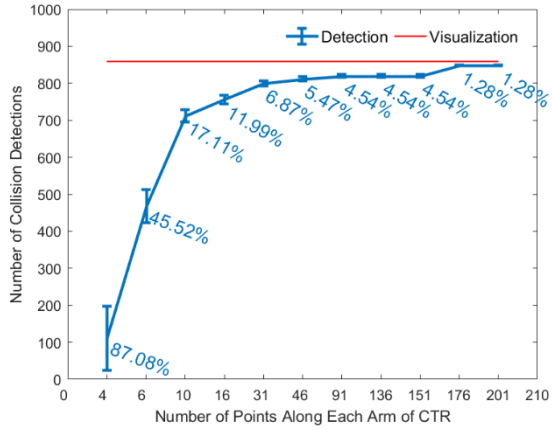

Fig. 2 Comparison of self-collision detection performance for various number of points along each arm.

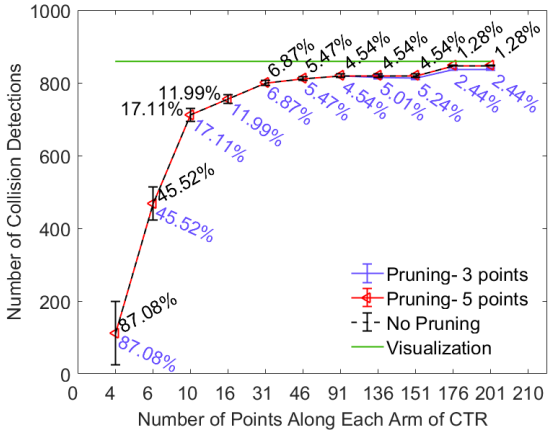

Fig. 3 Comparison of self-collision detection performance with and without pruning with safety factor=5%.

Additionally, the algorithm was validated in a clinical scenario similar to epileptic surgery to reach **15** target points on the surface of lateral ventricle as shown in Fig. 4. The implemented control system takes the position of two consecutive target points as desired tip position of each arm and detect inter-collision at each trajectory. Self-collision is predicted in **12** out of **15** target points. The average Root Mean Square (RMS) value of tip position error is computed to be **3.83e^{-6}**mm and **1.15e^{-4}** mm for Arm 1 and Arm 2 after **1000** iterations. The calculated joint values of both Arm 1 and Arm 2 are within the pre-defined physical constrains.

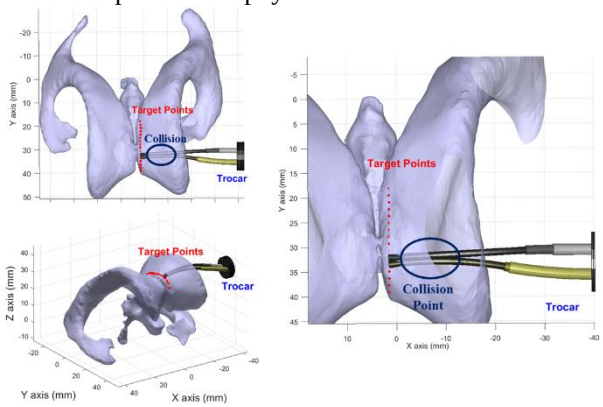

Fig. 4 3D model of ventricles used for self-collision detection.

DISCUSSION

Fig. 2 illustrates, as the number of points along dual arm CTR increases, the number of collision detection also increases until it plateaus at about **91** points. Fig. 3 highlights the efficiency of the pruning algorithm. With pruning using 5 neighboring points, similar results can be generated compared to no pruning with the benefit of **46.04%** reduction of computation time on average. This reduction is more significant with a higher number of points (from **0.0368±7.07e^{-4}** to **0.0086±2.78e^{-4}** seconds for 200 points). The collision detection results of the clinical scenario exemplify its importance in surgical application. The entry point is selected to have middle temporal incision point [1]. The entry point and tube design are selected to reach all target points; however, further optimization is required. Although, the reported tip position errors are significantly small, the tip position accuracy is expected to decrease with real systems due to fabrication uncertainties, sensing performance, and model deviations. In this clinical scenario, the CTR arms are working within the cerebrospinal fluid, thus, there is no interaction with soft tissue; accounts as free space. Future work will involve experimentally validation of proposed control system with self-collision detection in both free-space and contact therapy. Further, it will be tested in more surgical applications such as eye surgery.

REFERENCES

[1] C. Link, “Concentric Tube Robotics : Non-Linear Trajectories for Epilepsy Surgery The Harvard community has made this article openly available . Please share how this access benefits you . Your story matters . Accessed,” 2016.

[2] T. Anor, J. R. Madsen, and P. Dupont, “Algorithms for design of continuum robots using the concentric tubes approach: A neurosurgical example,” *Proc. - IEEE Int. Conf. Robot. Autom.*, pp. 667–673, 2011.

[3] H. Azimian, T. Looi, and J. Drake, “Closed-Loop Inverse Kinematics Under Inequality Constraints : Application to Concentric-Tube Manipulators,” no. Iros, 2014.

[4] J. Kuffner and K. Nishiwaki, “Self-Collision Detection and Prevention for Humanoid Robots,” *IEEE Int. Conf. Intell. Robot. Autom.*, no. May, pp. 2265–2270, 2002.

Mechanics Modelling of Eccentrically Arranged Concentric Tubes

Z. Mitros[1], M. Khadem[1], C. Seneci[1], L. DaCruz[1,2*], and C. Bergeles [1,2*]

[1] *Wellcome/EPSRC Centre for Interventional and Surgical Sciences, UCL, London*

[2] *UCL Institute of Ophthalmology*

*zisos.mitros.17@ucl.ac.uk , *Equal Senior Authorship*

INTRODUCTION

Continuum robots allow accessing surgical targets deep inside the human body by steering along 3D curves in confined spaces. Further, they provide enhanced dexterity compared to traditional instruments [1]. Concentric Tube Robots (CTRs) are representative continuum robots that exhibit shape change by the relative translation and rotation of precurved elastic tubes, telescopically inserted into each other. CTRs were originally envisioned as "single-arm" robots [2],[3] but are nowadays also considered as parts of "multi-arm" systems for surgical procedures (*e.g.*, in the prostate [4] or brain [5]).

Although mechanics-based models have been developed that can describe the shape of a single CTR of any number of tubes and different precurvatures [6, 2], limited work on multi-arm CTRs and their modelling has been performed. Contrary to prior work that considers the backbone that houses multiple robotic arms as stiff and "decoupled" from the motion of the flexible arms [7, 4], the proposed work accounts for the interactions between an arbitrary number of CTR arms and the flexible backbone. The theory is developed for a multi-arm continuum robot comprising a flexible CTR backbone that houses several CTR arms as end-effectors (see Fig. 1).

MATERIALS AND METHODS

The robot that motivates the modeling research is being designed for optic nerve glioma applications. It is envisioned that it will navigate peri-ocularly to reach the optic nerve. The backbone CTR is a 3 Degree-of-Freedom (DoF) variable stiffness section, comprising two precurved tubes. It is a "navigation section" providing global positioning for two flexible instruments and a camera. The arms act as "manipulation sections", carrying the end effectors for tissue manipulation and lesion treatment. Each robotic arm comprises two tubes, *i.e.* 4 DoFs. A filling material is placed inside the navigation section to retain the separation of the flexible manipulation sections within the robot's navigation backbone (see Fig. 1). The filling material is required to avoid contact between the CTR arms and ensure continuous contact between the manipulation arms and the navigation arm.

To develop the theoretical model for a multi-arm CTR as an eccentric arrangement of multiple CTRs, the Cosserat rod theory is employed with the assumptions of the classical elastic-rod theory of Kirchoff [6]. To get the shape of each tube, a set of differential equations, with kine-

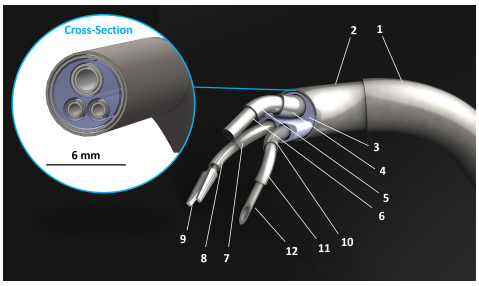

Fig. 1: Main components and architecture of the proposed microsurgical robot: (1) Main Body (MB) - Outer Tube (OT), (2) MB - Inner Tube (IT), (3) MB - Filling Material, (4) Camera Holder (CH) - OT, (5) CH - IT, (6) Camera head with integrated illumination, (7) Right Instrument (RI) - (OT), (8) RI - IT, (9) RI - end-effector, (10) Left Instrument (LI) - OT, (11) LI - IT, and (12) LI - end-effector.

matic variables the curvature of a referred tube and the torsion of each tube, are integrated simultaneously. The shape of each tube is determined by the position vector $\mathbf{r}_i^j = \mathbf{r}_i^j(s)$, where the coordinate $s \in [0, \ell]$ is the arc length, and ℓ is the tube's length and the rotation matrix of the frame moving along the tube's arc, $\mathbf{R}(s)$. Subscript i denotes the parameters and variables of the ith tube, while j denotes the section of the robot that the equation is referred to. For simplicity and without loss of generality, we present the model for the designed robot, *i.e.,* $i = \{1,2\}$ (two tubes per section, 1 denoting the inner tube, and 2 denoting the outer tube), and $j = \{1,2,3,4\}$ ($1-3$ for the manipulation sections and 4 for the navigation section). As the local curvature of a tube is obtained as $\mathbf{u}(s) = (\mathbf{R}^T(s)\mathbf{R}'(s))^\vee$, its shape can be computed by integrating $\mathbf{r}'(s) = \mathbf{R}(s)\mathbf{e_3}$ and $\mathbf{R}'(s) = \mathbf{R}(s)\hat{\mathbf{u}}$ where $\hat{\mathbf{u}}$ is a skew symmetric matrix. To preserve shape continuity, we "break" the robot into segments linking transitions points. Each transition point denotes the position where a tube goes from straight to curved or where a tube ends as is depicted in Fig. 2. The continuity of shape and internal moment must be enforced at each transition point. In our approach, we estimate the shape of each section in each

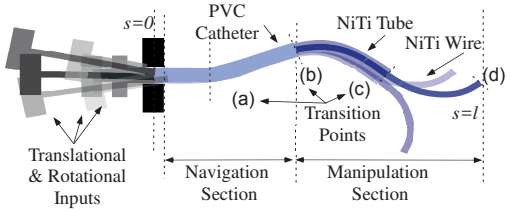

Fig. 2: Illustration of the concentric tube manipulation arms and the material filling the navigation section.

segment based on the deformed shape of a tube of reference. Without loss of generality, it is assumed that the navigation section 4 is the reference section for the segment that includes all tubes.

The twist of each tube is expressed with respect to the outer tube of the navigation section by introducing the angle $\theta_i^{(j)}(s)$ to parameterize tubes' twist. As a result every rotation can be expressed in relation to that tube taking also into account the eccentricity as

$$\begin{aligned}\mathbf{R}_{i=1,2}^{(j=1,2,3)} &= \mathbf{R}_{i=2}^{(j=4)}\mathbf{R}_{\phi}^{(j)}\mathbf{R}_{\theta_{i=1,2}}^{(j=1,2,3)} \\ \mathbf{R}_{i=1}^{(j=4)} &= \mathbf{R}_{i=2}^{(j=4)}\mathbf{R}_{\theta_{i=1}}^{(j=4)}\end{aligned} \tag{1}$$

where $\mathbf{R}_{\phi}^{(j)}$ is the rotation matrix that expresses the eccentricity of the outer tube of each manipulation arm with respect to the outer tube of the navigation section frame. By taking derivatives of the force and moment balances with respect to s and then by using a linear constitutive law we obtain derivatives of the kinematic variables:

$$\begin{aligned}\mathbf{u}_2^{\prime(4)}\Big|_{x,y} = -\mathbf{K}^{-1}\sum_{i=1}^{n}\mathbf{R}_{\kappa}(\mathbf{K}_i^{(j)}(\theta_i^{\prime(j)}\frac{\mathrm{d}\mathbf{R}_{\theta_i}^{T(j)}}{\mathrm{d}\theta_i^{(j)}}\mathbf{R}_{\phi}^{T(j)}\mathbf{u}_2^{(4)} - \mathbf{u}_i^{\prime *(j)}) \\ + \hat{\mathbf{u}}_i^{(j)}\mathbf{K}_i^{(j)}(\mathbf{u}_i^{(j)} - \mathbf{u}_i^{*(j)})\Big|_{x,y} \\ - \mathbf{K}^{-1}(\mathbf{e}_3 \times \mathbf{R}_2{}^{T(j)}\int_s \mathbf{f}_s(\sigma)\mathrm{d}\sigma + \mathbf{R}_2{}^{T(j)}\mathbf{l})\Big|_{x,y},\end{aligned} \tag{2}$$

where $\mathbf{K} = \sum_{i=1}^{n}\mathbf{K}_i^{(j)}$ and $\mathbf{R}_{\kappa}$ for the manipulation sections is $\mathbf{R}_{\kappa} = \mathbf{R}_{\phi}^{(j)}\mathbf{R}_{\theta_i}^{(j=1,2,3)}$ and for the navigation section is $\mathbf{R}_{\kappa} = \mathbf{R}_{\theta_i}^{(j=4)}$. As far as torsion is concerned, it can be derived from the third component of the equation that describes the curvature for a single tube, [6],

$$\begin{aligned}u_{i,z}^{\prime(j)} = u_i^{\prime *(j)} + \frac{E_i^{(j)}I_i^{(j)}}{G_i^{(j)}J_i^{(j)}}(u_{i,x}^{(j)}u_{i,y}^{\prime(j)} - u_{i,y}^{(j)}u_{i,x}^{\prime(j)}) + \\ \frac{G_i^{\prime(j)}I_i^{(j)}}{G_i^{(j)}J_i^{(j)}}(u_{i,z}^{\prime(j)} - u_{i,z}^{(j)}) - \frac{1}{G_i^{(j)}J_i^{(j)}}\mathbf{e}_3\mathbf{R}_i^{T(j)}\mathbf{l}.\end{aligned} \tag{3}$$

All equations are integrated simultaneously together with the equations that describe the change of the transformation matrix along the length of the tube. Based on the expression of the curvature of each tube to the outer one, the rest curvatures can be obtained.

RESULTS

To evaluate the developed theory, the experimental setup shown in Fig. 3 was developed. The setup mimics the behavior of the proposed robot and has a single manipulation arm, placed eccentrically with respect to the navigation backbone longitudinal axis. The multi-lumen catheter is made of Polyvinyl Chloride (PVC) and emulates the flexible navigation section with its filing material. The manipulation arm is composed of a NiTi tube and a NiTi wire. To measure the shape of the tubes, two orthogonally arranged cameras observing the robot workspace from the top and the side were used. Moreover, since the actual values for the moduli of the tubes and the wire are uncertain (for the NiTi they are listed as 28-83 GPa and for the PVC, the Young's modulus varies from 2.3 to 4.8 GPa) , a calibration process was followed by solving an optimization problem for the parameter set $P = \{E_i^j I_i^j\}$ that identifies the moduli that minimise the error between the experiment and simulation. It was found for the NiTi tube and wire that $E \approx 20$ GPa while for the PVC is $E \approx 2$GPa.

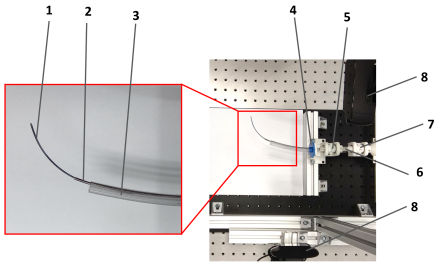

Fig. 3: Experimental setup: (1) Manipulation section - Instrument inner rod, (2) Manipulation section - Instrument outer tube, (3) Navigation section - PVC Multi-lumen catheter, (4) Catheter rotation control, (5), (6), (7) Rotation and translation control for the manipulation section, (8) Orthogonal cameras.

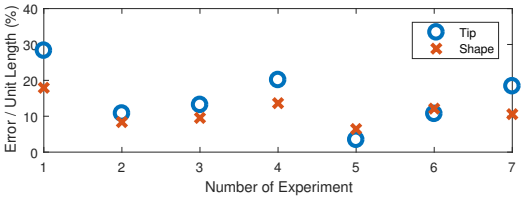

Fig. 4: Tip and shape error for 7 experimental trials.

In Fig. 4 the percentage of the error on the tip per unit length of the mechanism and the mean error in predicting the overall shape of the robot are shown. The average error per unit length on the whole shape is around 11%, which is reasonable for CTRs [6]. The sources of error in experimental data include the refraction caused by the PVC catheter, the camera calibration matrix, and triangulation of the selected points used to convert two 2D images into 3D shape of the robot.

REFERENCES

[1] J. Burgner-Kahrs *et al.* Continuum robots for medical applications: A survey, *IEEE Trans. Robot.*, 2015.
[2] P. E. Dupont *et al.* Design and control of concentric-tube robots, *IEEE Trans. Robot.*, 2010.
[3] A. Garriga-Cassanovas *et al.* Complete follow-the-leader kinematics using concentric tube robots, *Int. J. Robot. Res.* , 2018.
[4] R. J. Hendrick, *et al.* Hand-held transendoscopic robotic manipulators: A transurethral laser prostate surgery case study, *Int. J. Robot. Res.* , 2015.
[5] J. Burgner *et al.* A telerobotic system for transnasal surgery, *IEEE/ASME Trans. Mech.*, 2014.
[6] D. C. Rucker, *et al.* A Geometrically Exact Model for Externally Loaded Concentric-Tube Continuum Robots, *IEEE Trans. Robot.*, 2010.
[7] J. Ding, *et al.* Design and Coordination Kinematics of an Insertable Robotic Effectors Platform for Single-Port Access Surgery, *IEEE/ASME Trans. Mech.*, 2013.

Design of an Extensible Colonoscopy Robot

T. Altinsoy, B. A. Baydere, S. K. Talas, O. M. Erkan, C. Tutcu, and E. Samur

Department of Mechanical Engineering, Boğaziçi University, Turkey
{*timur.altinsoy,evren.samur*}*@boun.edu.tr*

INTRODUCTION

Colonoscopy is the most common method to diagnose colorectal cancer. Some complications faced in colonoscopy are patient discomfort, pain and perforation. To overcome these complications, robotic systems are proposed. For instance, colon capsule endoscopy (CCE) is an alternative approach in which the patient swallows a capsule and the colon is screened through an embedded camera [1]. Another example is the Aer-O-Scope consisting of a flexible body and two balloons: one stationary and one moving. It propels itself and does not put pressure on the bowel wall. However, both CCE and Aer-O-Scope do not have a working channel and can only be used for screening purposes. Another robotic system is the NeoGuide Endoscopic System (NES). NES has different segments that can be actuated separately to take the colon's shape but still has to be propelled by a surgeon using conventional methods [2].

We are currently developing an extensible and flexible colonoscopy robot that can eliminate complications faced during the procedure. The robot will navigate through the colon via growth by means of a novel pneumatic actuator. The proposed colonoscope will also have the ability to accomplish conventional tasks, unlike most of the robotic systems.

MATERIALS AND METHODS

The proposed colonoscope consists of two main sections: *in-vivo* and *in-vitro* (See Fig. 1). The in-vivo section consists of a main body and a distal end.

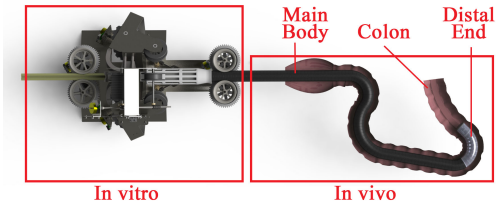

Fig. 1: Sections of the proposed robotic colonoscope.

The colonoscope is actuated from its tip by means of a novel pneumatic actuator, henceforth referred to as the pinch-roller (PR) actuator. There are three PR actuators at the tip. Each actuator consists of a thin-walled tubing and two frictionless rollers. A schematic view of the PR actuator is given in Fig. 2. When the tubing is pressurized from the inlet and squeezed by the two rollers preventing any air leakage, pressure energy is built up inside the tubing. This energy is converted into rolling kinetic energy if

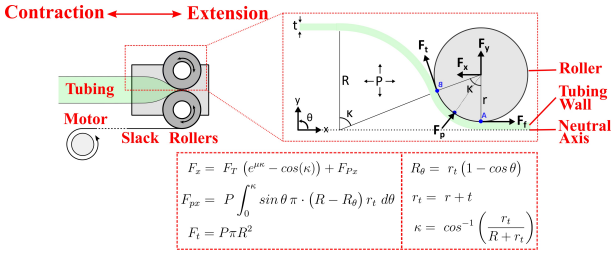

Fig. 2: Pinch roller actuator and forces on the roller at static equilibrium (top). Equations for the resultant forces (bottom).

the deflated section is released. A free-body diagram of the PR actuator can be seen in Fig. 2. F_P is the resultant force due to tubing pressure on the roller surface. F_T is the tangential force due to axial stress on the inflated tubing and F_f is the opposing friction force at the pinch point A. Using a balance of forces and assuming the tubing has a shape that fills the entire width between the rollers while maintaining the circumference of the fully inflated section (R), axial force applied on the rollers (F_x) can be calculated (Fig. 2). Constant μ is the friction coefficient between the roller and the tubing outer surface that is determined experimentally.

The main body consists of 3 segments: sheath, shell and shaft as seen in Fig. 3. The length of the main body was set as 2 meters since the length of the colon is 167 cm in average with a standard deviation of 21 cm [3]. The sheath is similar to ones used in conventional colonoscopes with a few changes in order to make it suitable for feed and retraction. It has a thickness of 0.7 mm and an outer diameter (OD) of 16.6 mm. Conventional colonoscopes have an OD around 13-14 mm [4]. Since we use actuation from the tip, an OD of 16.6 mm is sufficient for navigation through the bowel. The sheath enables other parts of the main body including the shell and tubings to move through the colon without dismounting. It is retracted at the beginning of the *in-vitro* section with a folding mechanism when the axial force is applied. The shell supports inflated tubings against buckling. It consists of 3 co-radial identical pieces of silicone rubber (Shore 30A) which interlace through the main body and are drawn apart at the rollers in the in-vitro where they are accumulated. While the shell supports the tubings from outside, the shaft provides inner support (Fig. 3). Necessary cabling and channels pass through the center of the shaft.

The distal end has a more flexible structure compared to the main body to steer the tip at high cur-

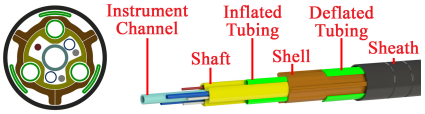

Fig. 3: A section view of the main body. All components that lie along the main body can be seen. Instrumentation channel, CO_2/water channels, lighting fibers and camera cabling are at the center of the shaft. Inflated tubings lie between the shaft and shell while deflated tubings slide between the shell and sheath.

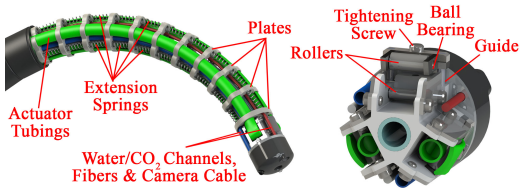

Fig. 4: Distal end design (left), and the tip with three PR actuators connected in parallel (right). Pneumatic actuator tubings, visual instruments and CO_2/air channels reach to the tip from holes on the consecutive plates.

vatures. It contains the PR actuators at the tip. Its consecutive plates are connected to each other via low stiffness extension springs to restore its original orientation when tubings are deflated (Fig. 4).
While extension of the colonoscope (forward movement) is supplied by the PR actuators, it is restricted, controlled and retracted (backward movement) by the feed/retraction mechanisms (Fig. 5 left). These mechanisms are located in the *in-vitro* section for sheath, shell, shaft and tubings. Also pressure sensors and solenoid valves for the control of air flow are present at the inlet. The spools in this section rotate at given amounts according to user input. Worm gears are used to lock reverse movement.

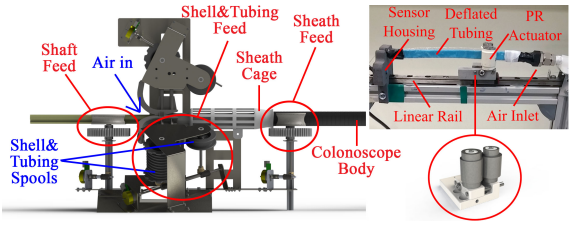

Fig. 5: *In-vitro* section components (left) and experimental setup used for force tests of a PR actuator (right)

RESULTS AND DISCUSSION

We performed force output measurements on a single PR actuator with 10 mm OD tubings using the experimental setup in Fig. 5. The actuator was mounted on a linear rail and tubing length was kept constant at 100 mm. Force measurements were taken using an ATI Nano 17 force/torque sensor while the actuator was in stationary position. Friction coefficient (μ) was estimated as 0.2 between the tubing (nylon 12) and rollers (aluminum). Force measurements are compared with the model predictions in Fig. 6. Force output was slightly lower than the model prediction which was obtained by using the equations given in Fig. 2, most probably due to slight differences in tubing geometry at the roller

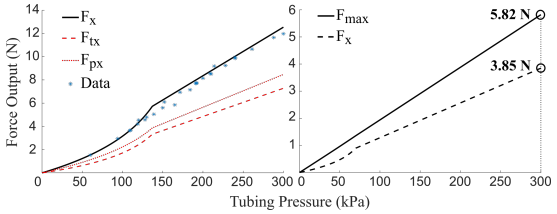

Fig. 6: Comparison of the experimental data with the model predictions for a tubing with 10 mm OD (left), and the estimated total axial force for three tubings of 3 mm OD (right). F_{max} denotes the maximum force output neglecting losses.

surface and additional friction losses. We calculated the maximum tubing OD for a shaft diameter of 16.6 mm to be around 3 mm. Our model predicts an axial force of 3.85 N at the tip of the robotic colonoscope at 300 kPa. This total output force can be 5.82 N when the losses are ignored. Considering the mostly linear pressure-force relationship obtained from the experiments (Fig. 6) it is possible to obtain much higher forces by increasing the tubing pressure over 300 kPa. However, this also increases the chance of complications due to air leak between rollers or fatigue failure at the tubing wall.
As a future work, we will work on the biggest challenges of the project which are manufacturing and assembly of the miniaturized components in the distal end. Once a working prototype is developed, first, it will be tested on a mock-up system, and then animal tests will be conducted. We hypothesize that the prototype tests will prove reduced pressure on the environment, and faster operation. Therefore, the proposed device for robotic colonoscopy could greatly reduce operation time, eliminate patient discomfort, and prevent complications due to its novel actuation principle.

ACKNOWLEDGMENTS

This work was supported by the Scientific and Technological Research Council of Turkey (TÜBİTAK, #115E717).

REFERENCES

[1] D. E. Yung, E. Rondonotti, and A. Koulaouzidis, "Review: capsule colonoscopy—a concise clinical overview of current status," *Annals of Translational Medicine*, vol. 4, no. 20, pp. 398–398, 2016.
[2] A. Eickhoff, J. Van Dam, R. Jakobs, V. Kudis, D. Hartmann, U. Damian, U. Weickert, D. Schilling, and J. F. Riemann, "Computer-Assisted Colonoscopy (The NeoGuide Endoscopy System): Results of the First Human Clinical Trial ("PACE Study")," *The American Journal of Gastroenterology*, vol. 102, no. 2, pp. 261–266, feb 2007.
[3] A. Eickhoff, P. J. Pickhardt, D. Hartmann, and J. F. Riemann, "Colon anatomy based on CT colonography and fluoroscopy: Impact on looping, straightening and ancillary manoeuvres in colonoscopy," *Digestive and Liver Disease*, vol. 42, no. 4, pp. 291–296, apr 2010.
[4] J. C. Brooker, "A new variable stiffness colonoscope makes colonoscopy easier: a randomised controlled trial," *Gut*, vol. 46, no. 6, pp. 801–805, jun 2000.

Design of a Novel Compliant Robotic Instrument for Organ Retraction by Exploiting the Buckling Principle of a Continuum Bending Beam

Yuanpei Cai[1], K. W. Samuel Au[1], H. W. Yip[1], T. Y. Chung[1], Jason Y. K. Chan[2], and Stuart Moran [3]

[1] *Department of Mechanical and Automation Engineering, The Chinese University of Hong Kong*
[2] *Department of Otorhinolaryngology, Head & Neck Surgery, The Chinese University of Hong Kong*
[3] *Retraction. inc. Hong Kong, China*
samuelau@cuhk.edu.hk

INTRODUCTION

Organ retraction is an essential task in minimally invasive surgery. It is a surgical technique to push aside or manipulate tissues/organs to improve the access and visualization of surgical sites [1]. As typical manual retractors are rigid and without articulation, physicians often struggle with minimizing the force applying onto tissue while positioning the retractor to maintain optimal exposure. Over the years, different kinds of liver damages related to misuse of retractor instruments have been reported [1][2].

In the past decades, only a few robotic research efforts have been made to mitigate the aforementioned clinical risks. [2] focused on enhancing the retractor sensing capabilities, while [3] proposed a new mechanical retractor design based on whole-hand organ grasping concept. In fact, these solutions may not be clinically viable from the packaging, sterilization, reliability, and ease-of-use standpoints. Although [4] proposed to use a soft fiber-reinforced actuator for organ retraction, their actuator was too soft to provide sufficient maneuverability and not compact enough to be deployed through a typical $8mm$ robotic cannula.

In this paper, we present a novel concept of robotic organ retractor that exploits the buckling of a continuum bending beam mechanism (Figs. 1 and 2). Analytical and FEA models are proposed to understand the deflection behavior of the retractor and verified through experiment. Initial prototype was also integrated with the da Vinci Research Kit (dVRK) for basic functional evaluation. Preliminary results demonstrated the capability of the proposed device for organ retraction.

MECHANICAL DESIGN

On the contrary to the "rigid" retractor design [2], our retractor is designed based on the buckling principle of a Nitinol beam (Fig. 2a). Nitinol beams are pre-curved to avoid instability when actuated at straight configuration. A telescopic, push-pull rod is installed inside the instrument and is used to control the expansion of the retraction surface. As shown in Fig. 2a (i), when pulling the rod backward, the retractor will be folded to a collapsed state, allowing it to be inserted through a cannula. Once it reaches the surgical site, the surgeon can move the rod forward

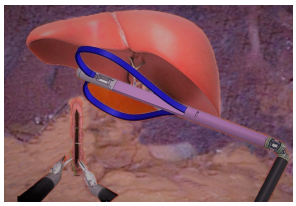

Fig. 1: Concept of the organ retraction (or liver retraction) using proposed retractor. The retractor beam (blue one) was expanded to support the liver.

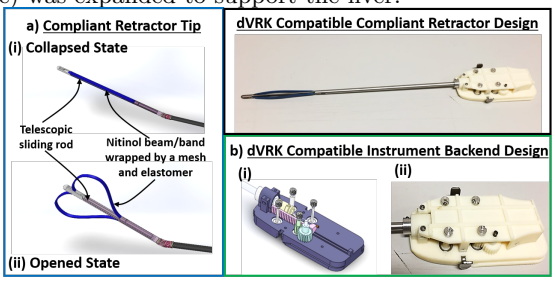

Fig. 2: Proposed dVRK compatible compliant retractor design: a) Compliant Retractor Tip (blue box); b) dVRK Compatible Backend Design(green box).

to expand the retractor (Fig. 2a (ii)) and adjust it dynamically to support different sizes of organs. The compliant nature of the Nitinol beam minimizes the excessive interaction force applied by the users inadvertently. In addition, a braided, composite material is embedded onto the beam to increase the holding friction against the organ, preventing it from sliding during the operation.

MECHANICS-BASED MODEL

Developing a model to describe the tip behavior will help us to design the retractor tip parameters (such as dimension, material), and achieve large deflection without risking of kinking the bending beam. As shown in Fig. 3, we model the retractor tip as a

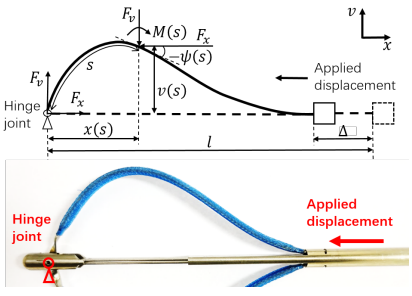

Fig. 3: Mechanics-based model

bending beam with a hinge joint at one end and an applied input displacement, Δ, at the other end. l is the overall length of the bending beam. The input displacement will cause the beam to bulge out and form a curve illustrated as in Fig. 3. Here, we are interested to derive the deflection function $v(s)$ and slope function $\psi(s)$ of the curve, where s is the segment length along the curve. Using the basic force analysis, we obtain the force and moment equation:

$$-EI \cdot \frac{d\psi}{ds} = F_x \cdot v(x) - F_v \cdot x(s)$$

where EI is the flexure rigidity and

$$v(s) = \int_0^s \sin\psi ds, x(s) = \int_0^s \cos\psi ds.$$

with the boundary conditions (B.C.), $\psi(l) = 0, v(l) = 0, x(l) = l - \Delta$.

Due to the complexity of the above PDE problem, both analytical and FEA approaches are adopted to predict the tip deflection. For small to moderately large deflection,we address the problem analytically. The analytical solution of $v(s)$ is given by $v(x) = -\frac{F_v(l-\Delta)}{F_x sin\beta} sin\lambda x + \frac{F_v}{F_x}x$, where $\lambda^2 = \frac{F_x}{EI}$ and $\beta = \lambda(l-\Delta) \approx 1.4303$ is the smallest positive non-zero solution of the transcendental equation, $\tan\beta = \beta$. Meanwhile,

$$F_v = \sqrt{\frac{\Delta - \frac{F_x l}{EA}}{\frac{\beta^2}{2F_x^2 sin^2\beta}\left(\frac{sin2\beta}{4\lambda} + \frac{l-\Delta}{2}\right) - \frac{l-\Delta}{2F_x^2}}}$$

FEA model is used to study the beam deflection when $\Delta \geq 15mm$. We conducted FEA in Abaqus (Version 6.14). Representative material parameters for Nitinol were chosen ($E = 40GPa$, Possions Ratio $v = 0.33$) and 100 beam segments were used in the simulation.

RESULTS

Different input displacements were applied to study the variation of overall beam deflection. Fig. 4a compares the results between the FEA and analytical model. It can be seen that when the input displacement was small ($\Delta \leq 5mm$), both FEA and analytical model matched very well with each other. Most of the discrepancy happened at the region of $60mm \leq x(s) \leq 120mm$, for which the slope of the beam was large, violating the small angle $\frac{dv}{dx}$ assumption in the analytical model. Fig. 4b compares the results between the simulations and experiments for different input displacements. As can be seen, our FEA model can predict the actual beam deflection behaviors very well. The prediction errors were small with the maximum percentage error (divided by the maximum deflection) less than 7.5%. Preliminary experiment (Fig. 5) demonstrated the loading capability of proposed retractor for organ retraction.

SUMMARY

In this work, we proposed and built a novel compliant robotic organ retractor tip based on the buckling principle of a continuum bending beam mechanism.

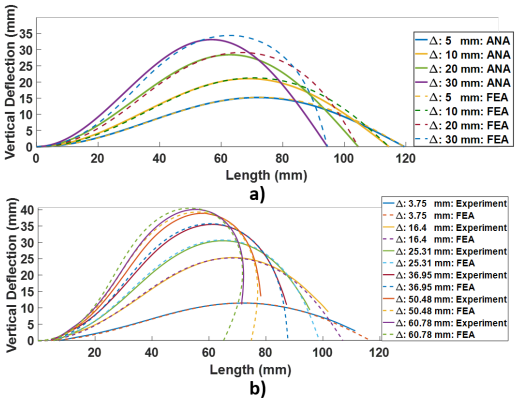

Fig. 4: Simulation and experimental results: a) FEA and analytical results comparison; b) FEA and experimental results comparison for large deflection

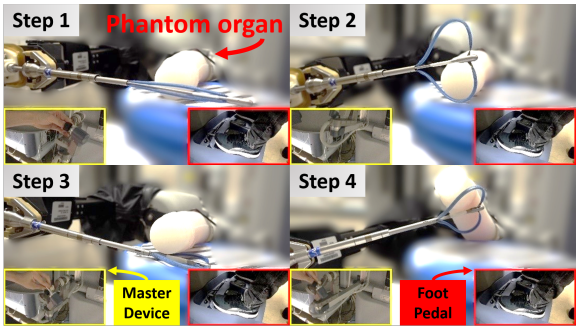

Fig. 5: Snapshots of tele-operated control of the retractor. The user used the master device to position the retractor (Yellow Framed Box) and the foot pedal to adjust the expansion of the retractor tip (Red Framed Box). Step 1: The retractor was in the collapsed state; Step 2: Opened the retractor; Step 3: Re-orientated it to prepare for retraction; Step 4: Demonstrated the retractor has sufficient strength to push against a phantom organ

Both mechanics-based and computational models were developed and utilized to identify key design parameters. Initial experimental results demonstrated the basic capabilities for organ retraction. As a future work, we will develop a wrist joint, that can provide sufficient range of motion without sacrificing structural strength. We will also conduct a comprehensive performance evaluation in both phantom and animal lab settings.

REFERENCES

[1] T. Nozaki et al., Retraction-related acute liver failure after urological laparoscopic surgery, *Curr Urol*, vol. 7, no. 4, pp. 199-203, 2014.

[2] G. S. Fischer et al., Ischemia and force sensing surgical instruments for augmenting available surgeon information, *Proc. IEEE Int. Conf. on Biomed. Robotics and Biom. (BioRob)*, 2006.

[3] M. Osaki et al., Single-Trocar assemblable retractor-hand for laparoscopic surgery, *Proc. IEEE Int. Conf. on Robotics Autom.*, pp. 3490-3495, 2009.

[4] J. Gafford et al., Shape Deposition Manufacturing of a soft, atraumatic and deployable surgical grasper, *ASME Journal of Mechanisms and Robotics*, vol. 7, no. 2, 2015.

Interactive Wound Segmentation and Automatic Stitch Planning

Giuseppe Andrea Fontanelli[1], Lin Zhang[2], Guang-Zhong Yang[2], and Bruno Siciliano[1]

[1] *ICAROS Centre, University of Naples Federico II* , [2] *Hamlyn Centre, Imperial College of London,*
{*giuseppeandrea.fontanelli*}*@unina.it*

INTRODUCTION

In Minimally Invasive Robotic Surgery suturing is one of the most critical and delicate tasks, even for a skilled surgeon, because of its time demanded, high dexterity required and risks of causing damage to organs and/or tissues. Several works have been proposed, in the last years, to help the surgeon during this task. For instance in [1] and [2], an automatic multi-throw framework and a supervised paradigm have been developed to investigate fully autonomous and supervised suturing procedure. To adapt the suturing planner to environment changes, e.g. wound motion and deformation, the wound needs to be tracked on-line. In literature, some methods have been proposed relying on edge and color based segmentation [3] or Near-Infrared Fluorescent (NIRF) markers [2]. In this work, we propose a simple and efficient GrubCut-based wound segmentation method and an automatic stitch planning that can be used to on-line obtain the optimal stitch poses.

MATERIALS AND METHODS

Consider a suturing procedure composed of N stitches, the k-th stitch can be defined as a circular trajectory, for the needle tip, from the point a_k to b_k in the stitch frame $O_{s,k}$[1] (see Fig. 1). $O_{s,k}$ can be defined by choosing: (i) the axis $\boldsymbol{x}_s$ along the direction from $\boldsymbol{x}_{e,k}$ to $\boldsymbol{x}_{i,k}$ (extraction and insertion points); (ii) the $\boldsymbol{z}_s$ axis along the tissue normal unit vector $\boldsymbol{n}_k$, (iii) the axis $\boldsymbol{y}_s$ to have an orthonormal frame; (iv) the frame origin in the center of the circle, with radius equal to the chosen needle radius r, passing through the points $\boldsymbol{x}_{i,k}$ and $\boldsymbol{x}_{e,k}$. Hence, each stitch k can be uniquely defined by the n-upla $s_k = [\boldsymbol{x}_{i,k}, \boldsymbol{x}_{e,k}, \boldsymbol{n}_k, r]$ extracted from the wound shape. In this work we model the wound using: (i) a central spline ($\boldsymbol{\Sigma}_c(\sigma)$) defining the wound shape, (ii) two lateral splines ($\boldsymbol{\Sigma}_r(\sigma)$, $\boldsymbol{\Sigma}_l(\sigma)$) defining two guides for the stitch insertion and extraction points, (iii) a parametric unit vector $\boldsymbol{n}(\sigma)$ locally orthogonal to the tissue[2].

Each stitch s_k have been calculated by equally spacing N points imposing a relative 25% of overlap between the stitches: $N = \lceil 1.25l/D \rceil$ where, both the wound length l and the wound depth D are obtained on-line respectively from the length of the central wound spline and the average distance between the wound borders.

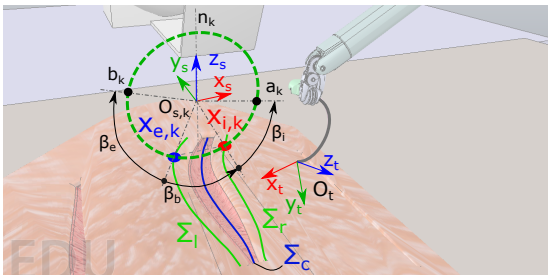

Fig. 1: Stitch plan. β_i/β_e: insertion/extraction angles

Wound segmentation and registration

Using the force measure, obtained using our trocar force sensor [4] and the surgeon's visual perception in the loop, we design an effective method to interactively initialize the wound pose. In details, the wound initialization is obtained by touching the tissue at the beginning and at the end of the wound, moving along the wound shape. All the collected points are smoothed using a spline and used to initialize the segmentation by defining a set of pixels belonging to the foreground.

To on-line segment the wound we rely on the efficient and widespread GrabCut method [5]. The GrabCut algorithm addresses the visual bilayer segmentation task as an energy minimization problem, based on statistical models of the foreground (FGD) and the background (BGD). For an input image, we denote by $\alpha = [\alpha_i]_{i=1}^{N}$ the set of the unknown binary labels of the pixels ($\alpha_i = 0$ for the BGD pixels, $\alpha_i = 1$ for the FGD). Estimating the values $\hat{\alpha}$ of an unknown pixel can be formulated as the minimization of an energy-based Markov Random Field objective function

$$E(\alpha) = \sum_i (U_i(\alpha_i)) + \gamma E_s(\alpha)$$

with respect to α, where, E_s is a smoothness energy term, γ is a gain, and $U_i(\alpha_i)$ is a term accounting for the observation probability $p(\mathbf{p}_i|\alpha_i)$ for a pixel $\mathbf{p}_i$ to belong to the FGD or to the BGD. In our implementation this therm is computed as Gaussian Mixture Models (GMM), based on image color distribution, learned, during the initialization process, for both the FGD and BGD layers.

[1] The stitch and PSM base frame has been calibrated w.r.t. the camera frame using a standard hand-eye approach

[2] $\sigma \in [0, 1]$ is the curvilinear abscissa.

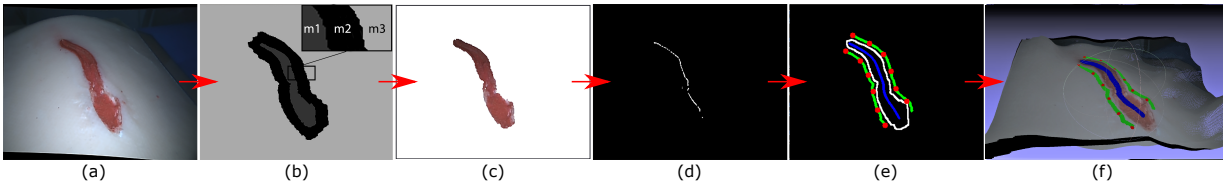

Fig. 2: Snapshots: (a) initial image, (b) segmentation trimap mask, (c) segmented image, (d) wound skeleton, (e) wound model and stitching points overlapping, (f) registration onto the 3D point cloud. In (e,f) the central spline is indicated in blue, the lateral splines are indicated in green while the stitch points are indicated in red.

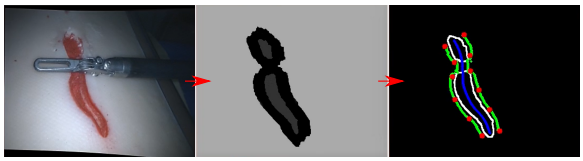

Fig. 3: Robustness w.r.t. partial occlusion occurrence.

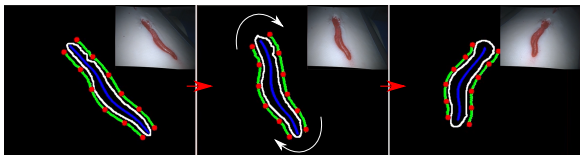

Fig. 4: Robustness w.r.t. wound motion or deformation.

Once the initial image is segmented through user interaction, the following frames are evaluated by considering a defined mask. In details, from the previous segmented foreground, we calculate the distance transform, providing a signed distance map. On this distance map, we define a narrow strip composed by three areas (trimap) with different probabilities of the pixels to be FGD or BGD. With reference to Fig. 2 (b) we have been defined. m1: $U_i(\alpha_i = 1) = inf$ (FGD); m2: $U_i(\alpha_i = 1) = -\log(p(\mathbf{p}_i|\alpha_i))$ (probably FGD/BGD); m3: $U_i(\alpha_i = 0) = inf$ (BGD). In this manner, temporal consistency is ensured, since energy minimization is only effective within the strip in the vicinity of the previous segmentation boundary, avoiding some outliers outside or inside, and reducing computations [6].

From the segmented image, the straight morphological skeleton of the polygon has been extracted[3]. The role of the skeleton is to account the topological structure of the incision. Moreover, the wound contours have been extracted relying to well known Open-Cv functions (*Canny* and *find contours*). Hence, we fitted: (i) the image central spline $\mathbf{\Sigma}_{c,i}(\sigma)$ on the skeleton points; (ii) the two image lateral splines ($\mathbf{\Sigma}_{r,i}(\sigma)$, $\mathbf{\Sigma}_{l,i}(\sigma)$) by a defined offset w.r.t. the wound contours points belonging to the central spline normals unit vectors in the image plane. Finally, by resorting on the efficient stereo (ELAS) approach [7] the 3D point cloud of the tissue has been calculated. From the point cloud we obtained the wound normals $\boldsymbol{n}(\sigma)$, the 3D splines ($\mathbf{\Sigma}_c(\sigma)$, $\mathbf{\Sigma}_r(\sigma)$, $\mathbf{\Sigma}_l(\sigma)$), by registering the image plane splines, and the 3D stitch points in order to have a 3D description of the wound.

EXPERIMENTS AND RESULTS

Our experimental setup is composed of the full da Vinci Research Kit commanded in teleoperation mode. All the visual computations, including the 3D point cloud generation, have been obtained using the da Vinci endoscopic cameras acquired at 30 Hz. Figure 2 shows some snapshots resulting from the segmentation. From left to right all the segmentation phases and the stitch point selection and registration have been reported in a case study tested on a suturing phantom. Moreover, in Fig. 3 we report some snapshots showing the robustness of the proposed approach w.r.t. partially occluded images. Our preliminary experiments show also the capability of the method to maintain the segmentation during the wound motion or deformation allowing a wound tracking at 10Hz (Fig. 4).

[3] felix.abecassis.me/2011/09/opencv-morphological-skeleton/

CONCLUSIONS

In this work, a wound segmentation method supported by an interactive force-enabled wound initialization and an automatic stitch point selection are presented. Preliminary experiments show good results and robustness in the segmentation. In future work, a GPU-based GrabCut algorithm will be used to improve the tracking capability.

References

[1] S. Sen, A. Garg, D. V. Gealy, S. McKinley, Y. Jen, and K. Goldberg, "Automating multi-throw multilateral surgical suturing with a mechanical needle guide and sequential convex optimization," *IEEE Int. Conference on Robotics and Automation*, pp. 4178–4185, 2016.

[2] A. Shademan, R. S. Decker, J. D. Opfermann, S. Leonard, A. Krieger, and P. C. W. Kim, "Supervised autonomous robotic soft tissue surgery," *Science Translational Medicine*, vol. 8, no. 337, 2016.

[3] S. Leonard, K. L. Wu, Y. Kim, A. Krieger, and P. C. Kim, "Smart tissue anastomosis robot (STAR): A vision-guided robotics system for laparoscopic suturing," *IEEE Transactions on Biomedical Engineering*, vol. 61, no. 4, pp. 1305–1317, 2014.

[4] G. A. Fontanelli, L. Buonocore, F. Ficuciello, L. Villani, and B. Siciliano, "A novel force sensing integrated into the trocar for minimally invasive robotic surgery," in *IEEE/RSJ Int. Conf. on Intelligent Robots and Systems*.

[5] C. Rother, V. Kolmogorov, and A. Blake, "Grabcut: Interactive foreground extraction using iterated graph cuts," vol. 23, pp. 309–314, 08 2004.

[6] A. Petit, V. Lippiello, G. A. Fontanelli, and B. Siciliano, "Tracking elastic deformable objects with an RGB-D sensor for a pizza chef robot," *Robotics and Autonomous Systems*, vol. 88, no. September, pp. 187–201, 2017.

[7] A. Geiger, M. Roser, and R. Urtasun, "Efficient large-scale stereo matching," *Asian conference on computer vision*, pp. 25–38, 2010.

Designing a Flexible Instrument for Confined Workspace Suturing - A Feasibility Study Base on a Simulated Suturing Task

Y. Hu[1], L. Zhang[1], Y. Gu[1], and G.-Z. Yang[1]

[1] *The Hamlyn Centre for Robotic Surgery, Imperial College London, UK*
{*y.hu12, lin.zhang11, y.gu16, g.z.yang*}*@imperial.ac.uk*

INTRODUCTION

Transanal Endoscopic Micro-surgery (TEMS) is a well developed technique for the resection of selected rectal tumours. In TEMS, the surgeon operates specialised instruments in the rectum which is a tubular lumen with narrow space. The limited access to the operating site requires considerable skill and training. Robotic systems that allow complex surgical manoeuvre in confined workspace while improving the precision of operation and the ergonomics for the surgeon [1]. Although the robotic system provides various types of flexible instruments including the needle driver and grasper, performing suturing is still a challenging task. To drive the needle to pierce the tissue and later perform knot tying, the tools involve complex movements which may violate the workspace constraints. Recently, specialised suturing devices [2, 3] have been developed to simplify the needle handling and thread manipulation during laparoscopic surgery. However, the applicability and effectiveness of the specialised device in TEMS is undetermined. In this paper, two flexible suturing devices with different joint configurations were proposed and their performance were compared in a user study based on a simulated suturing task.

MATERIALS AND METHODS

A simulation platform, which is capable of simulating surgical suturing of a wound with flexible instruments, has been developed (illustrated as Fig.1) (a). The visualisation of the simulation uses the CHAI3D library [1] and the collision detection is powered by the Bullet physic engine [2]. A physical thread model was implemented by using the method proposed by [4], which is based on the Cosserat elastic rod theory. In the simulation, the thread is a dynamic object with changing shape subjected to internal and external force. The flexible instruments are kinematic objects controlled by the master devices. The rectum lumen and the wound are static. The suturing task consists of two instruments. A suturing device for performing stitching and a grasper for thread manipulation. Unlike the triangulated configuration in laparoscopic surgery, the two instruments used for TEMS are passed through a single surgical port and

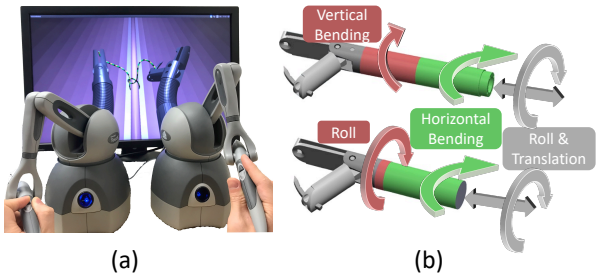

Fig. 1: (a) The setup for the simulated suturing task. (b) Two joint designs for the suturing device (top: design A, bottom: design B).

parallel with each other. The instruments need to bend downwards to work on the operating site which is beneath the instruments. Two Phantom Omni devices are used to control the flexible instruments by mapping the end-effector pose of the master to the slave through using inverse kinematics.

The suturing devices proposed by us have a jaw-like tip structure which can switch a surgical needle to perform stitching. The thread is attached to the middle of the needle. Similar with the suturing devices for laparoscopic surgery, by providing the local needle manipulation, it requires less movement and space to perform the tissue piercing and knot tying task. Two designs are proposed with same suturing tip but different joint structures as illustrated by Fig. 1(b). The design A has two flexible bending sections, which are perpendicular with each other. The design B has a one section flexible joint and a 360° rotational tip. Besides the above two DoFs, each tool has a rotational and a translational DoF at its proximal end. The length of the flexible joint is selected based on the workspace constraints and some practical mechanical design considerations.

The purpose of the experiment is to investigate which joint design is preferable for the confined space suturing. In each trial, the subject was asked to perform stitching and knot tying using both designs under two different wound orientations: 1) vertically placed in the camera view; 2) horizontally placed in the camera view. Fig. 2 illustrates the suturing process which contains five phases (vertical case). The tip trajectories of the left and right instruments were recorded during the suturing process. The joint configurations for the left grasper and the right suturing device are the same in each trial. For each configuration, five trials were performed. The task completion

[1] `http://www.chai3d.org`
[2] `http://bulletphysics.org`

Fig. 2: An illustration of the suturing process in a narrow lumen using the suturing device design B. The colour bar indicates the phases of the suturing task.

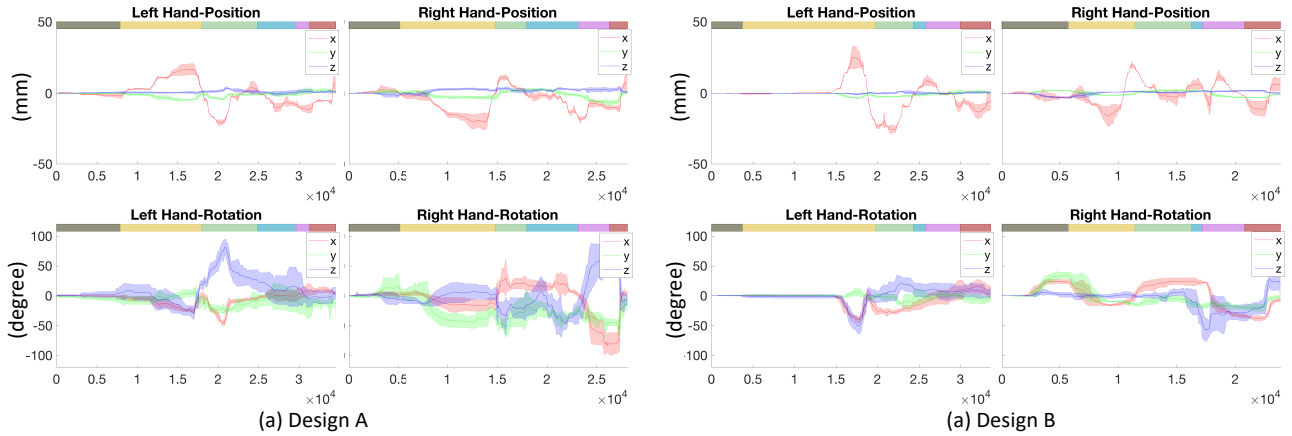

Fig. 3: Plots of the instrument tip trajectories. The envelope is showing the motion variance of the corresponding axis.

Table 1: Statistical results of the suturing experiment.

		Design A		Design B	
		Horizontal	Vertical	Horizontal	Vertical
	Avg. Time (s)	42.0	41.3	32.5	29.9
Grasp. (Left)	Pos. Var. (mm)	9.0/1.8/0.9	10.3/2.1/1.0	16.4/1.4/0.8	12.0/1.4/0.5
	Pos Amp. (mm)	29.3/6.8/4.4	24.4/5.6/4.6	41.3/5.2/2.6	35.2/4.0/1.7
	Rot Var. (deg)	21.9/12.1/13.8	25.7/11.3/13.2	29.7/9.1/16.8	15.8/5.6/15.8
Suture (Right)	Pos Var. (mm)	7.8/2.6/1.7	8.5/2.8/1.8	10.4/1.3/1.1	8.5/1.7/1.5
	Pos Amp. (mm)	27.2/7.5/4.8	28.2/9.2/5.3	29.4/3.4/3.0	24.9/3.6/3.4
	Rot Var. (deg)	25.1/19.7/20.1	27.3/24.3/25.8	21.8/12.6/14.7	19.8/16.6/20.3

X/Y/Z correspond to the three local axes.

time (Avg. Time) and the variance of the instrument motion (Pos. Avg. & Rot. Avg.) were evaluated to show how easy and consistent a subject can accomplish the same task using the two different designs. Furthermore, amplitudes of the instrument motion (Pos. Amp.) were also calculated to understand whether the instruments exceed the workspace.

RESULTS

As shown in Table 1, the average task completion time is 41 and 31 seconds when using design A and B, respectively. While the movement along X axis (lumen axial direction) can be ignored, design B has shown slightly smaller variance along the Y and Z axis. Fig. 3 depicts the trajectory plots of the translational and rotational movements of the vertical case. Dynamic time warping was performed on the trajectories in order to match the different phases across the trials. The motion demonstrated by the design B has smaller variance especially the rotation part. The position range of the design B is also smaller than the design A. Overall, the results show that design B may be preferred to design A in terms of less task completion time, lower trajectory variance, and smaller space occupation.

DISCUSSION

The purpose of this simulated study is to validate two suturing device designs before performing mechanical synthesis and design iteration. In this simulated study, we found that both suturing device designs are capable for performing the target suturing tasks. Design B is more preferable according to the experiment results. For the simulation, the movement of the instruments for the knot tying procedure may quite similar with the real situation, while for the tissue piercing procedure, the simulation may not be accurately reflect the real situation, because we did not implement a deformable tissue model at current stage. For the future work, the two proposed designs will be prototyped and compared in real suturing tasks to validate and improve the authenticity of our simulation. In addition, to achieve an optimal joint design, some practical issues such as the joint length, maximum bending angle and the port location will be also considered in future study.

REFERENCES

[1] Shang, et al. 2017. A Single-Port Robotic System for Transanal MicrosurgeryDesign and Validation. IEEE Robotics and Automation Letters, 2(3), pp.1510-1517.

[2] Meade, et al. EndoEvolution LLC, 2017. Apparatus and method for minimally invasive suturing. U.S. Patent 9,808,238.

[3] Nolan, et al. United States Surgical Corp, 1996. Method of employing surgical suturing apparatus to tie knots. U.S. Patent 5,480,406.

[4] Umetani, et al. Position-based elastic rods. Proceedings of ACM on Computer Animation, pp.21-30.

Transfer Learning for Surgical Suturing Segmentation

Ya-Yen Tsai[1], Bidan Huang[1], and Guang-Zhong Yang [1]

[1]*Hamlyn Centre for Robotic Surgery,Imperial College London*

y.tsai17@imperial.ac.uk

Introduction

Robotic assisted surgery offers a possibility of automating tiring surgical subtasks such as suturing to reduce the workload of surgeons. This automation is challenging as surgical subtasks involve complex multi-step motions and intricate manipulation skills. To this end, task segmentation is used to break down the entire task into smaller and simpler motion units, i.e. motion primitives, which are easier to model and reproduce by robots. However, segmenting task manually is time consuming, while automatic task segmentation algorithms are largely task specific and are not easy to be generalized to new tasks [1, 3]. In this paper, we propose a framework to utilise previously-learned knowledge to segment new but similar surgical subtask by transfer learning.

Starting from a set of manually labeled data, e.g. segmented motion sequences of blanket stitch, and un-annotated data of a new task, we identified the common features and then segment the new data in the same feature space. We evaluated this approach by segmenting new types of stitches according to previously annotated data. Initial results suggest that our approach can segment new tasks that match closely with manual segmentation.

Methods

Surgical suturing consists of repetitive cycles of stitch, and in this paper, we focus on segmenting a single cycle of a stitch. In our previous work [2], multiple demonstrations of single blanket stitch cycle have been collected (Fig. 1a). In each trial, the motion trajectories of the two needle drivers were recorded and manually segmented into nine phases according to the different stages of the process as illustrated in Fig. 2. For learning new stitches, demonstrations of single stitch of the Purse String Stitch (Fig. 1b) and the Continuous Stitch (Fig. 1c) were then collected. Three stitches are different in the needle piercing locations and the trace of the thread, hence the motion of reproducing them is different. Our goal is to utilise the segmentation patterns of the blanket stitches and hence identify the segmentation points of the latter two new stitches.

In manual task segmentation, segmentation points are determined based on the different phases of the process, e.g. needle piercing and passing. These changes can be reflected by the changes of the features of the data. These features are task dependent and could range from physical motions, such as displacement, velocities and accelerations, to the status of the targeted object, such as the open or close state of the needle gripper. In the task of surgical suturing, we chose the displacement, velocity, acceleration, open/close state of the needle gripper, as our candidate features for the feature selection.

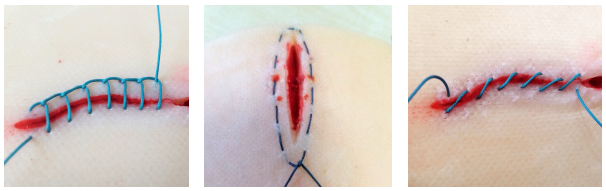

(a) (b) (c)

Fig. 1: Three different types of stitches (a) Blanket Stitch (b) Purse String Stitch (c) Continuous Stitch

The following equation was applied on every point along the selected features trajectory of the blanket stitch data to learn the associated weights for each feature:

$$E = \sum_{i=1}^{N} \omega_i F_i \tag{1}$$

where N, F_i and ω_i are the number of candidate features, the confidence of the i-th candidate feature and weight respectively.

Features were filtered to remove noise and the data were normalised before assigning weights to them. A weight was given such that a highly correlated feature with one segmentation point would be given more weights.

The algorithm used grid search to find candidates of weights combination that produced peaks at segmentation points along the trajectory from a blanket stitch data. This set of weights combination was examined and optimised over the rest of blanket stitch datasets until a weight combination that worked on all the blanket stitch datasets was found. A threshold was determined by using the selected weight combination to find the lowest E value that separated the segmentation points from other local maxima in the trajectory across the eight datasets.

Finally, the learned weight combination $\omega = \{\omega_1, \omega_2, \omega_3, ..., \omega_N\}$ and the threshold T were then transferred to automatically segment new purse string stitches and continuous stitches.

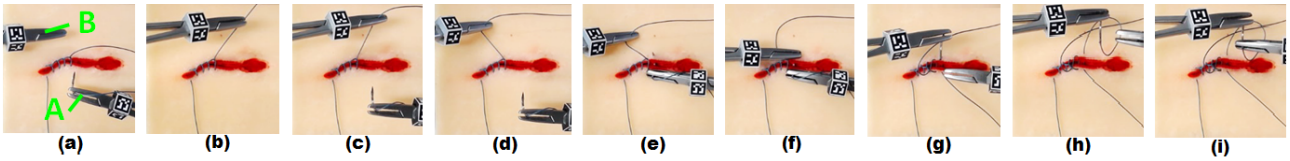

Fig. 2: Nine motion primitives of blanket stitch. Each needle driver is attached with a marker for visual tracking. (a) Gripper A pulls the thread. (b) Gripper B approaches the thread. (c) A approaches suturing point. (d) B pulls the thread to form a blanket stitch. (e) A pierces in the needle. (f) B grasps the needle tip. (g) B pierces out the needle. (h) A approaches the needle end. (i) B passes needle to A.

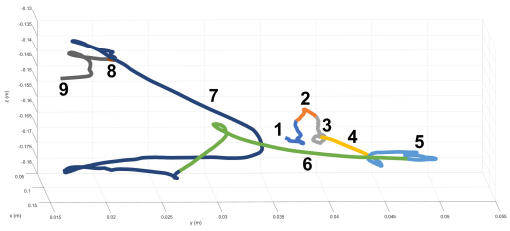

Fig. 3: Single cycle blanket stitch trajectory for tool B. A motion primitive is labeled with one color and the number placed next to each trajectory represents the motion primitive sequence.

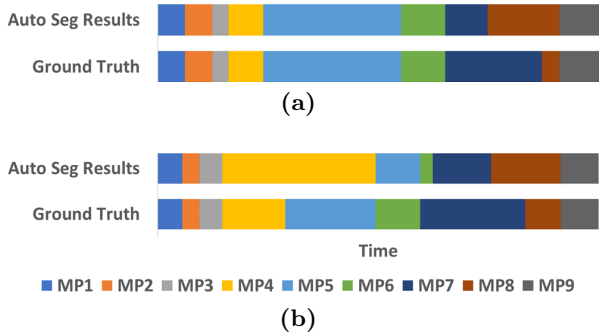

Fig. 4: Ground Truths vs. Automatic Segmented Results. (a) Purse String Stitch. (b) Continuous Stitch.

Experiments and Results

As mentioned above, eight demonstrations of blanket stitch have been collect and segmented beforehand [2]. For the new types of stitches, i.e. the Purse String Stitch and Continuous stitch, we adopted a similar experimental setup to collect motion trajectories. The trajectories were then filtered and the candidate features, i.e. displacement, velocity and acceleration, were normalised. Gripper states were recorded in a binary fashion, where 0 represents open and 1 means close. When there was a change in the gripper state the algorithm assigned gripper state feature to 1, otherwise 0.

In feature selection process, the candidate features and manually segmented blanket stitches results were compared to find correspondence. Tools' physical motions, gripper states and the tools relative position were identified as features to segment a trajectory.

The weights and the threshold of the segmentation points were trained based on the eight demonstrations of blanket stitch. The optimisation results were then transferred to segment new types of stitches, i.e. purse string suture and simple continuous suture. Summary of all the results are presented in Table 1. For each type of stitch, 19 out of 24 segmentation points were correctly identified. One result from each stitch is compared with the ground truths shown in Fig. 4. The automatic segmentation points match closely with the ground truths.

Table 1: Segmentation results of new stitches compared to the manually segmented outcomes. Total number of segmentation points for each stitch type is 24.

Stitch types	Correctly identified points	Missed points	Over-segmented points	Incorrectly identified points
Purse String	19/24	2	-	3
Continuous Stitch	19/24	3	7	1

Discussion

The proposed algorithm uses the weighting function to find segmentation points. Initial results shows that this approach can extract segmentation points for new tasks according to the previously learned knowledge. To further improve the result, the segmentation points found by this approach can serve as the initial step of finding potential segmentation points and in the future work we will combine the motion templates of trajectories to eliminates false data and enhance the performance.

References

[1] M. J. Fard, S. Ameri, R. B. Chinnam, and R. D. Ellis. Soft boundary approach for unsupervised gesture segmentation in robotic-assisted surgery. *IEEE Robot. Autom. Lett.*, 2(1):171–178, 2017.

[2] B. Huang, M. Ye, Y. Hu, S.-L. Lee, A. Vandini, and G. Yang. A multi-robot cooperation framework for sewing personalised stent grafts. *IEEE Trans. Ind. Informat.*, 2017.

[3] H. C. Lin, I. Shafran, D. Yuh, and G. D. Hager. Towards automatic skill evaluation: Detection and segmentation of robot-assisted surgical motions. *Comput. Aided Surg.*, 11(5):220–230, 2006.

Enhancing Dexterity with a 7-DoF Laparoscopic Suturing Tool

M. Selvaggio[1], G. A. Fontanelli[1], F. Ficuciello[1], L. Villani[1], and B. Siciliano[1]
[1]*University of Naples, Federico II*
{*mario.selvaggio*}*@unina.it*

INTRODUCTION

Minimally invasive robotic surgery (MIRS) exhibits numerous benefits for patients compared to open surgery. MIRS procedures are possible thanks to dexterous instruments allowing to perform precise manipulation. In a previous work, we have developed a 7-degree-of-freedom (DoF) instrument for the da Vinci Research Kit (dVRK) that allows in-hand needle reorientation through rolling motion [1]. To alleviate the surgeon cognitive workload of simultaneously controlling all the instrument DoFs, shared-control techniques might be employed. This is motivated by the fact that steering a manipulator by simultaneously controlling its position and orientation is a rather complicated and cognitively demanding task. Joint limits and singularities of currently adopted instruments limit the surgeons' dexterity leading to several hand-off movements and reconfigurations.

In this work we propose: (i) the development of a shared-control technique for simultaneous teleoperation and joint limits avoidance; (ii) the assessment of the benefits introduced by the additional DoF on a single stitch trajectory through a dexterity analysis.

METHODS

We consider the modified laparocopic instruments presented in [1], that can be modelled as a 7-DoF manipulator whose end-effector is the needle tip Σ_t (see Fig. 1). Assuming that the manipulator is velocity controlled, it can be described by the equation $\dot{\boldsymbol{q}}_s = \boldsymbol{v}$, where $\boldsymbol{q}_s \in \mathbb{R}^7$ denote the vector of the manipulator generalized coordinates and $\boldsymbol{v}$ is the control input. Employing the standard inverse Jacobian map the joint control input $\boldsymbol{v} \in \mathbb{R}^7$ can be written as [2]

$$\boldsymbol{v} = \underbrace{\boldsymbol{J}_s^{\dagger}\boldsymbol{u}_s}_{\text{primary task}} + \underbrace{(\boldsymbol{I} - \boldsymbol{J}_s^{\dagger}\boldsymbol{J}_s)\dot{\boldsymbol{q}}_{s,0}}_{\text{secondary task}}, \tag{1}$$

where $\boldsymbol{J}_s \in \mathbb{R}^{6\times 7}$ is the manipulator task Jacobian, $\boldsymbol{J}_s^{\dagger}$ denotes its Moore-Penrose pseudoinverse. The control input includes a Cartesian space velocity vector $\boldsymbol{u}_s \in \mathbb{R}^6$ representing the primary task, and an additional velocity $\dot{\boldsymbol{q}}_{s,0} \in \mathbb{R}^7$, projected into the null space of the primary task.

The shared control strategy adopted in this work consists in a human operator action that steers the manipulator along its 6-D Cartesian space and an autonomous regulation of the manipulator redundancy for joint limits avoidance.

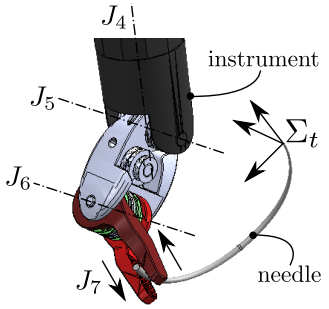

Fig. 1: Representation of the modified dVRK instrument proposed in [1]. $J_4, \ldots, J_7$ represent the joints 4 to 7 axes of the instrument.

This is realized by putting $\boldsymbol{u}_s = \boldsymbol{u}_m \in \mathbb{R}^6$, where $\boldsymbol{u}_m$ is the Cartesian velocity of the master input device, while $\dot{\boldsymbol{q}}_{s,0}$ is the autonomous control action that maximizes the distance from joint limits.

To compute $\dot{\boldsymbol{q}}_{s,0}$ we consider the scalar cost function $h(\boldsymbol{q}_s) : \mathbb{R}^7 \to \mathbb{R}$ [3]

$$h(\boldsymbol{q}_s) = \sum_{i=1}^{n} \frac{1}{4} \frac{(q_{si,max} - q_{si,min})^2}{(q_{si,max} - q_{si})(q_{si} - q_{si,min})}, \tag{2}$$

that is a differentiable function of the generalized coordinates vector $\boldsymbol{q}_s$ which tends to infinity as the i-th joint variable q_{si} approach one of the corresponding joint limits $(q_{si,min}, q_{si,max})$. The gradient $\nabla h(\boldsymbol{q}_s)$ is used to compute the autonomous control contribution for joint limits avoidance according to

$$\dot{\boldsymbol{q}}_{s,0} = -\nabla h(\boldsymbol{q}_s). \tag{3}$$

This term is used to implement the secondary task in (1). It is worth to note that the case $\dot{\boldsymbol{q}}_{s,0} = \boldsymbol{0}$ corresponds to the least-norm joint velocity solution. A suitable dexterity measure must be adopted to quantify the enhanced motion capability of the 7-DoF tool compared to the standard dVRK tool (6-DoF). This measure can be inferred directly from the robot Jacobian matrix. The influence of the joint limits on the robot dexterity can be taken into account by weighting the entries of the Jacobian matrix according to a joint limits performance criterion [4]. More in detail, a penalization matrix $L(\boldsymbol{q}_s) \in \mathbb{R}^{6\times 7}$

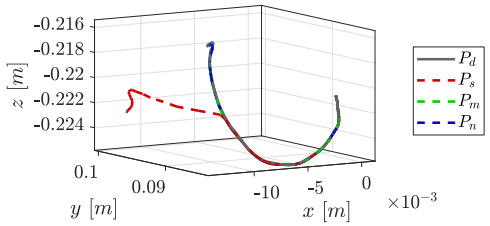

Fig. 2: Desired needle tip path (P_d) versus standard tool (P_s), modified tool least-norm (P_m) and null-space (P_n) paths.

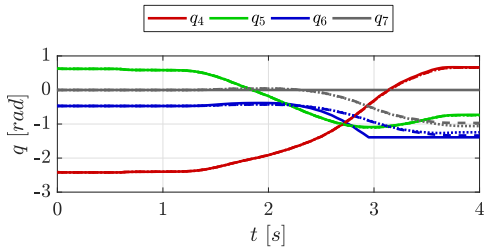

Fig. 3: Time history of joint angles during the proposed experiment. Solid lines represent the 6-DoF case, dashed and dotted lines represent the 7-DoF case least-norm and null-space solutions, respectively.

is introduced to compute the elements of the augmented Jacobian $\tilde{J}(\boldsymbol{q}) \in \mathbb{R}^{6\times 7}$ as

$$\tilde{J}_{i,j}(\boldsymbol{q}_s) = L_{i,j}(\boldsymbol{q}_s) J_{i,j}(\boldsymbol{q}_s), \quad i = 1,\dots 6, \quad j = 1,\dots 7, \tag{4}$$

where $J_{i,j}(\boldsymbol{q}_s)$ is the (i,j) element of the robot Jacobian and $L_{i,j}(\boldsymbol{q}_s)$ is defined as

$$L_{i,j}(\boldsymbol{q}_s) = \frac{1}{\sqrt{1 + |\nabla h_j(\boldsymbol{q}_s)|}}. \tag{5}$$

At this point, taking inspiration from [5], a weighted dexterity measure d can be computed from the augmented Jacobian as

$$d = \frac{\sqrt{rn}}{\sqrt{\mathrm{tr}\left[\left(\tilde{J}\tilde{J}^{\mathrm{T}}\right)^{-1}\right]}}, \tag{6}$$

where $\mathrm{tr}(\cdot)$ denote the trace operator, r and n denote the task and the joint space dimensions, respectively. This index provides similar information of the standard manipulability index [6], but allows comparing manipulators with the same task space dimension independently from the joint space dimension. Moreover, it takes into account the distance from both joint limits and singularities.

EXPERIMENTS AND RESULTS

We performed simulated experiment using the V-REP simulator. The simulated setup recreates the real dVRK slave side. We used a pre-recorded single stitch trajectory and compute $\boldsymbol{u}_m(t)$ from this. The task is executed using both the 6-DoF and 7-DoF tools. In the latter case both the least-norm (i.e., $\dot{\boldsymbol{q}}_{s,0} = 0$) and the null-space solutions are considered. Results of the proposed experiments are given in Figs. 2, 3 and 4. As it can be noticed in the 6-DoF case the trajectory is not successfully completed due to the occurrence of joint limit on the

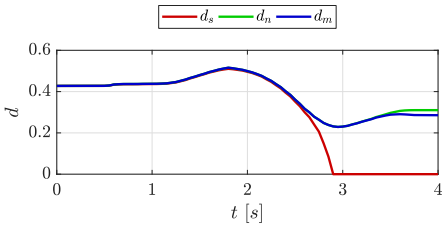

Fig. 4: Dexterity measure along the executed trajectory. d_s represents 6-DoF case, d_m and d_n the 7-DoF least-norm and null-space solutions, respectively.

sixth joint (Figs. 2 and 3). This is quantitatively explained by the dexterity measure which approaches zero accordingly (Fig. 4).

In the 7-DoF case both the least-norm and the null-space solutions are efficient in terms of joint limits avoidance (Figs. 2 and 3). However, the null space solution demonstrates slightly improved dexterity towards the end of the experiment (Fig. 4) .

We note that, although simulated results are encouraging, the 7-DoF case requires accurate and robust sensing technologies for needle-grasper relative pose estimation in the real scenario.

CONCLUSION

We have presented a shared-control approach for simultaneous teleoperation and joint limits avoidance for a 7-DoF laparoscopic instrument. The results have demonstrated improved dexterity with respect to the 6-DoF case along a single stitch suturing trajectory. Future works will focus on shared control with multi-objective optimization and experiments with the real prototype.

References

[1] G. A. Fontanelli, M. Selvaggio, L. R. Buonocore, F. Ficuciello, L. Villani, and B. Siciliano, "A new laparoscopic tool with in-hand rolling capabilities for needle reorientation," *IEEE Robotics and Automation Letters*, vol. 3, no. 3, pp. 2354–2361, July 2018.

[2] B. Siciliano and J. J. E. Slotine, "A general framework for managing multiple tasks in highly redundant robotic systems," in *Fifth Int. Conf. on Advanced Robotics*, 1991, pp. 1211–1216 vol.2.

[3] M. Selvaggio, S. Grazioso, G. Notomista, and F. Chen, "Towards a self-collision aware teleoperation framework for compound robots," in *IEEE World Haptics Conference*, 2017, pp. 460–465.

[4] N. Vahrenkamp, T. Asfour, G. Metta, G. Sandini, and R. Dillmann, "Manipulability analysis," in *IEEE-RAS Int. Conf. on Humanoid Robots*, 2012, pp. 568–573.

[5] S. Tadokoro, I. Kimura, and T. Takamori, "A dexterity measure for trajectory planning and kinematic design of redundant manipulators," in *Annual Conf. of IEEE Industrial Electronics Society*, 1989, pp. 415–420.

[6] T. Yoshikawa, "Manipulability of robotic mechanisms," *The International Journal of Robotics Research*, vol. 4, no. 2, pp. 3–9, 1985.

High Speed Fluorescence Endomicroscopy with Structured Illumination for Robot Assisted Minimally Invasive Surgery

Haojie Zhang and Guang-Zhong Yang

The Hamlyn Centre for Robotic Surgery, Imperial College London, UK
hz1112@ic.ac.uk

INTRODUCTION

While confocal fluorescence microscopy provides an effective means of eliminating signals from out-of-focus light, its costs, complexity and low frame rate have motivated the development of alternative microscope techniques. Structured illumination microscopy (SIM) offers confocal-like out-of-focus background rejection without the need of beam scanning [1]. In this technique, a predefined illumination pattern is projected onto the sample, where only in-focus information is modulated due to rapid attenuation of high spatial frequency pattern of defocussed areas [2].

The imaging speed of SIM is related to the process of shifting the illumination pattern. In many early SIM systems, physical gratings are used to generate patterned illuminations via a mechanically moving stage. This is difficult to realize a very precise pattern shift, especially at a high shifting rate, which can cause artefacts in reconstructed images. The spatial light modulator (SLM) based SIM system enables precise and rapid control of the excitation pattern, allowing an accurate fast pattern shifting [3]. SLM has therefore been considered in many SIM designs [1,2,3]. However, its use with flexible fibres suitable for robot assisted minimally invasive surgery remains largely unexplored. An initial implementation of this kind of design can only realise an effective SIM frame rate of about 2 fps [1].

In this work, a fluorescence endomicroscopy with a flexible fibre bundle is demonstrated using a SLM-based SIM to produce optically sectioned images at acquisition speed as high as 40 fps. The modulation and optical sectioning of the endomicroscopy is also demonstrated.

MATERIALS AND METHODS

Imaging system

A schematic of the proposed imaging system is shown in Figure 1. The output beam from a CW solid-state laser (Vortran Stradus, λ = 488 nm, TEM_{00}) is expanded by a 6× telescope to a beam diameter of approximately 9 mm. Then, it is projected onto the SLM via a polarizing beam splitter. The SLM incorporates a phase-only ferroelectric liquid crystal on silicon device (Forth Dimension Displays QXGA-3DM) with 2048 ×1536 pixels and 8.2 µm pixel pitch. The grid pattern was generated with the SLM by displaying a grating which diffracts the light [4]. Since the SLM only changes the phase of the light, the contrast of the projected pattern is strongly affected by the polarization state of the light. For maximal contrast, a half-wave plate is placed between the SLM and the beamsplitter to rotate the polarization state of the light. A polariser is used to remove unwanted polarisation light. A spatial filter is applied at the focus of two achromatic doublet (f = 150 mm) to allow only the ±1 diffraction orders to pass. The spatial filter blocks the extra small peak between two high peaks and offers better contrast modulation at the specimen plane [5].

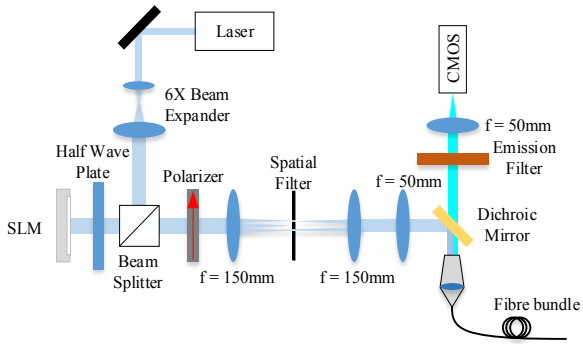

Fig. 1 Schematic of the proposed imaging system. A grid pattern is produced by a SLM and projected onto a sample via an imaging fibre bundle.

Image acquisition and processing

To construct the SIM endomicroscope, an imaging fibre bundle is used to guide both the grid patterned illumination to the specimen and the resulting fluorescence emission back to a CMOS camera. The imaging fibre bundle (Cellvizio Gastroflex UHD) has 30,000 cores with a 600 µm useful diameter. The distal end of the fibre bundle is equipped with a micro-objective (×2.5 magnification, working distance = 50 µm, field of view = 240 µm). The resultant fluorescence is relayed through the fibre bundle, isolated with a dichroic mirror and an emission filter, and imaged onto the CMOS camera (Point Grey FLEA 3) via an achromatic doublet (f = 50 mm). Typical image size is 512 × 512 pixels. Three fluorescence images (I_1, I_2, I_3) of the sample are taken at three different grid positions with a phase-shift of 90° between two adjacent grating [6]. A final optically-sectioned image (I_{SIM}) is then generated by using the following equation [6]:

$$I_{SIM} = \sqrt{(I_1 - I_2)^2 + (I_1 - I_3)^2 + (I_2 - I_3)^2}.$$

Since the maximum frame rate of the SLM is around 1 kHz, the speed of the endomicroscope depends on the camera frame rate, which is around 120 fps, resulting a SIM sectioning speed of 40 fps.

RESULTS

In order to investigate the modulation ability of the system, a uniform fluorescent plane was first illuminated. Figure 2(a) is a computer-generated rectangular grid pattern to be displayed on the SLM. Figure 2(b) is a raw image of the uniform plane illuminated with the pattern in Figure 2(a). The obvious contrast between the ON and OFF pixels of the projected pattern demonstrate good modulation and perfect ON/OFF photo-switching of the fluorophores. The 2D Fourier transforms of Figure 2(b) is shown in Figure 2(c)&(d). The outer ring in Figure 2(c) is from the honeycomb structure of the fibre bundle, which determines the system resolution. The excellent contrast between the ON and OFF pixels can be future proved by the numerous sidebands in Figure 2(d).

A lens tissue paper stained with acriflavine was then illuminated with the same rectangular grating pattern to test the optical sectioning ability of the endomicroscopy. A raw image of the grating-illuminated tissue paper is illustrated in Figure 3(a), showing a clear distinguish between the ON/OFF region. Figure 3(b) is reconstructed from three raw images by using the algorithm showing above. The widefield image in Figure 3(c) is the average of the three raw images, corresponding to the non-sectioned fluorescence image [1]. Figure 3(d) shows profile along the lines in (b) and (c), demonstrating a clear reduction in fluorescence background when comparing the intensity distribution in both cases.

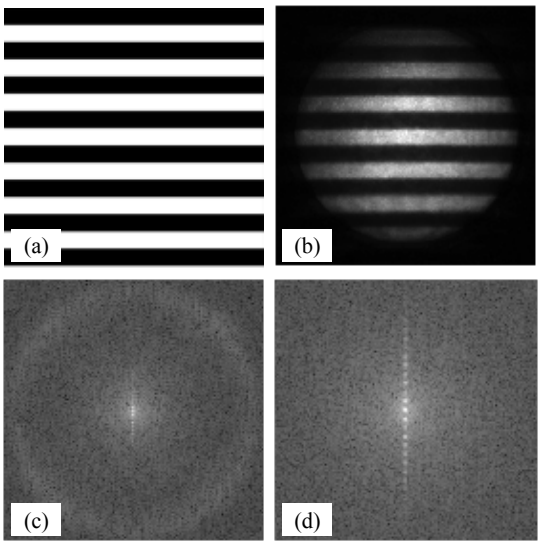

Fig. 2 (a) Pattern with a rectangular grating to be displayed on the SLM. (b) Image of a thin uniform fluorescent plane illuminated with the pattern in (a). (c) Corresponding Fourier transform of the image in (b). (d) Centre origin of the Fourier transform in (c).

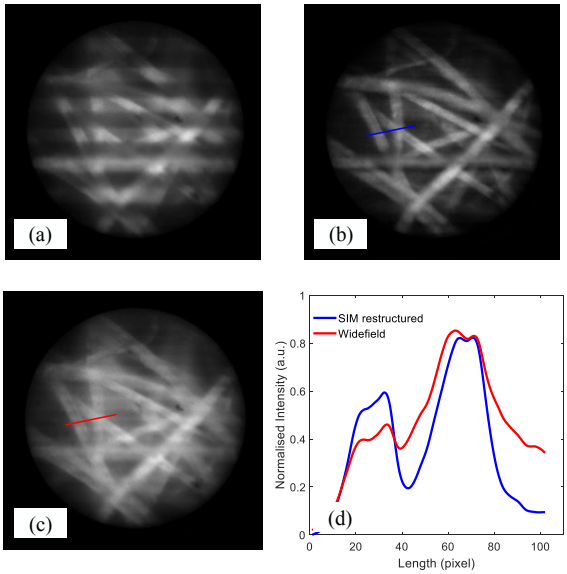

Fig. 3 (a, b and c) grating-illuminated, SIM and widefiled images of lens tissue paper stained with acriflavine. (d) SIM (blue) and wide-field (red) profile along the lines in (b) and (c).

DISCUSSION

A high-speed fluorescence endomicroscopy with a flexible fibre bundle is demonstrated using SLM-based SIM to produce optically sectioned images. The system can achieve camera frame rates up to 120 fps and a SIM image rates up to 40 fps, which is much higher than previous results with a similar design. Initial results show that the system has an excellent modulation and optical sectioning.

ACKNOWLEDGMENTS

This research is conducted with support from the EPSRC Grant EP/N019318/1 (REBOT: Robotic Endobronchial Optical Tomography).

REFERENCES

[1]. Bozinovic, Nenad, et al. “Fluorescence endomicroscopy with structured illumination.” Optics express 16.11 (2008): 8016-8025.

[2]. Xu, Dongli, et al. "Fast optical sectioning obtained by structured illumination microscopy using a digital mirror device." Journal of biomedical optics 18.6 (2013): 060503.

[3]. Kner, Peter, et al. "Super-resolution video microscopy of live cells by structured illumination." Nature methods 6.5 (2009): 339.

[4]. Martínez-García A, et al. “Operational modes of a ferroelectric LCoS modulator for displaying binary polarization, amplitude, and phase diffraction gratings.” Applied optics. 2009 May 20; 48(15):2903-14.

[5]. Fu HL, et al. “Optimization of a widefield structured illumination microscope for non-destructive assessment and quantification of nuclear features in tumor margins of a primary mouse model of sarcoma.” PloS one. 2013 Jul 23;8(7):e68868.

[6]. Neil, Mark AA, et al. “Method of obtaining optical sectioning by using structured light in a conventional microscope.” Optics letters 22.24 (1997): 1905-1907.

Building robust confocal endomicroscopy mosaics despite image losses

B. Rosa[1], K. Rabenorosoa[2], B. Tamadazte[2], P. Rougeot[2], N. Andreff[2], and P. Renaud[1]

[1]*ICube, UDS-CNRS-INSA, 300 bd Sébastien Brant - Illkirch, 67000 Strasbourg, France*
[2]*FEMTO-ST, University of Bourgogne Franche-Comté, CNRS, 25000 Besançon, France*
{*b.rosa*}*@unistra.fr* {*kanty.rabenorosoa*}*@femto-st.fr*

INTRODUCTION

Probe-based confocal laser endomicroscopy (pCLE) is a promising image modality for early cancer screening in various clinical applications. A typical limitation of probe-based systems, however, is the limited field-of-view (FOV) achievable with miniature optics. This is especially true with the high magnifications required for clinical assessment, namely for optical biopsy-based investigations. A widely accepted solution is to opt for high-resolution optics, and enlarge the FOV algorithmically by sweeping the probe along the tissue and reconstructing a mosaic.

While mosaicing effectively enhances the FOV, its accuracy is limited by the fact that the microscale movements required to sweep the probe are difficult to generate manually, especially in minimally invasive settings. For this reason, various approaches using a robotic micromanipulator and visual feedback control have been developed [1, 2, 3].

The above-mentioned methods have in common the fact that they rely on an accurate image-based motion estimation, which should be computed in real-time. Typically, pCLE-based visual servoing methods use a normalized cross correlation (NCC) computation between successive overlapping frames [4]. While this may be sufficient in *ex vivo* conditions, the constraints imposed by the *in vivo* environment make it more difficult. The image quality might be affected by a partial loss of contact with –or excessive force applied on– the tissue (e.g., due to non planar tissue geometry), or simply due to surgical debris present on the surface. Moreover, accelerations in the probe/tissue movement (due to various effects such as stick/slip effects or robot manufacturing inaccuracies) are detrimental for image quality and real-time matching. In summary, there may be parts of the trajectory where the image quality is insufficient for visual servo control, leading to the production of poor mosaics.

This abstract presents a Kalman filter-based approach, where both the image estimation and the (possibly inaccurate) robot trajectory are fused. We validate the proposed approach in controlled bench-top experiments, where the loss of contact with tissue is simulated. We show that it allows computing online mosaics with a coherent topology, despite an important loss of probe-tissue contact at several points along the trajectory. The method could be used for robustly estimating the probe-tissue movement online in a visual servo control loop.

MATERIALS AND METHODS

Let's consider the typical mosaicing situation in which a probe is moving with respect to a tissue. The robot moves with a speed $V_r(k)$, with k being a discrete time instance. $V_r(k)$ can be integrated in time to estimate a position $X_r(k)$. Due to various phenomena (encoder noise, mechanical inaccuracies, etc.), this position is estimated with a certain inaccuracy. We denote the noisy robot inputs $\hat{X}_r(k)$.

In parallel, thanks to online image-based methods such as the NCC method [4], an image trajectory $X_m(k)$ (i.e., the trajectory followed by successive images in the mosaic) can be estimated by integrating estimated displacements $dX_m(k)$.

We propose to estimate a filtered trajectory $X_f(k)$ by fusing together $\hat{X}_r(k)$ and $X_m(k)$ using a Kalman filter. The robot velocity at a given instant k is chosen as the process model, which governs the prediction we make about the next position. It is subsequently corrected using the measurement $dX_m(k+1)$, yielding a filtered position estimate $X_f(k+1)$.

At places where the image quality is good, the image estimates are likely to be more precise than the robot ones. Conversely, when there are image losses, the robot input is likely to be more accurate. We encode this information in the process and estimation covariances. To do so, we estimate an image matching confidence c_{img}. We hypothesize that at places where the image matches are of good quality, they are locally consistent with one another in direction. Therefore, we estimate c_{img} by subtracting the angle of the $dX_m(k)$ vector with its median-filtered value over the last five time instances. This value is subsequently normalized to be between 0 and 1. It is then integrated in the Kalman Filter by dividing the measurement covariance values by c_{img}.

The method was validated using a Mauna Kea Cellvizio system for pCLE imaging, and a *Ficus Benjamina* leaf as a tissue sample. The latter was placed on a high-accuracy 6-degrees-of-freedom

robot, which was moved with respect to the probe to produce a relative probe-tissue movement. In order to simulate varying contact conditions (which, for instance, would be created by breath in *in vivo* conditions), the z-axis of the robot was controlled with an oscillating movement of amplitude 150μm around the ideal contact point during the scanning movement. Since the robotic setup is of high accuracy, the programmed spiral trajectory was perfectly executed. Therefore, noise was artificially added to the robot trajectory to produce the noisy robot trajectory $\hat{X}_r$. This trajectory is similar to the ones obtained in *in vivo* conditions with minimally invasive settings, such as reported in [2].
In order to obtain a ground truth validation, the *Ficus Benjamina* leaf was imaged under a conventional microscope with back-light. pCLE images were then registered to this ground truth using Mutual Information (*imregister* function of MATLAB).

RESULTS

Figure 1 presents the mosaic obtained for a spiral trajectory when using only the image measurements. As expected, local image losses create estimation errors, which drive the overall mosaic topology very far from the input spiral trajectory. One can see on Fig. 1b that the estimated image confidence gets very low at places where the image trajectory is locally incoherent.

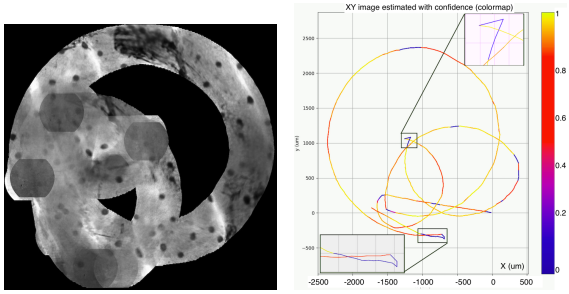

(a) Image-estimated mosaic (b) c_{img} values

Fig. 1: Reconstructed mosaic using only image measurements. Left: mosaic; Right: image-estimated trajectory X_m, with c_{img} shown as a colormap.

When using the noisy robot trajectory $\hat{X}_r$ (Fig. 2(a), the mosaic shape is partially recovered. However, branches of the spiral are superimposed, leading to a visually blurry mosaic very difficult to analyze. Finally, using the filtered output X_f for the mosaic yields the best result (Fig. 2(b)). Note that the mosaic could be further improved by offline bundle adjustment, but it is nonetheless important for the clinician to be able to assess the mosaic quality in real time [4].
Those results are confirmed by comparing the positions in the mosaic with the conventional microscopy ground truth. Using only the image estimates X_m, the average position error is very high (mean 686.7μm, std. dev. 1080.8μm). As expected, it decreases when using $\hat{X}_r$ (mean 291.0μm, std 134.9μm). The error is, however, high with respect to the pCLE images FOV (500μm). Finally, the filtered positions X_f exhibit the lowest errors (mean 100.8μm, std 63.9μm). Similar results were obtained using different trajectories (circle, line).

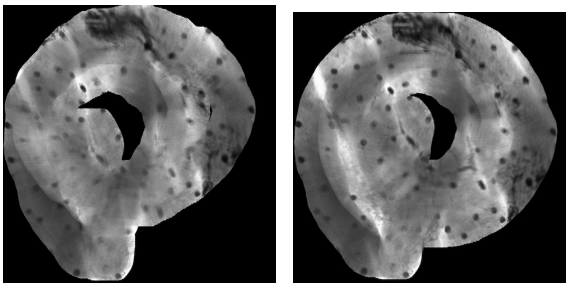

(a) Using $\hat{X}_r$ (b) Using X_f

Fig. 2: Reconstructed mosaics using robot measurements. Left: using the noisy robot inputs $\hat{X}_r$; Right: Using the filtered outputs X_f.

DISCUSSIONS

This abstract presents a method for robustly estimating the topology of online pCLE-based mosaics. Estimating the confidence of online image matches allows fusing them with noisy robot trajectory inputs, leading to improved mosaics, despite important local losses in image quality.
The method was validated on a bench-top setting using a high-accuracy robotic setup. Results show that mosaics obtained using the filtered outputs are of better quality, both in terms of visual appearance and with respect to the ground truth image positions. This is likely to help the surgeon perform real-time visual assessment, as well as to shorten computing time of subsequent bundle adjustment.
Further work will include validation on *ex vivo* and *in vivo* settings.

REFERENCES

[1] B. Rosa, et al. *Building large mosaics of confocal edomicroscopic images using visual servoing.* IEEE Trans. Biomed. Eng., 60(4), p. 1041-1049, 2013.

[2] M. S. Erden, et al. Conic-Spiraleur: A miniature distal scanner for confocal microlaparoscope. IEEE/ASME Trans. Mechatronics, 19(6), p. 1786-1798, 2014.

[3] Zhang, L., et al. *From Macro to Micro: Autonomous Multiscale Image Fusion for Robotic Surgery.* IEEE Robotics & Automation Mag., 24(2), p. 63-72, 2017.

[4] Vercauteren, T. et al. *Real time autonomous video image registration for endomicroscopy: fighting the compromises.* SPIE BIOS, vol. 6861, pages 68610C, 2008.

Intraoperative Optical Characterisation of Thermal Ablation

N.T. Clancy[1,2,3], K. Gurusamy[5], G. Jones[1,2,3], B. Davidson[5], M.J. Clarkson[1,2,4], D.J. Hawkes[1,2,4], D. Stoyanov[1,2,3]

[1]Wellcome/EPSRC Centre for Interventional & Surgical Sciences (WEISS), [2]Centre for Medical Image Computing (CMIC), [3]Department of Computer Science, [4]Department of Medical Physics and Biomedical Engineering, University College London, WC1E 6BT, UK.

[5]Division of Surgery and Interventional Science, UCL Medical School, Royal Free Hospital, University College London, NW3 2QG, UK.
n.clancy@ucl.ac.uk

INTRODUCTION

Delivery of thermal energy is used intraoperatively to cause local damage to diseased tissue, such as tumours, in cases where resection is deemed inappropriate. It is clinically used in the form of radio frequency (RF), microwave, laser and high energy focussed ultrasound (HiFU) ablation [1]. Ablation probes may be placed in tissue under image guidance, but delivery of the appropriate amount of energy is often at the discretion of the surgeon, with few feedback methods at their disposal. Online visualisation of the zone of thermal damage may allow surgeons to expand use of ablation to areas close to critical structures, such as inoperable pancreatic tumours, where destruction of diseased tissue could be balanced against the risk of collateral damage.

Optical spectral imaging and sensing techniques are capable of following functional and structural changes to tissue and have been used to estimate changes to the blood supply in numerous organs [2], including work by our group tracking oxygenation dynamics [3] and physical changes due to radiofrequency energy delivery [4]. In this preliminary study multispectral imaging (MSI) and diffuse reflectance spectroscopy (DRS) are used to assess changes in liver vasculature during microwave ablation (MWA). Spectral profiles consistent with expected physiological changes in the tissue are observed. These methods may also be used to monitor the organ-wide or systemic effects of new or experimental surgical treatments, where the mechanisms of action may not yet be fully-understood.

MATERIALS AND METHODS

During open abdominal surgery on a porcine subject (~45 kg) a microwave ablation needle (Solero MTA, Angiodynamics, Inc., USA) was introduced into the liver, placing the needle approximately 1 cm below the surface. 133 W of energy was delivered over two minutes. The tissue was monitored continuously using thermal imaging (A35sc; FLIR Systems, Inc., USA) and MSI (SpectroCam; Pixelteq, USA) with xenon illumination (XL300; Lemke, Germany) during a baseline period and throughout the ablation. DRS measurements of the tissue were acquired using an optical fibre reflectance probe (RP22; Thorlabs Ltd., UK), spectrometer (CCS200; Thorlabs Ltd., UK) and tungsten halogen lamp (SLS201L; Thorlabs Ltd., UK) at several points prior to, and immediately after ablation. Oxygen saturation (StO_2) and total haemoglobin (*Hbt*) were estimated from MSI and DRS spectral data using a regression algorithm described previously [3]. Both cameras were mounted over the operating table, allowing a top-down view, as shown in the experimental set-up schematic (Fig. 1).

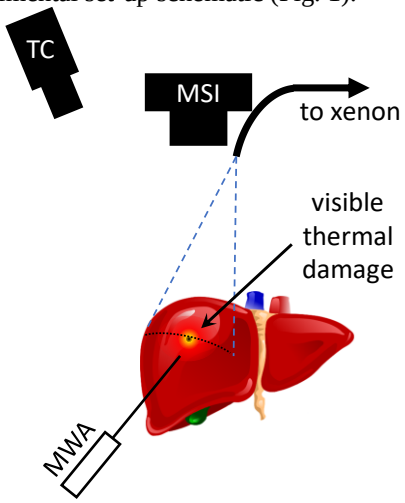

Fig. 1 Schematic of experimental set-up showing xenon light cable, MSI and thermal cameras (TC) in relation to the MWA site. The DRS probe and the trajectory used for point measurements is indicated (dashed line).

RESULTS

Figure 2 shows colour, MSI and thermal images of the organ, with MWA needle in place, before and after ablation. Initial changes in *Hbt* are noticed approximately 30 s after commencement of MWA. After two minutes of energy delivery a symmetrical thermal profile is seen to have developed around the needle head. During this period the entire organ becomes inflamed, as seen from the *Hbt* maps, with a particularly strong region of erythaema around a necrotic core at the needle entrance point. Strong specular highlights also characterise this central zone of greatest thermal damage, where there is an average temperature increase of approximately 25°C during ablation.

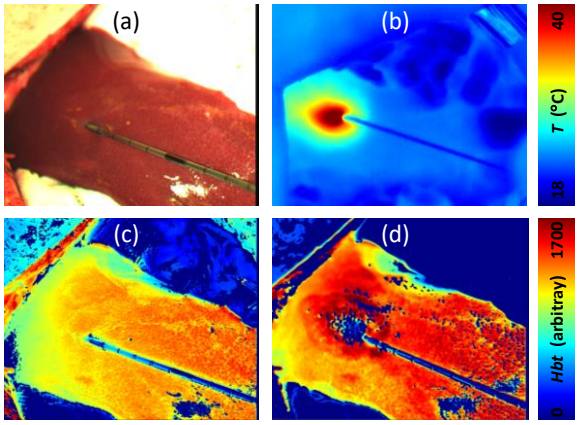

Fig. 2 (a) Baseline image of liver and (c) corresponding *Hbt* map. (b) Thermal image of liver during MWA showing local heating. (d) *Hbt* map after MWA energy delivery.

High resolution DRS data were recorded along the profile shown in Fig. 1. These were then converted to absorbance spectra and fitted to the light-tissue interaction model as shown in Fig. 3.

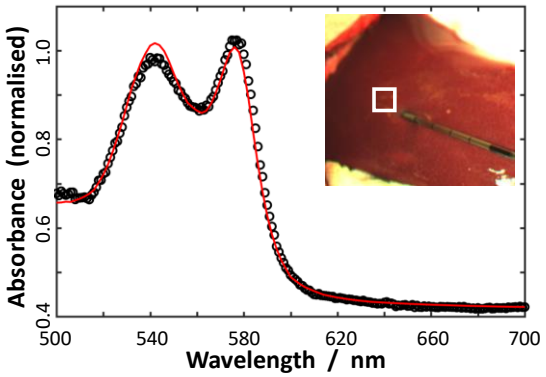

Fig. 3 Baseline StO_2 measurement with DRS. Experimentally-calculated absorbance (black circles) is fitted by a light attenuation model (red line). Inset: liver, with MWA needle, prior to ablation. DRS location indicated by white square.

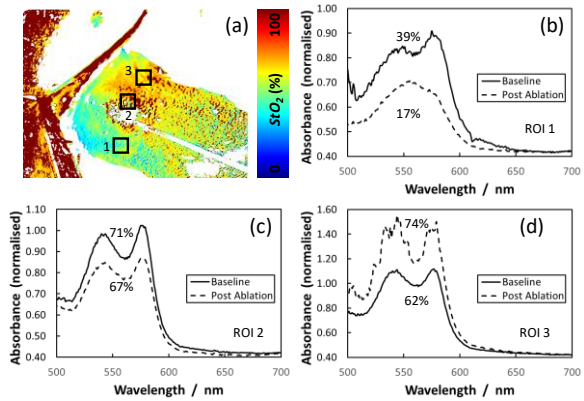

Fig. 4 (a) StO_2 map of liver, post ablation, featuring regions-of-interest (ROIs) indicating DRS measurement positions. (b-d) Corresponding absorbance spectra measured with DRS.

After ablation there is an observable change in the spatial oxygenation profile across the organ (Fig. 4). MSI indicates high StO_2 in erythaematous regions near the centre and towards the top of the image, while a large ischaemic patch is seen to have developed on the lower side. This is supported by DRS, dominated by oxyhaemoglobin features, apart from ROI 1, which exhibits the deoxyhaemoglobin shape post-ablation.

DISCUSSION & CONCLUSIONS

As tissue average temperature increases, erythaema develops as blood vessels dilate. These areas retain high oxygenation values similar to, or exceeding, baseline levels. As the temperature rises still further coagulative necrosis becomes apparent. Specular highlights prevent accurate StO_2 estimation in this region. While thermal imaging indicates symmetric energy delivery, the *Hbt* maps of Fig. 2 (c,d), which are direct measures of the vasculature, demonstrate an asymmetric effect on the vessels. The ischaemic patch, for example, may be due to damage to larger, deeper, vessels and heat-sink effects. DRS supports MSI results, showing clear spectral changes, particularly in the ischaemic region.

This preliminary study indicates the potential of optical imaging to quantitatively follow ablation processes. Further work will correlate temperature and haemodynamic changes with histologically-validated cellular damage. Cross-sectional analysis of ablated tissue *ex vivo* will show how damage beyond MSI/DRS sensitivity limits (1-2 mm) relates to surface measurements. This technology could also be used to assess possible collateral tissue damage during other ablation types, e.g., irreversible electroporation [5], where the mechanism is non-thermal.

ACKNOWLEDGEMENTS

This work is funded by a Wellcome Trust Pathfinder award (201080/Z/16/Z) and the EPSRC (EP/N013220/1, EP/N022750/1, EP/N027078/1, NS/A000027/1, EP/P012841/1). The authors thank the Northwick Park Institute for Medical Research (NPIMR) for assistance with the surgical experiment, conducted under local ethics approval. The microwave ablation needle and Solero unit were kindly provided by AngioDynamics.

REFERENCES

[1] Chu KF and Dupay DE. Thermal ablation of tumours: biological mechanisms and advances in therapy. Nat. Rev. Cancer. 2014;14(3):199-208.

[2] Lu G and Fei B. Medical hyperspectral imaging: a review. J. Biomed. Opt. 2014;19(1):010901.

[3] Clancy NT, Arya S, Stoyanov D, Singh M, Hanna GB, and Elson DS. Intraoperative measurement of bowel oxygen saturation using a multispectral imaging laparoscope. Biomed. Opt. Express. 2015;6(10):4179-4190.

[4] Clancy NT, Arya S, Stoyanov D, Du X, Hanna GB, and Elson DS. Imaging the spectral reflectance properties of bipolar radiofrequency-fused bowel tissue. Proc. SPIE, Clinical and Biomedical Spectroscopy and Imaging IV. 2015;9537:953717.

[5] Chen X, Ren Z, Zhu T, Zhang X, Peng Z, Xie H, Zhou L, Yin S, Sun J, and Zheng S. Electric ablation with irreversible electroporation (IRE) in vital hepatic structures and follow-up investigation. Sci. Rep. 2015;5:16233.

Towards intraoperative hyperspectral imaging: design considerations for neurosurgical applications

J. Shapey[1,2], Y. Xie[1], E. Nabavi[1], D. Ravi[1], S Saeed[2,3,4], R Bradford[2], S Ourselin[1], T. Vercauteren[1]

[1]*Wellcome / EPSRC Centre for Interventional and Surgical Science, UCL, London, UK*
[2]*The National Hospital for Neurology and Neurosurgery, London, UK*
[3]*The Ear Institute, UCL, London UK*
[4]*The Royal National Throat, Nose and Ear Hospital, London, UK*

j.shapey@ucl.ac.uk

INTRODUCTION

Successful neurosurgery to remove brain tumours depends on achieving maximal safe tumour removal; avoiding damaging sensitive areas that undertake vital functions and preserving crucial nerves and blood vessels. However, even with the most advanced current techniques, it is not always possible to identify critical structures during surgery and the identification of tumour tissue is still based on surgeons' subjective visual assessment.

Optical imaging techniques provide a promising solution for intraoperative tissue characterisation, with the advantages of being non-contact, non-ionising and non-invasive. Hyperspectral imaging (HSI) is a hybrid modality that combines optical imaging and spectroscopy and generates a three-dimensional (3D) dataset of the imaged area [1]. The spectral signature of each pixel may enable HSI systems to differentiate between tissue types and to identify various pathological conditions.

Hyperspectral imaging has the potential to deliver real-time images and is increasingly being developed for use in various medical applications including image-guided surgery. Preliminary results from a collaborative EU project (Hyperspectral Imaging Cancer Detection [HELICoiD] project) demonstrated the potential that *in vivo* hyperspectral imaging holds for use in brain tumour surgery [2, 3] but the hardware used to acquire the HSI data was large and cumbersome, restricting its use and limiting the amount of available training data [Fig. 1a]. High-speed computational processing is required to deliver real-time intraoperative image analysis but is reliant on a large training dataset.

In this study, we determine key design specifications for an optimal, yet practical, hyperspectral imaging system for use in neurosurgery. Our specifications are tempered by what can be realistically delivered but we believe that it is possible to design a more compact system than the HELICoiD one by focusing its compatibility and development on alternative visualisation systems rather than the standard operative microscope. The development of such a system will facilitate more widespread use of hyperspectral imaging, enabling the acquisition of larger training datasets that will support the development of a real-time imaging system.

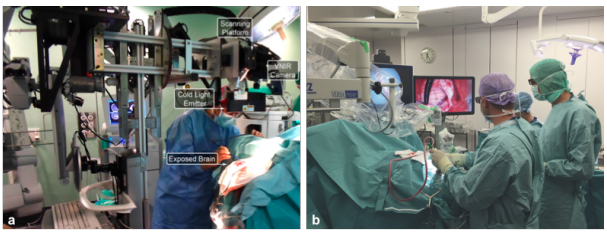

Fig 1: a) Large intra-operative hyperspectral imaging used in the HELICoiD neurosurgery project- courtesy of [3]; b) VITOM 3D exoscope in use during cranial neurosurgery- courtesy of KARL STORZ GmbH & Co, © Prof. Reisch, Prof. Hopf, Klinik Hirslanden, Zurich

METHODS

We reviewed current state-of-the-art solutions for intraoperative visualisation in order to determine the best method of integrating an intraoperative hyperspectral imaging system into the neurosurgical workflow and then conducted laboratory experiments to establish key design specifications for a prototype compatible with our chosen system.

RESULTS

Excellent visualisation and illumination of the surgical field is required to perform safe and successful neurosurgery. The operating microscope revolutionised neurosurgery and enables the operating surgeon to see 3D images at high magnification with the ability to adjust the focal length, magnification and brightness. More recently, the surgical "exoscope"- a high-definition video telescope operating monitor system (VITOM, KARL STORZ GmbH & Co, Germany), has been proposed as an alternative to the operating microscope. Its long focal distance of 20-50cm allows the camera to be positioned outside the surgical cavity allowing the surgeon to perform surgery in a more ergonomic position and has the added advantage of an improved depth of field of view, thereby minimising the need to refocus the scope at higher magnifications [Fig. 1b] [4]. Furthermore, recent iterations of the exoscope system have been

developed to permit 3D visualisation (VITOM-3D) [5] with a magnification range of x8 to x30.

We believe that designing a compact HSI prototype compatible with the surgical exoscope will facilitate its easy integration into the neurosurgical workflow. Further, it will be relatively straightforward to adapt future iterations of such a prototype for endoscopic use, enabling the technique to be used for a wider range of applications and procedures.

In our laboratory experiments, we attached various modules to the exoscope to determine the maximal weight and dimensions for the prototype camera system. We also tested its manoeuvrability whilst attached to a mechanical scope holder to ensure it did not impede the functionality of the exoscope system.

We concluded the following design specifications for a HSI prototype exoscope system:

- Individual components housed within a lightweight casing
- Maximal dimensions of casing: 10 x 12cm
- Maximal total weight: 1200g
- Ancillary arm to support casing in stationary position

Different tissue types possess unique spectral signatures between 400-1700nm. In order to develop a neurosurgical HSI system capable of label-free image acquisition it is essential that the prototype system is capable of imaging this range of wavelengths which may require the use of two different cameras [Fig. 2].

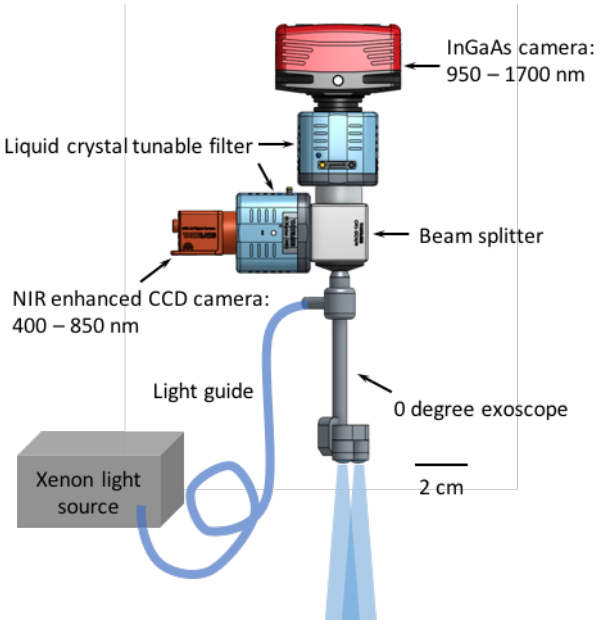

Fig 3. Illustration of prototype components

Finally, we tested our prototype setup to determine if the InGaAs camera is able to detect light in the wavelength range of 950-1700nm when using the exoscope [Fig. 3a]. The exoscope does not have any specific coatings to filter out light in the near infrared range so the InGaAs camera successfully imaged our gel-wax phantom model [Fig 3b].

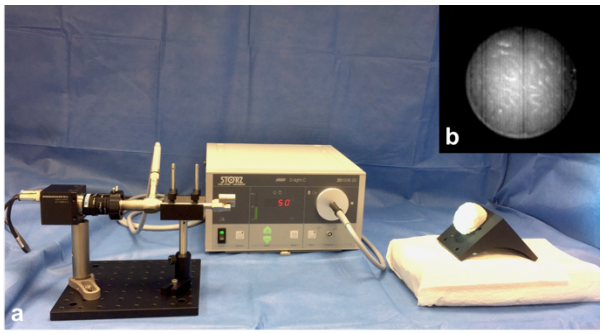

Fig 3. a) Experimental setup to test the imaging of a gel-wax phantom model under Xenon light illumination using the InGaAs-Exoscope setup; b) Image of gel-wax phantom taken with InGaAs camera

DISCUSSION

Hyperspectral imaging has the potential to transform intraoperative surgical visualisation. By classifying different tissue types within the operative field, an anatomical map of critical structures and tumour tissue may be generated to assist the surgeon. To achieve real-time image analysis, large amounts of HSI data are required to train a reliable model but current systems are impractical, prohibiting data collection. Here we present the design specifications for a prototype HSI system that may be easily integrated into the current neurosurgical workflow and would facilitate the creation of a large database for better model generation.

ACKNOWLEDGMENTS

This work is supported by Wellcome / EPSRC funding (Grant codes 203145Z/16/Z & NS/A000050/1) and the National Brain Appeal

REFERENCES

1. Lu, G. and B. Fei, *Medical hyperspectral imaging: a review.* J Biomed Opt, 2014. **19**(1): p. 10901.
2. Ravi, D., et al., *Manifold Embedding and Semantic Segmentation for Intraoperative Guidance With Hyperspectral Brain Imaging.* IEEE Trans Med Imaging, 2017. **36**(9): p. 1845-1857.
3. Fabelo, H., et al., *Spatio-spectral classification of hyperspectral images for brain cancer detection during surgical operations.* PloS one, 2018. **13**: p. e0193721.
4. Mamelak, A.N., T. Nobuto, and G. Berci, *Initial clinical experience with a high-definition exoscope system for microneurosurgery.* Neurosurgery, 2010. **67**(2): p. 476-83.
5. Oertel, J.M. and B.W. Burkhardt, *Vitom-3D for Exoscopic Neurosurgery: Initial Experience in Cranial and Spinal Procedures.* World Neurosurg, 2017. **105**: p. 153-162.

Abdominal Aortic Aneurysm Segmentation with a Small Number of Training Subjects

Jian-Qing Zheng[1], Xiao-Yun Zhou[1], Qing-Biao Li[1], Celia Riga[2,3], and Guang-Zhong Yang [1]

[1] *The Hamlyn Centre for Robotic Surgery, Imperial College London, UK*

[2] *Academic Division of Surgery, Imperial College London, UK*

[2] *Regional Vascular Unit, St Marys Hospital, London, UK*

j.zheng17@imperial.ac.uk

INTRODUCTION

Abdominal Aortic Aneurysm (AAA) mostly occurs among old people and potential rupture can be deadly. Fenestrated Endovascular Aortic Repair (FEVAR) is a common procedure for treating AAA when it involves aortic branches, where multiple customized stent grafts including the main, branch and iliac stent grafts are usually cascaded to exclude the aneurysm. For stent graft customization, the diameters of the Proximal Landing Zone (PLZ) and the Distal Landing Zone (DLZ) determine the top diameter of the main stent graft and the bottom one of the iliac stent graft; the position and orientation of the aortic branch, including the celiac trunk and the superior mesenteric artery, determine those of the fenestration and scallop. A 3D AAA shape and its corresponding main stent graft are respectively shown in Fig. 1(a) and Fig. 1(b). AAA segmentation, indicating the shapes of PLZ, DLZ and aortic branch, is vital to stent graft customization. Traditionally, expert-designed feature extractors were implemented to segment the AAA while deep neural networks with multiple non-linear modules were recently used for automatic feature extraction. For example, a deep belief network was utilized to detect, segment, and classify the AAA [1], however, without quantified segmentation results provided. A deep convolutional neural network (DCNN)-based segmentation and quantification of abdominal aortic thrombus [2] was implemented in totally 38 pre- and post-operative subjects to assess the EVAR treatments [2]. A multi-stage network including a detection network (holistically-nested edge detection network) and a segmentation network (fully convolutional network) was proposed to segment the thrombi from 13 post-operative CTA volumes [3].

Many training subjects were required in previous work. This paper caters for the overfitting caused by the small number of training subjects using data augmentation based on gray value variation and translation (G.&T.) for training a one-stage network - U-Net [4]. The methodology workflow illustrated in Fig. 1(c) includes data collection, data augmentation, network training, post-processing and 3D reconstruction. Dice Similarity Coefficients (DSCs) over 0.8 were achieved.

MATERIALS AND METHODS

Network Architecture and Training: U-net [4] with convolutional layers, max-pooling layers, and deconvolutional layers was adopted to train and segment the AAA slice-by-slice. Its detailed structure is shown in Fig. 1(c). The input is a 2D CTA slice while the output is the segmentation result. Cross-entropy was computed as the loss function:

$$\mathcal{L}_{CE} = -\sum_{i=1}^{W}\sum_{j=1}^{H}\sum_{k=1}^{N} \boldsymbol{G}_{(i,j,k))}\log(\boldsymbol{P}_{(i,j,k)}) \quad (1)$$

Here, $\boldsymbol{G}$ is the ground truth; $\boldsymbol{P}$ is the predicted probability; W is the image width; H is the image height; $N = 2$ is the class number.

Stochastic Gradient Descent (SGD) and Adam were employed to minimize the loss function with the batch size as 1 and no batch accumulation. For SGD, the initial learning rate was 0.1 and multiplied by 0.1 when the loss stops decreasing. A momentum of 0.9 was applied. The initial learning rate of Adam was 0.001. The loss converged after about 110k iterations (8∼12 hours).

Data Collection: Three pre-operative AAA CTA volumes were collected in a supine position from the celiac trunk to the iliac arteries from different patients. Two of them (Subject 2, Subject 3) scanned by Siemens Definition AS+ were contrast-enhanced while the other one (Subject 1) scanned by Philips ICT 256 was not. The pixel spacing was 0.645∼0.977mm and the slice thickness was 0.7∼1mm. The AAA in the transverse sectional slices were manually segmented as the ground truth using *Analyze* (AnalyzeDirect, Inc, Overland Park, KS, USA). All images were adjusted with a unified pixel spacing of 0.645×0.645mm by sampling or bilinear interpolation.

Data Augmentation: A small number of training subjects results in overfitting due to the inter-subject variations in the CTA slice contrast (different contrast media used) and the AAA position. In this paper, the inter-subject variation of image contrast was compensated using a linear mapping transformation, and that of AAA position was solved by translating a 512×512 image window along the CTA slices with a stride of 64. We also applied rotation and mirroring (R.&M.) data augmentation as a comparison,

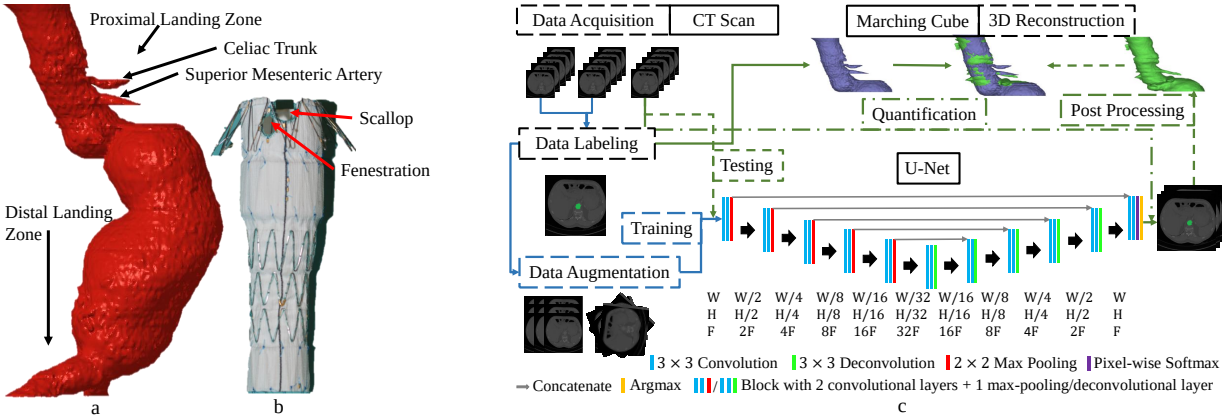

Fig . 1: (a) a 3D mesh model of one AAA, showing the PLZ, DLZ, etc.; (b) a main stent graft with customized fenestration and scallop; (c) a work flow chart of 3D AAA reconstruction, the 34-layer U-net with a convolution stride as 1, input width W = 512, input height H = 512, and initial feature number F = 64.

which was usually used with sufficient training subjects. The data were augmented 45∼72 times from hundreds of original slices.

Post-processing and 3D Reconstruction: *MATLAB*® functions "regionprops" and "bwareopen" were used to automatically extract the largest volume from the segmentation results. The 3D AAA shape was reconstructed using marching cube.

Validation: Cross-validation was adopted, in which respectively each subject was used for the testing while the other two for the training, except for Subject 1, as it was scanned without contrast media. DSC was computed for each slice to quantify the segmentation results, and *Cloudcompare* was used to evaluate the 3D AAA reconstruction.

Table 1: DSCs of AAA segmentation with cross-validation, different data augmentation, and U-Net with varying layers (Num.-Number).

Row	Train Subject	Augmentation	Layer Num.	DSC avg.±std
1	1, 2	R.&M.	34	0.500 ± 0.304
2	1, 2	G.&T.	28	0.757 ± 0.151
3	1, 2	G.&T.	34	0.802 ± 0.157
4	1, 3	G.&T.	34	0.824 ± 0.131

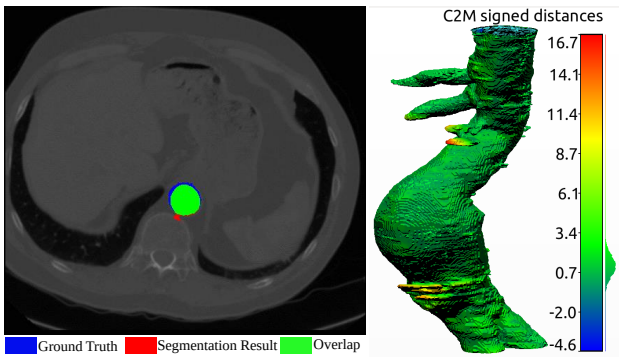

Fig . 2: (a) one segmentation example; (b) a 3D outcome model, with the colours showing the point cloud-to-mesh distances (C2M, unit: pixel) between the model and the ground truth calculated using iterative closest point, and a histogram of C2M distance-distribution.

RESULTS

The U-Net was trained on different subjects, with varying layers and augmentation methods, the corresponding DSCs are shown in Tab. 1. Row 1 and Row 2 illustrate that the proposed data augmentation with G.&T. outperformed the conventional R.&M.; Row 2 and Row 3 show that a 34-layer U-Net achieved a higher DSC than a 28-layer U-Net; Row 3 and Row 4 verify the robustness of the proposed method to variable datasets. A segmentation example is demonstrated in Fig. 2(a), and a 3D reconstruction result is illustrated in Fig. 2(b), showing that the PLZ, DLZ and aortic branch are all reconstructed reasonably.

DISCUSSION

In this paper, data augmentation G.&T. was proposed to reduce the requirement of training subject number to two. We achieved one-stage AAA segmentation with U-Net from pre-operative CTA images, which facilitates stent graft customization and will help intra-operative FEVAR navigation in the future.

REFERENCES

[1] H. A. Hong and U. Sheikh, "Automatic detection, segmentation and classification of abdominal aortic aneurysm using deep learning," in *CSPA*, pp. 242–246, IEEE, 2016.

[2] K. López-Linares, L. Kabongo, N. Lete, G. Maclair, M. Ceresa, A. García-Familiar, I. Macía, and M. Á. G. Ballester, "Dcnn-based automatic segmentation and quantification of aortic thrombus volume: Influence of the training approach," in *CVII-STENT and LABELS workshop in MICCAI*, pp. 29–38, Springer, 2017.

[3] K. López-Linares, N. Aranjuelo, L. Kabongo, G. Maclair, N. Lete, M. Ceresa, A. García-Familiar, I. Macía, and M. A. G. Ballester, "Fully automatic detection and segmentation of abdominal aortic thrombus in post-operative cta images using deep convolutional neural networks," *in MedIA*, 2018.

[4] O. Ronneberger, P. Fischer, and T. Brox, "U-net: Convolutional networks for biomedical image segmentation," in *MICCAI*, pp. 234–241, Springer, 2015.

Scene-preserving Contrast and Color Enhancement for Miniature Flexible Endoscopes in Fetoscopy

D.I. Shakir[1], S. Ourselin[1], J. Deprest[1,2,3], T. Vercauteren[1,2]

[1]*Wellcome / EPSRC Centre for Interventional and Surgical Sciences, UCL, UK*

[2]*Department of Obstetrics and Gynaecology, University Hospitals Leuven, Belgium*

[3]*Institute for Women's Health, UCL, UK*

d.shakir@ucl.ac.uk

INTRODUCTION

Flexible miniature endoscopes facilitate surgical navigation in challenging procedures such as pre-natal fetal surgery, which entails the navigation of the feto-placental unit, an inherently elusive anatomy that does not lend itself easily to imaging with conventional rigid endoscopes [1]. Beyond this, their miniature size could potentially play an instrumental role in enabling single-port robotic access in challenging fetal surgical procedures. However, in contrast to rigid endoscopes, flexible miniature endoscopes are constructed using compact hardware components to satisfy the physical constraints associated with miniaturization and flexibility. As a result, these devices suffer from sub-optimal illumination and sensitivity, leading to poor contrast in the obtained images. In addition, the images have an unusually bluish-cold color hue, in contrast to the reddish-warm tones clinicians are used to when using standard semi-flexible fiber or rigid rod lens endoscopes. These limitations prevent the utilization of flexible miniature endoscopes to their full potential in the current clinical workflow. Hardware-based enhancement strategies increase the hardware complexity and as such conflict with the physical constraints of flexible miniaturization [2]. On the other hand, a small number of software-based strategies are suitable for enhancing endoscopic images, owing to the special characteristics of the endoscopic environment and physics of the image acquisition process [2]. We present an image contrast and color enhancement method capable of partially compensating for sub-optimal illumination, while simultaneously shifting the color hue to a warmer range. We show results from a survey we have conducted to see how well our method preserves the appearance of surgically relevant anatomical information, such as blood vessels.

MATERIALS AND METHODS

Color and illumination model

Fully automated enhancement of an image's luminance (illumination) and chrominance (color) requires a model that can characterize these two properties independently. Despite perhaps being the most widely used model, the RGB color space is not suitable for this task, most prominently because it interleaves luminance with chrominance [3]. The CIE 1976 L*a*b* (CIELAB) color space models these two aspects separately [3]. It is also device-independent and perceptually linear [3]. Due to these interesting properties, we use CIELAB for enhancing flexible miniature endoscope images.

Comparison of rigid and flexible endoscope images

We have captured snapshots of selected surgical scenes using a rod lens and a flexible miniature endoscope (respectively: Hopkins® 26120 BHA 2.9 mm forward-oblique telescope 30° and Flex-XC, 2.8 mm, Karl Storz, Tutlingen, Germany). Inspecting these in the CIELAB color space, we observe that the luminance component (the `L` of `L*a*b*`) of both looks quite similar (see Fig. 1), although the histograms reveal that the rod lens endoscope images are in fact much brighter (see Fig. 2).

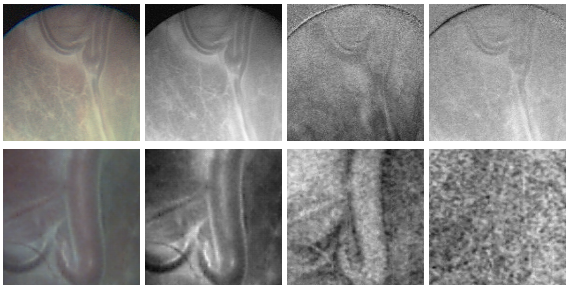

Fig. 1 Upper row, left to right: an RGB rod lens endoscope image showing vessels on the placenta, with its luminance (`L`), and chrominance (`a`, `b`) components in the CIELAB color space. **Lower row, left to right:** the same scene captured using a flexible miniature endoscope.

On the other hand, the chrominance channels (`a` and `b` of `L*a*b*`) seem to suggest that the rod lens scope's vividness comes from the yellow range contained in the `b` channel nicely blending in with the red range in the `a` channel. The clear distinctiveness of vessels in the rigid scope images is a result of the blue range in the `b` channel slightly balanced out with the indistinctive green-red intensities in the `a` channel (see Fig. 1). In contrast, the `a` channel of the flexible scope stands out with its "red" information content, albeit in a very limited range of values (see Fig. 2). The `b` channel shares the range limitations of `a`. In addition, it does not seem to contain much information (see Fig. 1).

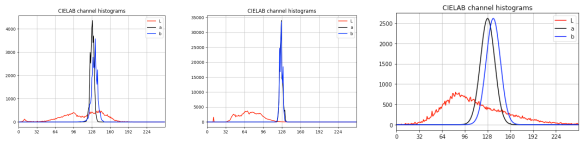

Fig. 2 Luminance (`L`) and chrominance (`a`, `b`) component histograms of the rod lens (left), original flexible (middle) endoscope images shown in Fig. 1, and the enhanced (right) version of the original flexible endoscope image.

Luminance and chrominance enhancement

We brighten images up by applying Contrast Limited Adaptive Histogram Equalization (CLAHE) [4] on the luminance component[1]. CLAHE shifts the peak of the luminance histogram from about the left quarter to the middle. This in turn expands the available value range of the `a` and `b` channels that fits into the sRGB gamut [5]. We use this observation to guide the chrominance adjustment: we specify target histograms for the `a` and `b` channels, based on a normal distribution that spans a range roughly twice the original range, and centered at the mean value of the respective channel in the rigid endoscope images. We impose these target histograms using [6]. Contrary to other histogram matching methods, this approach retains the order of the original pixel values, effectively preserving image features [6].

Implementation

We have implemented our method using Python and MATLAB[2]. A 256 x 256 image takes about a minute to process on a MacBook Pro (CPU: 2.5 GHz Intel Core i7, RAM: 16GB, OS: macOS Sierra).

RESULTS

Fig. 3 shows visual results of enhancing a darker capture of the surgical scene in Fig. 1 using our method.

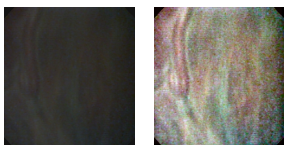

Fig. 3 Left: a flexible endoscope image with insufficient illumination. **Right:** the same image enhanced using our method.

We have conducted a survey asking nine participants to rank 19 such images enhanced using Automatic Color Equalization [7] (dubbed "FastACE"), histogram specification (as applied on the RGB image) [6] (dubbed "HistoSpec") and our method, according to how easily the arteries and veins on the background of the placenta can be distinguished. Both visual results and the positive outcome demonstrate that our method preserves the surgically relevant anatomical information (see Fig. 4); however a more thorough study is required to validate our method in the clinical context, as well as to assess its strengths and weaknesses with respect to the compared methods.

DISCUSSION

We have presented a method for image contrast and color enhancement that could play an instrumental role for harvesting the full potential of miniature flexible endoscopes in the clinical workflow. The main strength of this method is the independent handling of the luminance and chrominance components of an image.

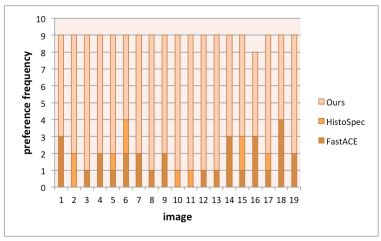

Fig. 4 The preference frequency of each method (y-axis) for each of the 19 enhanced surgical scenes (x-axis).

One limitation of our approach pertains to its general applicability. Different endoscope devices warrant fine-tuning for optimal application. Another direction for future research is the adaptive on-the-fly selection of the method parameters for full automation.

ACKNOWLEDGMENTS

This work was supported by Wellcome [WT101957; 203145Z/16/Z] and EPSRC [NS/A000027/1; NS/A000050/1]. Jan Deprest is funded by the GOSH Charity. Sebastien Ourselin receives funding from EPSRC [EP/H046410/1; EP/J020990/1; EP/K005278] and the MRC [MR/J01107X/1]. The histogram specification software used in this work was provided courtesy of Mila Nikolova.

REFERENCES

[1] Klaritsch P, Albert K, Van Mieghem T, Gucciardo L, Done E, Bynens B, Deprest J. Instrumental requirements for minimal invasive fetal surgery. BJOG: An International Journal of Obstetrics & Gynaecology. 2009 Jan 1;116(2):188-97.

[2] Sdiri B, Cheikh FA, Dragusha K, Beghdadi A. Comparative study of endoscopic image enhancement techniques. InColour and Visual Computing Symposium (CVCS), 2015 2015 Aug 25 (pp. 1-5). IEEE.

[3] Tkalcic M, Tasic JF. Colour spaces: perceptual, historical and applicational background. IEEE; 2003 Sep 22.

[4] Zuiderveld K. Contrast limited adaptive histogram equalization. Graphics gems. 1994:474-85.

[5] International Electrotechnical Commission. IEC 61966-2-1, 1999. Multimedia systems and equipment–Colour measurements and management–Part. 1999:2-1.

[6] Nikolova M, Steidl G. Fast hue and range preserving histogram specification: Theory and new algorithms for color image enhancement. IEEE transactions on image processing. 2014 Sep;23(9):4087-100.

[7] Getreuer P. Automatic color enhancement (ACE) and its fast implementation. Image Processing On Line. 2012 Nov 6;2:266-77.

[1] We use the CLAHE implementation provided by the scikit-image library (http://scikit-image.org/).

[2] We use the MATLAB API for Python.

Estimation of Tissue Oxygen Saturation from RGB Images based on Pixel-level Image Translation

Qing-Biao Li[1,3], Xiao-Yun Zhou[1], Jianyu Lin[1,3],Jian-Qing Zheng[1], Neil T. Clancy[2], Daniel S. Elson[1,3]

[1]*The Hamlyn Centre for Robotic Surgery, Imperial College London, London, UK,*

[2]*Centre for Medical Image Computing, University College London, London, UK*

[3]*Department of Surgery and Cancer, Imperial College London, London, UK*
q.li17@imperial.ac.uk

INTRODUCTION

Oxygenation and perfusion reflect tissue metabolic activity, which can be potentially used to monitor diseases including diagnosis or characterisation of cancer. A minimally-invasive endoscopy technique based on Hyperspectral Imaging (HSI) uses narrow spectral bands over a continuous spectral range to capture quantitative spectral information for live tissue diagnostics. StO2 can be estimated from HSI images using the Beer-Lambert law, if oxy- and deoxy-haemoglobin are considered to be the primary absorbers within the visible wavelength range, and using an approximation for scattering [1].

The Imperial College London, Structured Light and Hyperspectral Imaging system (ICL SLHSI) is an optical probe system combining sparse hyperspectral measurements and spectrally-encoded structured lighting, which can accurately estimate StO2 with high spatial resolution [2,3]. However, the requirement for an additional optical probe creates a barrier to widespread adoption. In contrast, colour (red, green, blue – RGB) cameras are widely used during minimally invasive surgery. Hence, it is worthwhile to develop methodologies for estimating the StO2 from RGB images captured by regular endoscope. Currently, HSI images were first recovered from RGB images via 'super-spectral resolution' and then used to estimate StO2 by linear regression (route 1 in Fig. 1)[3], [4].

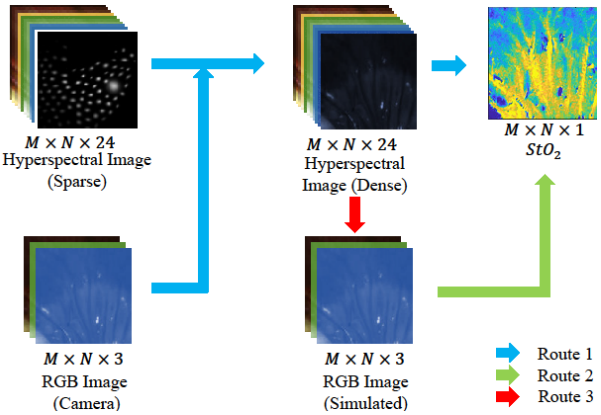

Fig. 1 Processing methods for StO2 estimation.

In this paper, conditional Generative Adversarial Networks (cGAN) [5] are introduced to achieve a pixel-level image to image translation, estimating the StO2 directly from RGB images without super-spectral resolution (route 2 in Fig. 1). The following sections will describe the network architecture, data collection, and validation setup. The test results on three types of *in vivo* data including rabbit uterus, lamb uterus, and porcine bowel are presented and discussed.

MATERIALS AND METHODS

Simulation of Dataset

Given an HSI image, an RGB image (input – 'x') can be accurately simulated based on the specific RGB camera responses to the corresponding wavelength range (route 3 in Fig. 1). The intensity ratio $\left(\frac{I_\lambda(x)}{I_{0,\lambda}(x)}\right)$ for each pixel (i,j) reflects the attenuation of the incident light spectrum ($I_{0,\lambda}(x)$) due to oxy- [HbO_2] and deoxy-haemoglobin [Hb] . Given the molar extinction coefficient of each haemoglobin $\varepsilon(\lambda)$ at specific wavelength λ, the concentration of both haemoglobins can be calculated based on a least squares method [2]:

$$I_\lambda(x) = I_{0,\lambda}(x)e^{-([\mathrm{HbO_2}]\varepsilon_{\mathrm{HbO_2}}(\lambda)+[\mathrm{Hb}]\varepsilon_{\mathrm{Hb}}(\lambda)+\alpha)}$$

Where, α is a constant value representing the attenuation caused by scattering and other components within tissue. Thus, the StO2 ground truth can be calculated (image – 'z').

Conditional Generative Adversarial Networks

In the training stage, the RGB images and the StO2 ground truth image are put into a generator whose structure is shown in Fig. 2, outputting an estimated StO2 (synthesized image – 'y'). Concat(x,y) and Concat(x,z) are separately put into a discriminator, outputting the probability of the input to be z. Here Concat() is concatenate, the probability map is a $30 \times 30 \times 1$ map which is useful for pixel-level rather than image-level translation [5]. The discriminator network architecture is shown in Fig. 3.

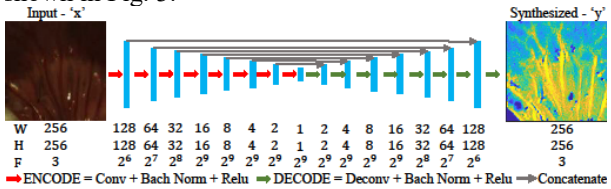

Fig. 2 Generator network architecture (G).

Adversarial learning is applied to update the generator and the discriminator models alternately with the loss function.

$$G^* = arg \min_G \max_D L_{cGAN}(G,D) + \lambda L_{L1}(G)$$
$$= arg \min_G \max_D (\log D(y) + \log(1 - D(G(x,z))) + \lambda \|y - G(x,z)\|_1$$

Here, D is the discriminator, G is the generator, λ is the L1 weight. The L1 loss $L_{L1}(G)$ is useful to translate the low-frequency information [5].

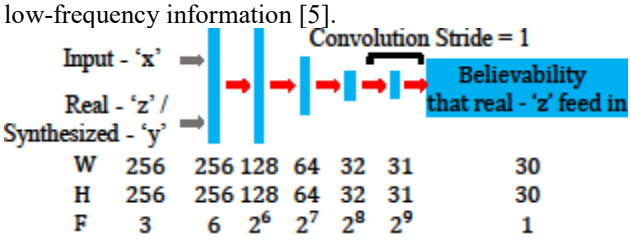

Fig. 3 Discriminator network architecture (D).

In the testing stage, the trained generator is used to estimate the StO2 from a new RGB image.

Validation Setup

HSI was previously carried out using an LCTF on three kinds of tissues *in vivo* (porcine bowel, lamb uterus and rabbit uterus 222 24-channel hypercubes with spatial sizes 192 × 256 [2]). Then, 167 images were used for training and 55 for testing. The dataset was augmented by slicing images using a 128×128 window with a stride of 16. These cropped images were interpolated to 256×256. The one-channel StO2 was copied to a three-channel image as channel difference between the Input and the Real image may introduce imbalance in the discriminator training. To demonstrate the influence of batch size and L1 weight, the testing was performed for separate cases (one image area cropped from each original image, called intercases) and within one case (the 45 image areas augmented from one original image, called intracases). An Nvidia Titan XP with 12G memory was used for the training. The maximum batch size for the training is 56 while that for the testing is 380. The loss curve usually converged after 10k iterations.

RESULTS

The trained model was tested in randomly selected tissue images among all its augmented data. In Table 1, the mean prediction error and structural similarity (SSIM) were summarized by different batch sizes with a fixed L1 weight of 100 (left column), and different L1 weights with a fixed batch size of 56 (right column). To clarify, the mean prediction error was calculated by the intensity difference between the ground truth StO2 image and synthesized StO2 image from cGAN in at each pixel by L1 norm, while SSIM was a perception-based method to measure the structural similarity. We can see that the increase in batch size and L1 weight reduces the mean error, which improve the pixel-level translation accuracy. Besides, these also contribute to the increase of the SSIM, which means the synthesized image is getting more structural similar with real image. The best model (bold in Table 1) was tested on all images in test set, achieving 14.75% in averaged mean error and 0.3207 in SSIM of all tissue images when their augmented data was recover back to origin size. These errors might be due to indiscernible tissue structures, spectral highlights, bias or noise.

Table 1. The StO2 prediction error and SSIM for different setup parameters.

L1 = 100			Batch Size = 56		
Batch Size	Mean Error	SSIM	L1 Weight	Mean Error	SSIM
1	0.161	0.235	50	0.088	0.381
16	0.119	0.299	100	0.089	0.376
32	0.095	0.354	200	0.082	0.411
56	0.089	0.376	400	**0.077**	**0.427**

Fig. 4 illustrates a comparison between the StO2 estimated from the synthesized image and the real image, while the intensity difference between them is also presented.

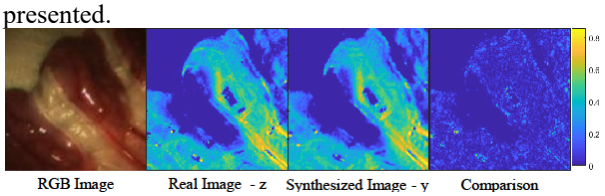

Fig. 4 Example StO2 images for porcine bowel.

DISCUSSION

In this paper, we realized the pixel-level image-to-image translation from RGB images to StO2, with an end-to-end Conditional GAN. The batch size and L1 weight were explored and set to compensate for the inter- and intra-case variations, achieving comparable StO2 predictions. In the future, we will work on the network architecture and the loss function to further improve the accuracy of the estimation as well as analysing the errors.

REFERENCES

[1] J.-L. Boulnois, 'Photophysical processes in recent medical laser developments: a review', *Lasers Med. Sci.*, vol. 1, no. 1, pp. 47–66, 1986.

[2] N. T. Clancy, S. Arya, D. Stoyanov, M. Singh, G. B. Hanna, and D. S. Elson, 'Intraoperative measurement of bowel oxygen saturation using a multispectral imaging laparoscope', *Biomed. Opt. Express*, vol. 6, no. 10, p. 4179, 2015.

[3] J. Lin, N. T. Clancy, Y. Hu, J. Qi, T. Tatla, D. Stoyanov, L. Maier-Hein, and D. S. Elson, 'Endoscopic Depth Measurement and Super-Spectral-Resolution Imaging', in *MICCAI*, 2017, pp. 39–47.

[4] G. Jones, N. T. Clancy, Y. Helo, S. Arridge, D. S. Elson, and D. Stoyanov, 'Bayesian Estimation of Intrinsic Tissue Oxygenation and Perfusion from RGB Images', *IEEE Trans. Med. Imaging*, vol. 36, no. 7, pp. 1491–1501, 2017.

[5] P. Isola, J.-Y. Zhu, T. Zhou, and A. A. Efros, 'Image-To-Image Translation With Conditional Adversarial Networks', in *CVPR*, 2017, pp. 1125–1134.

Role of Contextual Information in Skill Evaluation of Minimally Invasive Surgical Training Procedures

Anna French[1], Kristy Seidel[2], Thomas S. Lendvay[2,3],Timothy M. Kowalewski[1]

[1]Dept. of Mechanical Engineering, University of Minnesota, [2]C-SATS Inc,
[3]Dept. of Urology, University of Washington, Seattle Children's Hospital

INTRODUCTION

Compuational, objective methods for quantifying surgical skill have proved an important but challenging area of research. The overwhelming majority of prior work focuses on metrics derived from tool motion alone. What if progress in this field is stymied because contextual information plays an underappreciated role in the skill evaluation problem?

Methods that analyze tool position data and its derivatives may be missing important contextual information that is visible to human raters in video. The importance of context for motion detection and evaluation has been examined in other fields, with mixed findings. In [2] it was shown that human actions can be reliably discerned via point-light animation, and details of the actions being performed can be inferred--such as determining the weight of a box lifted by a figure in an animation. However, this same study showed that observers cannot categorize actions in these animations when the videos are turned upside down, even when told that the animations have been inverted. In [3] it was shown that skill in playing a musical instrument can be accurately determined by both experts and non-experts based solely on silent video footage of a person playing the instrument.

Since skill evaluation based solely on tool motion alone may ignore important context cues related to the task, the importance of these context cues in a surgical context should be assessed. For this investigation, context clues considered important include configuration of the grasped object, positions of the pegs in a peg transfer task, simulated tissue configuration for a suturing task, and other information about objects the tools interact with which can be gathered from footage of the procedure.

The objective of this investigation is to evaluate the importance of video context relative to tool motion alone in quantifying laparoscopic surgical skill. The overall hypothesis of this work is that removing context reduces the capacity of a human raters to distinguish skill level. Specicfically, we examine whether removing context decreases measured separation between top and bottom performers for all tasks and domains.

MATERIALS AND METHODS

This study used video footage and tool motion data gathered from the EDGE (Electronic Data Generation and Evaluation) study [1][4]. The EDGE dataset is made up of video recordings of laparoscopic training tasks including peg transfer (PegTx), pattern cutting, and suturing tasks. Each video has an accompanying set of tool motion data, a set of crowd ratings, and a Fundamentals of Laparoscopic Surgery (FLS) score. Each specific instance of a surgeon performing a training task is referred to as a trial. The crowd ratings are a set of votes gathered from non-experts rating the skill displayed in each video, gathered using the method described in [5]. Non-expert crowd workers (hereafter referred to as coders) were recruited by C-SATS. All data is de-identified, and all scoring is double-blind.

The FLS score was used to select which trials among the EDGE dataset would be submitted for crowd review. Due to an insufficient number of samples, the Cutting and Suturing tasks were grouped as tissue manipulation tasks. The quantities of trials were chosen based on a power assessment and are summarized in **Tab. 1**. The FLS scores were calculated using the method described in [7]. The minimum score observed was -.5900, the maximum score was 1.1037.

Table. 1 Number of videos from each task and skill group, along with the range of scores for each group

Task	Number of novice trials	Number of expert trials	Novice FLS Score Range	Expert FLS Score Range
Peg Transfer	*7*	*7*	*[-.1433, .4374]*	*[.9743, 1.0407]*
Suturing	*3*	*7*	*[0.1367, 0.4793]*	*[1.0226, 1.0494]*
Cutting	*5*	*0*	*[0.1533, 0.5138]*	--

Original Video (context +) ***Animation (context -)***

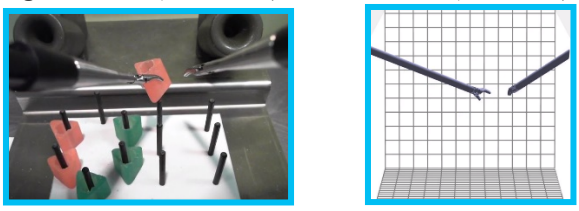

Fig. 1 Original video at left, showing tool motion in full context and no-context (animation) video at right showing tool motion alone, rendered using tool motion data synchronously collected with the original video.

To assess the importance of context, twin videos depicting the same procedure with and without context were presented for review. The recorded kinematic tool motion data for each video was used to generate no-context video animation for each trial. Models of the surgical tools were transformed for each corresponding video frame and compiled to form a matching 30fps context-free video. **Fig. 1** demonstrates one such

rendered frame, compared to a raw video frame.

The coders were shown videos from our source dataset and asked to rate the depicted surgeon on a 5-point Likert scale in four skill areas: depth perception, bimanual dexterity, efficiency and tissue handling [6]. In this preliminary analysis, the mean of the crowd ratings for each trial in each skill area is examined

Coders provided 50 ratings for each of the videos. Note that coders are not identical across all videos.

Box plots are used here to display these preliminary results. For each video n_i, the mean was taken over the m ratings from the coders for each skill area. Each box plot represents the distribution of these mean scores across all trials in that skill level, skill area and video type.

RESULTS

Fig. 2 and **Fig. 3** are the box plots of all scores delivered for a given task, domain and group. For example, the box plot for "High FLS, original" in Fig. 2 represents the mean score of each crowd rating for a given trial in the expert group when viewing original videos of the peg transfer task. Please note that the scores delivered by the crowd are Likert-scale scores, which is on a different rating scale than FLS.

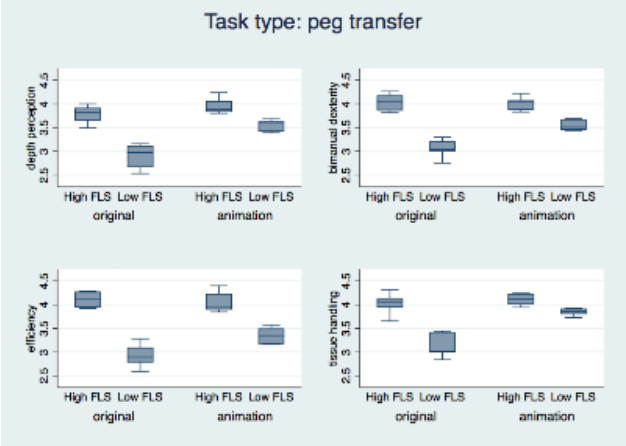

Fig. 2 Box plots of score distributions for the Peg Transfer task, n =7 for each box.

DISCUSSION

It is apparent from Fig. 2 and Fig. 3 that the ability to distinguish between novice and expert is substantially reduced in the video where contextual information is not present. Further, this is observable in each of the four skill areas, in both peg transfer and tissue manipulation, when comparing the difference in median of the novice and expert scores between animation and original videos. This supports our primary hypothesis.

These results introduce many interesting questions for future research. Further inquiry should be made into the impact that context has on the ratings delivered by expert raters, as this work only tests on non-experts. Though crowdsourced ratings are validated for their ability to predict expert ratings, removing context does not necessarily mean this validation still applies. Further investigation should also be done to determine the different aspects of context in video, and their value to the viewer. We conclude that the role of context should not be ignored in skill evaluation research.

ACKNOWLEDGEMENTS

C-SATS Inc. (Seattle, WA) provided in-kind support consisting of soliciting video scores and generating plots for this work.

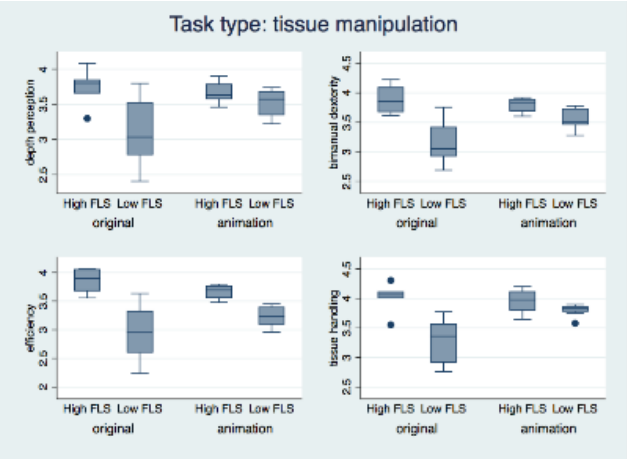

Fig. 3 Box plots of score distributions for Tissue Manipulation tasks (Cutting and Suturing), n=8 for novices, n=7 for experts for each box.

REFERENCES

[1] Kowalewski, T. M., Comstock, B., Sweet, R., Schaffhausen, C., Menhadji, A., Averch, T., ... & Knudsen, B. (2016). Crowd-sourced assessment of technical skills for validation of basic laparoscopic urologic skills tasks. The Journal of urology, 195(6), 1859-1865.

[2] Blake, R., & Shiffrar, M. (2007). Perception of human motion. Annual review of psychology, 58.

[3] Rodger, M. W., Craig, C. M., & O'Modhrain, S. (2012). Expertise is perceived from both sound and body movement in musical performance. Human movement science, 31(5), 1137-1150.

[4] Kowalewski, T. M., White, L. W., Lendvay, T. S., Jiang, I. S., Sweet, R., Wright, A., ... & Sinanan, M. N. (2014). Beyond task time: automated measurement augments fundamentals of laparoscopic skills methodology. journal of surgical research, 192(2), 329-338.

[5] Chen, C., White, L., Kowalewski, T., Aggarwal, R., Lintott, C., Comstock, B., ... & Lendvay, T. (2014). Crowd-sourced assessment of technical skills: a novel method to evaluate surgical performance. Journal of Surgical Research, 187(1), 65-71.

[6] Vassiliou, M. C., Feldman, L. S., Andrew, C. G., Bergman, S., Leffondré, K., Stanbridge, D., & Fried, G. M. (2005). A global assessment tool for evaluation of intraoperative laparoscopic skills. The American journal of surgery, 190(1), 107-113.

[7] Kowalewski, T. M. (2012). Real-time quantitative assessment of surgical skill. University of Washington.

Stress Resilience in Surgeons: A Neurophysiological Perspective

H.N. Modi, H. Singh, G.Z. Yang, A. Darzi, D.R. Leff

Hamlyn Centre for Robotic Surgery, Imperial College London, United Kingdom

Hemel.modi12@imperial.ac.uk

INTRODUCTION

Stressors in the operating theatre can increase surgeons' mental demands. Whilst some surgeons cope well under these conditions, for others the demands of the operating environment precipitates technical performance decline and threatens patient safety[1]. Although innovations in surgery, such as robotics, promise task automation[2] and may mitigate the deleterious effects of stress on technical performance, the risk to patient safety of operating under stressful conditions remains real. The reasons for disparity in stress resilience may relate to differences in activation of the prefrontal cortex (PFC), an area of the brain known to be important for attention and concentration[3], and one in which activation varies as a function of cognitive load[4].

The aim of this study is to compare the PFC activation response between surgeons exhibiting relative performance stability and those demonstrating significant performance decline when operating under temporal stress. The hypothesis is that performance stability under temporal demand is associated with sustained prefrontal "activation", whereas performance decline is accompanied by inverted responses, known as "deactivation"[5].

METHODS

33 higher surgical residents [median age (range) = 33 years (29–56), 27 males] performed a laparoscopic suturing task under *'self-paced'* (no time restriction) and *'time pressure'* (two-minute per knot time restriction) conditions.

A composite deterioration score was calculated based on between-condition differences in task performance metrics [(task progression score (au), error score (mm), leak volume (ml) and knot tensile strength (N)]. Based on the composite score, quartiles were computed reflecting performance stability (Q1, n=8) and decline (Q4, n=8). Changes in PFC oxygenated haemoglobin concentration (HbO_2) measured at 24 different locations using functional near-infrared spectroscopy were compared between Q1 and Q4 groups. Subjective workload was quantified using the Surgical Task Load Index (SURG-TLX), and a wireless heart rate monitor captured real-time changes in heart rate.

RESULTS

Q1 trainees demonstrated task-induced increases in HbO_2 across the bilateral ventrolateral PFC (VLPFC) and right dorsolateral PFC (DLPFC) in the SP condition, and across the bilateral VLPFC under TP (Figures 1 & 2). In contrast, Q4 residents demonstrated decreases in HbO_2 in both conditions (Figures 1 & 2). The amplitude of PFC activation (ΔHbO_2) was significantly greater in Q1 than Q4 across the bilateral VLPFC during both SP and TP conditions [*SP condition:* left VLPFC: Q1=0.44 ± 1.30μM vs. Q4=-0.21 ± 2.05μM, $p<0.001$; right VLPFC: Q1=0.46 ± 1.12μM vs. Q4=-0.15 ± 2.14μM, $p<0.001$; *TP condition:* left VLPFC: Q1=0.44 ± 1.36μM vs. Q4=0.03 ± 1.83μM, $p=0.001$; right VLPFC: Q1=0.49 ± 1.70μM vs. Q4=-0.32 ± 2.00μM, $p<0.001$]. There was no significant between-group difference in SURG-TLX (SP: $p=0.934$; TP: $p=0.500$) or heart rate (SP: $p=0.152$; TP: $p=0.694$) in either condition. Although no significant between-condition differences in ΔHR were observed in either group, subjective workload was significantly greater under TP compared to SP for both Q1 (mean SURG-TLX score ± SD: SP=144.25 ± 51.22 vs. TP=176.00 ± 59.32, $p=0.012$) and Q4 residents (SP=142.25 ± 43.51 vs. TP=194.63 ± 47.58, $p=0.010$).

Interestingly, there was no significant association between level of training or expertise and the degree of performance deterioration under time pressure ($p=0.168$)

DISCUSSION

Resilience to intraoperative stress is associated with sustained prefrontal activation indicative of preserved attention and concentration. In contrast, sensitivity to stress is manifest as prefrontal deactivation suggesting task disengagement[6]. Prefrontal deactivations have been observed in other experiments involving time-pressure and negative feedback[7], and during stressful working memory tasks[8], monetary incentive delay tasks[9], and video gaming[10]. Brain imaging assessments may help to ensure surgeons can cope with intraoperative demands prior to independent practice. However, future developments in medical robotics may increase automaticity of the surgical task[2] and help mitigate the effects of intraoperative stress on technical performance.

REFERENCES

1. Arora S, Sevdalis N, Nestel D, et al. The impact of stress on surgical performance: a systematic review of the literature. *Surgery* 2010; 147(3):318-330, 330 e1-6.

2. Yang G-Z, Cambias J, Cleary K, et al. Medical robotics—Regulatory, ethical, and legal considerations for increasing levels of autonomy. *Science Robotics* 2017; 2(4).
3. Miller EK, Cohen JD. An integrative theory of prefrontal cortex function. *Annu Rev Neurosci* 2001; 24:167-202.
4. Modi HN, Singh H, Orihuela-Espina F, et al. Temporal Stress in the Operating Room: Brain Engagement Promotes "Coping" and Disengagement Prompts "Choking". *Ann Surg* 2017.
5. Dolcos F, McCarthy G. Brain systems mediating cognitive interference by emotional distraction. *J Neurosci* 2006; 26(7):2072-9.
6. Lee TG, Grafton ST. Out of control: diminished prefrontal activity coincides with impaired motor performance due to choking under pressure. *Neuroimage* 2015; 105:145-155.
7. Al-Shargie F, Tang TB, Kiguchi M. Assessment of mental stress effects on prefrontal cortical activities using canonical correlation analysis: an fNIRS-EEG study. *Biomedical Optics Express* 2017; 8(5):2583-2598.
8. Qin S, Hermans EJ, van Marle HJF, et al. Acute Psychological Stress Reduces Working Memory-Related Activity in the Dorsolateral Prefrontal Cortex. *Biological Psychiatry* 2009; 66(1):25-32.
9. Ossewaarde L, Qin S, Van Marle HJ, et al. Stress-induced reduction in reward-related prefrontal cortex function. *Neuroimage* 2011; 55(1):345-52.
10. Matsuda G, Hiraki K. Sustained decrease in oxygenated hemoglobin during video games in the dorsal prefrontal cortex: A NIRS study of children. *NeuroImage* 2006; 29(3):706-711.

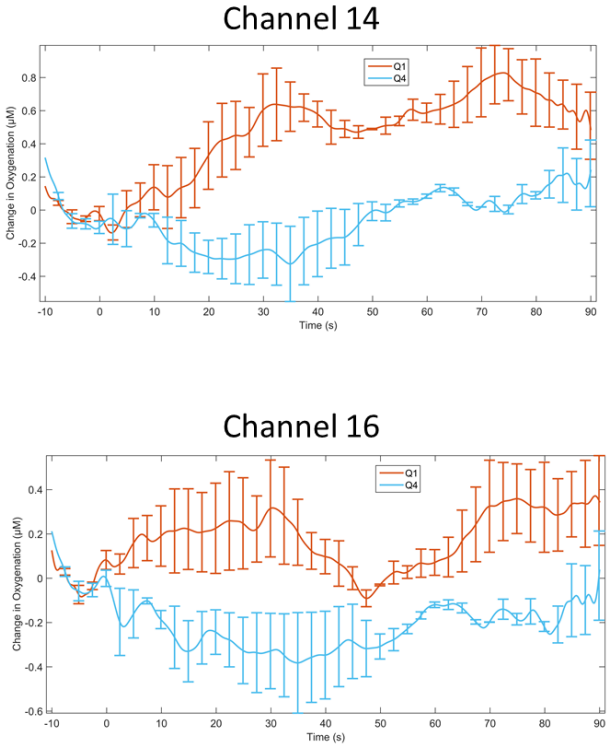

Figure 1. Group-average time courses demonstrating the typical *'activation'* response (HbO_2 increase) in Q1 residents (orange), and the *'deactivation'* response (HbO_2 decrease) observed in Q4 residents (blue) when laparoscopically suturing under time pressure, particularly in channels located in the ventrolateral prefrontal cortex (e.g. channels 14 and 16).

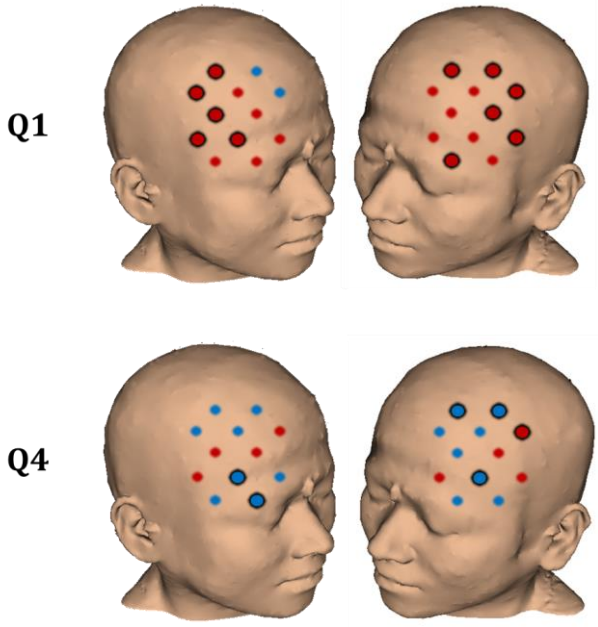

Figure 2. Prefrontal activation in each group during the time pressure condition. Channels in which there was an increase in in HbO_2 concentration are shown as red circles, and those in which there was a decrease in HbO_2 concentration are depicted as blue circles. Channels in which there was a statistically significant ($p<0.05$, paired samples t-test) change in HbO_2 concentration are highlighted (black circles). Typical activation responses are observed in the Q1 group in the ventrolateral prefrontal cortex in the time pressure condition, whereas deactivation responses are seen in the Q4 group.

Toward Real-time BCI Control of Assistive Robots: A Comparison of State-of-the-Art Methods

Daniel Freer[1], Yu Ma[1, 2], Guang-Zhong Yang[1]

[1]The Hamlyn Centre, Imperial College London

[2]Fudan University

df1215@ic.ac.uk

INTRODUCTION

After stroke, spinal cord injury, or other neurological conditions, survivors are often left requiring extensive physical assistance during daily tasks. A compelling solution to this problem is the use of an assistive robot, though many technical challenges persist with regard to adequately sensing the intent of the user. One of the most cutting-edge intention-sensing methods is a Brain Computer Interface (BCI), and the most commonly used BCI is electroencephalography (EEG) because of its noninvasiveness and temporal resolution. For robotic control using a BCI, motor imagery (MI), a name for imagining motor movements to evoke a particular response in the brain, has been a useful strategy. This is because the signal comes directly from the user without any controlled stimulus, and is somewhat intuitive for new users as similar brain regions and functions are activated for motor imagery and motor movement [1].

Typical methods of classifying motor imagery tasks have been the detection of event-related synchronization and desynchronization of brain waves in each hemisphere of the brain. While this method has led to some success in real-time application of EEG control, the total classification accuracy remains somewhat low even for 2 classes, and achieving adequate performance usually requires long training sessions with each user [2]. In recent years, new methods have been developed to improve classification of motor imagery, such as filter bank common spatial patterns (FBCSP) [3, 4] and the use of Riemannian geometry to distinguish features in the signal [5, 6]. These methods have increased the accuracy of MI tasks and allowed classifiers to distinguish more classes, but use entire (>2 s) trials of motor imagery. This would result in a long delay before the control sequence is engaged. As many of these methods are concerned with brain mapping rather than direct control, shorter windows of time were not considered. In addition, with the rapidly increasing popularity of deep learning, several groups have begun to investigate deep learning for BCI tasks using EEG [7]. While these deep learning models have not yet shown any major improvement on state of the art methods, they open up new and interesting ways of manipulating and understanding EEG data.

This paper attempts to compare and characterize several state-of-the-art methods of motor imagery classification based on their robustness to real-time application. The methods to be compared are direct event related potential calculation, the use of Riemannian space and covariant matrices, and a recently proposed deep learning framework that is comparable to FBCSP. These methods will be tested on BCI Competition IV Dataset 2a [8].

METHODS

Data - The BCI Competition IV Dataset 2a is a commonly used dataset because of the large number of trials for each participant and the overall quality of the data. Each subject performed motor imagery of the left hand, right hand, both hands, and of the tongue when prompted by a computer screen. There are 72 examples of each class included in the dataset, which were defined in this study to be between 0.5 seconds and 2.5 seconds after the prompt. This window was chosen to highlight a characteristic time of motor imagery while avoiding unwanted detection of visually evoked potentials from the stimulus. The data from all 22 channels was first passed through a bandpass filter (7-30 Hz). The data was divided into non-overlapping windows of time (with lengths from 2 seconds to 0.25 seconds), and each window was individually classified as one of the four motor imagery movements. In this study, two thirds of the data were used for training each method, while the remaining third was used for testing.

Event-Related Potential - For this method, only 5 channels were considered as relevant. Other methods were attempted, including using spatial filters and using all 22 channels, but were not as successful. For each of the 5 channels, a reference value was calculated during the first 4 seconds of the trial, which was subtracted during each of the events. The outcome was then put through a linear discriminant analysis (LDA) classifier, and the training and testing accuracy were recorded.

Riemannian Method - Following the example of [5], spatial covariance matrices were first calculated within each defined window of time, then the signal was considered in tangent space using Geodesic Filtering with Fisher discriminant analysis (FGDA). After this, classification was carried out by calculating the minimum distance to the Riemannian mean (MDM) of each class in the training data.

Convolutional Neural Network - The shallow convolutional neural network (CNN) from [7] that is based on FBCSP [3] was used as the basis for this method. The first layer is 1-dimensional temporal convolutions on each channel of the data, which is analogous to frequency selection and other temporal filters. After this, 2-dimensional convolutions on the

electrodes act as a spatial filter, similar to the CSP algorithm. Lastly, mean pooling and linear classification through a dense layer perform feature selection and act similarly to LDA, which are often the final two steps of FBCSP. Because many of the default parameters for this network were not compatible with shorter windows of time, the length and stride of the final pooling layer were changed to 20 and 5, respectively, while the length of the final convolutional kernel was reduced to 4. These parameters were applied for all window sizes.

RESULTS

Each of the implemented state-of-the-art methods achieved results that were comparable to those of their initial papers when considering entire trials as opposed to shorter windows of time, as shown in Table 1. The average accuracies were 62.0 and 66.7 percent for the Riemannian and convolutional methods, respectively, while using ERP achieved an accuracy of 40.7 percent. As has been reported in previous papers [4, 5], the data collected from subjects 1, 3, 7, 8, and 9 was much more discriminative than the remainder. For these subjects, the Riemannian method achieved an accuracy of 77.6 percent, while the convolutional method had an average of 81.2 percent classification accuracy.

Subject	ERP	Riemannian	CNN
1	0.4948	0.6979	**0.8333**
2	0.3402	**0.4410**	0.4375
3	0.4845	**0.8090**	0.8021
4	0.3196	0.4826	**0.5521**
5	0.2784	0.3194	**0.5104**
6	0.2990	**0.4583**	0.4375
7	0.5464	0.7222	**0.8542**
8	0.3918	**0.8264**	0.7500
9	0.5052	**0.8264**	0.8229
Average	0.4067	0.6203	**0.6667**

Table 1 The recorded accuracies for each of the methods on individual subjects in the dataset using data from a 2s window

All of the methods assessed showed lower classification accuracy when the window size was decreased. The CNN decreased the most, showing the best accuracy with a large window size, but was worse than the Riemannian method with a window size of 0.5 seconds or smaller. These results can be seen in Figure 1. Full training times were about 0.001, 200, and 20 seconds, while testing times were approximately 74.6 ns, 3.65 ms, and 5.97 ms for a single input for the ERP, Riemannian, and CNN methods, respectively.

DISCUSSION

The results of this study suggest a few things. Firstly, while the simplest method (ERP) is known to work adequately in a real-time environment with trained individuals, its performance on prerecorded datasets of untrained individuals is far inferior to other state-of-the-art methods. This is promising in the sense that the performance of each of the presented methods may also be improved by training with individuals who will use the system. Another takeaway from the results is that

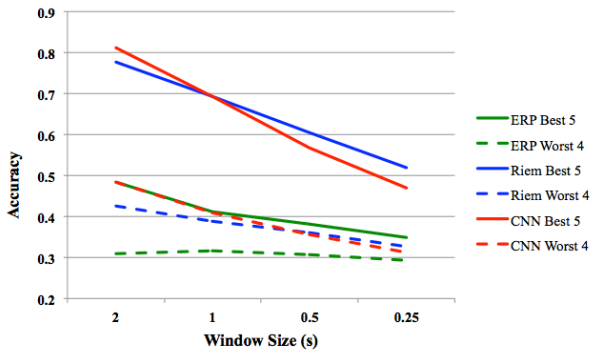

Fig. 1 The average performance of each method, considering window size and the subjects' performance

methods that are more empirical appear to be more robust to smaller window sizes when compared to "black box" methods like deep learning. This is intuitive, because deep learning relies on a large amount of features for training and classification. Of course, there may still be other configurations of neural networks that could be more effective in real time than any of the presented methods, but these have not yet been published. While none of the methods were entirely robust to a reduction of window size, the classification accuracy of the best 5 subjects with the smallest window size is still approximately the same as the performance of the worst 4 subjects with the largest.

In summary, existing state-of-the-art methods of motor imagery classification were compared with respect to a shrinking window size to assess their applicability to real-time application. Future steps include testing each of these methods in a robotic control scenario while streaming data in real time.

REFERENCES

[1] Pfurtscheller G, Neuper C. Motor imagery and direct brain-computer communication, Proceedings of the IEEE. 2001. 89(7):1123-1134

[2] Meng J, Zhang S, Bekyo A, Olsoe J, Baxter B, He B. Noninvasive Electroencephalogram Based Control of a Robotic Arm for Reach and Grasp Tasks, Scientific Reports. 2016;6(1):1-14

[3] Ang KK, Zhang YC, Zhang H, Guan C. Filter Bank Common Spatial Pattern (FBCSP) in Brain-Computer Interface. IEEE International Joint Converence on Neural Networks. July 2008;2390-97.

[4] Ang KK, Chin ZY, Wang C, Guan C, Zhang H. Filter bank common spatial pattern algorithm on BCI competition IV datasets 2a and 2b, Frontiers in Neuroscience. 2012. 6(1):1-9

[5] Barachant A, Bonnet S, Congedo M, Jutten C. Multiclass Brain-Computer Interface Classification by Riemannian Geometry, IEEE Transactions on Biomedical Engineering. 2012. 59(4): 920-928

[6] Yger F, Berar M, Lotte F. Riemannian Approaches in Brain-Computer Interfaces: A Review, IEEE Transactions on Neural Systems and Rehabilitation Engineering. Oct 2017. 25(10):1753-62

[7] Schirrmeister RT, et. al. Deep learning with convolutional neural networks for EEG decoding and visualization, Human Brain Mapping. November 2017. 38(11):5391-5420

[8] Tangermann M, et. al. Review of the BCI competition IV, Frontiers in Neuroscience. 2012. 6(55):1-31

Comparison of Bio-Inks for Free-Hand 3D Bioprinting Directly Onto Moving Human Anatomy

Reed A. Johnson[1], John J. O'Neill[1], Rodney L. Dockter[1], Carl J. Modl[1], Daniel Sorby[2], Angela Panoskaltsis-Mortari Ph.D[2], Timothy M. Kowalewski Ph.D[1]

[1]*Department of Mechanical Engineering, University of Minnesota*
[2]*Department of Pediatrics, University of Minnesota*
joh11170@umn.edu

INTRODUCTION

Advances in bioprinting have enabled synthetic tissue, organ, and skin construction via additive manufacturing techniques [1]. The most common bioprinting approach involves depositing hydrogel solutions embedded with bio-inks via pressure driven syringes [2] or via inkjetting [3]. Inkjet approaches are a viable alternative since they do not damage the cell yet permit high-speed control. Prior art has demonstrated the benefits of bioprinting for tissue engineering [4]. However, prior art has emphasized open loop deposition on planar, stationary surfaces. This is sufficient for laboratory settings where culture dishes are utilized or subjects can be sedated and the anatomy fixed. As envisioned in [5], some clinical settings may benefit from depositing bio-inks onto moving anatomy such as an unfixtured hand of a burn patient that must move during therapy to maintain range of motion for skin grafts. Alternatively, a hand-held precision bioprinting tool (Fig. 1 Top) may move relative to patient anatomy or be scaled down for use in laparoscopic surgery (Fig. 1 Middle) and contend with unpredictable anatomical motion.

The gap in prior art has been the demonstration of an additive manufacturing technique capable of depositing and adhering viable biomaterials directly onto unconstrained, non-planar, moving anatomy. The objective of this paper is to demonstrate the feasibility of robotically depositing and adhering bioprinting-compatible materials. We evaluated two bio-inks for their accuracy and adhesion during bioprinting directly onto moving human anatomy.

MATERIALS AND METHODS

As in [5], the Leap Motion (Leap Inc, Mountain View CA) was used to track the human hand at 120Hz and a Nordson EFD PICO Pµlse piezo jetting system was used to propel the fluid onto the hand when it was in the correct position. Here, the system ran on a Linux PC using the Robot Operating System (ROS), with a graphical display of the current position of the hand relative to the remaining pixels in the pattern, a suggested target highlighted (Fig. 2), and a height bar showing the acceptable distance from the hand to the jet (~1cm). The system allowed either the user to move their hand relative to the system, or an operator to move the system relative to the user's hand.

Two hydrogels were used. These hydrogels are biocompatible and are used as scaffolds for bioprinting [6]. The first consisted of Sodium Alginate that was deposited onto the hand, followed by an aqueous Calcium Chloride solution airbrushed onto the hand to crosslink the Alginate (as in [5]).

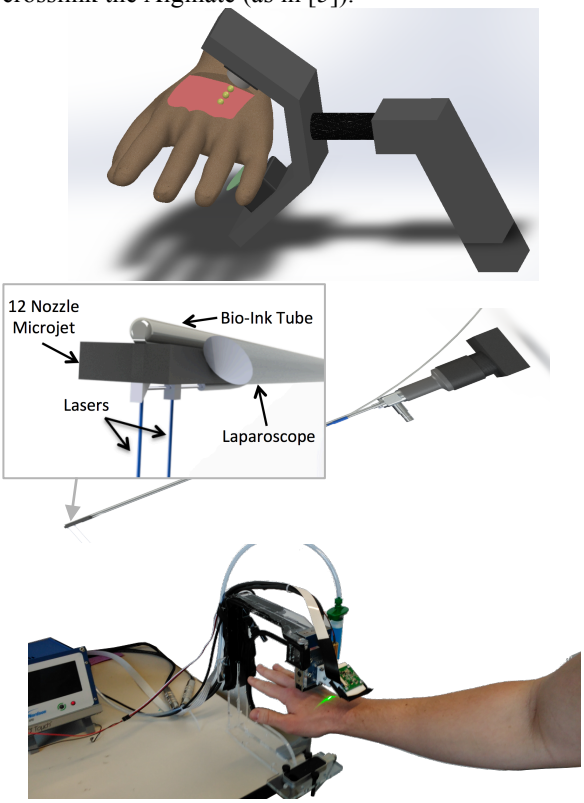

Fig. 1 Conceptual design of additive manufacturing directly onto moving human anatomy (Top). Conceptual printing device for laparoscopic surgery (Middle). Experimental setup, showing user's hand below the PICO Pµlse and above the Leap Motion (Bottom).

A second hydrogel was synthesized with deionized water containing 10% GelMA (gelatin methacrylate) and 0.5% LAP (lithium phenyl-2,4,6-trimethylbenzoyl-phosphinate) as a photoinitiator to allow use of a 405nm flashlight to crosslink between layers. This natural bio-ink is also proven to be compatible with a variety of cell types [7].

Blue food dye was used to color the hydrogels to allow for a computer vision-based evaluation of the 2D accuracy from scans of the finished gels on a flatbed scanner at 600 DPI (Fig. 4). The scans were then compared to the target template (Fig. 3) to determine

True Positive (TP), False Negative (FN) and False Positive (FP) areas. These values were then used to determine True Positive Rate (TPR), False Negative Rate (FNR) and False Discovery Rate (FDR) to provide metrics that were independent of the template image.

Fig. 2 The target template (Left) and an in-progress user view (Right). 1 pixel = 1mm width.

RESULTS

The robotic system was able to detect and track the subject's hands with sufficient speed. The user was able to ink at 1.8 pixels per second, leading to an average layer time of 182 seconds.

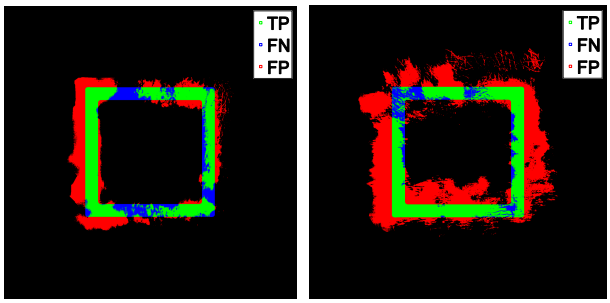

Fig. 3 True Positive (TP), False Negative (FN) and False Positive (FP) areas for the Calcium Alginate Hydrogel (Left) and the GelMA Hydrogel (Right)

The Calcium Alginate provided moderate layer to layer adhesion and poor adhesion to the skin of the hand, being easily peeled away by even stretching the underlying skin. The GelMA hydrogel provided good layer to layer adhesion, as well as good adhesion to the underlying skin. Table 1 shows True Positive Rate (TPR) and False Discovery Rate (FDR) for both gels.

	Bio Com-patibility	Cross Link	Adhesion	TPR	FDR
Alginate	Good	Slow	Poor	75%	46%
GelMA	Good	Fast	Good	82%	65%

Tab. 1 Comparison of Calcium Alginate to GelMA Hydrogel

DISCUSSION

Both proposed hydrogels show promise as bio-inks for additive manufacturing on moving anatomy, however both need further development. The Calcium Alginate's requirement of the aqueous Calcium Chloride caused the gel to run, and the crosslinking was incomplete leading to poor layer adhesion. The GelMA hydrogel became too warm in the PICO Pµlse thus becoming too liquid, causing the gel to run and not hold shape, leading to a large False Positive area. If this were adequately addressed (eg by controlling viscosity via temperature or an additive like glycerol) GelMA would prove superior to Alginate for this application.

Fig. 4 Raw scan of hydrogel on hand.

ACKNOWLEDGEMENTS

Research was sponsored by the Army Research Laboratory and was accomplished under Cooperative Agreement Number W911NF-14-2-0035. The views and conclusions contained in this document are those of the authors and should not be interpreted as representing the official policies, either expressed or implied, of the Army Research Laboratory or the U.S. Government. The U.S. Government is authorized to reproduce and distribute reprints for Government purposes notwithstanding any copyright notation herein.

REFERENCES

[1] Murphy, Sean V., and Anthony Atala. "3D bioprinting of tissues and organs." Nature biotechnology 32, no. 8 (2014): 773-785.

[2] Lee, Vivian, Gurtej Singh, John P. Trasatti, Chris Bjornsson, Xiawei Xu, Thanh Nga Tran, Seung-Schik Yoo, Guohao Dai, and Pankaj Karande. "Design and fabrication of human skin by three-dimensional bioprinting." Tissue Engineering Part C: Methods 20, no. 6 (2013): 473-484.

[3] Nakamura, Makoto, Akiko Kobayashi, Fumio Takagi, Akihiko Watanabe, Yuko Hiruma, Katsuhiro Ohuchi, Yasuhiko Iwasaki, Mikio Horie, Ikuo Morita, and Setsuo Takatani. "Biocompatible inkjet printing technique for designed seeding of individual living cells." Tissue engineering 11, no. 11-12 (2005): 1658-1666.

[4] Skardal, Aleksander, David Mack, Edi Kapetanovic, Anthony Atala, John D. Jackson, James Yoo, and Shay Soker. "Bioprinted Amniotic Fluid□Derived Stem Cells Accelerate Healing of Large Skin Wounds." Stem cells translational medicine 1, no. 11 (2012): 792-802.

[5] J. J. O'Neill, R. A. Johnson, R. L. Dockter and T. M. Kowalewski, "3D bioprinting directly onto moving human anatomy," 2017 IEEE/RSJ International Conference on Intelligent Robots and Systems (IROS), Vancouver, BC, 2017, pp. 934-940. https://www.youtube.com/watch?v=6VrozlyELdw&t=3s

[6] K. Y. Lee and D. J. Mooney, "Alginate: properties and biomedical applications," *Progress in polymer science*, vol. 37, no. 1, pp. 106– 126, 2012.

[7] Yue, Kan, Grissel Trujillo-de Santiago, Mario Moisés Alvarez, Ali Tamayol, Nasim Annabi, and Ali Khademhosseini. "Synthesis, properties, and biomedical applications of gelatin methacryloyl (GelMA) hydrogels." Biomaterials 73 (2015): 254-271.

Patient Satisfaction and PROMs in Computer Navigated vs. Non-navigated Total Knee Replacements(TKR)

K. Deep[1], K.K. Dash[1], S. Shankar[2], A. Ewen[1]

[1]Golden Jubilee National Hospital, Clydebank, Glasgow, UK

[2]Queen's Hospital, Romford, UK

Correspondence with author - mrkdeep@googlemail.com

ABSTRACT

Background: Literature and registry-data show up to 20% dissatisfaction rate for total knee replacements(TKR)[1,2]. This is used as a rationale by manufacturers for designing and introducing new implant options. However, not all new designs have necessarily been better. We believed that surgical technique is at least equally important, and we wanted to know if computer navigation assisted total knee replacements achieve better outcome. We decided to analyse patient satisfaction and PROMs (Oxford Knee Score(OKS)) in our high-volume arthroplasty unit and also compare between navigated and non-navigated techniques.

Methods: In this comparative retrospective analysis of prospectively collected data, all data were collected independently by Arthroplasty Nurses. Same protocols are followed in the hospital for all patients. Following power calculation, we included 229 patients in each group (238 (9 bilateral) knees in navigated, 229 in non-navigated). Three types of implants were used in both groups. Two different types of navigation systems were used in Navigated cases. Both the navigation systems (Orthopilot and Stryker) were image-free (CT - Free), and used passive optical trackers. Same protocols were followed for all before and after surgery. Both groups were similar pre-operatively -(Navigated: 68years (SD9), BMI32.28 (SD5.19), OKS:41.55 (SD7.45); Non-navigated: 70years (SD9), BMI:32.41 (SD5.12), OKS:42.6 (SD7.25)). Oxford Knee Score was scored in the original method (12 best score, 60 worst score). Satisfaction was enquired via a four point Likert scale - very satisfied, satisfied, unsure or dissatisfied.

Results: For satisfaction, this study had almost 100% response rate, with data available for all patients except one. This is very high when compared to existing published literature. In 238 navigated knees, 227(95.4%) were very satisfied or satisfied, 7(2.9%) unsure and 3(1.2%) dissatisfied (Fig. 1). In 229 non-navigated knees, 205(89.5%) were very satisfied or satisfied, 15(6.5%) unsure and 9(3.9%) dissatisfied (Fig. 2). The navigated group showed better satisfaction (p=0.009, Chi-Square Test) compared to the non-navigated. Even in the non-navigated group, our satisfaction data is similar to high end of the published data. There was no statistically significant difference in 6-week-OKS between navigated and non-navigated groups (Navigated: 28.48(sd7.8) ; conventional: 29.51(sd8.1); p=0.44, Analysis of Covariance). However, data for OKS was available for only 67% of patients – hence it may not reflect the true picture. There was no difference in 6-week-OKS between implant subtypes (p=0.25).

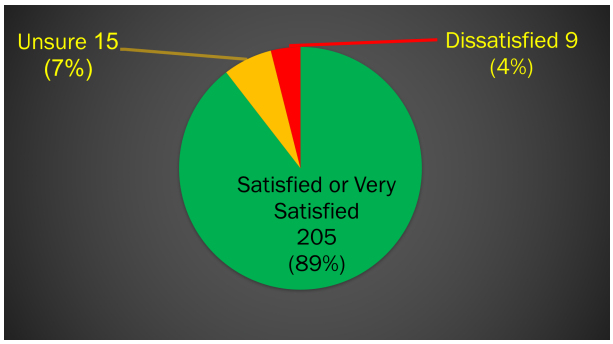

Fig. 1 Patient satisfaction after Total Knee Replacement in non-navigated surgical technique group.

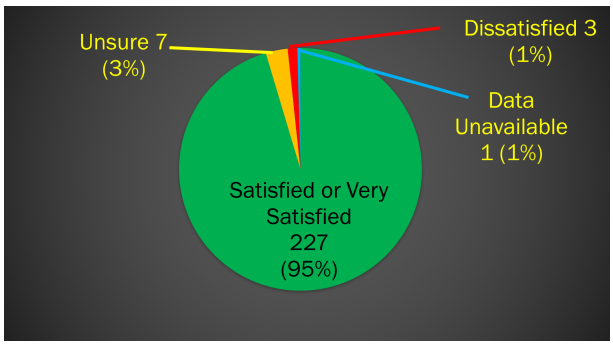

Fig. 2 Patient satisfaction after Total Knee Replacement in computer assisted navigated surgical technique group.

Conclusion: A modern elective arthroplasty service can deliver high satisfaction rates in TKR. Use of computer navigation further improves patient satisfaction from the best conventional satisfaction rates.

REFERENCES

[1] Robertsson O, Dunbar M, Pehrsson T, Knutson K, Lidgren L. Patient satisfaction after knee arthroplasty: a report on 27,372 knees operated on between 1981 and 1995 in Sweden. Acta Orthop Scand 2000;71:262-7.

[2] Baker PN, van der Meulen JH, Lewsey J, et al. The role of pain and function in determining patient satisfaction after total knee replacement. J Bone Joint Surg Br 2007;89:893–900.

The learning curve associated with robotic-arm assisted unicompartmental knee arthroplasty

B Kayani, S Konan, J Tahmassebi, FS Haddad

University College London Hospital, 235 Euston Road London, NW12BU
babar.kayani@gmail.com

ABSTRACT

Background:
The most common reason for implant failure and revision surgery in unicompartmental knee arthroplasty (UKA) is surgical error in implant positioning. Robotic-arm assisted UKA helps to improve the accuracy of implant positioning[1,2] but the learning curve for the implementation of this technology into surgical practice remains unknown.

The primary objective of this study was to determine the surgical team's learning curve for introducing robotic-arm assisted UKA into routine surgical practice. The secondary objective was to compare accuracy of implant positioning and limb alignment in conventional jig-based UKA versus robotic-arm assisted UKA.

Methods:
This prospective single-surgeon cohort study included 60 consecutive conventional jig-based UKAs compared with 60 consecutive robotic-arm assisted UKAs for medial compartment knee osteoarthritis. Surrogate measures of the learning curve were prospectively collected. These included operative times, the state-trait anxiety inventory (STAI) questionnaire to assess preoperative stress levels amongst the surgical team, accuracy of implant positioning, limb alignment, and postoperative complications.

Results:
Robotic-arm assisted UKA was associated with a learning curve of six cases for operating time ($p<0.001$) and surgical team comfort levels ($p<0.001$). Cumulative robotic experience did not affect accuracy of implant positioning ($p=0.52$), limb alignment ($p=0.65$), posterior condylar offset ratio ($p=0.71$), posterior tibial slope ($p=0.68$), and native joint line preservation ($p=0.55$) (Figures 1-2). Robotic-arm assisted UKA improved accuracy of implant positioning ($p<0.001$) and limb alignment ($p<0.001$) with no additional risk of postoperative complications compared to conventional jig-based UKA.

Conclusion:
Robotic-arm assisted UKA was associated with a learning curve of six cases for operating time and surgical team comfort levels but no learning curve for accuracy of implant positioning or limb alignment.

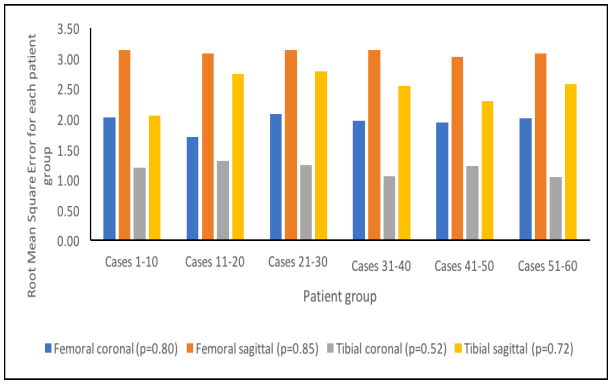

Fig. 1: Bar chart showing changes in root mean square error for accuracy in femoral and tibial implant positioning (degrees) with each patient group undergoing robotic-arm assisted UKA

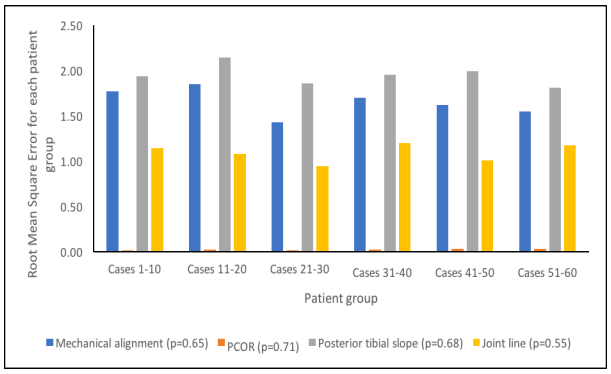

Fig. 2: Bar chart showing changes in root mean square error for accuracy in achieving planned mechanical alignment (degree), posterior condylar offset ratio (PCOR), posterior tibial slope (degrees), and joint line (mm) with each patient group undergoing robotic-arm assisted UKA

REFERENCES

1. Bell SW, Anthony I, Jones B, et al. Improved accuracy of component positioning with robotic-assisted Unicompartmental knee Arthroplasty: data from a prospective, randomized controlled study. J Bone Joint Surg Am 2016 98(8):627–635.
2. Cobb J, Henckel J, Gomes P, et al. Hands-on robotic unicompartmental knee replacement: a prospective, randomised controlled study of the Acrobot system. J Bone Joint Surg Br 2006;88(2):188.

Luminal Robots Small Enough to Fit Through Endoscope Ports: Initial Tumor Resection Experiments in the Airways

Margaret Rox[1*], Katherine Riojas[1*], Maxwell Emerson[1], Kaitlin Oliver-Butler[2], Caleb Rucker[2], and Robert J. Webster III[1] *shared first author

[1] *Vanderbilt University, Nashville, TN,* [2] *University of Tennessee, Knoxville, TN*
{*margaret.rox,katherine.e.riojas,maxwell.emerson,robert.webster*}*@vanderbilt.edu,*
{*koliverb@vols, drucker6@ibme*}*.utk.edu*

INTRODUCTION

In this paper, we present the first resection experiments with a new kind of luminal continuum robot that is small enough to fit through the port of a conventional flexible endoscope, yet provides a large open central lumen through which surgical instruments can pass. This robot enables dexterity at the tip of a flexible endoscope for port-delivered instruments (see Figure 1). These capabilities can be useful in a wide range of surgical procedures where flexible endoscopes are used, including those in the colon, lung, brain, and other natural orifice procedures throughout the body. Historically, obtaining this type of dexterity has required re-engineering the endoscope, increasing its diameter (e.g. the EndoSamurai from Olympus or the Anubiscope from Karl Storz, both of which are 16mm).

Our new luminal robot concept consists of two tubes, each of which has had material selectively removed from one wall [1]. The tubes are placed within one another and axially rotated so that the non-machined faces of each are opposite one another. The tips are then attached, so that these faces can act as push-pull actuation elements that make the overall structure bend. This actuation principle is analogous to the multiple backbones in the designs pioneered by Simaan et al. [2] but packages them into a thin, tubular form factor suitable for delivery through standard endoscope ports (see Figure 2.)

Here we perform the first tumor resection experiments with this new kind of robot. Specifically, we explore their potential for removing central airway tumors, which affect 80,000 patients per year in the USA [3, 4] and pose a life-threatening risk of asphyxiation. Surgery to remove these tumors is normally performed using either an open approach or a rigid endoscope. The latter approach, while less invasive, still has a 32% complication rate [5], with complications including broken teeth, damage to the neck, or in rare cases even death from ruptured blood vessels. Many of these complications are related to the need to tilt the patient's head back to straighten the throat so that the endoscope can reach the lung, combined with the fact that endoscope angulation is currently the only way to aim tools delivered through the rigid endoscope's port.

Figure 1: Conceptual drawing of a dual-channel flexible endoscope with our luminal manipulators delivered through its ports.

In this paper, we explore whether our dexterous manipulators can take the place of rigid endsocope angulation for instrument aiming, thereby enabling the procedure to be performed through a flexible endoscope with no wrenching of the patient's neck.

ROBOT PROTOTYPE

We created our luminal robot by machining two PEEK tubes using the method used for unidirectional wrists in [6]. The inner tube had an ID of 1.25 mm and an OD of 1.65 mm. The outer tube had an ID of 1.80 mm and an OD of 2.31 mm. We cut five 2.3 mm wide notches, 1.6 mm apart, at a depth of 70% of the outer diameter for each tube. After machining, the tubes were arranged concentrically and cyanoacrylate was used to attach their tips to one another.

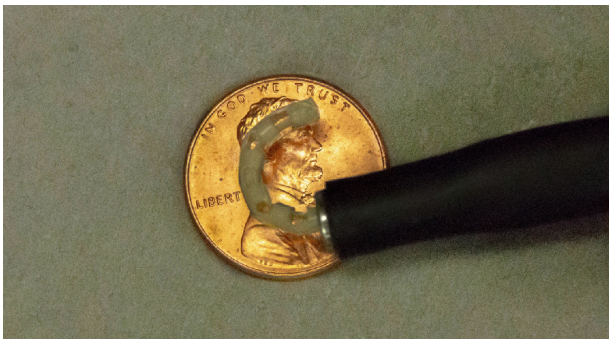

Figure 2: Prototype luminal manipulator delivered through a 6 mm diameter bronchoscope.

Figure 3: (a) Initial obstruction, (b) Removal of tumor with the manipulator, (c) Sheep trachea after tumor removal.

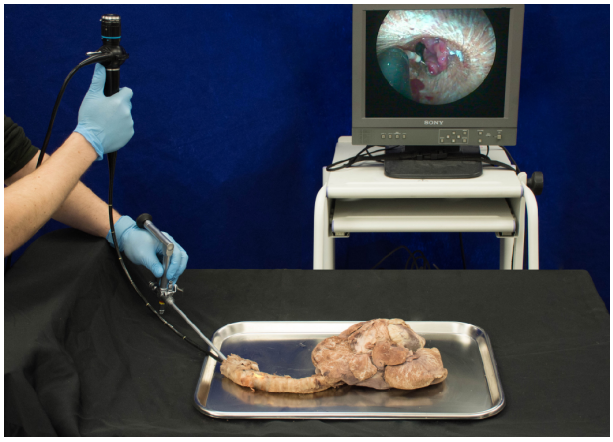

Figure 4: Experimental Setup: The bronchosope was used to deploy the luminal manipulator into the sheep trachea. A rigid endoscope was introduced beside it to capture the images shown in Figure 3.

EXPERIMENTS

To create a model of a tumor obstructing the central airway, we used a sheep trachea and attached a small piece of chicken liver to its inside wall with cyanoacrylate to simulate the tumor (see Fig. 3(a)). Once the obstruction was fixed in place, we deployed the luminal manipulator through the working channel of a commercial flexible bronchoscope (Olympus BF-1T20D) (see Fig 3(b)). The tip of the luminal manipulator was fitted with a blade for sharp dissection. Two people collaborated to operate the device in these experiments, one operating the endoscope controls and the other manually controlling extension and curvature of the port-delivered manipulator by coordinating the linear motions of both its tubes. After separation of the obstruction from the wall, the blade was removed, and a suction tube was placed through the lumen of the device to remove the excised tumor, resulting in the image shown in Fig 3(c). We note that in a clinical implementation this blade would likely be replaced by a fiber laser and the tumor removed intact by grasping it with forceps, to remove it from the body.

DISCUSSION

The results in this paper represent the first resection experiments using our new luminal manipulator. They also represent the first steps toward a new paradigm for central airway tumor resection using a flexible endoscope rather than a rigid one, an approach that is expected to reduce complications that come from wrenching the patient's head and neck as is required in the current rigid endoscopic approach. Future work will involve performing experiments similar to those in this paper using a flexible fiber optic laser for cutting, with en bloc removal of the tumor. The new manipulator itself also can be enhanced even further with optimization of materials, dimensions, and tolerances. A robotic actuation system is in development for this device; the experiments in this paper revealed the usefulness of it, since it was challenging for two different people to coordinate endoscope and manipulator motions. These proof-of-concept experiments, combined with the scalability and adaptability of this design, present exciting possibilities for enhancing dexterity in a wide variety of current flexible endoscopic procedures.

References

[1] K. Oliver-Butler, Z. H. Epps, and D. C. Rucker, "Concentric agonist-antagonist robots for minimally invasive surgeries," in *SPIE Medical Imaging*, 10135, 1–9, 2017.

[2] R. E. Goldman, A. Bajo, and N. Simaan, "Compliant Motion Control for Multisegment Continuum Robots With Actuation Force Sensing," *IEEE T. Robotics*, 30 (4), 1–13, 2014.

[3] E. Chan and N. Argintaru, "Malignant airway obstruction: treating central airway obstruction in the oncologic setting," *U. Western Ontario Med. Journal*, 80 (2), 7–9, 2011.

[4] K. Chen, J. Varon, and O. C. Wenker, "Malignant airway obstruction: recognition and management," *J. Emergency Medicine*, 16 (1), 83–92, 1998.

[5] G. Vishwanath, K. Madan, A. Bal, A. N. Aggarwal, D. Gupta, and R. Agarwal, "Rigid bronchoscopy and mechanical debulking in the management of central airway tumors: an indian experience," *J. of Bronchology & Interventional Pulmonology*, 20 (2), 127–133, 2013.

[6] P. J. Swaney, P. A. York, H. B. Gilbert, J. Burgner-Kahrs, and R. J. Webster, "Design, fabrication, and testing of a needle-sized wrist for surgical instruments," *J. Medical Devices*, 11 (1), 014501:1-9, 2017.

Safety and feasibility clinical trial of a novel single port flexible robot for Transoral Robotic Surgery

Jason Y K Chan[1], Raymond K Tsang[2], F. Christopher Holsinger[3], Michael C F Tong[1], Philip W Y Chiu[4], Simon S M Ng[4], Eddy W Y Wong[1]

[1] *Department of Otorhinolaryngology, Head and Neck Surgery, The Chinese University of Hong Kong, Shatin, N.T., Hong Kong SAR*

[2] *Department of Surgery, The University of Hong Kong, Pok Fu Lam, Hong Kong SAR*

[3] *Deparment of Otorhinolaryngology, Head and Neck Surgery, Stanford University, Palo, Alto, USA*

[4] *Department of Surgery, The Chinese University of Hong Kong, Shatin, N.T., Hong Kong SAR*

jasonchan@ent.cuhk.edu.hk

ABSTRACT

Introduction

The aim of this study is to describe the results of a safety and feasibility clinical trial of a novel flexible robot for transoral robotic surgery (TORS) for head and neck surgery.

Materials and Methods:

This was a Prospective Innovation, Development, Exploration, Assessment, Long-term Study (IDEAL) phase 1 clinical trial of both benign and malignant lesions of the head and neck utilizing the da Vinci SP system (Intuitive Surgical Inc., Sunnyvale, CA). The primary endpoint included conversion rates and perioperative complications within 30 days following surgery. The study was registered on www.ClinicalTrials.gov (NCT03010813).

Results:

Twenty-one patients underwent TORS with the da Vinci SP (Intuitive Surgical Inc., Sunnyvale, CA) demonstrated access to the nasopharynx, oropharynx, larynx and hypopharynx as seen in Figure 1 and 2. The male to female ratio was 1:0.4 with a mean age of 59.1 years (Range 41 – 75 years old). Nineteen (90.4%) of patients were Chinese. Most of the clinical cases were in the oropharynx (67%) followed by the larynx (14%), hypopharynx (10%) and nasopharynx (9%). The pathology of these cases included oropharyngeal carcinoma (38.0%), benign lesions of the pharynx (38.0%), laryngeal carcinoma (14.0%) and obstructive sleep apnoea (10.0%). Seven patients had oropharyngeal squamous cell carcinoma (SCC), six were HPV+ve and one HPV-ve. Five arose from the tonsil and underwent radical tonsillectomies (two T1 and three T2), one arose from the tongue base (T1) and underwent a tongue base resection, one patient had an unknown primary and underwent a unilateral tongue base resection. In addition, one patient with an HPV positive tonsil primary underwent a retropharyngeal lymph node excision simultaneously. Two patients had laryngeal SCC, one underwent an examination under anaesthesia of the lesion. The second patient with a laryngeal SCC underwent a transoral partial laryngectomy resection with clear margins. The mean docking time of the robot was 7.8 minutes, operative time was 61.1 minutes, blood loss was 39.2ml. There were no conversions of the robotic surgical system. There were no serious adverse events or adverse events related to the use of the robot at 30-day follow-up for all patients.

Conclusions:

This safety and feasibility trial of a novel flexible robotic system clearly demonstrates that the device is safe and that it is feasible to use in TORS to operate in the nasopharynx, oropharynx, larynx and hypopharynx.

Fig. 1 da Vinci SP in use for examination of the supraglottis with the camera arm and all three instrument arms deployed transorally as seen in the insetted figure. The mouth is opened and suspended with a Crowe–Davis mouthgag. The cannula is located about 10 cm from the oral opening.

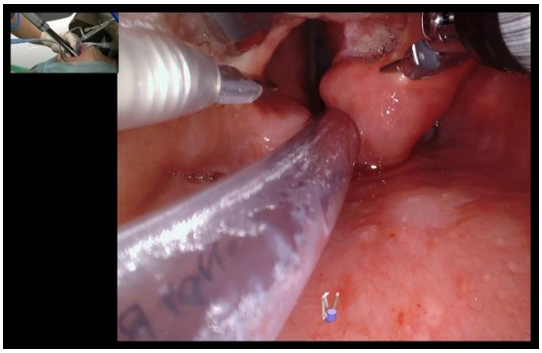

Fig. 2 da Vinci SP in use for examination of the supraglottis through an internal view. The monopolar spatula tip is seen on the left, the Maryland bipolars are opened at the right aryepiglottic fold exposing the tumor, while the fenestrated bipolar is retracting the epiglottis superiorly. The insetted figure shows the assistant holding a Yankaur suction and the location of the port about 10 cm from the oral opening.

Computational Inverse Design of Anatomy-Specific Soft Robot Actuators with Physically-Realizable Material Conditions

Mark D. Gilbertson[1], Gillian J. McDonald[1], Chaitanya Awasthi[1], Rumi Faizer MD[2], and Timothy M. Kowalewski Ph.D[1]

[1] *Department of Mechanical Engineering, University of Minnesota*
[2] *Department of Vascular Surgery, University of Minnesota*
gilbe767@umn.edu

INTRODUCTION

Soft robotics has empowered robots to maneuver, traverse, and complete tasks where traditional rigid robots fall short [1]. Traditionally, soft robots rely on forward design. This limits robots' spectrum of potential actuator shapes [2], but what if a specific patient's anatomy requires a unique actuator shape not realizable by such methods? Inverse design, on the other hand, centers around the desired task and produces a robot geometry for that task. Currently, there exists no technique for the inverse design of a soft robot that can actuate from arbitrary anatomy-specified initial and final shapes. Worse, computational methods may easily result in designs that are physically impossible to realize with real-world materials, e.g., such designs may easily violate volumetric compressibility properties of realistic elastomers.

We introduce a method of computational inverse design of soft robot actuators that simultanesouly achieves required arbitrary actuator shapes dictated by unique patient anatomy and ensures realistic volumetric compressibility throughout the actuator body. We propose a 3 degree of freedom (DOF) parameterization. We test the hypothesis that partitioning 2 DOF to parameterize the required actuator surface shape and 1 DOF for volumetric compressibility provides compuational designs that achieve desired shapes and meet compressibility requirements for typical hyperelastic elastomers.

MATERIALS AND METHODS

The process for creating an anatomy-specific actuator consists of two steps. The first step involves segmenting medical scans to find anatomical centerlines from which the soft robotic actuator shapes are determined. The second step focuses on designing a soft actuator given the parametric representation of the anatomy (e.g. centerline, radius) and selecting the desired actuator shape.

The anatomy-specific soft actuator design method is applied to an abdominal vasculature scan as shown in Fig. 1a. For our demonstration case, we design a spiral actuator in the renal artery as outlined in Fig 1b. The renal artery was selected due to the need for vascular surgeons to anchor guidewires in the renal artery without obstructing blood flow. Moreover, the artery's small size and need for such shapes could not be achieved with the methods in [2].

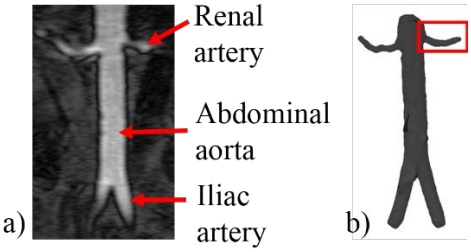

Fig. 1 a) MRI scan data of patient anatomy. b) 3D model, where the actuator is designed for the renal artery (boxed region).

Anatomy Segmentation & Centerline Creation

Our process for creating an anatomy-specific actuator started with processing the abdominal medical image using the Vascular Modeling Toolkit Lab (VMTKLab) [3]. Thresholding and segmentation were performed on the image and a 3D model was created. The 3D model was uploaded into the centerline function in VMTKLab and the centerline data was exported.

The centerline points were loaded into MATLAB and fit with a cubic spline followed by a polynomial fitting as a function of the parametric variable for length, w. This resulted in a 3D parametric centerline with coefficients β and order N=5 as written in eq. 1.

$$\boldsymbol{c_a}(w) = \sum_{i=0}^{N} \beta_i w^i \tag{1}$$

$$r_a = \sum_{i=0}^{N} \gamma_i w^i \tag{2}$$

The cubic spline and polynomial fit were also applied to the anatomical radius data, resulting in eq. 2, with coefficients γ. Eqs. 1-2 yield a continuously differentiable basis for an arbitrary robot actuator shape.

Soft Actuator Design

A helical spiraling actuator was selected for the renal artery as it can anchor in place without obstructing blood flow. The spiral actuator design was created by wrapping a helix about the anatomical centerline and extruding a cylinder about the obtained helical centerline. We start by assigning coordinate frames along the anatomical centerline which is parameterized by w. These frames are defined using Frenet-Serret method by computing the tangent, $\boldsymbol{T}$, normal, $\boldsymbol{N}$, and binormal, $\boldsymbol{B}$, vectors along the centerline $\boldsymbol{c_a}(w)$.

$$\boldsymbol{T} = \frac{\frac{\partial \boldsymbol{c_a}}{\partial w}}{\left|\frac{\partial \boldsymbol{c_a}}{\partial w}\right|},\ \boldsymbol{N} = \frac{\frac{\partial \boldsymbol{T}}{\partial w}}{\left|\frac{\partial \boldsymbol{T}}{\partial w}\right|},\ \boldsymbol{B} = \boldsymbol{T} \times \boldsymbol{N} \tag{3}$$

With eq. 3 defined we move to fit a helix around $\boldsymbol{c_a}(w)$ by applying modifications to the standard helix parameterization resulting in $\boldsymbol{c_f}(w)$ as shown in eq. 4.

$$\boldsymbol{c}_f(w) = \boldsymbol{c}_a(w) + R(w)\left[cos\left(\frac{2\pi kw}{L}\right)\boldsymbol{N} + sin\left(\frac{2\pi kw}{L}\right)\boldsymbol{B}\right] + \rho\boldsymbol{T} \quad (4)$$

$$R(w) = \frac{1}{2} f_{env}(w) r_a(w) \quad (5)$$

$$f_{env}(w) = \frac{1}{\sqrt{2}} tan^{-1}(15w) \quad (6)$$

The radius of the helix is described by $R(w)$, eq. 5, where $f_{env}(w)$, eq. 6, is an envelope function that ensures the ends of the actuator centerline smoothly blend into the anatomical centerline. In eq. 4 the k represents the number of helical turns, ρ is the pitch of the spiral, and L is the length of the centerline. In this specific case, $L = 20.63\,mm$, $k = 3.18$, $\rho = 0.8\,mm$, inner radius $r_i = 0.99\,mm$, and outer radius $r_o = 1.00\,mm$. These can be modified to fit specific design criterions, such as occlusion ratio, actuator contact area with anatomy, or a combination of other objectives.

The next step is to create the actuator body about $\boldsymbol{c_f}(w)$. Since the body is a volume, we must use three parametric variables and choose to use a cylindrical coordinate basis resulting in $X = [u, v, w]$, where $u = [r_i\ r_o]$ represents the radius of the cylindrical actuator, $v = [0\ 2\pi]$ represents the wrap angle, and $w = [0\ L]$ is the length along the centerline. A Frenet-Serret frame is then defined using $\boldsymbol{c_f}(w)$, resulting in $(\boldsymbol{T}_f,\ \boldsymbol{N}_f,\ \boldsymbol{B}_f)$. The actuator body is then created as a function of parametric variables X as written in eq. 7. The function $f(u)$ is introduced to modify the local thickness of the actuator body at each point as illustrated in Fig. 2.

$$\boldsymbol{\varphi}(X) = \boldsymbol{c_f}(w) + \big(u + f(u)\big)\,\bar{n} \quad (7)$$

$$\bar{n} = \left[\boldsymbol{N_f}\,cos(v) + \boldsymbol{B_f}\,sin(v)\right] \quad (8)$$

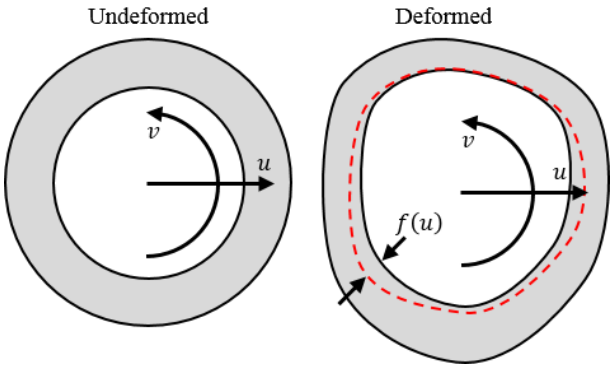

Fig. 2 The cross section of the soft robot is displayed in its initial underformed cylindrical state and its deformed spiral state. The initial design focuses on creating a design over [*v*, *w*] and does not directly account for *u*. The function *f(u)* was created to modifiy the thickness to enforce incompressibility. The thickness adjusted by *f(u)* is shown by the red dashed line.

To enforce material incompressibility of the design, we use the deformation gradient $\boldsymbol{F}$ as calculated by eq. 9 with the reference basis being in cylindrical coordinates, X, and the deformed basis being in Cartesian coordinates, $\boldsymbol{\varphi}(X)$ [4]. If the determinant of $\boldsymbol{F}$ is sufficiently close to one, we consider the design incompressible.

When solving eq. 10 for incompressibility, a first order differential equation is produced in terms of $f(u)$. If we assume that $f(u)$ takes the form in eq. 11, we can solve for α_0 and α_1 at every spatial location X.

$$\boldsymbol{F} = \left[\frac{\partial\boldsymbol{\varphi}(X)}{\partial u}\quad \frac{1}{u}\frac{\partial\boldsymbol{\varphi}(X)}{\partial v}\quad \frac{\partial\boldsymbol{\varphi}(X)}{\partial w}\right] \quad (9)$$

$$\varepsilon = |det(\boldsymbol{F}) - 1| < 10^{-6} \quad (10)$$

$$f(u) = \alpha_0 + \alpha_1 u \quad (11)$$

RESULTS

The renal artery centerline and mesh are shown in Fig. 3. Additionally, Fig. 3 contains the soft robot's centerline and final computational design. The incompressibility constraint was numerically satisfied in eq. 11 with all ε less than 10^{-6} over the whole range of $X = [u, v, w]$, 2000 spatial locations in all.

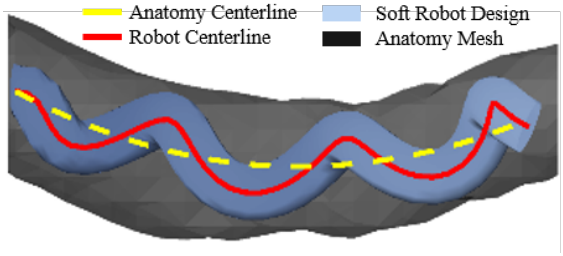

Fig. 3 Spiral actuator design inside the renal artery.

DISCUSSION

The method produced a parametric soft robot actuator design for a specific renal artery while ensuring local volumetric compressibility by partitioning the DOF as hypothesized. This method is highly generalizable for nearly arbitrary shape requirements. It expands the possible design space of soft robots to new patients with unique anatomy. It also alleviates constraints such as those caused by wrap angles in fiber-reinforced actuators, and creates a design based upon the task (specific patient-needs) and not the manufacturing method with which a soft robot designer begins. With the actuator shape created future work can continue on incorporating additional and anisotropic material properties into the computational design to realize a physical robot device.

ACKNOWLEDGEMENTS

This work was supported by the MnDRIVE Robotics, Sensors, and Advanced Manufacturing initiative for financial support. Additionally, this material is based upon work supported by the National Science Foundation Graduate Research Fellowship Program under Grant 00039202. We thank VMTKLab for providing the MRI scan.

REFERENCES

[1] D. Rus and M. T. Tolley, "Design, fabrication and control of soft robots," Nature, vol. 521, no. 7553, pp. 467-475, 2015.

[2] Gilbertson, M. D., McDonald, G., Korinek, G., Van de Ven, J. D., & Kowalewski, T. M, "Serially actuated locomotion for soft robots in tube-like environments," IEEE Robotics and Automation Letters, 2(2), 1140-1147, 2017.

[3] Luca Antiga, D. S. VMTK, the Vascular Modeling Toolkit 2004

[4] Tadmor, E. B., Miller, R. E., & Elliott, R. S., "Continuum mechanics and thermodynamics: from fundamental concepts to governing equations," Cambridge University Press, 2012.

Development of thin double-arm device for bladder tumor resection

U. Yagyu[1], E. Kobayashi[2], K. Nakagawa[1], Y. Komai[3], M. Ito[4], I. Sakuma[1]

[1] School of Engineering, the University of Tokyo,

[2] Institute of Advanced Biomedical Engineering and Science, Tokyo Women's Medical University

[3] Cancer Institute Hospital

[4] National Cancer Center Japan

yagyu@bmpe.t.u-tokyo.ac.jp

INTRODUCTION

In TUR-BT (Trans Urethral Resection of the Bladder Tumor), which is an endoscopic surgery for superficial bladder cancer, tumors are crushingly removed with a device inserted from the urethra. Crushing resection leads to risks of seeding tumors and degradation of diagnostic accuracy. Therefore, a device for en bloc resection is desired. With a device, tumors are lifted, and the roots are cut (Fig.1). To achieve this, the device should have double arms; grasping and cutting.

There are some double-arm devices such as the SPIDER [1], "R" scope [2] and Endomaster [3], in which each arm can move 3-dimensionaly. However, in TUR-BT, the device is inserted from the urethra. The diameter of the device must be smaller than that of the urethra. Diameter of SPIDER, "R" scope, and Endomaster are 18 mm, 14.3 mm and around 14 mm respectively; too large forTUR-BT. Therefore, our objective is to develop a device whose diameter is small enough for TUR-BT, and has enough arm's degree of freedom (DOF) and sufficient operability.

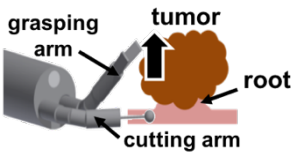

Fig. 1 En bloc resection with double arm device.

DEVELOPMENT OF THE DEVICE

1. Device concepts and requirements

The size of most bladder tumor is less than 10 mm[4]. There, the target tumor size is 10 mm.

The device consists of two arms. One is grasping arm and the other is cutting arm. The device also includes an endoscope, which is passed through a single tube with the two arms. Movement of the arms is achieved by operating the interface by hand.

The grasping arm has 4 DOF; opening and closing of the tip for grasping, bending for lifting tumor, rotation for raising direction adjustment, and sliding for alignment of the tumor and the arm. The cutting arm has 3 DOF; bending and sliding for cutting, and rotation for cutting path adjustment. Each arm can move 3-dimensionaly.

Table 1 Numerical requirement specification

insertion length	> 110 mm
outer diameter	< 12 mm
bending length	grasping: > 5 mm, cutting: > 10 mm
tumor lifting force	> 250 mN

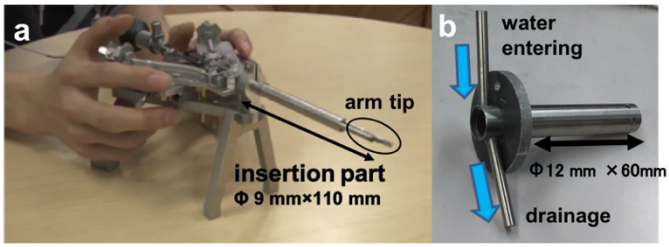

Fig. 2 Developed device (a: double arm device, b: trocar with irrigation)

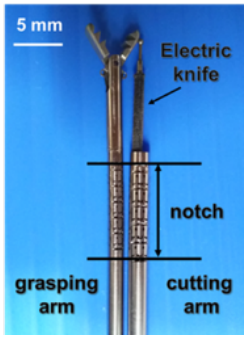

Fig. 3 Arm devices

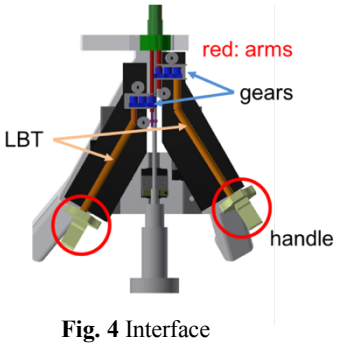

Fig. 4 Interface

We have decided to develop the device initially targeting on women. Then, requirements were determined from the size of the bladder, women's urethra, and tumors as shown in Table 1.

In TUR-BT, irrigation system is necessary to flush out bleeding and inflate the bladder. Since the resected tumor needs to be removed through the urethra, there is a problem that a tumor larger than the diameter of the urethra will be removed with rubbing on the urethra. In TUR-BT, removal of large tumors has been a difficulty when trying to collect the tumor without breaking it up into pieces. To equip irrigation system and to achieve large tumor removal, we adopted a system that used the double-arm device and a trocar, and developed them both. The outer diameter of the trocar must be smaller than 12 mm. Flow rate of irrigation must be greater than 3.1 mL/L, decided from the current TUR-BT.

2. Design of the device

Figure 2 shows the device developed. Fig.2a is the device and Fig.2b is the trocar. For irrigation, trocar was designed to have a two-layer structure, and a flow path was formed between them. The width of the flow path was 0.5 mm. Then the insertion part of the device is inserted into the bladder through the trocar. The outer diameter was 9 mm for the double arm device and 12 mm for the trocar. Insertion length was 110 mm.

The grasping and cutting arms are shown in Fig.3. Because the diameter should be less than 12 mm including the trocar, the diameter of the insertion part should be less than 9 mm. To achieve this, we have developed a grasping arm with a diameter of 2.65 mm and a cutting arm with a diameter of 3.30 mm. They both have one DOF bending mechanism with wire. Also the cutting arm is hollow with an inner diameter of 2 mm, and an electric cutesy knife was inserted. Bending length was 16.2 mm (grasping), 18.5 mm (cutting), and the lifting force of the grasping arm was 310 mN. We used an endoscope with a diameter of 2.60 mm.

Fig.4 shows the details of the interface. As for operability, the bending direction of the arm tip varies according to the rotation of the arm. To intuitively comprehend the bending direction of the arm, we integrated the rotating handle and the bending one of the interface. Integration of rotation and bending was achieved by transmitting rotation from the interface to the arm with the Liner Blade Tube (LBT) and gears. LBT is a flexible metal tube and can transmit rotation. The arm and the rotating lever of the interface were connected by gears and a bent LBT (Fig.4). The bending of the arm is achieved by connecting the wire in the arms to the bending handle at the interface and applying tension to it. Sliding of the arms is achieved by miniature linear guide. Opening and closing of the arm tip is achieved by pushing a wire inside the grasping arm.

EVALUATION OF THE DEVICE

All DOF can be moved without malfunction. The angle error between the interface and the arm was 1.4 degrees (grasping) and 0.9 degrees (cutting) on average. This makes it possible to intuitively comprehend the bending direction of the arm at the interface. Trocar's irrigation flow rate was 3.7 mL/s on average.

Finally, the excision experiment of extracted swine bladder using the double arm device was conducted by a urology doctor. Bladder tumor model was made from bladder tissue. The doctor performed the experiment while watching endoscopic images. En bloc resection (grasping the tumor model, lifting and cutting it) was succeeded as shown in Fig.5.

DISCUSSION AND CONCLUSION

We developed the double arm device for en bloc resection of tumors in TUR-BT. Under the constraint of the outer diameter, we developed the device that allows each arm to move in three dimensions at the outer diameter of 9 mm. By the transmission of rotation, intuitive bending was made possible. From the swine bladder resection experiment, it was shown that our device is effective in TUR-BT for en bloc resection of bladder tumors. Since rotation can be induced by transmitting the rotation of the handle, all DOF can be manipulated at the interface without having to largely maneuver the device as shown in Fig.2a.

Furthermore, we developed the trocar whose outer diameter is 12 mm. It has an irrigation system with enough flow rate and removal of large tumors without rubbing them on urethra is possible.

As our next work, applying this device to male patients should be realized. Diameter of the male's urethra is 9 mm, so the entire system including the double arm device and the trocar must be smaller than 9 mm. In our device, the outer diameters of the arms are 2.65 mm for the grasping arm, and 3.30 mm for the cutting arm, which are not so small. By developing smaller arms and the double-arm device whose diameter is enough small to insert into males' urethra. Furthermore, water resistance and sterilization must be fulfilled for this device to be used in the clinical practice as a medical device.

REFERENCE

[1] Aurora D. Pryor, *et al.,* Single-port cholecystectomy with the TransEnterix SPIDER: sinmle and safe. *Surg Endosc,* vol.24, 917-923, 2010.

[2] Bardaro SJ, *et al.,* Development of advanced endoscopes for Natural Orifice Transluminal Endoscopic Surgery (NOTES). *Minimally Invasive Therapy,* vol.6, 378-383 2006.

[3] Phee SJ, *et al*., Robot-Assisted Endoscopic Submucosal Dissection Is Effective in Treating Patients With Early-Stage Gastric Neoplasia. *Clinical Gastroenterology and Hepatology,* vol.10, 1117-1121, 2012

[4] K Muraya, *et al*., Clinical statistical examination of bladder tumor. *Japanese society of National Medical Servces,* 1995.

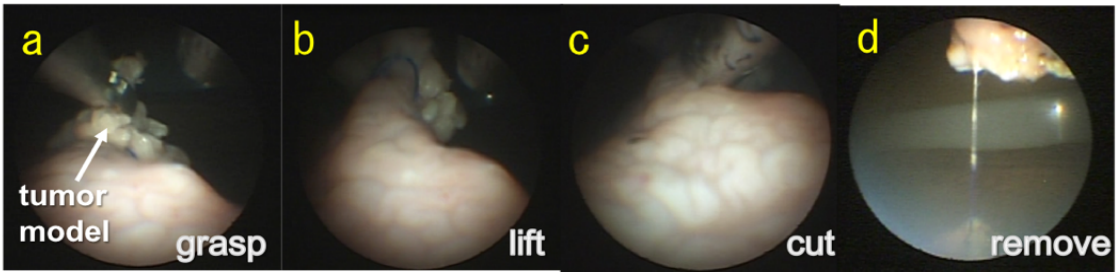

Fig. 5 Endoscopic image of swine bladder resection experiment,
a: grasping, b: lifting, c: cutting, d: removal.
(left arm: grasping arm, right arm: cutting arm)

Unsupervised Learning of Depth Estimation from Video for Bronchoscopic Navigation

Mali Shen *[1], Yun Gu *[1], Pallav Shah[2], and Guang-Zhong Yang[1]

[1] The Hamlyn Centre for Robotic Surgery, Imperial College London
[2] National Heart & Lung Institute, Imperial College London
mali.shen09@imperial.ac.uk

INTRODUCTION

Bronchoscopic intervention remains a challenging task for pulmonologists due to the difficulty in orienting the scope through complicated airway bifurcations. Developing navigation systems that provide localisation of the scope camera is important for taking biopsies or delivering implants at target locations. 2D/3D registration approaches are often favoured for the localisation task due to the ease of setup and robustness to tissue deformation. The similarity measure using depth is shown can be more robust to endobronchial surface texture and illumination artefacts compared to image intensity [1]. However, depth recovery based on conventional Shape From Shading (SFS) approach [2] is too time-consuming for real-time applications. Since the rise of deep learning, two main categories of depth estimation approaches from monocular images have been proposed: 1) supervised methods [3, 4] that rely on intensive labelled data; 2) unsupervised methods [5, 6] based on shape from motion which is not applicable for low texture bronchoscopic images.

In this paper, we propose an unsupervised depth learning from broncoscopic video sequences without using the motion information. Only the unpaired video frames and virtual depth maps generated from CT airway models are required for training. The generative adversarial network (GAN) with cycle-consistency [7] is employed to learn the mapping between these two modalities. The proposed framework is validated in comparison with depth recovered with SFS [2] and supervised method based on fully convolutional networks [8]. The results show that the proposed depth estimation approach provides satisfying qualitative and quantitative results for bronchoscopic images.

MATERIALS AND METHODS

The proposed depth estimation framework is illustrated in Fig.1. The bronchoscopic video frames X are captured during routine examinations. The airway model is reconstructed from high-resolution CT scans. The intrinsic parameters of the bronchoscopic camera was estimated using standard camera calibration with checkerboard. The virtual depth maps Y are generated by setting a virtual camera with the same intrinsic parameters as the bronchoscope. To mimic all possible views, the virtual camera pose is set to follow the airway centrelines with controlled variations. Instead of learning the mapping $G_{Depth} : X \rightarrow Y$ based on manually paired data, we adopt an unsupervised framework by introducing the inverse mapping $G_{Video} : Y \rightarrow X$ as well as the discriminators D_{Depth} and D_{Video} to identify the real depth/bronchoscopic frames respectively.

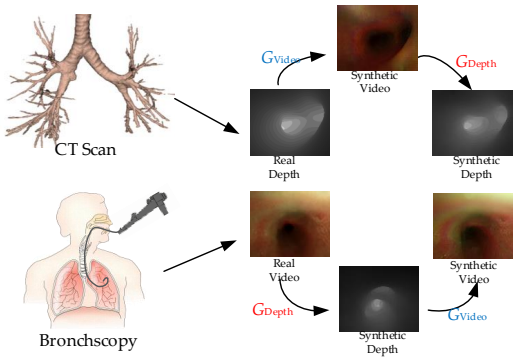

Fig. 1: The main framework of the proposed method.

Following the general settings in adversarial learning, adversarial losses are applied to both mapping functions. For G_{Depth} and D_{Depth}, we express the objective as the cross entropy for real/synthetic depth data classification:

$$\begin{aligned} &\min_{G_{Depth}} \max_{D_{Depth}} \mathcal{L}_{adv}(G_{Depth}, D_{Depth}) \\ &= \mathbb{E}_{y \sim Y} log D_{Depth}(y) + \\ &\mathbb{E}_{x \sim X}(1 - log D_{Depth}(G_{Depth}(x))) \end{aligned} \tag{1}$$

where G_{Depth} tries to generate depth $G_{Depth}(x)$ that looks similar to real depth from CT data, while D_{Depth} aims to distinguish between synthetic samples $G_{Depth}(x)$ and real samples $y \in Y$. Unlike the supervised methods, the corresponding depth maps of the bronchoscopic frames are not available in this work. Considering the similar morphology shared by bronchoscopic frames and depth maps, the reasonable depth estimation should be informative to recover the original bronchoscopic frames as a cycle [7]:

$$\begin{aligned} &\min_{G_{Depth}} \mathcal{L}_{cycle}(G_{Depth}) = \\ &\mathbb{E}_{x \sim X} \| x - G_{Video}(G_{Depth}(x)) \| \end{aligned} \tag{2}$$

where the error between the original and recovered bronchoscopic frames is minimised. To avoid the

*indicates equal contribution.

Table 1: The error measurement of the depth estimation. The best results are shown in **bold**.

Methods	*PSNR*		*SSIM*	
	Mean ↑	Var↓	Mean↑	Var↓
SFS	14.10	2.07	0.54	0.12
Supervised	13.42	2.47	0.46	0.11
Ours	**16.40**	**1.64**	**0.61**	**0.10**

bias, we also introduce the adversarial loss and recovery loss to G_{Video} and D_{Video} which finally formulates the overall objective function:

$$\begin{aligned} &\min_{G_{Depth},G_{Video}} \mathcal{L}_{cycle}(G_{Depth}) + \mathcal{L}_{cycle}(G_{Video}) \\ &\min_{G_{Depth}} \max_{D_{Depth}} \mathcal{L}_{adv}(G_{Depth}, D_{Depth}) \\ &\min_{G_{Video}} \max_{D_{Video}} \mathcal{L}_{adv}(G_{Video}, D_{Video}) \end{aligned} \tag{3}$$

where the depth estimation function G_{Depth} is obtained by alternatively optimising the problem in Eq.(3).

RESULTS

The proposed framework is validated on an *in-vivo* dataset from one subject. The CT scans with voxel spacing of $[0.4, 0.4, 0.5]mm$ are acquired by Siemens SOMATOM Definition Edge CT scanner. Videos were collected using an Olympus BF-1T260 bronchoscope. SFS and supervised FCN are employed as baselines for comparison. The supervised FCN is based on the residual blocks and trained with manually paired CT depth maps and video images. We use the same network settings in [7] for the depth estimation function, inverse mapping function and discriminators. The PyTorch library is used to implement the deep convolution neural networks and the experiment platform is a workstation with Xeon E5-2630 and NVIDIA GeForce Titan Xp. For quantitative analysis, we report the Peak-Signal-Noise-Ratio (PSNR) and Structural SIMilarity (SSIM) in Table 1. As shown in Table 1, the proposed method outperforms all baselines with higher accuracy and smaller variations on both PSNR and SSIM. The poor performance of the supervised method is due to the limited number of paired data and partial misalignment between video and CT data due to the tissue deformation in video images. Compared to SFS, the generative networks are capable of learning the specific features of real depth maps from the unpaired data. These observations are further supported by sample images in Fig.2. For clear views in the first two rows, all the methods are able to estimate the size and the presence of bifurcations while the proposed method illustrates better local structures of lumens. In contrast, the case with illumination artefacts in the third row deteriorates the supervised method, leading to the false depth estimation within the artefact area.

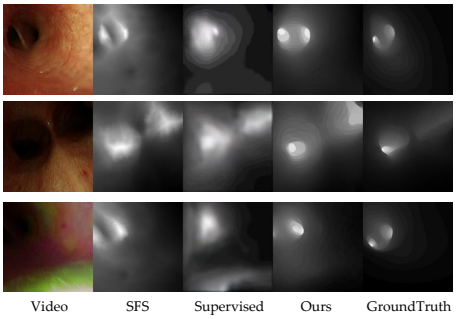

Fig. 2: Qualitative results of the proposed method.

DISCUSSION

This work presents an unsupervised depth estimation method for bronchoscopic video images. Based on unpaired depth and video, the generative adversarial networks with cycle-consistency are able to recover the structures of bifurcations and are more robust to illumination artefacts compared to baseline methods. Our method runs at 30 fps which is feasible for real-time applications. In the future, the temporal information from video sequences will be considered to preserve the consistency between consecutive frames for more accurate depth estimation. The depth estimation will also be integrated into a bronchoscopic navigation framework to validate its reliability for camera localisation.

REFERENCES

[1] Mali Shen, Stamatia Giannarou, and Guang-Zhong Yang. Robust camera localisation with depth reconstruction for bronchoscopic navigation. *IJCARS*, 10(6):801–813, 2015.

[2] Marco Visentini-Scarzanella, Danail Stoyanov, and Guang-Zhong Yang. Metric depth recovery from monocular images using shape-from-shading and specularities. In *ICIP*, 2012.

[3] Marco Visentini-Scarzanella, Takamasa Sugiura, Toshimitsu Kaneko, and Shinichiro Koto. Deep monocular 3d reconstruction for assisted navigation in bronchoscopy. *IJCARS*, 12(7):1089–1099, 2017.

[4] Fayao Liu, Chunhua Shen, and Guosheng Lin. Deep convolutional neural fields for depth estimation from a single image. In *CVPR*, 2015.

[5] Tinghui Zhou, Matthew Brown, Noah Snavely, and David G Lowe. Unsupervised learning of depth and ego-motion from video. In *CVPR*, 2017.

[6] Huangying Zhan, Ravi Garg, Chamara Saroj Weerasekera, Kejie Li, Harsh Agarwal, and Ian Reid. Unsupervised learning of monocular depth estimation and visual odometry with deep feature reconstruction. *CVPR*, 2018.

[7] Jun-Yan Zhu, Taesung Park, Phillip Isola, and Alexei A Efros. Unpaired image-to-image translation using cycle-consistent adversarial networks. *ICCV*, 2017.

[8] Jonathan Long, Evan Shelhamer, and Trevor Darrell. Fully convolutional networks for semantic segmentation. In *CVPR*, 2015.

Autonomous image-based ultrasound probe positioning via deep learning

G. Toporek, H. Wang, M. Balicki, H. Xie

Philips Research North America, Cambridge, MA, USA
grzegorz.toporek@philips.com

INTRODUCTION

Although ultrasound (US) is a widely used, non-invasive, and radiation-free imaging modality, manual adjustment of the US probe can be cumbersome and time consuming. An autonomous US scanning device could not only reduce dependence on sonographer's skills and experience but also improve workflow efficiency especially during interventional procedures. Robot-assisted ultrasound imaging has the potential to improve patient care in rural and underserved areas. There are many previous efforts in this direction but none is fully automatic or sufficiently accurate [1], [2].

In this work, as an initial small step towards operator-independent US imaging workflow solution, we developed and evaluated a robot-assisted fully autonomous ultrasound (RAFAUS) probe positioning system. Desired motion of the probe toward the target view is directly derived from anatomical features implicitly extracted via deep neural network; thus, making this technique (a) invariant to anatomical differences (patient size or organ displacement), (b) decoupled from the robotic system, (c) registration-free, and (d) independent from any external tracking technologies.

MATERIALS AND METHODS

A 36-weeks fetal US training phantom (CIRS) is used to mimic patient anatomy. Images of the anatomy are captured using an US transducer (X5-1, EPIQ 7, Philips). Probe is rigidly attached to the end effector of a commercial robotic manipulator (Universal Robotics), see Fig. 1a. During the operation of the system user chooses any target view with important anatomical structurers according to a scanning protocol. As soon as the sufficient acoustic coupling is provided velocity of the end effector towards target view is derived from predictions made by a convolutional neural network (CNN), therefore precise calibration between transducer and holder is not necessary. Because prediction accuracy improves proportionally with the distance to the target view (see Fig. 3a), the robot system control loop continuously updates velocity based on the target position estimates from the CNN (see Fig. 1b).

During the development of RAFAUS, an arbitrary reference view (see Fig. 2) is chosen and the entire phantom is extensively scanned from different views according to a pre-defined acquisition scheme. Each US image is labelled with a relative position of the transducer with respect to the reference view and stored as unique data points in the database. The data is divided into two separate sets: (a) development dataset (38,900 frames)

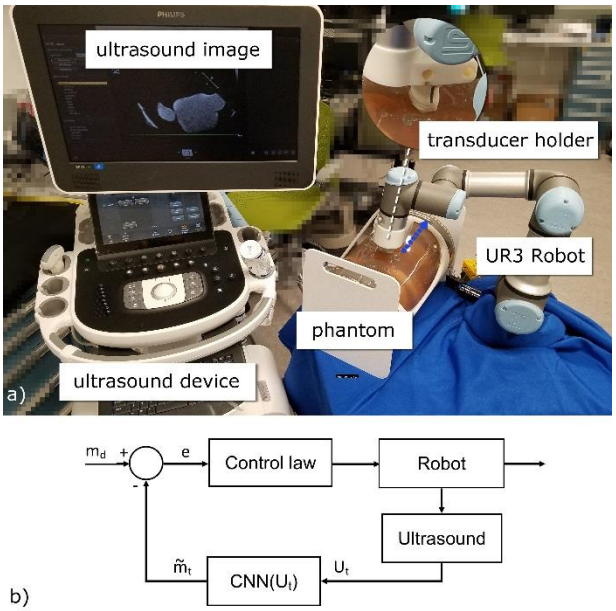

Fig. 1: a) Components of RAFAUS system; US transducer is mounted to serial robot manipulator using custom-made holder and is positioned above US training phantom. Images are sent to processing server with a CNN predicting the motion of the probe (blue arrow) towards the target view in the US probe coordinate frame; b) Schematic diagram of a robot control loop in which the desired Cartesian velocity $\tilde{m}_t$ of the end effector is derived from the prediction provided by a CNN using current US image U_t.

for training the weights of the CNN (of which 15% are randomly chosen for validation), and (b) test dataset (5,400 frames) consisting of data points the model was not trained on (to optimize for generalizability).

In this study, we used a 18-layer CNN with linear residual connections similar to the network described in [3]. In contrast to [3] we increased the size of the last fully connected layer to 2048 and replaced softmax with two 4-dimensional regression layers representing both translational (magnitude and unit direction vector) and rotational (quaternion) components of the rigid transformation. We trained this CNN to predict relative motion of the US transducer towards the reference view using the loss function introduced in [4]. Adaptive Moment Estimator (Adam) optimizer was used as optimization function with an initial learning rate of 0.001, and being decayed every 8,000 samples with an exponential rate of 0.5. Batch normalization, and pre-initialization with weights from the same network trained on ImageNet dataset were used. We used early stopping criteria, and a dropout probability of 0.4 before the last two regression layers to avoid overfitting. We set batch size to 64 and augmented the training data using scale and

aspect ratio augmentation. Input images were center-cropped and normalized based on their mean values and standard deviations to the range of 0–1.

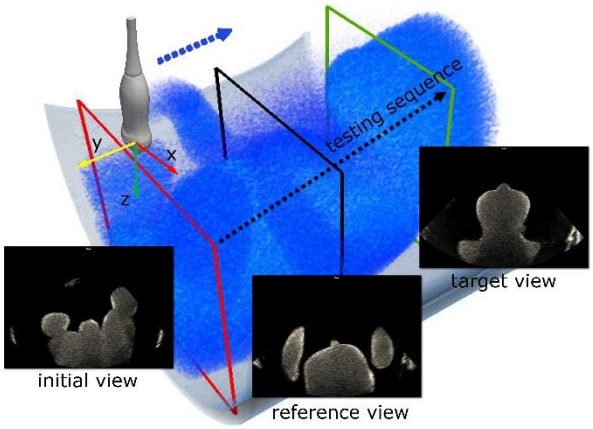

Fig. 2: Schematic overview of a testing sequence (5,400 frames), overlaid on top of a 3D reconstruction of the US phantom, on which prediction accuracy was evaluated. It starts at an initial view located near lower limbs (red outline) and finishes at a target view located at the fetus head (green outline). For the sake of clarity, reference view that was used during the development of the deep learning model is shown as a black outline. Additionally, a predicted motion of the probe (blue dashed line) is depicted in the coordinate system of the ultrasound transducer. This coordinate system is used to calculate errors in the result section (see Fig. 3a-b).

RESULTS

We evaluated the accuracy of RAFAUS using a challenging motion sequence (5,400 frames, see Fig. 2). The average translational accuracy our system achieved was 2.38 ± 2.73 mm, 3.11 ± 3.08 mm, and 1.09 ± 1.29 mm along x, y, and z axis respectively (see Fig. 3b). The overall translational accuracy increased when the distance to the target position decreased (see Fig. 3a). The average prediction inaccuracy measured around 90 mm from the target view was significantly higher (p-value < 0.0001, unpaired, two-tailed t test) than at 20 mm, 4.67 ± 2.8 mm and 1.41 ± 0.88 mm respectively. The average rotational accuracy was 0.68 ± 0.58°, 0.45 ± 0.26°, and 1.72 ± 1.03° around Z, Y, and X axis respectively (see Fig. 3c). We evaluated robustness of the RAFAUS in challenging imaging conditions (e.g. compromised acoustic windows and externally induced phantom motion); quantitative evaluation is not provided in the paper for the sake of brevity.

DISCUSSION

In this work we demonstrated that US transducer can be autonomously positioned with respect to a target view, at an average translational accuracy of 1.41 ± 0.88 mm. The image-based positional feedback using deep learning continuously estimates target position as robot converges on the target view. Naturally, the target position estimate accuracy increased when probe was closer to the target, thus suggesting potential for incorporating a series of former predictions into the deep learning model, for instance, by using temporally recurrent layers, such as Long Short-term Memory (LSTM) units. A clinical system will require safety measures, such as precise regulation of patient-contact forces, collision monitoring, and adjustment of the acoustic coupling. Force control methods will definitely add to the safety by maintaining constant contact and optimal force for image acquisition. The main limitation of this study is the usage of a single phantom for both training and testing. The phantom is static and absent of strong acoustic artifacts, e.g. reverberation artifacts, which are normally encountered in a clinical scan.

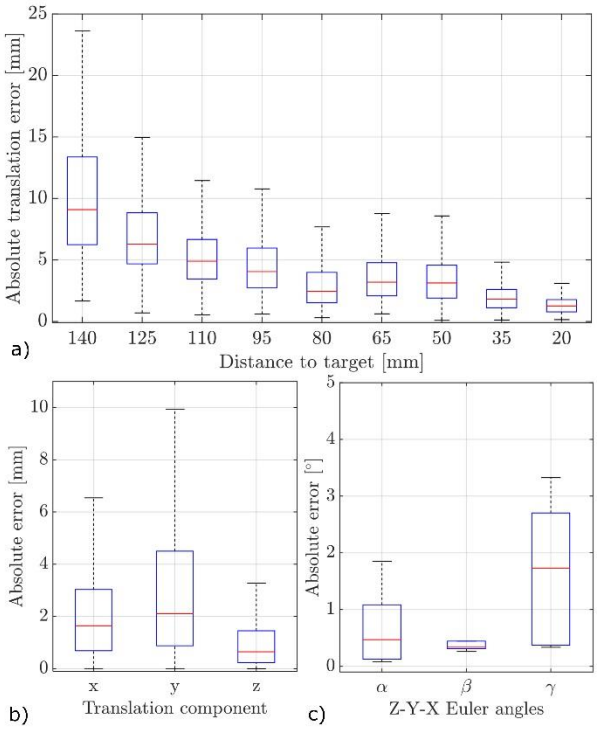

Fig. 3: Boxplots of the pose prediction errors calculated on the testing sequence (see Fig. 2) consisting of 5,400 frames; boxplot (a) shows a prediction accuracy at various distances from the target view along the testing sequence; an overall system accuracy separated into (x, y, z) translational components (b) as well as rotation angles (c) around each axis (Z, Y, X) are also presented.

REFERENCES

[1] A. Safwan, B. Mustafa, S. Member, T. Ishii, Y. Matsunaga, R. Nakadate, H. Ishii, K. Ogawa, A. Saito, M. Sugawara, K. Niki, and A. Takanishi, "Development of Robotic System for Autonomous Liver Screening Using Ultrasound Scanning Device," *Proceeding IEEE Int. Conf. Robot. Biomimetics*, no. December, 2013.

[2] K. Liang, A. J. Rogers, E. D. Light, von D. Allmen, and S. W. Smith, "3D Ultrasound Guidance of Autonomous Robotic Breast Biopsy: Feasibility Study," *Ultrasound Med Biol*, vol. 36, no. 1, pp. 173–177, 2010.

[3] K. He, X. Zhang, S. Ren, and J. Sun, "Deep Residual Learning for Image Recognition," *arXiv:1512.03385v1*, 2015.

[4] A. Kendall and K. College, "PoseNet: A Convolutional Network for Real-Time 6-DOF Camera Relocalization," *Comput. Vis. Pattern Recognit.*, 2016.

Unsupervised Learning of Surgical Smoke Removal from Simulation

L. Chen[1], W. Tang[1], and N. W. John [2]

[1] *Department of Creative Technology, Bournemouth University*

[2] *School of Computer Science, University of Chester*

{*chenl, wtang*}*@bournemouth.ac.uk, nigel.john@chester.ac.uk*

INTRODUCTION

The surgical smoke produced during minimally invasive surgery can not only reduce the visibility of the surgeons, but also severally affect the performance of image processing algorithms used for image guided surgery such as image tracking, segmentation, detection and retrieval. Besides from physical smoke evacuation devices, many research works [3] [1] [4] [6] [7] address this issue by using vision-based methods to filter out the smoke and try to recover the clear images. More recently, end-to-end deep learning approaches [2] have been introduced to solve the dehazing and de-smoking problems. However, it is extremely difficult to collect large amounts of data for the effective learning of the implicit de-smoking function, especially for surgical scenes. In this paper, we propose a computational framework for unsupervised learning of smoke removal from rendering smoke on laparoscopic video. Compared to conventional image processing approaches, our proposed framework is able to remove local smoke and recover more realistic tissue colour but will not affect the areas without smoke. Although trained on synthetic images, the experimental results show that our network is able to effectively remove smoke on laparoscopic images with real surgical smoke.

MATERIALS AND METHODS

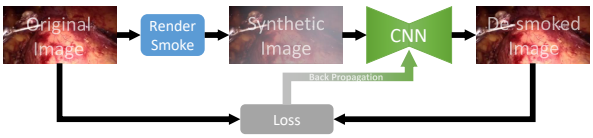

Fig. 1: Overview of our framework for unsupervised learning of smoke removal

With the recent development of Convolutional Neural Networks (CNNs), machines can solve many computer vision problems when provided with large-scale ground-truth data for supervised learning. However, the acquisition of ground truth is an expensive, time-consuming and labour-intensive task. Especially for surgical scenes, the amount of data and the accuracy of data must be satisfied to ensure acceptable results for clinical use. To address this issue, we proposed an unsupervised framework for learning smoke removal. As can be seen from Figure 1, our framework is composed of a render engine for synthesizing smoked images from laparoscopic videos and a CNN for the end-to-end training of de-smoking.

Fig. 2: The random smoke is rendered on the background of laparoscopic images to synthesize smoke image.

Smoke Synthesis

We use Blender [1] – an open source 3D creation software for the synthesis of smoke image for training. As shown in Figure 2, the real laparoscopic images from Hamlyn Centre Laparoscopic / Endoscopic Video Datasets [2] [8] are used as background images, and the smoke is rendered with randomly intensity, density and location on the background to simulate the real smoke. The variation of smoke render ensures that our network will not over-fitting to certain smoke intensity, density and location. With the help of powerful render engine, we are able to synthesize unlimited amount of realistic images with the presence of simulated surgical smoke. More importantly, this process is done automatically without any human intervention and cost.

End-to-end Learning of Smoke Removal

As smoke removal is a pixel-wise task, we adopt a fully convolutional encoder-decoder network to generate the same size de-smoked image with the input image. Since the smoke removal task needs to preserve most of the details from the input images, following the U-Net structure [5], skip connections are implemented for directly transferring high-level information to the bottom of the network to prevent the loss of high quality details.

[1] https://www.blender.org/

[2] http://hamlyn.doc.ic.ac.uk/vision/

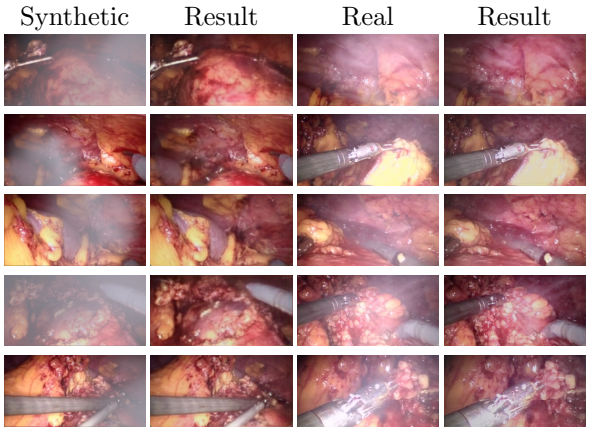

Fig. 3: The result for our smoke removal framework. Left: Synthetic smoke images and results; Right: Real surgical smoke images and results

The loss function for the network is the L1 error of original image and de-smoked image from synthesized smoke image.

$$L = \sum_{xy} |I_{original}(x,y) - I_{desmoked}(x,y)| \quad (1)$$

RESULTS

Our smoke removal network was implemented on Tensorflow platform and trained on a workstation with a single NVidia Titan X GPU. We used an *in-vivo* partial nephrectomy procedure dataset from Hamlyn Centre Laparoscopic / Endoscopic Video Datasets [8] that contains 20,000 stereo image pairs from 11 video sequences, in which 7,553 images without surgical smoke are manually picked as ground-truth dataset. We randomly rendered smoke on these 7,553 images to construct our training dataset. The images are scaled to 256x128 to accelerate training and inference. After training, our model only takes 12ms to remove smoke for a 256x128 image.
For testing, we run our trained network on laparoscopic images with real surgical smoke, the results are shown in Figure 3. The qualitative visual inspection of the results shows that our proposed framework can effectively remove real surgical smoke and recover correct tissue colours. The code used for data synthesis and training can be found at here [3].

DISCUSSION

In this work, we present a novel unsupervised deep learning framework for automatic surgical smoke removal during minimally invasive surgery. Our framework only needs laparoscopic images as input, and 3D render engine is used to randomly render smoke on these images to synthesize dataset for training. The preliminary results show that although our network is fully training on synthesize dataset, it has the ability to remove real surgical smoke during minimally invasive surgery at real-time speed. This solves the problem that deep learning need large amounts of hand-labelled ground truth for training, especially for medical datasets that profession knowledge is needed for labelling data. In future work, it is interesting to see whether training networks from synthetic dataset can be extended to many other tasks such as laparoscope tracking, surgical instruments detection and tissue/organ segmentation, which will overcome the shortage of medical ground-truth data and greatly benefit the deep learning technology to be used in surgical scenes.

[3]https://github.com/melights/cnn_desmoke

REFERENCES

[1] A. Baid, A. Kotwal, R. Bhalodia, S. N. Merchant, and S. P. Awate. Joint desmoking, specularity removal, and denoising of laparoscopy images via graphical models and bayesian inference. In *IEEE ISBI*, apr 2017.

[2] B. Cai, X. Xu, K. Jia, C. Qing, and D. Tao. DehazeNet: An end-to-end system for single image haze removal. *IEEE Transactions on Image Processing*, 25(11):5187–5198, nov 2016.

[3] A. Kotwal, R. Bhalodia, and S. P. Awate. Joint desmoking and denoising of laparoscopy images. In *IEEE ISBI*, apr 2016.

[4] X. Luo, A. J. McLeod, S. E. Pautler, C. M. Schlachta, and T. M. Peters. Vision-based surgical field defogging. *IEEE Transactions on Medical Imaging*, 36(10):2021–2030, oct 2017.

[5] O. Ronneberger, P. Fischer, and T. Brox. U-net: Convolutional networks for biomedical image segmentation. In *MICCAI*, 2015.

[6] K. Tchaka, V. M. Pawar, and D. Stoyanov. Chromaticity based smoke removal in endoscopic images. In *SPIE Medical Imaging*, feb 2017.

[7] C. Wang, F. Alaya Cheikh, M. Kaaniche, and O. J. Elle. A Smoke Removal Method for Laparoscopic Images. *ArXiv e-prints*, Mar. 2018.

[8] M. Ye, E. Johns, A. Handa, L. Zhang, P. Pratt, and G.-Z. Yang. Self-supervised siamese learning on stereo image pairs for depth estimation in robotic surgery. In *Hamlyn Symposium on Medical Robotics*, 2017.

Towards Concentric Tube Robots for Microsurgery: First Results in Eye-to-hand Visual Servoing

Vincent Modes*[1], Sontje Ihler*[2], Tobias Ortmaier[2], Arya Nabavi[3], Lüder A. Kahrs[2], and Jessica Burgner-Kahrs[1]

[1]*Laboratory for Continuum Robotics, Leibniz Universität Hannover*

[2]*Institute for Mechatronic Systems, Leibniz Universität Hannover*

[3]*International Neuroscience Institute, Hannover*

modes@lkr.uni-hannover.de, sontje.ihler@imes.uni-hannover.de

INTRODUCTION

Concentric tube continuum robots (CTCR) have high potential in robotic surgery. Due to the small size and high flexibility they can reach targets through small orifices along non-linear paths. Thus far, CTCR have been mainly considered for minimally invasive surgery through small incisions or natural orifices [1]. We see them particularly promising for microsurgical applications in multiple disciplines around the head, e.g. neurosurgey, otolaryngology, or phoniatrics. Our vision is an integrated setup of one or more CTCR integrated with a surgical microscope to assist the physician in tasks such as biopsy, targeted drug delivery, tissue manipulation, electrosurgery, or local imaging using US or OCT (see Fig. 1). This setup allows for semi-autonomous assistance functions to be carried out by the robot defined by the physician in the microscopic stereovision (e.g. biopsy location, cutting trajectory). As microscopic surgery requires high accuracy of the robot, the prevalently existing model-based control strategies are not suitable. This issue has recently been addressed with visual servoing with eye-in-hand configuration [2].

In this paper, we propose visual servoing of a CTCR (3 tubes, 6 DOF) using a position-based look-and-move approach employing an eye-to-hand configuration for microsurgical applications. We evaluate the achievable absolute accuracy and demonstrate feasibility in an ex-vivo study with a tissue sample.

MATERIALS AND METHODS

The experimental setup is illustrated in Fig. 2 (left). The CTCR consists of 3 precurved Nitinol tubes, all tubes can rotate and translate independently (tube parameters: outer diameter 1.16/1.78/2.18 mm, inner diameter 0.86/1.16/2.02 mm, straight length 435/275/150 mm, curved length 66/62/30 mm, curvature 7.3/3.4/3.0 m^{-1}). The setup includes a stereoscopic surgical microscope (Haag-Streit) with a 300 mm working distance. The stereo images are captured with two rgb-cameras (GigE uEye SE) at 30 Hz (600×600 px).

Fig. 1: Example of an integrated setup with a concentric tube robot and a surgical microscope.

Stereoscopic Vision We compute a dense depth map by stereo reconstruction [4]. The tissue surface is then reconstructed in Cartesian coordinates with known metrics relative to the camera base. We track the robot's tip in image space using a small blue sphere mounted to the tip (framewise blob detection by colour-based segmentation, morphological image operations, and computation of the blobs centroid) and we retrieve the location (lateral, depth) from the continuously updated depth map. To register the robot tip in the stereo-camera base a rigid transformation is calculated from four pre-defined tip positions determined in robot and camera base respectively. These positions span a plane which defines the microsurgical workspace of the CTCR, i.e. the region of interest. We report a fiducial registration error of 5.5 mm (registration) and a reprojection error of 0.362 px (stereo calibration).

Position-Based Closed Loop Control A task space closed-loop controller based on finite differential inverse kinematics is used to move the robot tip to the desired position. The forward kinematics uti-

*Both authors contributed equally to this work.

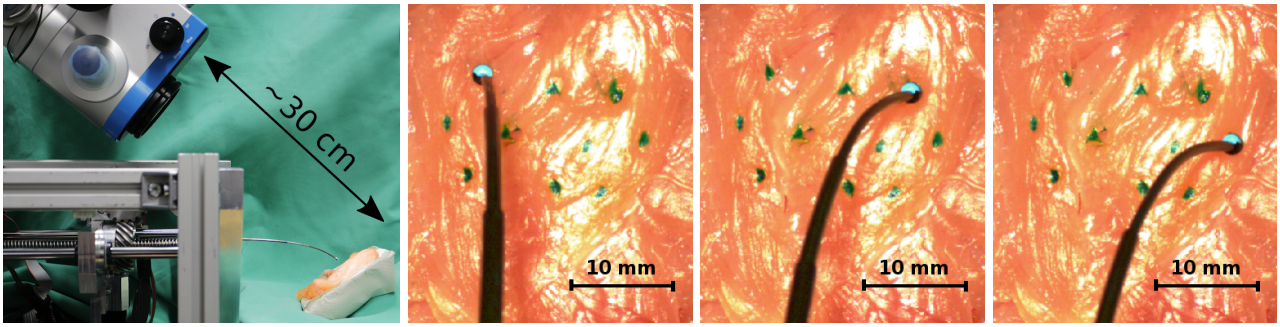

Fig. 2: Experimental setup (left). CTCR approaching three example target positions on ex-vivo tissue samples (microscopic view). Scale is given for working distance of 30 cm. Target positions are marked in green. All targets are reached with minimum accuracy of 0.2 mm

lizes Cosserat rod theory [3]. To avoid singularities a weighted damped least squared Jacobian is applied in the control algorithm. Target positions are defined in image space and then transformed to the CTCR task space to estimate the control deviation of the robot actuators. The tracked tip position is continuously fed back to the control loop at the same rate. The inner control loop has a cycle time of 12 ms and a control gain of 0.3 .

Experiment 1: Accuracy In order to determine the achievable accuracy, 25 target positions distributed equally in the workspace plane are commanded to the robot (see Fig. 3 (left)). Using stereoscopic vision we evaluate how accurate the robot can approach each grid position under closed-loop control in terms of Euclidean distances.

Experiment 2: Tissue Targeting To prove the feasibility of our setup, experiments on an ex-vivo tissue sample (chicken breast) are performed. By defining 10 target points in the camera image, the robot is commanded to approach each point from a predefined starting position as shown in Fig. 2. To reach a point, a two-step-strategy is implemented: At first, the robot moves to a pre-position approximately 5 mm above the tissue surface. Continuing from this position, it approaches the commanded point on the tissue surface. A point is considered as reached, if the Euclidean distance between the tracked robot tip and the target point is below 0.2 mm. All measurements are taken from the reconstructed depth map.

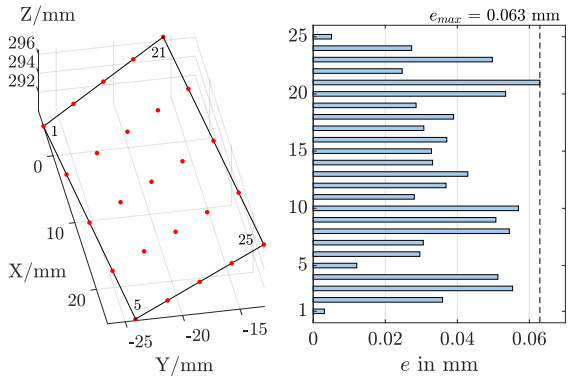

Fig. 3: 25 sampled points in the workspace plane in camera coordinates (left). Minimum Cartesian distance e between commanded target and tracked tip position (right).

RESULTS

For Experiment 1, all 25 grid positions are reached precisely with a maximum Euclidean error of 0.063 mm as shown in Fig. 3 (right). The error has been determined with the stereo vision system.

The tissue targeting experiments confirmed our promising previous results. After selecting a target position in the camera image, each position has been reached successfully without manual intervention. Fig. 2 shows three example scenes right after the control algorithm signaled the arrival at the target position.

DISCUSSION

A semi-autonomous robotic assistance is desirable for physicians in tasks which require accurate positioning in microsurgery as this is particularly challenging with manually operated surgical tools. The achievable submillimetre accuracy with our eye-to-hand CTCR setup is well suited for microsurgical applications. Thus far, our experiments considered the CTCR tip position. As the controller allows for consideration of poses, the next set of experiments will include the pose of tools at the CTCR tip to prove feasibility of different tasks such as electrosurgery, biopsy, or imaging. In future work, we will integrate our soft tissue tracking methods [4] such that targeting a moving target with the CTCR can be realized. Overall, this is the first study on the achievable accuracy of CTCR in microsurgical applications.

REFERENCES

[1] J. Burgner-Kahrs et al. Continuum Robots for Medical Applications: A Survey. *IEEE Transactions on Robotics*, 31(6):1261–1280, 2015.

[2] A. V. Kudryavtsev et al. Eye-in-hand visual servoing of concentric tube robots. *IEEE RA-L*, 3(3):2315–2321, 2018.

[3] D. C. Rucker et al. A geometrically exact model for externally loaded concentric-tube continuum robots. *IEEE T-RO*, 26(5):769–780, 2010.

[4] A. Schoob et al. Comparative study on surface reconstruction accuracy of stereo imaging devices for microsurgery. *IJCARS*, 11(1):145–156, 2016.

Fused MRI-ultrasound Augmented-Reality Guidance System For Robot-Assisted Laparoscopic Radical Prostatectomy

G. Samei[1], K. Tsang[1], J. Lobo[1], C. Kesch[2], S. Chang[3], P. Black[2], S. Salcudean[1]

[1]Robotics and Control Laboratory, UBC Vancouver, Canada,

[2]Vancouver Prostate Center, UBC Vancouver, Canada,

[3]Department of Radiology, UBC Vancouver, Canada,
sameig@ece.ubc.ca

INTRODUCTION

Radical prostatectomy (RP), or the surgical removal of the prostate gland, is a standard treatment for prostate cancer (PCa). RP requires a delicate trade-off between removing all the cancer, yet sparing critical structures. A major barrier to better RP outcomes is the inability of the surgeons to visualize PCa intra-operatively.

Transrectal ultrasound (TRUS) is a real-time and easily accessible method to image the prostate gland itself, but TRUS cannot image PCa accurately. MRI achieves the most accurate PCa imaging but cannot be used for RP with present techniques.

In this paper we describe a novel augmented reality (AR) guidance system that provides preoperative MR images, annotated with regions of high cancer probability, registered to intra-operative 3D ultrasound. The system also provides real-time 2D TRUS images of the prostate and peri-prostatic anatomy. We describe methods for displaying this information in a virtual 3D scene containing 3D models of the prostate, the surgical instrument, the TRUS probe and registered MR images. Prior work addressing the same problem [3] presented TRUS and MRI images but did not place these images in a 3D scene that facilitates navigation.

MATERIALS AND METHODS

Fig. 1 illustrates an overview of our system. It comprises: (i) the da Vinci (DV) surgical system (ii) a motorized TRUS probe, (iii) an Ephiphan Pearl™ to record the surgery and (iv) an external computer for MR-TRUS registration, DV-TRUS calibration, controlling the TRUS and rendering the 3D virtual scene. The transferred signals between units consist of parameters (lines in Fig. 1), images and videos (solid blue and double red lines in Fig. 1 respectively).

An ultrasound machine (BK Medical, Herlev, Denmark) with an 8848 4-12 MHz biplane transducer was used for imaging the prostate. Screenshots were captured at 43.07 Hz sampling rate and saved into the Epiphan through a DeckLink Quad 2 frame grabber card (Blackmagic Design, Port Melbourne, Australia).

The motorized TRUS is used for 3D TRUS volume acquisition, by rotating the probe over a 100 degree span about the probe axis with images acquired at

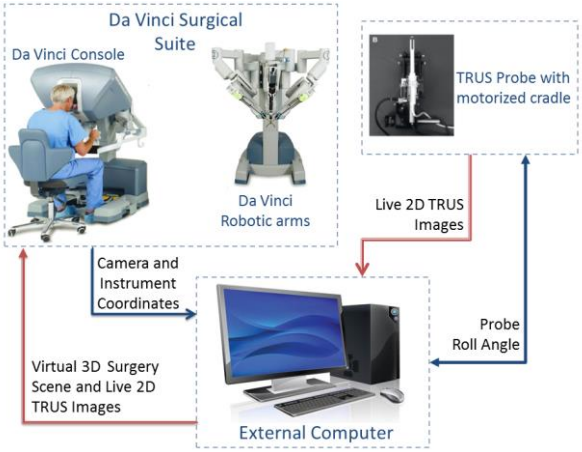

Fig. 1 An overview of the proposed AR system.

increments of 0.5 degrees. The TRUS is rotated automatically during the procedure to follow the current position of the instrument tip as described in [2].

The clinical flow is as follows. A T2-weighted MRI is acquired prior to the intervention. The prostate and the cancerous tissue are segmented by a clinician. A volumetric mesh is created for the prostate and neighbouring tissue in MRI, with a K matrix based on the average reported stiffness of the prostate [5].

The intra-operative prostate position and shape might differ from the pre-operatively acquired MRI which is usually acquired days or weeks before the surgery, with a patient in a different position and different bladder or rectum fill. Therefore, a 3D TRUS volume is acquired intra-operatively. The pre-operative MRI is then registered to this TRUS volume semi-automatically. To allow the clinician to locally modify and correct the results, we designed a real time interface where the MR and TRUS are displayed side by side. The clinician can apply a set of rigid (translation, rotation), affine (shrinking and expanding along three axes) transformations, followed by a deformable biomechanically constrained registration. The latter is applied by identifying pairs of corresponding points that are not aligned. The displacements between corresponding points on MR and TRUS are computed and are applied to the mesh nodes of its enclosing element. The K matrix is updated based on the new

boundary condition and the displacement of the rests of the nodes are computed.

During the surgery, the Application Programming Interface (API) [1] of the DV system,\ streams the 3D location of the instruments and the laparoscopic camera. The set point for the roll angle and the actual roll angle of the probe are also transmitted between the TRUS manipulator and the PC. Socket communication was established between the API, the controller software of the probe manipulator and the guidance software.

Fig. 2 displays two snap-shots of our image-guidance display during an actual surgery. The display consists of two sub-windows: the one on the left displays the 3D virtual surgery field and the one on the right shows live TRUS B-Mode images. The 3D virtual scene contains: (i) a 2D axial slice of the MR volume at the inferior-superior position of the DV instrument tip and projected on the clipped prostate model, (ii) a 3D model of the prostate updated based on the 3D TRUS sweep to match the prostate's most recent position and shape, (iii) A 2D plane placed at the same position as the actual TRUS image plane (green plane in Fig. 2) to help the surgeon locate the TRUS image in 3D relative to the other elements, and (iv) the 3D models of the TRUS probe and the DV surgical instrument (blue cone in Fig.2). All of the virtual elements (prostate, TRUS probe, surgical instrument and the laparoscopic camera) are registered to the DV coordinate system and have the same location as their real world counterparts. Hence, the virtual scene is a 3D reconstruction of the surgeon's surgical view. This scene is rendered from the viewpoint of the laparoscopic camera separately for the left and the right eye and the outputs are connected to the specific ports on the TilePro™ multi-input display of the DV console to give the surgeon a true 3D experience.

Since the TRUS image is registered to the preoperative MR volume, the surgical instrument itself is used as an intuitive and easy to use control device for the surgeon to manipulate both MR and TRUS images in real-time.

To display the deformed MRI in real-time and project it on the prostate mesh, we employ a deformed-volume image slicing strategy based on a reference volume and a mesh-based deformation model. We use the algorithm for fast synthesis of 2D slices in a deformed 3D volume presented in [4].

RESULTS

To date, five patients with clinically organ confined prostate cancer undergoing RALRP have participated in our institutional review board approved study. Our system was successfully employed in the OR without interfering with the normal course of surgery. The TRUS acquisition and registration to MR was done in under 2 minutes. The target registration error for 8 landmarks on 4 cases was 2.06±0.90mm. Given the DV-TRUS calibration error of 1.8mm [2] and the TRUS-MR registration error of 2.06mm, we expect the overall error (DV-MR registration) to be smaller than 4mm.

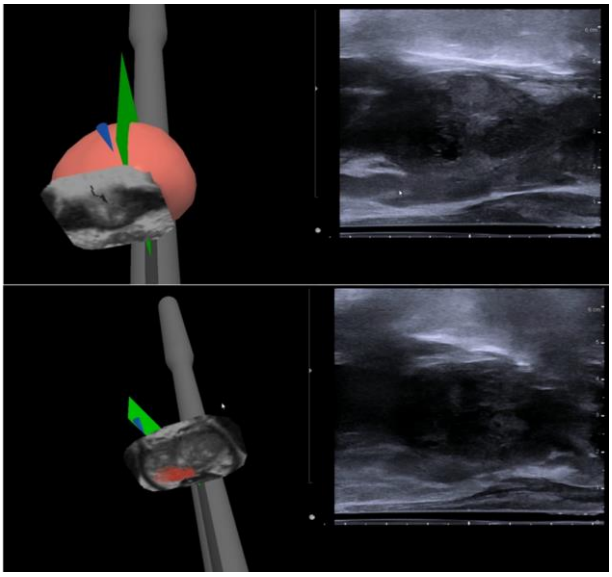

Fig. 2 Snapshots of our image-guidance display during an actual surgery consisting of the 3D virtual surgery scene (left) and the live TRUS Bmode image (right).

This is close to the mean error in our two phantom studies (3.06±1.05mm).

DISCUSSION

We believe that our system has the potential to improve the outcomes of RP by providing the surgeon with real-time, image-guidance tools that accurately show the prostate anatomy and the prostate cancer location, extension, and proximity to critical structures. Future work will incorporate our real-time non-rigid registration of 2D B-mode TRUS to MR [5] for continuous tracking and update to the prostate shape and MRI. This will provide more reliable guidance throughout the surgery in the presence of prostate motion and deformation.

REFERENCES

[1] D. S and H. C, “The da Vinci research interface,” MIDAS Journal - Systems and Architectures for Computer Assisted Interventions

[2] O. Mohareri, J. Ischia, P. C. Black, C. Schneider, J. Lobo, L. Goldenberg, and S. E. Salcudean, “Intraoperative registered transrectal ultrasound guidance for robot-assisted laparoscopic radical prostatectomy,” The Journal of urology, vol. 193, no. 1, pp. 302–312, 2015.

[3] O. Mohareri, G. Nir, J. Lobo, R. Savdie, P. Black, and S. Salcudean, “A system for MR-ultrasound guidance during robot-assisted laparoscopic radical prostatectomy,” in MIICAI 2015, pp. 497–504

[4] O. Goksel and S. E. Salcudean, “B-mode ultrasound image simulation in deformable 3-d medium,” in TMI vol. 28, no. 11, pp. 1657–1669, 2009.

[5] G. Samei, O. Goksel, J. Lobo, O. Mohareri, P. Black, R. Rohling, and S. Salcudean, 2018. Real-time FEM-based Registration of 3D to 2.5D Transrectal Ultrasound Images. IEEE Transactions on Medical Imaging

Visual-Kinematic Monocular SLAM using a Magnetic Endoscope

Samuel L. Charreyron[1], Quentin Boehler[1], Alexander J. Millane[2], and Bradley J. Nelson [1]

[1]*Multi Scale Robotics Lab, ETH Zurich*

[2]*Autonomous Systems Lab, ETH Zurich*

{*samuelch,qboehler,bnelson*}*@ethz.ch*

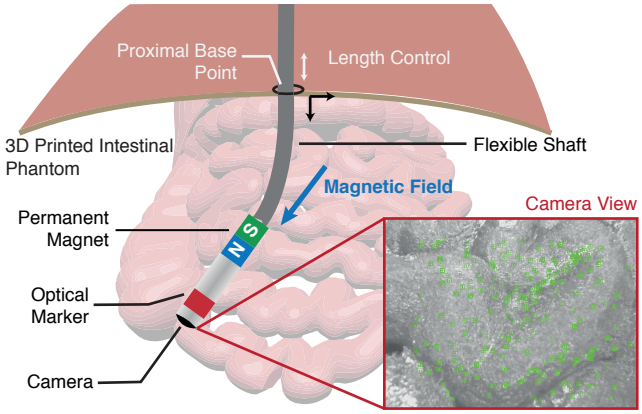

Fig. 1: Diagram of the magnetic laparoscope prototype used in this work. The inset shows an image capture of the observed phantom and the green squares correspond to the tracked image features used for localization.

INTRODUCTION

Visual Simultaneous Localization and Mapping (v-SLAM) is an active field of robotics research concerning the localization of camera-equipped mobile robots, while simultaneously building 3D maps of their environment. While most research has been focused on mobile robots, early applications to minimally invasive surgery date to the early 2000s [1]. In particular, a camera's pose could be tracked while moving it inside the human body during surgery, and 3D models of the observed anatomy could be reconstructed. Tracking the camera pose could be useful for augmented reality endoscopic surgery, where additional information such as preoperative scans could be overlaid on the surgeon's endoscopic view, or for generating rich visual data from the 3D reconstructions [2].

Monocular v-SLAM suffers from the notorious scale-ambiguity problem [3], and results may drift due to incremental positional errors, something which can not be detected unless the camera revisits a previous view and a loop is detected. In the case of robotic endoscopes, an estimate of the camera pose can be obtained using kinematics. Thas is to say, if the kinematics can accurately be modeled, the scale-accurate kinematics can be used to correct visual scale drift.

Earlier approaches to endoscopic SLAM [1] relied on extended Kalman filter (EKF) combined with image feature matching systems. Many such approaches used stereoscopic cameras to obtain depth information rather than the more prevalent monocular endoscopes. Nevertheless, the release of ORB-SLAM [3], a popular open-source monocular SLAM system, has spurred some recent interest in monocular endoscopic SLAM [4] with improved performance over previous EKF-based systems. Recently, a dense monocular v-SLAM system was demonstrated for a magnetically controlled gastrointestinal capsule endoscope and it was augmented with positional information from magnetic sensors, solving the scale-ambiguity problem in [5].

In this work, we adapt the existing ORB-SLAM feature-based system to be used with a flexible robotic endoscope that is magnetically actuated. By modelling the kinematics of the endoscope, camera localization is modified to penalize tracking results which are inconsistent with the endoscope kinematics. Using this kinematic prior, we can correct for monocular scale drift, and are able to obtain metric results due to the removal of scale-ambiguity.

MATERIALS AND METHODS

The magnetic endoscope used in this work consists of a miniature high-definition camera MD-B20904L-76 (Misumi, Taiwan), with a flexible silicon rubber shaft. An axially-magnetized Nd-Fe-B magnet sits behind the camera at the distal end of the endoscope. The maximum outer diameter of the endoscope is 8 mm. A diagram of the endoscope in Fig. 1.

We model the magnetic endoscope as a one-dimensional magnetic continuum consisting of - from proximal to distal ends - a uniform flexible segment of variable length which can be inserted and retracted, and a rigid segment that constitutes the magnet and camera. The proximal pose of the tube is assumed to be fixed.

The endoscope is manipulated by applying magnetic fields using a magnetic manipulation system (MMS), which induces torques on the magnetic segment of the endoscope, and cause the tip to align in the direction of the applied field. The kinematics of the endoscope are obtained by solving a Cosserat rod problem depending on the applied magnetic field and insertion length [6]. Unknown parameters of the en-

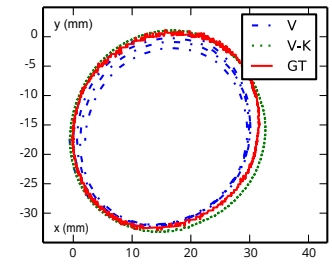

(a) Circle trajectory

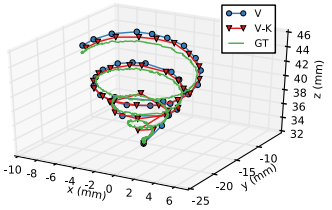

(b) Spiral trajectory

Fig. 2: Endoscope camera trajectories comparing visual only (V) and visual-kinematic (V-K) SLAM with the ground truth (GT) for a movement tracing a repeated circle (left) and an upwards spiral (right).

doscope including the bending stiffness of the flexible segment were identified from data using non linear least-squares fitting of the Cosserat rod.

In short, ORB-SLAM extracts image keypoints in each frame, and jointly optimizes camera poses and triangulated landmark positions corresponding to matched keypoints by a process called bundle adjustment (BA). Kinematic information was integrated by associating camera poses with kinematic poses, and adding a regularization term to BA which penalized camera poses deviating from the kinematic model. The poses from the kinematics and the tracked visual poses are related by a similarity transform which was estimated during the first few frames of a trajectory using the method of Horn [7]. Each experiment was run once using visual-only information, and using visual and kinematic information for comparison.

RESULTS

Evaluation of our system was performed on a scaled 3D phantom representing a human intestine. The anatomical data was obtained from the BodyParts3D database (The Database Center for Life Science). The endoscope was moved over the phantom surface using two predefined trajectories, a circular trajectory and a spiral trajectory. The position of a visible marker on the endoscope was tracked using a calibrated stereo camera rig and was used as ground truth (GT) information in our experiments. The visual-only trajectories were scale-aligned for comparison by using the similarity transform computed in the initialization phase of the visual-kinematic variant. Because the marker does not coincide with the camera origin and does not provide full pose information, the marker positions were transformed by an offset rigid transformation that was computed such that it minimized the average sum of square distance between the marker positions and the predicted camera center from the kinematic model.

In order to make the effect of scale-drift more apparent, we disabled ORB-SLAM's loop closure in our experiments. In the circle experiment of Fig. 2a, the circle was repeated four times. The position RMSE to the ground truth was 1.28 mm for visual-only and 0.82 mm for visual-kinematic SLAM. For the spiral trajectory of Fig. 2b, it was 0.78 mm and 0.60 mm respectively.

DISCUSSION

By combining SLAM with the endoscope's kinematics, we are able to obtain results that are correctly scaled, without using a stereo endoscope. Additionally, we showed that the kinematics can be used to correct drifting results, provided a long enough trajectory. This can be seen in Fig. 2a, as without the loop closure, the trajectories drift in the visual-only case, while remain on track for visual-kinematic. The improvement for the spiral trajectory is less pronounced due to the increased covisibility between frames, resulting in less drift.

ACKNOWLEDGEMENTS

This work was partially funded by the Swiss National Fund grant 200021_165564.

REFERENCES

[1] P. Mountney, et. al, Simultaneous Stereoscope Localization and Soft-Tissue Mapping for Minimal Invasive Surgery, in Medical Image Computing and Computer-Assisted Intervention MICCAI 2006, vol. 9, no. Pt 1, 2006, pp. 347354.

[2] B. Lin, et. al, Video-based 3D reconstruction, laparoscope localization and deformation recovery for abdominal minimally invasive surgery: a survey, Int. J. Med. Rob. Comput. Assisted Surgery, vol. 12, no. 2. pp. 158178, 01-Jun-2016.

[3] R. Mur-Artal, et. al, ORB-SLAM: A Versatile and Accurate Monocular SLAM System, IEEE Trans. Robot., 2015.

[4] N. Mahmoud, et. al, ORBSLAM-based endoscope tracking and 3d reconstruction, in Lecture Notes in Comput. Sci., 2017, vol. 10170 LNCS, pp. 7283.

[5] M. Turan, et. al, A deep learning based fusion of RGB camera information and magnetic localization information for endoscopic capsule robots, Int. J. Intell. Robot. Appl., pp. 19, Nov. 2017.

[6] J. Edelmann, et. al, Magnetic control of continuum devices, Int. J. Rob. Res., vol. 36, no. 1, pp. 6885, 2017.

[7] B. K. P. Horn, Closed-form solution of absolute orientation using unit quaternions, J. Opt. Soc. Am. A, vol. 4, no. 4, p. 629, 1987.

Validation of Kinematic Registry and MRI Compatibility for Pediatric Surgical Robot with Modular Tooling for Bone Biopsy

Alexander N. Alvara[1,2], Thomas Looi[1], Rami Saab[1], Amanda Shorter[1], Andrew Goldenberg[2], James Drake[1]

The Hospital for Sick Children, CIGITI Lab[1], Engineering Services Inc[2].

aalvara@uci.edu

I. INTRODUCTION

The current technique of performing MR-guided bone biopsy involves an interrupted process of placing the needle in a predetermined position (based on pre-operative MRI), scanning the patient and re-positioning the needle to ensure correct trajectory to the target. In addition, unlike soft-tissue biopsy, a relatively high constant force must be applied to biopsy the bone for sampling. With the current technique, it is challenging for the radiologist to simultaneously scan the area to verify the target and perform the biopsy. Thus, the Pediatric Surgery Robot with Bone Biopsy Tooling (PSR-BBT), seen in **Fig.1**, is designed as an MR-guided bone biopsy robotic system that can allow simultaneous imaging and sampling. The system provides stability, accuracy, sufficient force, and reduction of overall procedure time.

The workflow for bone aspiration and biopsy is a six-step process that can take 20-60 minutes. This technique is an important tool for the early detection of cancer, as well as hematological (blood related) malignancies and nonmalignant diseases. For pediatric patients, bone tumors account for 6% of all cancers, typically occurring between the ages of 10-20 [1]. Currently, inspection of bone marrow is considered one of the most valuable diagnostic tools for evaluating hematologic disorders, such as chronic lymphocytic leukemia, Hodgkin and non-Hodgkin lymphoma, hairy cell leukemia, myeloproliferative disorders, and myelodyspladtic syndrome [2].

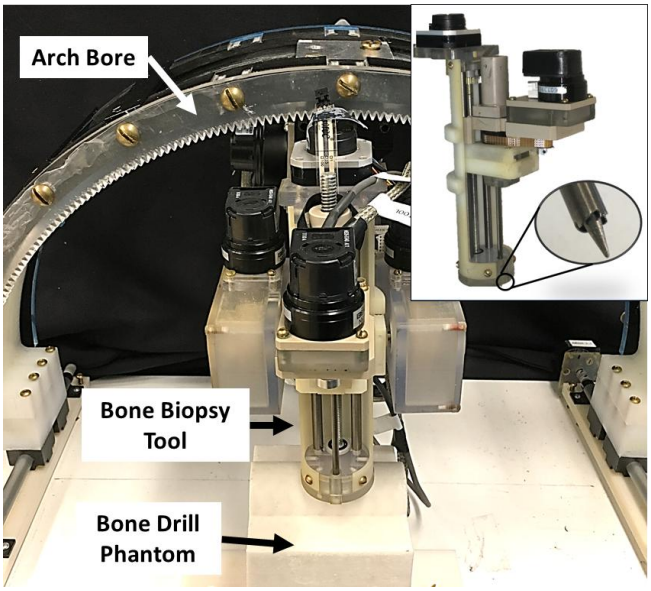

Figure 1. Pediatric Surgery Robot with Bone Biopsy Tool module showing test set up for phantom bone drilling test. Inset shows BBT module with a zoomed in view of the tissue stylet and hollow serrated drill tip.

Groups have studied and characterized bone drilling forces [3] but there has not been any development to create a closed-loop MR-guided robotic system that is designed for bone biopsy. The configuration currently under study aims to validate the use of the MR-compatible modular robot for higher load applications such as bone biopsy. This paper describes the design, development, and validation of PSR-BBT for performing MR-guided bone biopsy.

II. DESIGN CONSIDERATIONS

The PSR-BBT is an upgraded version of PSR [4] which includes the addition of a pseudo-linear rotational motion module that allows for rotation around the perimeter of the arch for greater mobility and access. PSR-BBT is the second iteration of the system and has been changed to offer greater rigidity and increased workspace, allowing for both larger and smaller patients. Given the clinical target and MRI constraints, the following requirements are specified:

A. MR Compatibility: A critical requirement is that both the PSR and BBT are non-magnetic, or negligibly magnetic. This also means that they neither significantly affect imaging quality nor should any of the MRI scanning protocols integral to a Philips Achieva 3.0T MRI significantly affect the robotic actuation that is required for any part of the biopsy process.

B. Workspace and Accuracy: As an image-guided system, the PSR-BBT must be able to detect the position of the patient, region of interest (ROI), and itself relative to these positions. Additionally, the PSR-BBT must retain the ability to reliably reach target points and entry points within the ROI, plan a path, and orient and position itself relative to the path, throughout the biopsy process with high accuracy and reliable control.

III. RESULTS

A. MR Compatibility: The phantoms used were the Philips QA fluid grid phantom for Geometric Distortion (GD) and a 1L cylindrical container of copper sulfate ($CuSO_4$, 2.5 g/L) solution for Uniformity and SNR

1) Geometric Distortion: The GD was evaluated by using ImageJ to map the centroid of the pillars on the Philips phantom**.** The GD data was taken under the coronal viewing plane, with a Field of View (FOV) of 256 mm, a slice thickness of 1 mm, and a pixel bandwidth of 777 Hz/pixel. A maximum geometric distortion of 0.55% was recorded (NEMA Standards MS 2-2008).

2) Signal-to-Noise Ratio: Signal to Noise Ratio (SNR) was used to quantify the image quality and define the degree to which the PSR affects the imaging. MR imaging was shown to not be significantly affected by the PSR in either scenario. The recorded SNR values show a maximum

32.61% SNR drop. The MRI scans can be seen in **Fig. 2**.

3) Visual Inspection: The effect of MRI scans on the PSR-BBT's performance was verified visually by observing encoder values, joint motion, drilling motions, and positioning. None of the MRI test scans resulted in any significant changes in encoder values, joint positions, or drilling capabilities from normal operation in free space.

B. Workspace and Accuracy: To verify the experimental workspace and positional accuracy of the PSR-BBT, we used the NDI Aurora magnetic tracker and 5DOF sensor to accumulate position, as well as orientation data.

1) Experimental Workspace Validation: The experimental workspace was constructed using random joint acquisition (to simulate positioning around a target) and spans all joints except for the bore rotation and the base linear motions. The reachable workspace spanned offers a viable drilling volume of 4602cm^3. Here the joint values were randomly selected to span 90% of their capable angular range and combinations of the angular motion produced tip position (black circles) and tip orientation (black vectors) data as shown in **Fig.3**. Each black vector represents the drill length and therefore also represents capable drilling volume.

2) Free-Space Accuracy Tests: Accuracy was evaluated by repeatedly articulating to specified points within the ROI (highlighted in yellow) in **Fig. 3**. Free-space tests show that for the 5 test points, there was an RMS accuracy of 1.65 +/- 1.77 mm.

IV. Discussion

SNR drop was most prevalent (-32.61%) in the case of drilling under T2-FFE scan, which is seen in **Fig. 2** as not showing any significant signal loss or irregularities in imaging as compared to baseline readings. GD was at its most extreme value at 0.55% under Baseline (No Robot) T2-FFE scan, which is likely due to possible movement of the test phantom while removing the robot. The geometric distortion for the most extreme functional case (with the PSR-BBT system present) occurred under Powered-On T1-SE scan at 0.45%. In either case, these results show negligible SNR loss and GD under these test conditions as verified by visually inspecting images for uniformity. Results from NDI Aurora verify a workspace volume of 4602 cm^3 and that tip position had an RMS accuracy of 1.65 +/- 1.77mm. Visual evaluation of independent joint tests and drilling in presence of MRI, under each test condition, showed no significant changes in operation. Other tests utilizing quantifiable positional accuracy measurements must be performed to verify exact errors in joint positioning under MRI.

The PSR-BBT shows that is possible to develop a MR-guided robotic system that is designed to perform bone biopsy where the system shows compatibility in a 3.0T MRI and generates sufficient forces to drill through bone [5]. However, additional work is required to verify the system performance under *in vivo* models where the live tissue will exhibit different physical properties for drilling and MR imaging. If the system can be verified with *in vivo* models, the PSR-BBT will have a positive impact to workflow and improve clinical outcomes.

REFERENCES

[1] Bone cancer stats (http:www.ped-onc.org/diseases). Acquired Feb 02, 2018 3:15 PM.

[2] N. Hata, J. Tokuda, S. Hurwitz, and S. Morikawa, "MRI-compatible manipulator with remote-center-of-motion control," J. Magn. Reson. Imaging, 2008.

[3] A. Islam, "Bone marrow aspiration before bone marrow core biopsy using the same bone marrow biopsy needle: A good or bad practice?," *J. Clin. Pathol.*, vol. 60, no. 2, pp, 2007.

[4] T. Looi, L. Ma, Y. Yi, A. Goldenberg, and J. Drake, "Paediatric Surgical Robot (PSR) – MRI guided bone biopsy system," , in Hamlyn Symposium on Medical Robotics, 2015

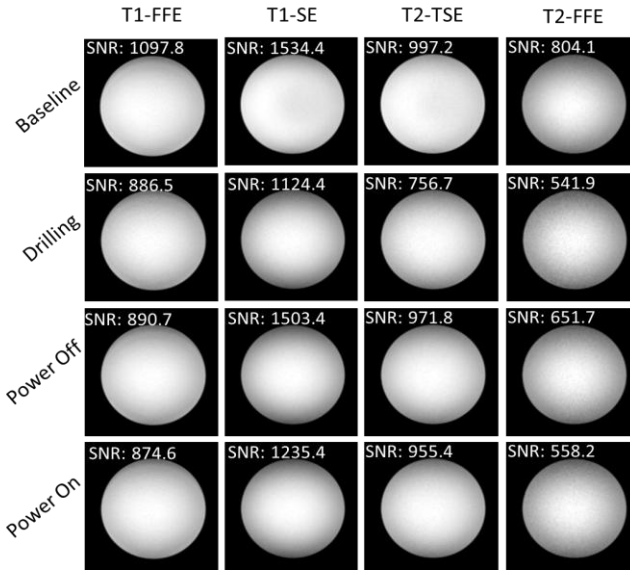

Figure 2. SNR images showing no significant qualitative uniformity change across tests, with SNR values for each image.

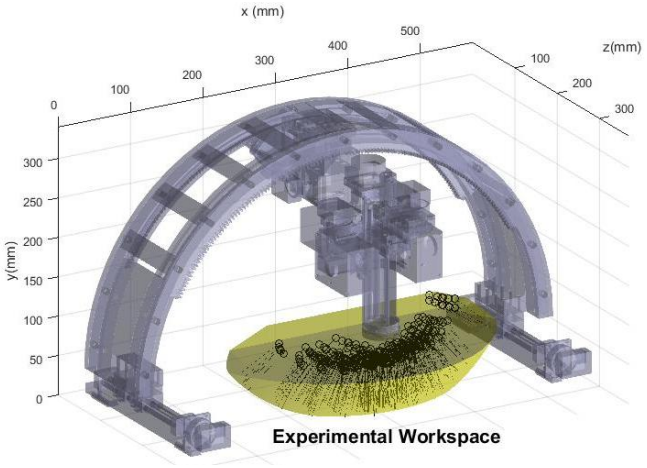

Figure 3. Size of the workspace relative to the PSR-BBT to scale. Theoretical workspace shown in yellow, and experimental joint space in black. Black circles indicate potential insertion points, and black vectors represent possible drill lengths for a given configuration

Sunram 5: An MR Safe Robotic System for Breast Biopsy

V. Groenhuis[1], F.J. Siepel[1], M.K. Welleweerd[1], J. Veltman[2], S. Stramigioli[1,3]

[1]Robotics and Mechatronics, University of Twente, The Netherlands
[2]Ziekenhuisgroep Twente, Almelo, The Netherlands
[3]ITMO, Saint Peterburg, Russia
v.groenhuis@utwente.nl

INTRODUCTION

The conventional MRI-guided breast biopsy procedure is inaccurate due to manual needle insertions and the necessity of rescanning. Therefore, the procedure would benefit from an MR safe robotic system to manipulate the needle precisely towards suspicious lesions under near-realtime MRI guidance. The main challenge is to design a system consisting of non-metallic, non-magnetic and non-conductive materials in order to eliminate safety hazards and imaging artifacts due to interference with the MRI's magnetic field.

Pneumatic stepper motors have been proved an effective actuation method in several state-of-art robotic systems[1, 2]. These systems are limited in bandwidth as 5 m long pneumatic tubes are needed between the valve manifold and the robotic system. This results in a stepper motor frequency of approximately 10 Hz when maximum force is necessary. The Stormram 4 needs approximately one minute to move from one position to another considering an axis of 640 steps. Higher velocities are desirable for practical applications[2].

Workspace is important for the breast biopsy robot: a suspicious lesion may be identified at the medial side or close to the chest wall. These locations are difficult to reach in state-of-art systems. Safety is also a concern: in case of emergency (including loss of pressure or mains power), the system should be able to eject the needle from the patient within one second.

This research aims to develop a new robotic system addressing the aforementioned challenges. The specific novelties are enhanced speed and accuracy, enlarged workspace and improved safety.

MATERIALS AND METHODS

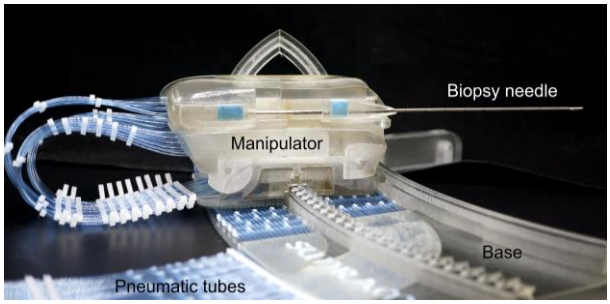

Fig. 1 Photo of Sunram 5.

The Sunram 5 robot is shown in Fig. 1. The five degree of freedom manipulator is actuated by six pneumatic stepper motors, measures 107 x 72 x 56 mm and has a mass of 260 g. Two of the motors have a relatively large step size of 1.7 mm, allowing for high-speed lateral and needle insertion movements. These motors are coupled with small-step motors (step size 0.3 mm) to maintain sub-millimeter accuracy in the same direction.

Each stepper motor consists of two or three pneumatic cylinders which alternatingly press against a straight or curved rack to make discrete steps[2]. Besides these six stepper motors three individual cylinders are also present to fire the biopsy gun and activate the needle ejection safety mechanism.

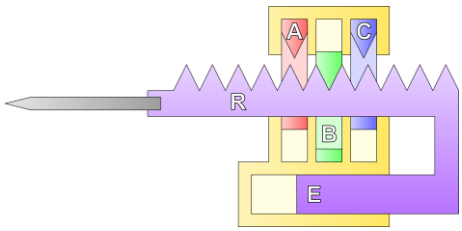

Fig. 2 Needle insertion actuator with safety ejection mechanism.

Fig. 2 shows a schematic of the three-cylinder needle insertion stepper motor with integrated safety ejection mechanism. In normal operation pistons A, B and C are alternatingly pushed down and up, nudging the rack (with needle) to the left or right in discrete steps. In case of emergency all three pistons A, B and C are lifted up and piston E is pushed to the right by a separate cylinder. As piston E is connected to the rack holding the needle, the needle is retracted out of the breast.

The robot is attached to a breast fixation system inspired by Machnet's device to immobilize the breast[3]. It can be manually positioned at a range of orientations relative to the breast allowing to adapt the compression direction and biopsy access window to the specific location of the lesion to be targeted. Fig. 3 shows a photograph of the entire system during the biopsy process.

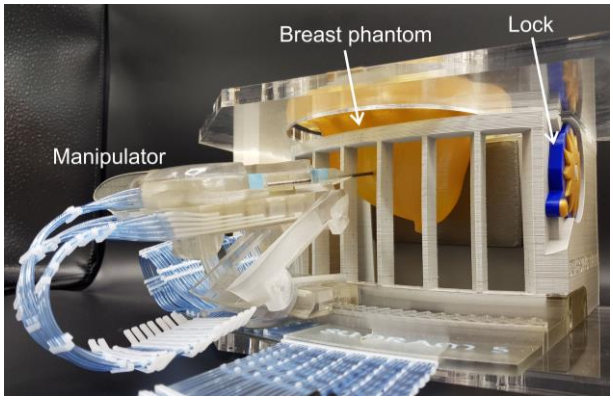

Fig. 2 Sunram 5 (left) targeting a breast phantom inside the fixation system (right).

The majority of the Sunram 5 parts was printed using a high-resolution polyjet printer. Acrylic rods support the hinges and laser-cut silicone rubber seals make the cylinders airtight. The removable 14G (2.1 mm) MR conditional titanium needle is the only metallic component of the system.

Three aspects of the robotic system were tested including speed/accuracy, workspace and safety. The highest manipulation time from one configuration to another is based on the range of motion of the different motors expressed as the number of steps, while the step sizes determine the theoretical positioning accuracy. The workspace was evaluated by estimating the volume percentile of the breast phantom which can be reached by the biopsy system, taking both the positioning freedom of the fixation system and the range of motion of the robot into account. The safety aspect was evaluated by first inserting a needle in the phantom to a depth of 50 mm and then activating the safety mechanism at pressures ranging from 0.1 to 0.4 MPa while recording the needle movement with a high-speed camera to measure the needle ejection time.

RESULTS

Speed and accuracy

The six stepper motors have a range of motion varying from 61 to 167 steps. At a stepping frequency of 10 Hz the upper bound of the manipulation time from one position to another is 16.7 seconds. When starting in a mid-way position and/or taking into account that two motors can work together in certain directions the effective maximum manipulation time is reduced to 8.4 seconds.

In the lateral and needle-insertion directions the small-step actuators yield a step size of 0.3 mm. In vertical direction two rotational joints have a step size of 0.3°, which translates to a 0.52 mm displacement at 100 mm from the rotation axis. Based on these step sizes, sub-millimeter accuracy can be achieved. Further enhanced accuracy is possible by coordinating movements of two motors: in collinear motor pairs, the smallest achievable step is 0.1 mm which is the greatest common divisor of its individual step sizes.

Workspace

The orientable fixation system significantly enhances workspace when the approximate location of the target lesion is already known. In combination with the high dexterity of the robotic system, any lesion that is situated below the fixation system's top surface is reachable by the robotic system.

Safety

A minimum pressure of 0.2 MPa is required to successfully activate the safety mechanism, ejecting the needle out of the phantom in 1.8 s. At 0.3 MPa, the time is reduced to 0.53 s, while at 0.4 MPa the needle is ejected in 0.31 s.

DISCUSSION

Pneumatic stepper motor technology has shown to be an effective actuation method for the Sunram 5. The six degrees of freedom combined with a versatile breast fixation system has potential to target lesions in the whole breast. Thanks to the dual-speed motors the manipulation time is under ten seconds, making it an order of magnitude faster than state-of-art robotic systems without compromising on accuracy. In case of emergency the safety mechanism is able to eject the needle out of the breast within one second at a pressure of 0.3 MPa or higher. A limitation might be that no direct position feedback is employed, so a calibration routine based on MRI or visual feedback may be necessary prior to the procedure.

The next steps in this research involve quantitative evaluation of targeting accuracy when performing biopsies in phantoms under MRI guidance. Needle-tissue interaction may contribute to deformations of the needle and/or the breast, potentially introducing localization errors which need to be assessed and mitigated. While the Sunram 5 has shown to be a major advancement over its predecessors, additional work is required concerning the placement of RF coils inside the breast fixation system and in sterilization of the device.

REFERENCES

[1] D. Stoianovici et al., "Multi-Imager Compatible, MR Safe, Remote Center of Motion Needle-Guide Robot," in IEEE Transactions on Biomedical Engineering, vol. 65, no. 1, pp. 165-177, Jan. 2018.

[2] V. Groenhuis et al., "Design and characterization of Stormram 4: An MRI-compatible robotic system for breast biopsy," 2017 IEEE/RSJ International Conference on Intelligent Robots and Systems (IROS), Vancouver, BC, 2017, pp. 928-933.

[3] J. Veltman et al., "Magnetic Resonance-Guided Biopsies and Localizations of the Breast: Initial Experiences Using an Open Breast Coil and Compatible Intervention Device," Investigative Radiology, 2005, vol. 40, no. 1, pp. 379-384

Pressure-sensitive Bio-compatible Skin Sleeve for Millimetre-Scale Flexible Instruments

P. Wasylczyk[1*], F. Ozimek[2], M. Tiwari[1,3], L. Da Cruz[1,4], C. Bergeles[1]
[1]*Wellcome/EPSRC Centre for Interventional and Surgical Sciences, UCL, UK*
[2]*Mullard Space Science Laboratory, UCL, UK*
[3]*Nanoengineered Systems Laboratory, UCL Mechanical Engineering, UCL, UK*
[4]*Moorfields Eye Hospital, UK*
**p.wasylczyk@ucl.ac.uk*

INTRODUCTION

During robot-assisted medical interventions robotic arms, tools and end effectors usually encounter contact forces from the surrounding tissues. While most procedures rely on images for guiding the tools, tactile feedback could provide valuable complementary information. Figure 1a shows an illustration of a 5 mm diameter flexible robotic arm, covered with a flexible skin comprising tens of tactile elements (tactels) functioning as pressure sensors. The tactels are connected via an array of electrodes that read out the external forces exerted on the robot on its way to the operating area inside the body. We have developed such flexible skin with piezoresistive pressure sensors, that may cover a robotic arm or other tools (such as endoscope probes) and provide continuous information on these reactive forces (Fig. 1b).

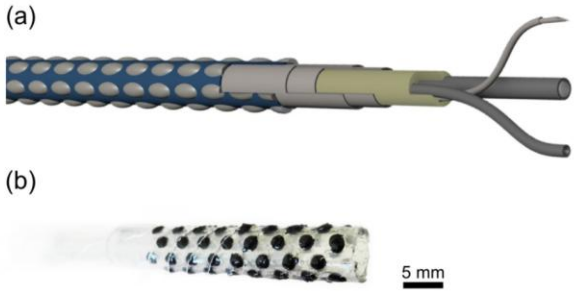

Fig. 1 Tubular pressure-sensitive soft sensor skin. (a) Illustration of a concentric tube soft robotic arm covered with a pressure sensor array. **(b)** Prototype sensor with 8×8 tactile pixel array and wire electrodes embedded in a soft silicone rubber carrier membrane; the outer diameter is 7 mm.

MATERIALS AND METHODS

Flexible pressure sensors use a grid of capacitance [1], piezoelectric [2] or piezoresistive [3] elements to measure the distribution of external forces. Piezoresistive sensors usually rely on arrays of tactels embedded on or within a soft carrier membrane. Most of the devices demonstrated to date have planar geometry and tens to hundreds of tactels on a millimetre-spaced grid. The tactels are most often made of a soft material (such as carbon-loaded silicone rubber) [4, 5] or micro-channels filled with eGaIn – a metal alloy that remains liquid at room (and body) temperature [6]. The membranes are typically made of soft silicone rubber or polyimide films with the electrodes in the form of printed paths (e.g. screen-printed with silver-loaded ink) or embedded metal wires. While eGain may offer sophisticated sensing geometries (such as measuring pressure and shear forces with the same tactel), it is unlikely to be approved for medical use inside the body. Silicone rubbers, on the contrary, are bio-compatible and, in combination with suitable carbon compounds, can be the material of choice for sensing elements in medical applications.

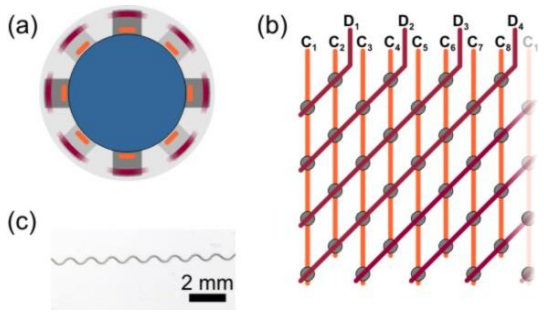

Fig. 2 Pressure-sensitive sensor design. (a) Cross section of a robot or instrument arm (blue) covered with the soft silicone membrane (light gray). Embedded in the membrane are tactile pixels (tactels, dark grey) and two layers of wire electrodes – bottom, column electrodes (orange) and top, diagonal ones (purple). **(b)** Electrode layout (shown on a plane) with 8 column ($C_{1\text{-}8}$) and four diagonal ($D_{1\text{-}4}$) electrodes. **(c)** Photograph of the undulating wire used for the electrodes.

Figure 2a presents the cross section of the sensitive skin sleeve on a cylindrical instrument. The 1 mm thick carrier membrane is cast in a two-part poly(methyl methacrylate) **(**PMMA) mould from soft silicone rubber (Gumosil AD-1, Silikony Polskie, 30°Sh A, 650% elongation at break) in the form of a tube – its 5 mm inner diameter matches the instrument size. The electrode array, with the layout sketched in Fig. 2b, is made of silver-plated copper wire (Scientific Wire Company, 0.1 mm diameter). As a straight wire mesh embedded in the silicone tube would significantly reduce the soft skin flexibility, the wire has been processed to make an undulating shape with 0.6 mm width and 0.8 mm period (Fig. 2c). This allows the electrode to follow the membrane expansion, as the

flexible instrument bends. Each of 32 tactels is a 1.4 mm cylinder made of carbon-loaded silicone (AD-1 with 10% w/w carbon black, Super P, Conductive, H30253, Alfa Aesar) with a bottom and top electrodes. The tactels are made by injecting the carbon-loaded silicone into cavities laser-milled in the silicone membrane. The resistance of an individual tactel measured between the bottom and top wire electrodes with no force applied is 0.5±0.1 kΩ.

The two-dimensional tactel array is read out with a set of column and diagonal electrodes [7, 8]. Eight column electrodes are addressed one by one in sequence via a multiplexer, and in every cycle the voltage on the four diagonal electrodes is measured. The multiplexer (MUX, DG509, Maxim) is driven with digital outputs of a USB DAQ card (USB-1608G, Measurement Computing) and the same card's four analog inputs sequentially read out the diagonal electrode potentials. As such electrode arrangement suffers from the crosstalk between tactels, a virtual ground technique with high-gain op-amps (TL084, Texas Instruments) [9] is used (Fig. 3a). Data acquisition, processing and visualisation is performed in LabView.

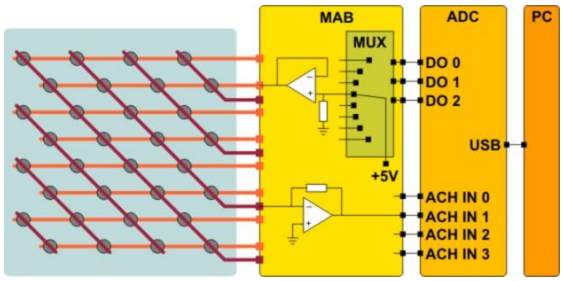

Fig. 3 Sensor array readout electronics. MAB - multiplexer and op-amp board, ADC – analog and digital I/O card, DO 0-2 – digital outputs, ACH IN 1-4 – analog inputs, PC - personal computer. For clarity only one addressing line (out of 8) and one readout channel (out of 4) are shown.

RESULTS

Figure 4a presents the normalized, background-subtracted response of a single tactel, measured with a digital balance. The useful pressure range extends to around 400 kPa (assuming uniform load onto the tactel area), above which the sensor saturates. Measured single tactel transient response to an impulsive load in Fig. 4b shows rise and fall times of around 50 ms. Figure 4c shows the 4×8 sensor array readout in the LabView front panel with 620 kPa pressure applied to one tactel.

DISCUSSION

A flexible, soft pressure sensing sleeve using only medical grade materials was designed, built and characterized. With similar technologies the sensor can be scaled down to cover 1-2 mm diameter tools and smaller with silicone 3D printing. The parameters to be optimised are the tactel diameter, thickness and material. Uniformity of the tactels within the sensor, tactel-electrode contact as well as the readout noise and signal processing are also to be further researched.

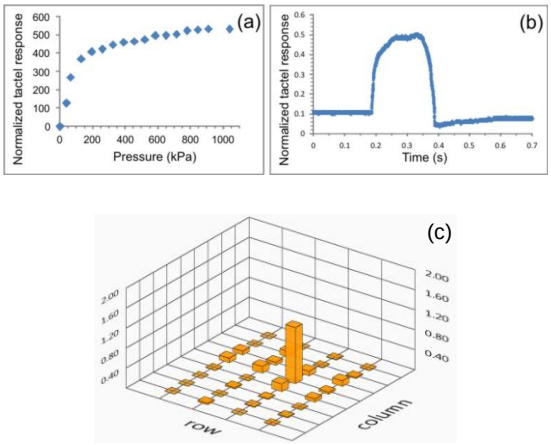

Fig. 4 Pressure sensor response. (a) Measured response of a single tactel to the applied pressure. **(b)** Measured transient response of a single tactel to an impulsive load. The horizontal scale spans 700 ms, the rise and fall times are around 50 ms. **(c)** Snapshot of the 4×8 sensor array readout with 620 kPa pressure applied one tactel (assuming even load distribution over the tactel area, with the background signal subtracted).

REFERENCES

[1] J.M. Engel, et al., Multi-layer embedment of conductive and non-conductive PDMS for all-elastomer MEMS, Proc. IEEE MEMS, 2006, pp. 246-250.

[2] M.A. Qasaimeh, S. Sokhanvar, J. Dargahi, M. Kahrizi, PVDF-Based Microfabricated Tactile Sensor for Minimally Invasive Surgery, Journal of Microelectromechanical Systems 18(1) (2009) 195-207.

[3] P. Alpuim, et al., Piezoresistive silicon thin film sensor array for biomedical applications, Thin Solid Films 519(14) (2011) 4574-4577.

[4] H. Mei, et al., A flexible pressure-sensitive array based on soft substrate, Sensors and Actuators A: Physical 222 (2015) 80-86.

[5] T.D. Nguyen, H.S. Han, H.-Y. Shin, C.T. Nguyen, H. Phung, H.V. Hoang, H.R. Choi, Highly sensitive flexible proximity tactile array sensor by using carbon micro coils, Sensors and Actuators A: Physical 266 (2017) 166-177.

[6] Patrick J. Codd, Arabagi Veaceslav, Andrew H. Gosline, Pierre E. Dupont, Novel pressure-sensing skin for detecting impending tissue damage during neuroendoscopy, Journal of Neurosurgery: Pediatrics 13(1) (2014) 114-121.

[7] R.S. Saxena, R.K. Bhan, A. Aggrawal, A new discrete circuit for readout of resistive sensor arrays, Sensors and Actuators A: Physical 149(1) (2009) 93-99.

[8] T. D'Alessio, Measurement errors in the scanning of piezoresistive sensors arrays, Sensors and Actuators A: Physical 72(1) (1999) 71-76.

[9] R.S. Saxena, R.K. Bhan, N.K. Saini, R. Muralidharan, Virtual Ground Technique for Crosstalk Suppression in Networked Resistive Sensors, IEEE Sens. J. 11(2) (2011) 432-433.

A Novel Cannula Brain Biopsy Device with Pressure Control

Minxin Ye[1,2], Danny T.M. Chan[1, 3] , Philip W.Y. Chiu[1,2] and Zheng Li[1, 2]

[1]*Department of Surgery, the Chinese University of Hong Kong (CUHK)*

[2]*Chow Yuk Ho Technology Centre for Innovative Medicine, CUHK*

[3] *Otto Wong Brain Tumor Centre, CUHK*

lizheng@cuhk.edu.hk

INTRODUCTION

Brain and central nervous system cancer is the 10th leading cause of death for both men and women and its five-year survival rate is around 35% [1]. To decide the best treatment for a brain tumor, oncologists need to know both the type and grade of the tumor. Stereotactic brain biopsy is the procedure for histological confirmation of brain tumors. During the procedure, neurosurgeons insert a biopsy cannula into the target region and acquire the brain tissue by manually applying an aspiration pressure with a syringe. By side cutting the tissue being sucked into the cannula, neurosurgeons obtain the biopsy yield.

The accuracy and safety of this procedure have been demonstrated by multi-institute studies. In these studies, the positive diagnostic yield ranges from 88.9% to 96.9%. The complication (mostly hemorrhage) rate ranges from 4% to 10% and the mortality rate is less than 1% [2-11]. The biopsy yield and complication are related to the lesion location, lesion histology and biopsy techniques [4, 8]. For the biopsy techniques, these include the selection of needle size and syringe size, as well as the control of the applied aspiration pressure. Jason et al from our group concluded that the 1.8-mm outer diameter needle carried a lower risk of postoperative hemorrhage than the 2.5-mm one [12], although it is reported that larger needles provide much more biopsy specimen than the thin needles [13]. In terms of the syringes, smaller syringe is recommended for better control and less pulling force during operating [13]. It is noted that in the literature there is few work on understanding the pressure required in the brain biopsy and no device that could help to control the aspiration pressure during the procedure. In this work, we developed a novel cannula brain biopsy device with pressure control to help understanding the desired pressure.

MATERIALS AND METHODS

In the current practice, during the brain biopsy, a cannula is connected to the syringe directly. The aspiration pressure during the biopsy is unknown. To measure this pressure, we integrate a pressure sensor (model: XGZP6847100(030)KPGN, range -30kPa ~ 0kPa, accuracy 0.3kPa) to the existing biopsy setup (BrainLAB brain biopsy cannula with 10mm side-window connected to a 2.5ml syringe). What's more, to accurately control the aspiration pressure, we use a stepper motor to drive the plunge of the syringe. The motion of the stepper motor is controlled using Arduino Nano, with feedback control. The syringe, cannula and the pressure sensing/control system are connected using a three-way valve. The design is shown in Fig. 1. To facilitate the operation, a LCD screen is designed to visualize the real-time pressure, and a set of buttons are designed to input the desired pressure. What's more, a software is programmed in Matlab® to record the pressure during the biopsy. The GUI of the software is shown in Fig. 2.

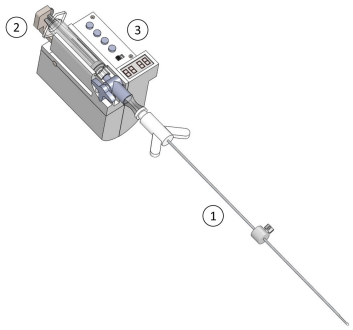

Fig. 1 The cannula brain biopsy device with pressure control: ① - cannula; ② - syringe; ③ - pressure sensing and control system.

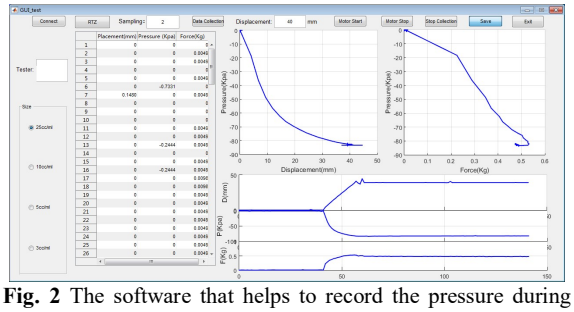

Fig. 2 The software that helps to record the pressure during the biopsy procedure.

The designed cannula biopsy device is prototyped and used to study the aspiration pressure during the brain biopsy as shown in Fig. 3. In the experiment setup, the fresh pig brain is used to mimic the human brain. The position of the cannula is fixed. An extension tube is used to connect the syringe and the cannula needle for easy operation. In the tests, we increase the pressure from 1 kPa to 20 kPa and measure the length of the biopsy yield. Each of the test is repeated for three times.

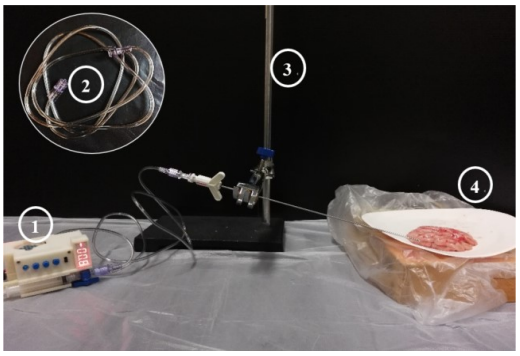

Fig. 3 Experimental setup: ① - the developed biopsy device with BrainLAB brain biopsy cannula; ② - extension tube; ③ - fixing stent; ④ - fresh pig brain.

RESULTS

The results of the obtained biopsy yield are shown in Fig. 4. The curve shows the length of the biopsy yield with respect to the applied pressure. The pictures below show the acquired biopsy yield of pressure from 1 kPa to 10 kPa. Results show that for fresh pig brain, the developed device could acquire the brain tissue even at small aspiration pressure. The length of the biopsy yield increase with the pressure nonlinearly. When the pressure is less then 5 kPa, the biopsy yield could not fully cover the side-window of the cannula. When the pressure reaches 10 kPa, the length of the biopsy yield is 11.22 mm, which fully covers the length of the side-window. If the pressure is further increased to 20 kPa, the length of the biopsy yield is 13.4 mm.

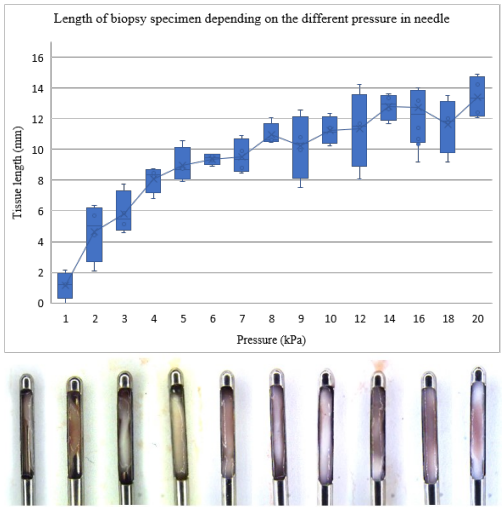

Fig. 4 Length of the biopsy yield w.r.t applied aspiration pressure, and the acquired brain tissue in the cannula needle (from left to right: 1kPa ~10kPa).

DISCUSSION

The aim of this work is to develop a device that could control the aspiration pressure during brain biopsy, therefore reducing complications and improving efficiency. Through the ex vivo trial with pig brain, we conclude that the volume of biopsy yield depends on the pressure being applied. If the adequate amount of biopsy yield is considered between 5 mm and 12 mm, then the recommended pressure is from 3 kPa to 12 kPa. Higher pressure would lead to excessive biopsy yield, which may leads to hemorrhage and damage to the surrounding neural structures due to overstretching. However, it should be noted that, the results are based on the ex vivo pig brain. The tissue biomechanics can differ significantly between ex vivo and in vivo condition, as well as between pig brain and human brain. Further study is needed to advance the proposed technique to in vivo human brain.

REFERENCES

[1] Brain tumor statistics, at: https://www.cancer.net/cancer-types/brain-tumor/statistics

[2] Lobato R D, Rivas J J, et al. Stereotactic biopsy of brain lesions visualized with computed tomography. Stereotactic and Functional Neurosurgery. 1982; 45(4-5): 426-430.

[3] Wild A M, Xuereb J H, et al. Computerized tomographic stereotaxy in the management of 200 consecutive intracranial mass lesions. Analysis of indications, benefits and outcome. British journal of neurosurgery. 1990; 4(5): 407-415.

[4] Sawin P D, Hitchon P W, et al. Computed imaging-assisted stereotactic brain biopsy: a risk analysis of 225 consecutive cases. Surgical neurology. 1998; 49(6): 640-649.

[5] Chandrasoma P T, Smith M M, et al. Stereotactic biopsy in the diagnosis of brain masses: comparison of results of biopsy and resected surgical specimen[J]. Neurosurgery. 1989; 24(2): 160-165.

[6] Lu Y, Yeung C, et al. Comparative Effectiveness of Frame-Based, Frameless, and Intraoperative Magnetic Resonance Imaging–Guided Brain Biopsy Techniques. World neurosurgery. 2015; 83(3): 261-268.

[7] Malone H, Yang J, et al. Complications following stereotactic needle biopsy of intracranial tumors. World neurosurgery. 2015; 84(4): 1084-1089

[8] Tsermoulas G, Mukerji N, et al. Factors affecting diagnostic yield in needle biopsy for brain lesions. British journal of neurosurgery. 2013; 27(2): 207-211.

[9] Woodworth G F, McGirt M J, et al. Frameless image-guided stereotactic brain biopsy procedure: diagnostic yield, surgical morbidity, and comparison with the frame-based technique. Journal of neurosurgery. 2006; 104(2): 233-237.

[10] Bekelis K, Radwan T A, et al. Frameless robotically targeted stereotactic brain biopsy: feasibility, diagnostic yield, and safety. Journal of neurosurgery. 2012; 116(5): 1002-1006.

[11] Chen C C, Hsu P W, et al. Stereotactic brain biopsy: Single center retrospective analysis of complications. Clinical neurology and neurosurgery. 2009; 111(10): 835-839.

[12] Yuen J, Zhu C X L, et al. A sequential comparison on the risk of haemorrhage with different sizes of biopsy needles for stereotactic brain biopsy. Stereotactic and functional neurosurgery. 2014; 92(3): 160-169.

[13] Haseler L J, Sibbitt R R, et al. Syringe and needle size, syringe type, vacuum generation, and needle control in aspiration procedures. Cardiovascular and interventional radiology. 2011; 34(3): 590-600.

Robot-Assisted Subretinal Surgery: initial *in-vivo* animal validation

J. Smits[1*], A. Gijbels[1*], K. Willekens[2,3], B. Stanzel[3,4], D. Reynaerts[1,5]

[1]*Dept. of Mechanical Engineering, KU Leuven - University of Leuven;*

[2]*Dept. of Ophthalmology, KU Leuven - University Hospitals Leuven;*

[3]*Knappschaft Eye Hospital, Sulzbach/Saar;*

[4]*Fraunhofer Institute for Biomedical Technology, Sulzbach/Saar;*

[5]*Member Flanders Make, Belgium*

jonas.smits@kuleuven.be; andy.gijbels@kuleuven.be; dominiek.reynaerts@kuleuven.be

INTRODUCTION

Vitreoretinal (VR) surgery is a branch within ophthalmologic microsurgery involving procedures targeting the eye's posterior segment. VR procedures are performed via small incisions created in the sclera, which are equipped with sealed trocars through which the required instruments are inserted. During the procedure, the surgeon views the surgical scene through a stereoscopic microscope placed above the patient's eye (Fig. 1, left).

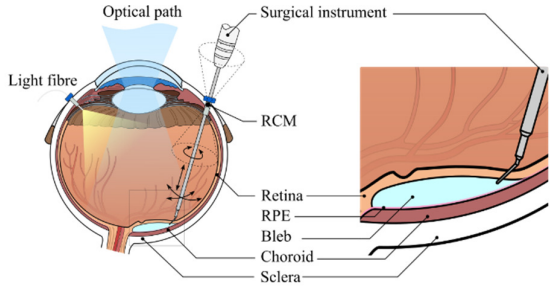

Fig. 1 (Left) A cross section image of a human eye, showing an annotated overview of a typical vitreoretinal surgical scene. (Right) A close-up view of the area of interest, providing a conceptual illustration of the first part of an RPE replacement procedure.

The retinal pigment epithelium (RPE) is a thin cellular layer between the retina and the choroid (Fig. 1, right). It plays a vital role in the good functioning of the retina, the photoreceptive organ that provides us with vision. RPE degeneration is the cause of several retinal diseases. One of these is Age-related Macular Degeneration (AMD). AMD is affecting nearly 200 million people worldwide, making it the leading cause of blindness in the developed world [1]. Patients diagnosed with AMD suffer from a local degeneration of the RPE layer at the fovea, leading to loss of central vision and eventually to non-reversible loss of photoreceptors. Currently, no curative treatment is clinically available.

A promising experimental treatment is RPE replacement therapy, using stem-cell based RPE grafts [2], [3]. During this procedure a small retinal detachment is created at the area of interest, referred to as a 'bleb', providing local access to the damaged RPE cells. The original cells are removed through scraping [4], after which the RPE graft containing new RPE cells is placed between the retina and the choroid [2]. Such a procedure is extremely demanding for even the most skilled surgeons, as it requires µm precision manipulation. Furthermore, the interaction with the fragile posterior anatomy of the eye imposes high risks, as it could cause vision-impairing damage to the retina.

It is believed that with the aid of surgical robotic technology, the required level of surgical skills and the overall risk of this type of procedures can be strongly reduced. This is key if these procedures are ever to be offered on a widespread basis. The presented in-vivo animal study provides an initial evaluation of the feasibility of using an eye-surgical robotic system during RPE replacement therapy.

MATERIALS AND METHODS

An updated version of the Leuven eye-surgical robotic system [5] was used, which has been previously demonstrated at the 2017 Hamlyn Surgical Robotics Challenge. It consists of two subsystems: the surgical system and the alignment system. The surgical system is used to perform the treatment inside the eye. It keeps the eye from rotating during the intervention, increases the surgeon's positioning precision more than tenfold, and is able to immobilize the instrument when required. The alignment system is used to preoperatively position the surgical system with respect to the patient.

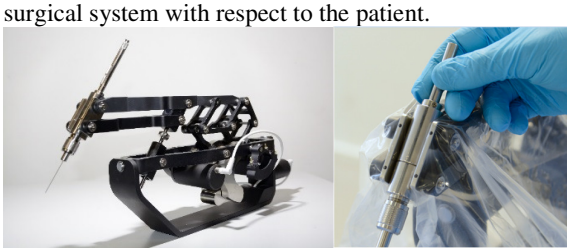

Fig. 2 (Left) The updated surgical system. (Right) A close-up view of the draped system, equipped with sterile tool holder.

Contrary to the stereotypical master-slave approach, perhaps most well-known from the Da Vinci system

*Jonas Smits and Andy Gijbels are designated as co-first authors

(Intuitive Surgical), the Leuven eye-surgical robotic system relies on a comanipulation approach. First introduced by Taylor et al. [6], this approach does not require an additional joystick, as it allows the surgeon to directly manipulate the surgical instrument. Key advantages here are a reduced complexity and cost, a more intuitive usage, keeping the surgeon in the vicinity of the surgical scene, and a smaller footprint in the OR. The interested reader is referred to [5], [7] for more information on Leuven eye-surgical robotic system. Both commercial 41G microneedles as well as custom produced 30 µm tip glass microneedles [8] were provided for the RPE replacement procedures. All procedures were performed in a sterile manner.

RESULTS

The performed animal study was approved by the Ethical Committee for Animal Research at Medanex Clinic, and performed in accordance with the applicable ethical standards of the institution. At the time of writing, three rabbits have been treated with the aid of the Leuven eye-surgical robotic system. In all three cases, surgeons were able to safely inject BSS in the subretinal space in order to create a localized bleb of the desired size. Injection times ranged from 15 s to 30 s, and were dosed manually using a 100 µL Hamilton syringe. Injection volumes ranged between 15 and 30 µl in order to create an adequately sized bleb.

Fig. 3 (Left) Dr. Willekens and (Right) Prof. Dr. Stanzel both using the surgical robotic system during in-vivo RPE replacement therapy on rabbits.

DISCUSSION

The performed animal study shows that it is technically feasible to safely and successfully perform a crucial step of RPE replacement therapy with the aid of a robotic comanipulation system. In all three instances, a precise injection in the subretinal space enabled the creation of a local retinal detachment, referred to as a ‘bleb’.

Future efforts will look at further integration of the surgical robotic system in the surgical workflow of RPE replacement therapy. Once concluded, the surgical outcomes of the performed animal study will be reported on in detail in a future publication.

ACKNOWLEDGEMENTS

This research is funded by an SB Fellowship of the Research Foundation Flanders (1S41517N), an Innovation Mandate of Flanders Innovation & Entrepreneurship (HBC.5016.0250), and KU Leuven. The *in-vivo* study is supported by BMBF ReSight (bvs), Fraunhofer Institute for biomedical engineering, and Knappschaft Eye Clinic Sulzbach. Furthermore, the authors would like to thank Geuder AG and D.O.R.C. for providing surgical equipment at no cost.

REFERENCES

[1] W. L. Wong, X. Su, X. Li, C. M. G. Cheung, R. Klein, C. Y. Cheng, and T. Y. Wong, “Global prevalence of age-related macular degeneration and disease burden projection for 2020 and 2040: A systematic review and meta-analysis,” *Lancet Glob. Heal.*, vol. 2, no. 2, pp. e106–e116, 2014.

[2] B. V Stanzel, Z. Liu, S. Somboonthanakij, W. Wongsawad, R. Brinken, N. Eter, B. Corneo, F. G. Holz, S. Temple, J. H. Stern, and T. A. Blenkinsop, “Human RPE Stem Cells Grown into Polarized RPE Monolayers on a Polyester Matrix Are Maintained after Grafting into Rabbit Subretinal Space,” *Stem Cell Reports*, vol. 2, no. 1, pp. 64–77, 2014.

[3] L. da Cruz, K. Fynes, O. Georgiadis, J. Kerby, Y. H. Luo, A. Ahmado, A. Vernon, J. T. Daniels, B. Nommiste, S. M. Hasan, S. B. Gooljar, A.-J. F. Carr, A. Vugler, C. M. Ramsden, M. Bictash, M. Fenster, J. Steer, T. Harbinson, A. Wilbrey, A. Tufail, G. Feng, M. Whitlock, A. G. Robson, G. E. Holder, M. S. Sagoo, P. T. Loudon, P. Whiting, and P. J. Coffey, “Phase 1 clinical study of an embryonic stem cell–derived retinal pigment epithelium patch in age-related macular degeneration,” *Nat. Biotechnol.*, no. March, pp. 1–5, Mar. 2018.

[4] F. Thieltges, Z. Liu, R. Brinken, N. Braun, W. Wongsawad, S. Somboonthanakij, M. Herwig, F. G. Holz, and B. V. Stanzel, “Localized RPE Removal with a Novel Instrument Aided by Viscoelastics in Rabbits,” *Transl. Vis. Sci. Technol.*, vol. 5, no. 3, p. 11, Jun. 2016.

[5] A. Gijbels, K. Willekens, L. Esteveny, P. Stalmans, D. Reynaerts, and E. B. Vander Poorten, “Towards a clinically applicable robotic assistance system for retinal vein cannulation,” in *6th IEEE International Conference on Biomedical Robotics and Biomechatronics (BioRob)*, 2016, pp. 284–291.

[6] R. Taylor, P. Jensen, L. Whitcomb, A. Barnes, D. Stoianovici, Z. Wang, and L. Kavoussi, “A Steady-Hand Robotic System for Microsurgical Augmentation,” *Int. J. Rob. Res.*, vol. 18, no. 12, pp. 1201–1210, 1999.

[7] A. Gijbels, J. Smits, L. Schoevaerdts, K. Willekens, E. B. Vander Poorten, P. Stalmans, and D. Reynaerts, “In-Human Robot-Assisted Retinal Vein Cannulation, a World First,” *Ann. Biomed. Eng.*, 2018 (accepted).

[8] K. Willekens, A. Gijbels, L. Schoevaerdts, L. Esteveny, T. Janssens, J. H. M. Feyen, C. Meers, D. Reynaerts, E. B. Vander Poorten, and P. Stalmans, “Robot-assisted retinal vein cannulation in an in vivo porcine retinal vein occlusion model,” *Acta Ophthalmol.*, vol. 95, no. 3, pp. 270–275, 2017.

A Modular Robotic Catheter Driver for Programmable Bevel-tip Steerable Needles

R. Secoli, E. Matheson, F. Rodriguez y Baena [1]
[1] *The Mechatronics in Medicine Laboratory, Imperial College, London, UK*
{email: f.rodriguez@imperial.ac.uk}

INTRODUCTION

Percutaneous intervention has attracted significant interest in Minimally Invasive Surgery (MIS) due to the better perceived clinical outcomes [7]. To achieve complex tool path trajectories, recent effort has been applied to the development of flexible needles [1, 6], which can successfully reach targets whilst avoiding critical areas of particular importance in neurosurgery. These needles often have complicated kinematics, and require suitable mechatronics systems for their control. Existing commercial neurosurgical robots for MIS neurosurgery, reviewed in [3],include the neuromate®, the ROSA® robot, and historical references, such as the PathFinder, the NeuRobot, the NeuroArm and the SurgiScope system. These robots can undertake a variety of neurosurgical procedures including instrument delivery, resection, and electrode implantation. However, there is currently no existing commercial solution for the delivery and control of programmable bevel-tip needles [5].
This paper presents the first modular robotic catheter driver of a 4-segment programmable bevel-tip needle (4-segment PBN). Details of the catheter design can be found in [2].

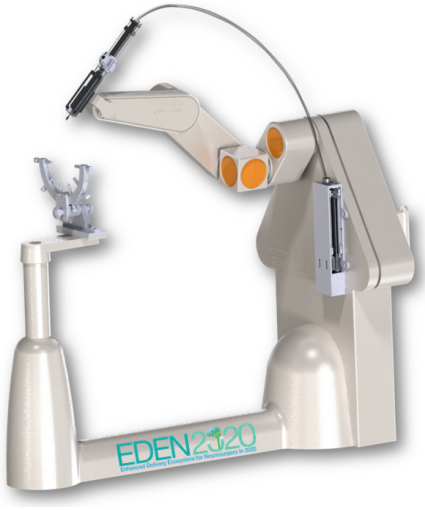

Fig. 1: EDEN2020 robotic system render: the robotic catheter driver is integrated within the hardware of the neuromate® (Renishaw Plc)

MATERIALS AND METHODS

The robotic catheter driver system will be integrated within the neuromate® robot (Renishaw Plc), as shown in Fig. 1), using a bespoke connection to the last link of the robot arm. The system consists of five sub-modules, as shown in Fig. 2: the neuromate® End-Effector, the Actuation box, the Flexible Transmission Link, the Control Box and the Joystick Controller. The surgeon will control the needle via a visual interface and haptic joystick controller. Control commands, as well as the power supply and regulation, will be managed by the Control Box, which embeds an industrial EtherCAT master controller. Power and signal cables connect the Control Box with the Actuation Box, which is physically located on top of the neuromate® in order to minimise the bending radius of the flexible transmission link. Inside the Actuation box are four high-precision motors, each equipped with a rotary magnetic encoder (1024cpr), that move carts on linear stages (1mm/rev) connected to the flexible transmission links. These nitinol wires in turn actuate push rods connected to the catheter, allowing for the movement of individual catheter segments, which produces the required offsets to accurately adjust both curvature plane and curvature magnitude at the needle tip [4].
The neuromate® End-Effector is composed of two

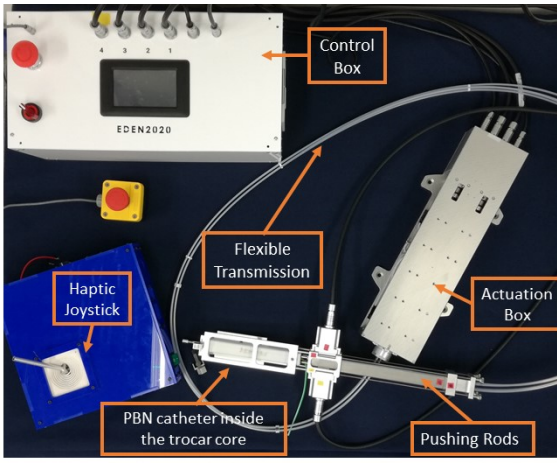

Fig. 2: Key components of the robotic catheter driver system

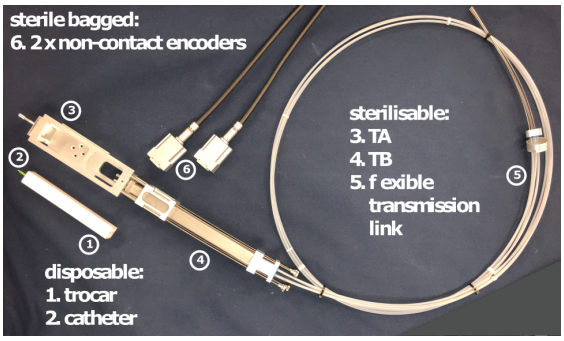

Fig. 3: Sterilisable components within the system

main parts; Trocar A (TA) that holds the disposable biocompatible trocar-core and catheter, and Trocar B (TB) that holds the push rods and connection to the flexible transmission links. Linear magnetic encoders measure the movement of the push rods (RLC2IC, $1\mu m$ resolution), ensuring that any backlash present in the system from the flexible transmission is accounted for by the controller. The mechanical design of all components has been optimised with sterility in mind, and the different types of sterilisation that will be employed in a clinical setting are summarised in Fig. 3. The components have been machined from aluminium 7070 for mass savings, or rapid prototyped or extruded from biocompatible resin (ABS30Mi) in the case of the disposable parts. The mechanical connections between the sub-modules have been designed such that a surgeon is able to connect the components within an operating theatre scenario.

RESULTS

In order to provide an accurate cyclic motion [2] during the insertion of the needle, an assessment of position accuracy was carried out. The robotic catheter driver performed position control, using the secondary magnetic encoders for position feedback and the motor encoders for velocity feedback. The flexible transmission was set in a single bending configuration in order to mock the system configuration as in Fig. 1. The following sequence of random target positions was reached by each actuator: 10mm, 70mm and 5mm, with three different velocities: 0.5mm/s, 1mm/s and 2mm/s. For each case, 3 trials were recorded, with a total of 9 trials for each actuator. The motion profile of each actuator (motor and push-rod position) was recorded by the real-time controller.

The average backlash introduced by the flexible transmission is shown in Fig. 4 as the difference between the motor-cart position and the push-rod position. Fig. 5 shows the error between the set position target and the push rod positions. The overall performance of the system, measured as the average positional error over all cases, was 0.009±0.025mm.

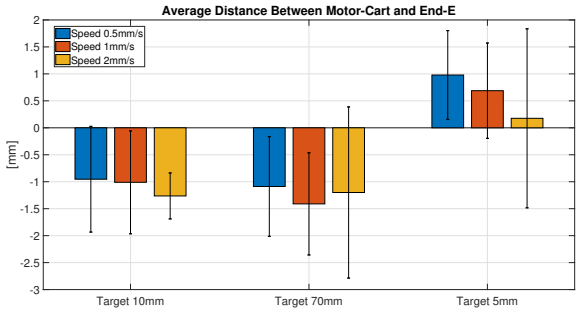

Fig. 4: Average backlash for the three set reference positions

DISCUSSION

A new pre-clinical robotic system to drive Programmable Bevel-tip Needles has been presented.

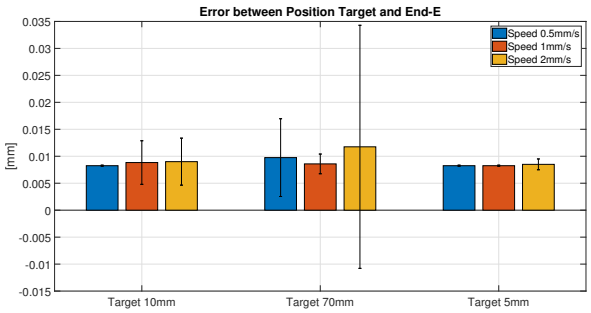

Fig. 5: Position error between the set references ($5mm$, $70mm$ and $10mm$) and the end-effector push rods for three different cruise speed profiles ($0.5mm/s$, $1mm/s$ and $2mm/s$)

The system has shown to achieve suitable low-level control accuracy for catheter positioning. Future work will concentrate on integrating the system with high-level controllers already demonstrated for this needle design [2, 5], and then sharing this control with the surgeon via an adaptive human-machine interface aided by the haptic joystick and visual interface.

ACKNOWLEDGMENTS

The research leading to these results has received funding from the European Union's EU Research and Innovation Programme Horizon under grant agreement No 688279.

REFERENCES

[1] J. A. Engh, G. Podnar, D. Kondziolka, and C. N. Riviere. Toward effective needle steering in brain tissue. In *2006 International Conference of the IEEE Engineering in Medicine and Biology Society*, pages 559–562, Aug 2006.

[2] E. Matheson, R. Secoli, C. Burrows, A. Leibinger, and F. Rodriguez y Baena. Cyclic motion control for programmable bevel-tip needles to reduce tissue deformation. *Journal of Medical Robotics Research*, 2018.

[3] T. A. Mattei, A. H. Rodriguez, D. Sambhara, and E. Mendel. Current state-of-the-art and future perspectives of robotic technology in neurosurgery. *Neurosurgical Review*, 37(3):357–366, Jul 2014.

[4] R. Secoli, F. Rodriguez, and Baena. Experimental validation of curvature tracking with a programmable bevel-tip steerable needle. In *2018 International Symposium on Medical Robotics (ISMR)*, pages 1–6, March 2018.

[5] R. Secoli and F. Rodriguez y Baena. Adaptive path-following control for bio-inspired steerable needles. In *2016 6th IEEE International Conference on Biomedical Robotics and Biomechatronics (BioRob)*, pages 87–93, June 2016.

[6] N. J. van de Berg, D. J. van Gerwen, J. Dankelman, and J. J. van den Dobbelsteen. Design choices in needle steering; a review. *IEEE/ASME Transactions on Mechatronics*, 20(5):2172–2183, Oct 2015.

[7] E. Westebring, P. van der Putten, R. H. M. Goossens, J. J. Jakimowicz, and J. Dankelman. Haptics in minimally invasive surgery - a review. *Minimally Invasive Therapy and Allied Technologies*, 17(1):3–16, 2008.

Versatile, Force Range-Adjustable, Tri-axial Force Sensor with Integrated Micro Camera for the Tip of Endoscopic Devices

I. Sušić[1], P. Cattin[2], A. Zam[3], G. Rauter[1]

{[1]BIROMED-Lab, [2]CIAN, [3]BLOG}, Dept. of Biomed. Engineering, University of Basel, CH

ivan.susic@unibas.ch

INTRODUCTION

A minimally invasive examination is a technique which allows medical doctors or surgeons to examine inner tissue of the human body using endoscopes. However, surgeons can only base their examination on visual observations of structures, colour, and shape of the tissue. But the sense of touch for palpation is partially or completely lost. To reestablish the sense of touch to the surgeons, we first aim to measure contact forces at the tip of the endoscope. Therefore, we developed a tri-axial force sensor (TFS) that can measure both normal and shear forces in terms of direction (positive and negative) and magnitude. Tactile data and a video stream can be simultaneously provided by integrating a camera in the tip of the TFS. During examinations, any injuries to the tissue can be prevented when predefined interaction force thresholds are not exceeded. In combination with precise position measurement of the endoscope and thus precise deformation measurement of the tissue, the TFS will enable the surgeon to determine elasticity properties of the tissue, e.g. to aid the differention of cancerous tissue from healthy by palpation [1].

To our knowledge, available Minimally Invasive Surgery (MIS) systems only integrate a camera at the tip or a TFS. For example, Puangmali et al. [2] reported a miniature TFS for MIS relying on an optical sensing scheme. This TFS is integrated in a laparoscope and measures forces within a force range (FR) of ±3 N in axial and ±1.5 N in radial direction with the resolution of 0.02 N. Li et al. [3] presented a TFS for MIS based on force sensitive resistors with a FR of 0÷8 N in both lateral (x, y) and longitudinal (z) direction. Nakadegawa et al. [1] presented a capacitor-based TFS for tumour tissue detection. However, to our knowledge, a TFS with an integrated camera has not been reported so far.

In this paper, we first present an Encapsulated Force-sensing Device (EFD) that houses a miniature TFS together with an integrated camera. The dimensions of the EFD (without thread for mounting) are 17 mm length and 10 mm diameter (see Figure 1). The EFD will be used to extend the force sensing capabilities of current endoscopes with regard to force range, simple mounting/dismounting, readjustment, and calibration. In particular, the range of the TFS can be readjusted for different applications, i.e. the force range can be shifted up or down. For recalibration after readjustment, we developed a setup based on the industrial force sensor Nano17 (ATI Industrial Automation, USA) (Figure 1b).

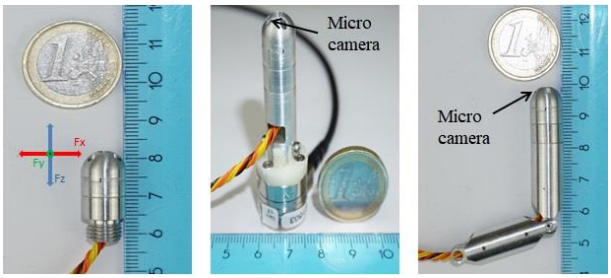

(a) (b) (c)

Fig. 1 The Encapsulated Force-sensing Device (EFD) houses a tri-axial force sensor and a micro camera. (a) shows the force sensor with the integrated camera and its possible directions of force measurement (both positive and negative directions are possible in all three axes). (b) shows the calibration setup where the endoscope tip is mounted on a Nano17 (ATI Industrial Automation, USA). (c) shows the integration of our device in a part of an articulated endoscope.

As a first application, we plan to install our EFD on the tip of an articulated endoscope (see Figure 1c).

MATERIALS AND METHODS

For the TFS implemented in the EFD, three commercially available Unidirectional Single Sensors (USSs) of type HSFPAR003A (ALPS ELECTRIC CO, Japan) were used. The main advantages of these sensors are their size ($2.0\times1.6\times0.66$ mm^3), price (4.53 CHF/piece), FR (0÷8 N), overload protection (up to 50 N), high-sensitivity (3.7 mV/N), and linearity (<3% over the entire force range). These properties allow the USSs to be used in a wide range of applications from industry to medicine. Our EFD comprises three of these sensors directly mounted on a Printed Circuit Board (PCB). To convert 3D forces that are externally applied to the EFD into normal forces for the three USSs, a mechanical Force Converting Structure (FCS) was designed. This FCS is suspended by a spring and mechanically redistributes 3D forces in form of normal forces to the sensors (Figures 2 and 3). The suspension of the FCS by a spring is the key element that allows adapting the force sensor's FR by adapting the spring's pretension with one Adaptation Screw (AS).

In detail, the force adaptation mechanics consists of the support for the lower spring (2), a conically-shaped head spring (3), a top spring (6), and an Adaptation Screw (AS) (11). By turning the AS, the support for the lower spring is moved towards or away from the FCS. Thus, the conically-shaped head spring and the top spring are compressed or released. In this way the

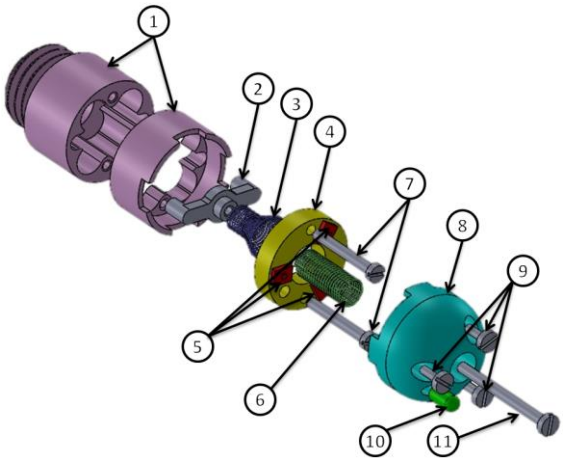

Fig. 2 Explode view of the Encapsulated Force-sensing Device (EFD). (1) Outer encapsulation, (2) support for the lower spring, (3) conically-shaped head spring, (4) Printed Circuit Board (PCB), (5) Unidirectional Single Sensors (USSs), (6) top spring, (7) fixation screws (M1×8 mm), (8) Force Converting Structure (FCS), (9) fine tuning screws (M0.8×4 mm), (10) camera, (11) Adaptation Screw (AS) (M1×16 mm).

preload and also the FR can be adjusted. In addition, the fine tuning-screws (9) placed in the FCS are used for fine adjustment of the preload for each USS. The fine-tuning screws must always be in contact with the force sensitive area of the USSs (see Figure 3a). The suspension of the FCS by the top spring (6) and the adaptation screw allow small rotations around the sensor's horizontal axes and a small translational movement in the vertical direction. All other motions and also large motions that damage the USSs are mechanically prohibited (see Figure 3a).

Testing of our TFS was carried out by comparing its output to the data obtained from a 6-axis force/torque sensor Nano17. Therefore, data of both sensors were measured by a hardware setup that uses TwinCAT3 (Beckhoff Automation GmbH & Co, Germany) as a real-time data acquisition platform at 1 kHz. Hereby, the Nano17 was connected to the Beckhoff system by the EtherCAT F/T Interface (ATI, USA) and the TFS data

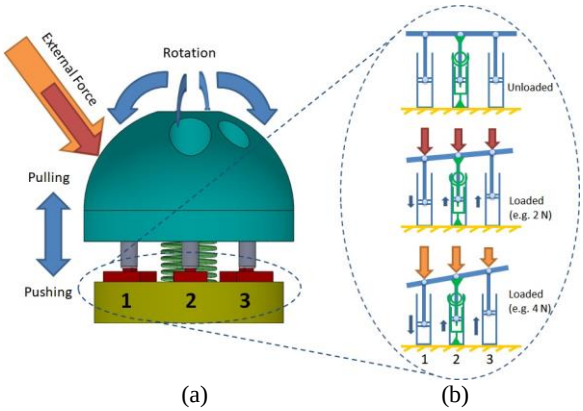

(a) (b)

Fig. 3 The working principle of the tri-axial sensor. (a) indicates the possible motion directions of the FCS. (b) depicts the working principle of the TFS and how an external force is redistributed to the USSs by the FCS. NOTICE: The USSs and spring are not in the same vertical plane.

was digitalized by EL3602 slaves (Beckhoff, Germany). For the experiment, the EFD was mounted on top of the Nano17 (see Figure 1b).

Two experiments were performed. Initially, a calibration was conducted to obtain the calibration matrix for the TFS based on standard pseudoinverse calculations between TFS and Nano17 data. Experiment 1: A measurement for comparing the resulting forces from our TFS (FR -4÷4 N) with Nano17 was performed. Forces were applied manually in three different directions (x, y, and z) for 40 seconds each, one after the other. Experiment 2: The TFS's force range was adapted (FR -5÷35 N) and the procedure of experiment 1 was repeated for a higher force range.

RESULTS

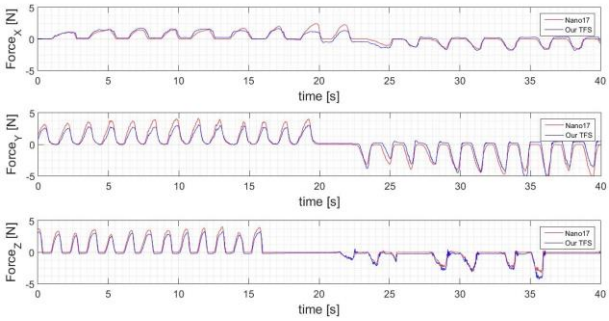

Fig. 4 Comparison of the resulting force signals from the Nano17 (red) and our TFS (blue) during Experiment 1.

Experiment 1 (FR -4÷4 N): Mean absolute error in x, y, and z-direction: 0.225 N, 0.405 N and 0.28 N.

Experiment 2 (FR -5÷35 N): Mean absolute error in x, y, and z-direction: 0.27 N, 0.20 N and 0.89 N.

DISCUSSION

In this paper, the design, working principle, integration, and successful testing of an Encapsulated Force-sensing Device (EFD) for endoscopes with an integrated camera was described. The force measurements of the TFS correspond well to those of Nano17 on a small force range (FR -4÷4 N) as well as on an adapted larger force range (FR -5÷35 N).

ACKNOWLEDGMENT

We gratefully acknowledge funding by the Werner Siemens Foundation through the MIRACLE project.

REFERENCES

[1] Nakadegawa, Takuro, et al. Three-axis scanning force sensor with liquid metal electrodes. Sensors and Actuators A: Physical, 264:260–267, 2017.

[2] Puangmali, Pinyo, et al. Miniature 3-axis distal force sensor for minimally invasive surgical palpation. Ieee/Asme Transactions On Mechatronics, 17(4):646–656, 2012.

[3] Li, Lu, et al. Development of an inexpensive tri-axial force sensor for minimally invasive surgery. In proceedings of the International Conference on Intelligent Robots and Systems. IEEE, 2017.

The variable stiffness catheter: third-generation magnetic catheters

C. Chautems[1], A. Tonazzini[2], Q. Boehler[1], S. Charreyron[1], A. Zemmar[3]
D. Floreano[2], B.J. Nelson[1]

[1]*Multi-Scale Robotics Lab, ETH Zurich*

[2]*Laboratory of Intelligent System, EPF Lausanne*

[3]*Hernesniemi Center, Henan Provincial People´s Hospital, Zhengzhou University*
chautemc@ethz.ch

INTRODUCTION

Remote magnetic navigation (RMN) of radiofrequency ablation catheters has been used to treat more than 100,000 cardiac arrhythmias. In RMN, an external magnetic field is used to deflect the magnetic tip of a catheter. RMN is claimed to be a safer alternative to manual catheter navigation by reducing the risk of heart wall perforation due to a softer magnetic catheter [1]. Additionally, RMN requires allows for reduced X-ray exposure to the patient and operating staff [2].

First generation magnetic catheters consisted of one tip magnet followed by a flexible segment. In the second generation, catheters were designed with three magnets separate by flexible segment [3]. A clinical study showed an increase in the procedure success rate from 67% for the one-magnet catheter to 92% for three-magnet catheters with four electrodes [4].

To improve the performance of the three-magnet magnetic catheter, we have designed a multi-segment magnetic catheter using a low melting point alloy that transforms from a solid to liquid phase upon joule heating. In the rigid state, the bending stiffness is sufficient to lock the shape of each segment individually [5]. In the soft state, the catheter has a similar bending stiffness as existing magnetic catheters. In this paper, we compare the achievable workspace between the first-generation catheters, the three-magnet second-generation, and the third-generation with variable stiffness (Fig. 1).

MATERIALS AND METHODS

During a magnetic ablation procedure, a sheath is inserted in the patient's groin through which instruments can be guided to the heart's right atrium. At the proximal end of the sheath, a mechanical advancer unit controls the catheter insertion length. The amount a catheter can deflect depends on its length, as a longer catheter is easier to deflect.

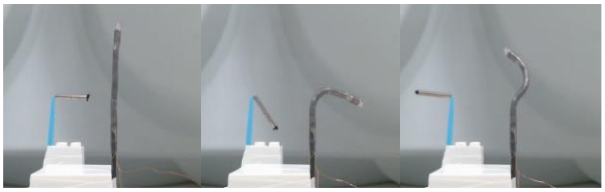

Fig. 1 Sequence illustrating variable stiffness catheter deflection in an external magnetic field: (right) catheter is rigid and the catheter does not deflect; (middle) the first segment is soft and is deflected; (right) the first segment is rigid and the second segment is soft and deflected.

The magnetic catheter is modeled as an Euler-Bernoulli beam assuming a constant curvature along the length of the device [6]. The direction of the magnetic field and orientation of the tip are expressed in spherical coordinates with the zenith direction collinear with the introducer sheath center axis. This coordinate system introduces rotational symmetry about the zenith axis. The magnetic field at a given location is defined by an inclination angle, an azimuthal angle, and a magnitude. The motion of the tip when changing one of the control parameters and keeping the other constant is represented in Fig. 2. A change in magnetic field magnitude results in a similar trajectory as for change in the inclination angle because the combination of both control inputs determine the catheter deflection. Only the maximal field magnitude is important as it determines the maximal catheter deflection.

The workspace can be computed by varying the full range of catheter insertion lengths and magnetic field inclination angles and is symmetric about the introducer insertion axis.

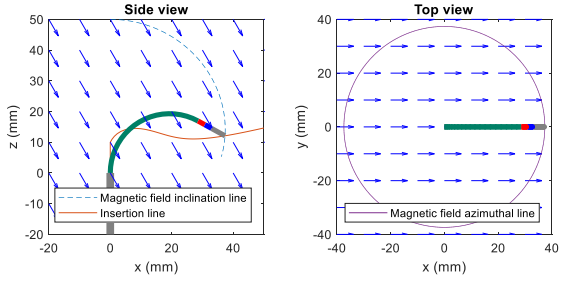

Fig. 2 Magnetic catheter kinematics: (left) the insertion line represents the motion of the catheter tip for changes of catheter insertion length, and the magnetic field inclination line represents motion for changes of the magnetic field inclination angle; (right) the magnetic field azimuthal line represents catheter tip motion for change of the magnetic field azimuthal angle.

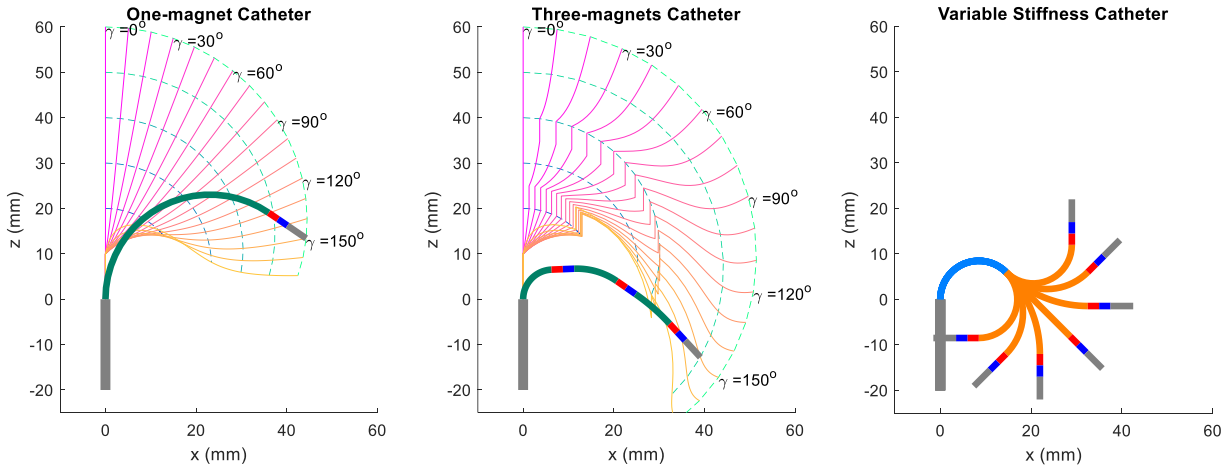

Fig. 3 Catheter workspace for the first-generation (left) and second-generation magnetic catheters (middle) with γ representing the magnetic field inclination angle (flexible segment in green, magnet in red-blue). A subset of catheter configurations for the third-generation magnetic catheter (right) with two variable stiffness segments (first segment in rigid state in blue and second segment in soft state in orange).

RESULTS

The workspace for one-magnet catheter and for three-magnet catheter is displayed in Fig. 3. Any position in the workspace is associated with a unique catheter configuration. Both catheters are unable to reach positions in the vicinity of the insertion sheath. For the three-magnet case, there are tip position discontinuities when smoothly varying the insertion as the rigid magnets exit the sheath. Such discontinuities make control more difficult due to jump discontinuities in the Jacobian.

An equivalent workspace plot for the variable stiffness catheter is infeasible due to the infinite number of catheter configurations. Each variable stiffness segment can take an infinite number of shapes and adds two degrees of freedom (DoF) to the entire catheter. With two variable stiffness segments, four DoFs are obtained, twice as many as for first-generation and second-generation magnetic catheters. Combining more variable stiffness segments increases the number of DoFs without increasing the outer diameter because only two small conductive wires are required to control the stiffness and the magnetic torque is applied wirelessly.

With a variable stiffness catheter, the configuration associated with a given tip position is not unique. For example S-shape configurations with two opposite bending radii can be obtained as well as configurations out of an azimuthal plan, both infeasible for existing magnetic catheters.

DISCUSSION

The third-generation of magnetic catheters expands the possibilities for magnetic navigation. Variable stiffness catheters can exhibit multiple bending radii and can form S-shapes, have increased stability in their rigid state, a small outer diameter, and provide a precise control with an external magnetic field. The large number of available DoF makes it difficult for a user to control a variable stiffness catheter in an optimal way. Our future research will focus on providing algorithmic control methods and an intuitive user interface to simplify the control task.

ACKNOWLEDGEMENT

This work was partially supported by the Swiss National Science Foundation through grant number 200021-165564.

REFERENCES

[1] C. Pappone *et al.*, “Robotic magnetic navigation for atrial fibrillation ablation,” *J. Am. Coll. Cardiol.*, vol. 47, no. 7, pp. 1390–1400, 2006.

[2] M. Kawamura, M. M. Scheinman, Z. H. Tseng, B. K. Lee, G. M. Marcus, and N. Badhwar, “Comparison of remote magnetic navigation ablation and manual ablation of idiopathic ventricular arrhythmia after failed manual ablation,” *J. Interv. Card. Electrophysiol.*, pp. 1–8, Jun. 2016.

[3] K. R. J. Chun *et al.*, “Catheter Ablation – New Developments in Robotics,” *Herz Kardiovaskuläre Erkrankungen*, vol. 33, no. 8, pp. 586–589, Dec. 2008.

[4] J. K.-R. Chun *et al.*, “Remote-controlled catheter ablation of accessory pathways: results from the magnetic laboratory,” *Eur. Heart J.*, vol. 28, no. 2, pp. 190–195, Jun. 2007.

[5] C. Chautems, A. Tonazzini, D. Floreano, and B. J. Nelson, “A variable stiffness catheter controlled with an external magnetic field,” *2017 IEEE/RSJ Int. Conf. Intell. Robot. Syst.*, pp. 181–186, 2017.

[6] I. Tunay, “Modeling magnetic catheters in external fields,” in *The 26th Annual International Conference of the IEEE Engineering in Medicine and Biology Society*, 2004, vol. 3, pp. 2006–2009.

Analysis of Concentric Tube Manipulator Workspace Improvements Using Anisotropic Pattern Tube Cutting

K. Ai Xin Jue Luo[1], S. Sabetian[1], T Looi[1], J. Drake[1]

[1]*Centre for Image-Guided Innovation and Therapeutic Intervention, Sickkids Hospital*

kevin.aixinjueluo@mail.utoronto.ca

INTRODUCTION

In recent years, there has been extensive research and development on concentric tube robots for use in minimally invasive medical procedures[1], [2]. A concentric tube manipulator is a steerable rigid needle which is typically 1-4 mm in diameter, making it very well-suited for use in minimally invasive surgery[1], [3]. Such a robot is typically composed of 2 or 3 pre-curved tubes that are assembled together concentrically to form a continuum manipulator. The rotation and translation of each tube are separately controlled via actuators at its straight proximal end. This steers the end effector at the distal tip of the concentric tube robot and changes its shape. However, a major limitation on the operation of concentric tube robots is the high build-up of torsional strain energy between tubes as they rotate against one another[4]–[6]. This build up in torsional strain can be suddenly released as the tip "snaps" to a new position. Thus the system is statically unstable between these two points. The stability condition for any set of two tubes has been derived previously by Azimian et al. [4]. and Dupont et al. [5] and be summarized in Eq. 1 below.

$$L\sqrt{u_1 u_2} < \frac{\pi}{2\sqrt{c}} \quad \textbf{(1)}$$

$$c = \frac{k_{z1}^{-1}+k_{z2}^{-1}}{k_{x1}^{-1}+k_{x2}^{-1}} \quad \textbf{(2)}$$

Here, L is the amount of overlap between the curved sections of the tubes, u_1 and u_2 are the curvatures of tubes 1 and 2 respectively. c is defined in Eq.2, where k_{xi} and k_{zi} are the bending and torsional stiffness for an individual tube. Thus from Eq.1 we can deduce that the key for improving stability is minimizing the bending to torsional stiffness ratio (BTSR), represented in Eq.3.

$$BTSR = \frac{k_x}{k_z} = 1 - v = \frac{EI}{GJ} \quad \textbf{(3)}$$

Here, v is Poisson's ratio, E is the elastic modulus, I is the second moment of area, G is the shear modulus, and J is the polar moment of area. Prior work has shown that an effective way to decrease the BTSR of an entire tube is by laser-cutting an anisotropic pattern on the tube. The patterns demonstrated in the past by Azimian et al. [4] and Kim et al. [7], [8] have mostly resembled a horizontal slit pattern repeated along the curved section of the tube. This paper attempts to analyze the impact on the stable workspace by reducing the BTSR of tubes using a distinct cut pattern which was designed with the aid of topology optimization. The pattern to be studied (Fig. 1) is a diamond-shaped cut pattern repeated around the circumference and the length of the tube. This design was generated based on the results of topology optimization using the Solid Isotropic Material with Penalization method, developed by Sigmund et al.[9]. The effectiveness of this pattern was validated using both FEA and experimental testing, the performance is summarized in Table I.

Fig. 1 Diamond-shaped tube cutting pattern

Table I. The effects of pattern cutting on tube BTSR (above), and the tube sizes used for the actuated experiment (below).

Tube	Test	Torsional Stiffness (N· m^2)	Bending Stiffness (N· m^2)	BTSR
Blank	Experiment	0.0236	0.0290	1.23
Patterned	Experiment	0.0127	0.0119	0.94
Tube	**ID (mm)**	**OD (mm)**	**Curve Radius (mm)**	**Curve Length (mm)**
Blank	1.33	2.03	47.5	77
Patterned	1.33	2.03	47.5	77
Outer	2.13	2.33	50.25	77

The patterned tube was tested in a concentric tube system and was successful in avoiding the snapping problem compared to its blank tube set counterpart (see Fig.1). Based on these results, we can observe the differences in workspace between patterned tubes and blank tubes. This will provide a visual and quantitative identification of how diamond-shape patterning of tubes can improve the usability of concentric tube robots by allowing a greater stable operational work space.

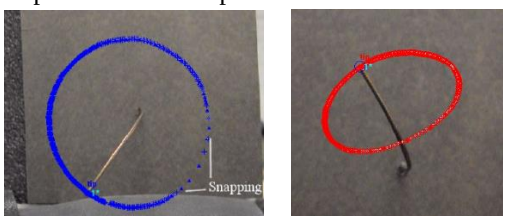

Fig. 2 Elimination of snapping in the set with a patterned tube (right) compared to a set of blank tubes.

MATERIALS AND METHODS

In order to demonstrate the improvement in the workspace of a concentric tube system, we chose nitinol tube combinations that satisfied the stability condition.

For consistency, the tube sizes used in this analysis are kept to be the same as those used in Table I. The tube curvatures and curve lengths used for the workspace analysis are documented in Table II.

Table II. Tube parameters used in workspace analysis

Set	Tube	Curve Radius	Curve Length
1	Blank Inner Tube	47.5 mm	77 mm
	Blank Outer Tube	61.68 mm	
2	Patterned Inner Tube	47.5 mm	77 mm
	Blank Outer Tube	52.84 mm	
3	Patterned Inner Tube	47.5 mm	77 mm
	Patterned Outer Tube	47.15 mm	

The curvature of the inner tube in all analyses was kept at 47.5mm, while the outer tube's curvature chosen so that the robot would be stable at all points throughout its workspace. A third set of tubes was also used in this analysis where the outer tube also assumed the same percentage decrease in stiffness and BTSR. To create a representation of the workspace for a single set of tubes, a Matlab concentric tube forward kinematics model was used to generate a point cloud where every point was a possible tip position of the robot. The point cloud was generated by incrementally translating and rotating the inner tube as well as rotating the outer tube, thus the longitudinal position of the outer was fixed. A 3D volume was then created using fitted curves around the outer surfaces of this point cloud. The size and dimensions of the workspace volume were then compared between different tube sets.

RESULTS

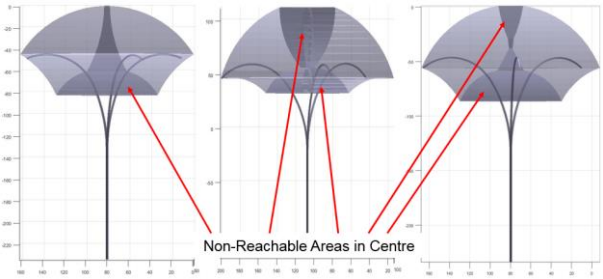

Fig. 3 From left to right: Side view of workspaces of tube sets 1, 2, and 3. Dark grey areas are not reachable by the manipulator

The workspace volumes for tube sets 1, 2, and 3 are displayed in Fig.2 together with 3 tube configuration examples to show the reach of a concentric tube robot. Tube set 2 showed a workspace increase of 21.4%, and tube set 3 had a workspace increase of 20.5%. The maximum width of the workspace for tube set 2, where a patterned tube was paired with a blank outer tube, was the largest (186.75mm). But with loss of centre distal workspace. The sizes and dimensions of the three workspaces are presented in Table III.

Table III. Results of the workspace analysis for all tube sets

Tube Set	Workspace Dimension		
	Volume (mm^3)	Max. Width (mm^3)	Height (mm^3)
1	$8.33x10^5$	161.35	82.39
2	$1.06x10^6$	186.75	82.39
3	$1.05x10^6$	175.46	87.45

DISCUSSION

Tube sets 2 and 3 both showed a similar increase in overall workspace volume. However tube set 2 had a wider lateral reach, while tube set 3 had better reach in the distal centre area of the workspace. Due to the imbalance of bending stiffness between the tubes, the centre distal area of the workspace for tube set 2 is less accessible than tube sets 1 or 3. Tube set 3 would likely be better for endoscopic applications. From Table II, we observe that the BTSR reduction achieved by using the cut pattern was 23.57%. The Table III analysis showed that with this pattern being used in either tube set 2 or 3, the workspace volume would be increased by at least 20%. A tube set with a larger workspace can be very beneficial to MIS if the right tube parameters can be implemented (which can be difficult). This is because surgeries that can potentially use concentric tube robots (i.e. intraventricular neurosurgery and cardiac surgeries) often need the tube to follow complicated and windy anatomical paths [1], [10]. The optimized diamond cut pattern alleviates the highly unstable snapping problem, makes the process of choosing tube parameters much easier and opens up many possibilities for the application of concentric tube robots for MIS procedures.

REFERENCES

[1] Dupont P Dupont P Gosline A Vasilyev N Lock J et. al., "Concentric Tube Robots for Minimally Invasive Surgery," *Hamlyn Symp. Med. Robot. 2012*, 2012.

[2] C. Bergeles, A. H. Gosline, N. V. Vasilyev, P. J. Codd, P. J. del Nido, and P. E. Dupont, "Concentric Tube Robot Design and Optimization Based on Task and Anatomical Constraints," Institute of Electrical and Electronics Engineers Inc., 23-Jan-2015.

[3] "Benefits of Minimally Invasive Surgery – AIMIS," 2012. [Online]. Available: https://www.aimis.org/benefits-of-minimally-invasive-surgery/. [Accessed: 14-Nov-2016].

[4] D. J. Azimian H, Francis P, Looi T, "Structurally-redesigned concentric-tube manipulators with improved stability," *2014 IEEE/RSJ Int. Conf. Intell. Robot. Syst.*, pp. 2030–2035, 2014.

[5] B. E. Dupont P, Lock J, Itkowitz B, "Design and Control of Concentric-Tube Robots," *IEEE Trans. Robot.*, vol. 26, no. 2, pp. 209–225, 2010.

[6] W. I. R. Gilbert H, Hendrick R, "Elastic Stability of Concentric Tube Robots: A Stability Measure and Design Test," *IEEE Trans. Robot.*, vol. 32, no. 1, pp. 20–35, 2016.

[7] D.-Y. Lee, J. Kim, J.-S. Kim, C. Baek, G. Noh, D.-N. Kim, K. Kim, S. Kang, and K.-J. Cho, "Anisotropic Patterning to Reduce Instability of Concentric-Tube Robots," *IEEE Trans. Robot.*, vol. 31, no. 6, pp. 1311–1323, Dec. 2015.

[8] J.-S. Kim, D.-Y. Lee, K. Kim, S. Kang, and K.-J. Cho, "Toward a solution to the snapping problem in a concentric-tube continuum robot: Grooved tubes with anisotropy," in *2014 IEEE International Conference on Robotics and Automation (ICRA)*, 2014, pp. 5871–5876.

[9] O. Sigmund, "A 99 line topology optimization code written in Matlab," *Struct Multidisc Optim*, vol. 21, pp. 120–127, 2001.

[10] T. Anor, J. R. Madsen, and P. Dupont, "Algorithms for design of continuum robots using the concentric tubes approach: A neurosurgical example," in *2011 IEEE International Conference on Robotics and Automation*, 2011, pp. 667–673.

Synthesis of biodegradable microrobots for biomedical applications

Xiaopu Wang[1], Xiao-Hua Qin[2], Chengzhi Hu[1], Xiang-Zhong Chen[1], Salvador Pané[1], Katharina Maniura[2], Bradley J. Nelson[1]

[1] Multi-Scale Robotics Lab,

Institute of Robotics and Intelligent Systems, ETH Zurich,

[2] Laboratory for Biointerfaces,

Empa-Swiss Federal Laboratories for Materials Science and Technology
wanxiaop@ethz.ch

INTRODUCTION

Microrobots have been proposed for future biomedical application, such as diagnostics[1] and targeted delivery[2]. Most microrobots are composed of non-biodegradable materials including metals[3] and commercial photoresists[4]. Poor biodegradability greatly impedes the use of microrobots for *in vivo* applications. Biodegradable materials have been widely employed in many biomedical applications, such as tissue engineering[5] and brain sensors[6]. Applying biodegradable materials to microrobots will greatly expand their application in biomedical fields. Helical microrobots have been widely studied[7]. In this work, a nontoxic photocrosslinkable hydrogel composed of gelatin methacryloyl[8] is used to fabricate biodegradable helical microrobots by means of two-photon polymerization (TPP), also known as 3D laser photolithography.

MATERIALS AND METHODS

The photoresist used in this work consists of gelatin methacryloyl (GelMA, 0.2g/ml)[8], a highly efficient water-soluble two-photon photoinitiator (P2CK, 1.1mg/ml)[9], and PBS (pH=7.4). Fe_3O_4 nanoparticles (20~30nm) are added to make the microrobots magnetic. The fabrication is based on TPP using the Photonic Professional GT System from NanoScribe GmbH. The wavelength of the laser is 780 nm.

RESULTS

By scanning a near-infrared femtosecond laser inside the photoresist, photopolymerization occurs only within the laser focal spot due to the non-linear absorption of two-photon photoinitiators and subsequent formation of free radicals. The illustration of this process is shown in Fig. 1. In this work, four kinds of helical microrobots with varying cross-section diameter were fabricated (Fig. 2a). The laser power was kept at 100mW, and two scanning speeds of the laser (10mm/s and 3mm/s) were used for comparison. As shown in Fig. 2b and 2c, highly reproducible hydrogel-based helical microrobots were structured. NB: the thinnest structures (design 1) were too weak to withhold deformation during washing in PBS. It was found that the higher the laser scanning speed, the more the structure swells, indicating a variation in crosslinking density. To make the microrobots magnetically responsive, Fe_3O_4 nanoparticles, which have been well proven to be biocompatible[10], were pre-dispersed in PBS. Then GelMA and the photoinitiator were dissolved in this Fe_3O_4-PBS suspension to prepare the photoresist. Photo-rheology analysis reveals that the addition of nanoparticles did not significantly influence the photocrosslinking of GelMA and mechanical properties of resultant gels. The mesh size in these crosslinked networks is approximately 10 nm. After polymerization, the magnetic nanoparticles are physically trapped inside these networks, as shown in Fig. 3. Thus, the movement of GelMA microrobots can be precisely manipulated by magnetic fields. Fig. 4 shows the trajectory of a helical microrobot under an applied rotating magnetic field.

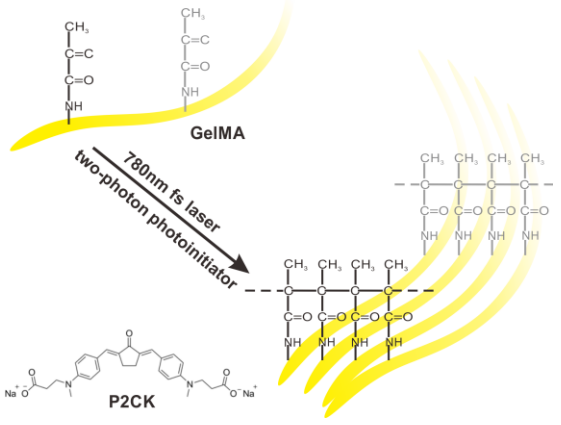

Fig. 1 Illustration of the polymerization process.

DISCUSSION

GelMA has been used in many biomedical applications due to its superior biodegradability[5-6]. However, similar materials, including GelMA, have not been applied to biomedical microrobots thus far. In this work, we successfully fabricated helical microrobots using GelMA and analyzed how fabrication parameters and designs affect the properties of microrobots. Finally, the motion of a GelMA helical microrobot in a rotating magnetic field was demonstrated.

Because of the swelling properties of GelMA, the cross-section of the printed helices appeared thicker than expected for a non-swelling structure. A critical parameter for adjusting the swelling properties of the microrobot is the laser scanning speed. As shown in Fig. 2b and 2c, the lower the laser scanning speed, the higher is the degree of polymerization and the less swelling is expected. Fig. 2c shows the microrobots are fluorescent. This may help *in vivo* image processing. The structural design significantly affects the mechanical properties of the hydrogel microrobot. As shown in Fig. 2, since design 1 is too thin, the microrobots fabricated based on it are too soft and prone to deformation. In conclusion, we have developed a fabrication approach to tailor both the biodegradability and the mechanical attributes of helical devices. The use of biodegradable microrobots eliminates the concerns that microrobots themselves may be harmful to the human body if they cannot be withdrawn after performing their tasks.

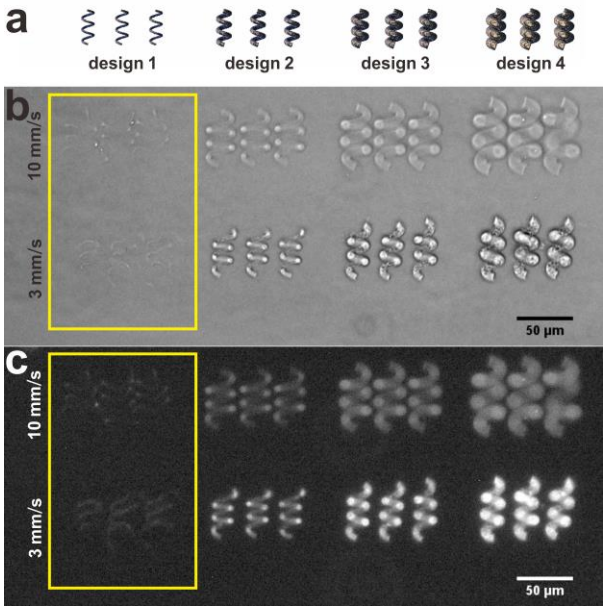

Fig. 2 Designs and fabrication of four kinds of helical microrobots. (a) Designs of helical microrobots. (b) Bright field images of helical microrobots. (c) Fluorescence images of helical microrobots.

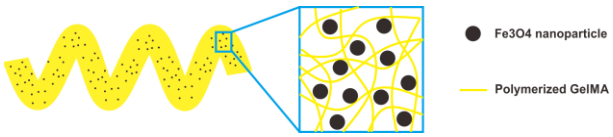

Fig. 3 Illustration of a helical microrobot with magnetic nanoparticles trapped inside of the crosslinked networks.

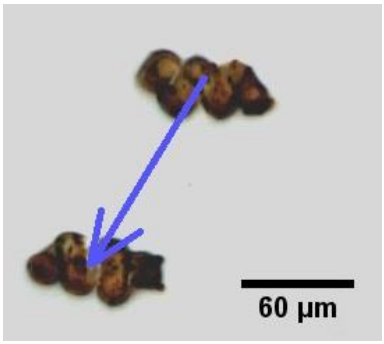

Fig. 4 Trajectory of a helical microrobot under a rotating magnetic field of 7mT.

ACKNOWLEDGEMENTS

This work was partially supported by the European Research Council Advanced Grant: 743217 – Soft Micro Robotics (SOMBOT). X.W. acknowledges financial support from China Scholarship Council (No: 201504910817).

REFERENCES

[1] Chałupniak, A.; Morales-Narváez, E.; Merkoçi, A., Micro and Nanomotors in Diagnostics. *Adv. Drug Delivery Rev.* **2015,** *95*, 104-116.

[2] Qiu, F.; Mhanna, R.; Zhang, L.; Ding, Y.; Fujita, S.; Nelson, B. J., Artificial Bacterial Flagella Functionalized with Temperature-Sensitive Liposomes for Controlled Release. *Sens. Actuators, B* **2014,** *196*, 676-681.

[3] Zhang, L.; Peyer, K. E.; Nelson, B. J., Artificial Bacterial Flagella for Micromanipulation. *Lab on a Chip* **2010,** *10* (17), 2203-2215.

[4] Kim, S.; Qiu, F.; Kim, S.; Ghanbari, A.; Moon, C.; Zhang, L.; Nelson, B. J.; Choi, H., Fabrication and Characterization of Magnetic Microrobots for Three-Dimensional Cell Culture and Targeted Transportation. *Adv. Mater.* **2013,** *25* (41), 5863-5868.

[5] Lee, K. Y.; Mooney, D. J., Hydrogels for Tissue Engineering. *Chem. Rev.* **2001,** *101* (7), 1869-1880.

[6] Kang, S.-K.; Murphy, R. K.; Hwang, S.-W.; Lee, S. M.; Harburg, D. V.; Krueger, N. A.; Shin, J.; Gamble, P.; Cheng, H.; Yu, S., Bioresorbable Silicon Electronic Sensors for the Brain. *Nature* **2016,** *530* (7588), 71-76.

[7] Servant, A.; Qiu, F.; Mazza, M.; Kostarelos, K.; Nelson, B. J., Controlled in Vivo Swimming of a Swarm of Bacteria-Like Microrobotic Flagella. *Adv. Mater.* **2015,** *27* (19), 2981-2988.

[8] Yue, K.; Trujillo-de Santiago, G.; Alvarez, M. M.; Tamayol, A.; Annabi, N.; Khademhosseini, A., Synthesis, Properties, and Biomedical Applications of Gelatin Methacryloyl (Gelma) Hydrogels. *Biomaterials* **2015,** *73*, 254-271.

[9] Li, Z.; Torgersen, J.; Ajami, A.; Mühleder, S.; Qin, X.; Husinsky, W.; Holnthoner, W.; Ovsianikov, A.; Stampfl, J.; Liska, R., Initiation Efficiency and Cytotoxicity of Novel Water-Soluble Two-Photon Photoinitiators for Direct 3d Microfabrication of Hydrogels. *RSC Adv.* **2013,** *3* (36), 15939-15946.

[10] Wang, L.; Wang, Z.; Li, X.; Zhang, Y.; Yin, M.; Li, J.; Song, H.; Shi, J.; Ling, D.; Wang, L., Deciphering Active Biocompatibility of Iron Oxide Nanoparticles from Their Intrinsic Antagonism. *Nano Research*, 1-10.

Towards Robotic Bioprinting Directly onto Moving, Stretching Anatomy

Rebecca G. Smith[1], Reed A. Johnson[1], Gabriella Shull[2], Daniel Sorby[3], Carl J. Modl[1], Angela Panoskaltsis-Mortari Ph.D[3], Timothy M. Kowalewski Ph.D[1]

[1]*Department of Mechanical Engineering, University of Minnesota,*
[2]*Department of Biomedical Engineering, University of Minnesota*
[3]*Department of Pediatrics, University of Minnesota*
smit8842@umn.edu

INTRODUCTION

Biomedical engineering has combined tissue engineering with additive manufacturing, yielding the ability to 3D print a tissue scaffold for human anatomical organs available for transplant [1]. Traditionally, bioprinting techniques are open-loop processes which are limited to printing on a stationary rigid surface. Recently, O'Neill et al. demonstrated the ability to 3D print hydrogel onto a moving human hand [2][3]. While this work exhibited adaptation to unpredictable motion of the print surface, it was unable to account for any print surface deformation. However, by accounting for the motion, stretch, or shear of a print surface, bioprinting could be used to apply therapy directly onto a biological surface, such as human skin or tissue. Additionally, the work presented in [2] stayed within the bounds of printing non-cellular materials, which is an unrealistic expectation for clinical bioprinting applications.

With these bioprinting challenges in mind, the objective of this paper is twofold. There are two experiments presented in this paper, each of which use the same piezojet robotic system. Experiment 1 demonstrates the level of cell viability attained upon 3D printing cellular fibroblasts suspended in a gelatin methacrylate (gelMa) solution, and additionally demonstrates the level of cell survival upon curing the gelMa solution via ultraviolet (UV) exposure. Experiment 2 introduces a closed-loop bioprinting procedure which accounts for the motion, shear, and stretch of the print surface.

MATERIALS AND METHODS

Experiment 1: Printing fibroblasts suspended in gelMa

In the first experiment, a gelMa solution was prepared by mixing 0.05g of LAP photoinitiator and 1g of gelatin into 10mL of phosphate buffered solution (PBS) at 37°C. Fibroblast cells were seeded on collagen and cultured in Dulbeccos modified Eagles medium (DMEM) with 5% fetal bovine serum (FBS) at 37°C until 80% confluent in 50 mL flasks. Fibroblast cells were printed on passage 3. On the day of the print, cells were suspended in 5mL of trypsin and ethylenediaminetetraacetic acid (EDTA) for 5 minutes at 37°C, after which 5mL of DMEM was added to the flask to neutralize trypsin. The cell suspension was then transferred to a 15mL tube and centrifuged at 1200 RPM for 5 minutes. GelMa was prepared as described previously and filtered under a biohood for sterilization. For control samples (-UV/-inkjet), LAP was not added to the gelMa. After removing the supernatant from the centrifuged cells, the gelMa solution was added to the left-over cell mass. The cells were then resuspended in gelMa using a low level vortexer and allowed to sit in the water bath to remove the bubbles. The gelMa/cell solution was then loaded into the inkjet printer and ejected onto 10 mL petri dishes. UV curing was induced after the print for 10 seconds. 1mL of DMEM was then added to the resulting gelMa/cell construct, and cells were cultured for 2 hours, 24 hours. After the period of cell culture, 2 drops of NucBlue(R) Live and NucGreen(R) Dead (ThermoFisher Scientific, Carsbad, CA) dyes were added to each petri dish sample to quantify cell viability. Fluorescence imaging was performed using a Leica fluorescence microscope.

Experiment 2: Bioprinting onto a non-rigid surface

In the second experiment, an IniLabs DAVIS-240C sensor was used to record the motion of four circular fiducials marking the boundary of the print surface. A Nordson EFD PICO Pμlse piezo jetting system was used to deposit a 2% Sodium Algenate solution onto the print surface. The DAVIS-240C sensor and the Pico Pμlse printer were both mounted onto a robotic gantry system. Two lasers were also fixtured onto the gantry system, and were oriented such that they projected onto the print surface (see Fig. 1).

The DAVIS-240C captured the motion of the projected lasers relative to the fiducials on the print surface, and the relative displacement between the projected lasers and fiducials was computationally determined. Using this relative displacement, the robotic gantry system was used to compensate for any motion of the print surface. The Pico Pμlse was used to deposit the print material onto the print surface whenever it was in the right position relative to the printer. Three different fiducial templates were used: a square template, a rectangular template, and a parallelogram template (see Fig. 3.e-f). The desired print geometry was a solid square lying within the boundary of the print surface (see Fig. 3.a). The same print geometry template was used to print on each of the three fiducial templates.

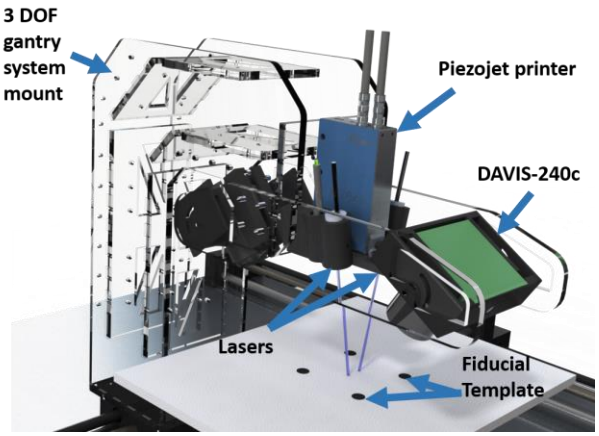

Fig. 1 Experimental setup of experiment 2

RESULTS

Experiment 1:

The bar plots given in Figure 2 show the cell viability results of fibroblasts suspended in gelMa for 3 different scenarios: the control sample which was neither printed with the inkjet nor cured with UV (blue), a sample which was cured using UV but not printed with the inkjet (orange), and a sample which was both UV cured and printed via the inkjet (grey).

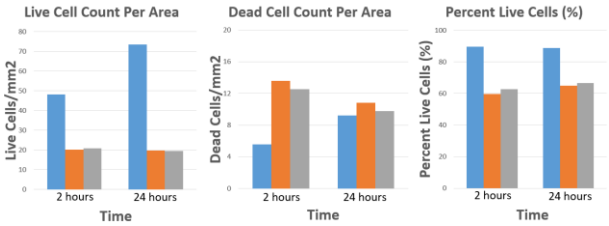

Fig. 2 Live/dead cell count measured after 2 hrs and 24 hours of printing. Blue indicates - UV/- Inkjet (control), orange indicates +UV/- Inkjet, and grey indicates + UV/+ Inkjet

Experiment 2:

The results of printing onto different fiducial templates are shown in Fig. 3. Fig. 3.a represents the original print template provided for each trial, Fig. 3.b-c depicts the anticipated print deformation given the change in fiducial geometry, Fig. 3.d depicts printing on an undeformed surface (square fiducial template), Fig. 3.e depicts printing on a template mimicking a stretched surface (rectangular template), and Fig. 3.f depicts printing on a template mimicking a sheared surface (parallelogram template).

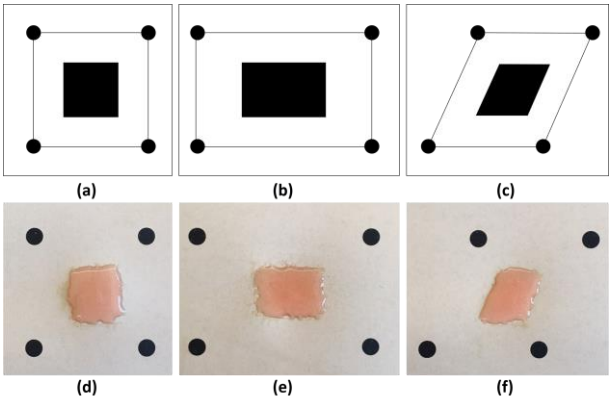

Fig. 3 Results of printing on each fiducial template. (a) original print template, (b)-(c) expected print deformation corresponding to (e)-(f), (d) non-deformed control case, (e) template mimicking surface stretch, and (f) template mimicking surface shear

DISCUSSION

As summarized in Fig. 2, there was no significant decrease in cell viability due to ink jetting versus that caused by UV curing, which is a process already ubiquitously used in bioprinting.

Additionally, from the images shown in Fig. 3, it can be seen qualitatively that the printing algorithm used is able to adapt to different fiducial geometries. While the same square print template was provided for each of the fiducial templates, the print algorithm was able to adapt the print such that it mimicked the deformation of the fiducial template. The adaptation of the print algorithm to fiducial template deformation indicates that it may be feasible to print on a surface which undergoes some type of deformation mid print. This could prove extremely valuable in clinical applications where it is necessary to print on non-rigid biological tissue.

These results suggest that, in conjunction with previous work, bioprinting viable cells onto moving, stretching, and shearing anatomy is feasible, and merits further investigation.

REFERENCES

[1] Murphy, Sean V., and Anthony Atala. "3D bioprinting of tissues and organs." Nature biotechnology 32, no. 8 (2014): 773-785.

[2] John O'Neil, Reed Johnson, Rodney Dockter, and Timothy Kowalewski. "3D bioprinting directly onto moving human anatomy." IEEE/RSJ International Conference on Intelligent Robots and Systems. IEEE (2017) https://www.youtube.com/watch?v=6VrozlyELdw

[3] Anna M. French, John J. O'Neill, and Timothy M. Kowalewski. "Design of a dynamic additive manufacturing system for use on free-moving human anatomy." ASME Journal of Medical Devices (2016)

Cobra-type robotic arm for tissue traction attachable to robotized endoscopy system (EasyEndo)

D.-H Lee, M. Hwang, D.-S. Kwon

Korea Advanced Institute of Science and Technology (KAIST)
leedh90@kaist.ac.kr

INTRODUCTION

Endoscope was originally a device for diagnosis, but it has been used therapeutic procedure with various instruments. However, there are many inconvenience in the usage. Steering is not intuitive, and it is physically cumbersome for physicians due to weight. Also, unintended communication often occur because the physician should cooperate with assistants, which can decrease the efficiency of the procedure.

Robotics is one of ways to overcome these problems, and many studies are underway. There are some stuides of robotizing convention endoscope such as Robotic Steering and Automated Lumen Centralization (RS-ALC) and Endoscopic Operating Robot (EOR), and there are some other developing new platforms such as MASTER, FLEX, and Viacath, and so on [1].

We proposed a robotized endoscopy system called EasyEndo [2, 3]. The conventional endoscope and the instrument inserted into a working channel were robotized. The feasibility was verified through a lab-level experiment for novices. Physicians have also used it for a test and evaluated that it will be useful in clinical environment. However, what physicians most need was tissue traction that could be helpful in the procedures.

This paper describes advanced EasyEndo that not only robotized conventional endoscope and instrument, but also an additional cobra-type robotic arm attachable to the endoscope for tissue traction. Endoscopic camera view was considered in the design of the cobra-type robotica arm becasue physicians perform the procedure while viewing the endoscopic camera view.

MATERIALS AND METHODS

A. System (EasyEndo) Overview

EasyEndo consists of a robotized endoscope, a cobra-type robotic arm, and two input devices (Fig. 1). The robotized endoscope is mounted on a positioning arm, which is fixed to a moving cart. The cobra-type robotic arm is an additional instrument handler for tissue traction, and it is driven by a tendon-sheath mechanism. It is attached on a rigid section at the extremity of the bending section. Since the robotic arm is hollow, commercial tools can be inserted.

Two input devices are used to manipulate the system. One input device can only manipulate the robotized endoscope. The other can manipulate the instrument inserted into working channel in the diagnosis phase or the cobra-type robotic arm in the procedure phase.

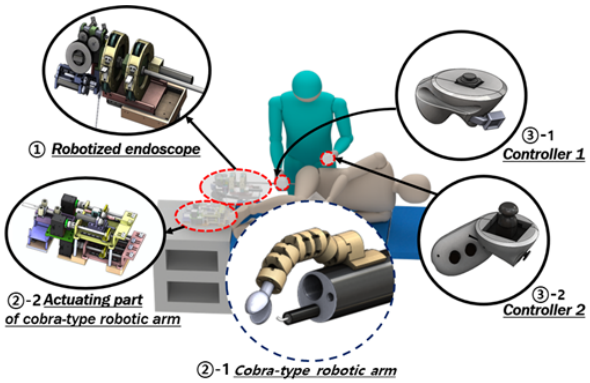

Fig. 1 System (EasyEndo) Overview

B. Cobra-type robotic arm

A robotic arm should be capable of tissue traction in the desired direction during the procedure. Because the endoscope can be moved to the desired location by bending, rotating, and introducing, it is difficult to define a required workspace.

The endoscopic camera view can be important factor for defining the workspace, since physicians perform the endoscopy while viewing the view. Most of the endoscopic camera view angles were about 140 degrees and came out in pyramid or cone shapes.

Depth of the view must be determined to define the workspace. Thus, it is necessary to know how much instruments protrude from the end of the endoscope. Since there was no reference depth in use, we have been consulted by physicians. Most answered that the instruments were usually protruded by 10 to 25mm.

Prior to designing a robotic arm that can cover the pyramid or cone shape workspace, we examined joint configurations for surgical robotic arm. Arkenbout at al. categorized surgical robot system having multi-branched instruments according to branch segment configuration [4]. The configurations are represented by combinations of a straight segment providing axial Degrees of freedom, i.e., rotation and translation, and a deflecting segment providing bending in one or two orthogonal planes.

Among the various configurations, it can be seen that a configuration in the order of the deflecting segment-straight segment can easily cover the endoscopic camera view. If the deflecting segment can bend as much as the angle of the endoscopic camera view, it is possible to cover the endoscopic camera view with a translation of the straight segment, even if the desired depth is not set.

Triangulation is an important consideration in tissue traction. Triangulation is the ability to pull tissue to desired position. Many systems have tried to secure

triangulation by adding joints that deflect outward first and then back inward [2, 3]. We also added a joint for triangulation. Because the shape of the joint is similar to a cobra, the robotic arm is called a cobra-type robotic arm. Consequentially, the order of segment configuration is the triangulation-deflecting-straight segment.

For the kinematic analysis, the cobra-type robotic arm is represented according to the Denavit-Hatenberg (DH) and the parameters are shown in Fig. 2. The triangulation segment consists of two pitch joints, one is for opening outward and the other is for bending inward. Currently, the triangulation segment can have 0 or 45 degrees. The deflecting segment has a yaw and pitch joint and the bending range is from -90 to 90 degrees. The straight segment consists of an axial rotation and translation. The translation is allowed to move up to 50 mm and the rotation is allowed to rotate infinitely. To summarize, the order of the joints is pitch (outward) – pitch (inward) – yaw – pitch – translation – rotation.

Since the kinematics model enables workspace estimation based on each joint movement, we have estimated the workspace of the cobra-type robotic arm. It can be seen that all of the endoscopic camera view between 10 and 25 mm deep are covered (Fig. 3).

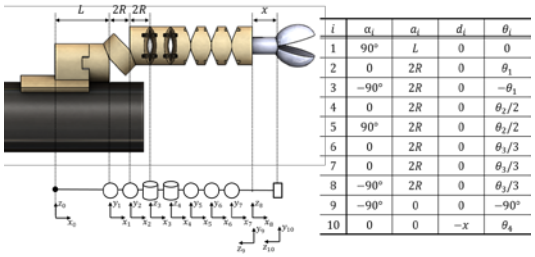

i	α_i	a_i	d_i	θ_i
1	90°	L	0	0
2	0	$2R$	0	θ_1
3	−90°	$2R$	0	$-\theta_1$
4	0	$2R$	0	$\theta_2/2$
5	90°	$2R$	0	$\theta_2/2$
6	0	$2R$	0	$\theta_3/3$
7	0	$2R$	0	$\theta_3/3$
8	−90°	$2R$	0	$\theta_3/3$
9	−90°	0	0	−90°
10	0	0	$-x$	θ_4

Fig. 2 Configuration and DH paprameters of the cobra-type robotic arm

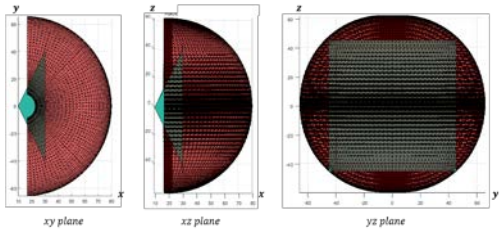

Fig. 3 Workspace analysis (blue: endoscopic camera view, red: cobra-type robotic arm)

RESULTS

Since the performance of the robotized endoscope was already verified in previous study [2, 3], an experiment was conducted to confirm the feasibility of cobra-type robotic arm. Since it takes time and cost risks to manufacture the unproven cobra-type robotic arm into metal, we decided to make a prototype with a 3D printer as double scale for lab-level test.

Self-made testbed was set up to imitate the tissue traction with rubber band. One end of the band was fixed to the testbed and the other was allowed to move freely (Fig. 4). First, the robotized endoscope was made to reach near the band. Then, the cobra-type robotic arm was used to hold the free end and pull it in various directions.

It was verified that the cobra-type robotic arm can gasp objects and pull them to the desired direction. The students who participated in the experiment also acknowledged the traction capability of the cobra-type robotic arm. However, it is pointed out that the current cobra joint for triangulation only extends at one angle, 45 degrees, and the ergonomic aspect should be improved.

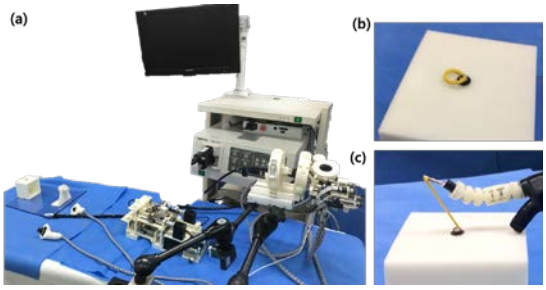

Fig. 4 (a) Overview of experimental setup, (b) Cut rubber ring, (c) Rubber ring traction with the cobra-type robotic arm

DISCUSSION

This paper presented the robotic endoscopy system (EasyEndo) that can operate by one physician not only the robotized endoscope but also one additional cobra-type robotic arm for tissue traction. Through the tissue traction simulation approaching to the rubber band and pulling it with the cobra-type robotic arm, the traction effectiveness and solo operation was verified.

Following these positive results, we will manufacture the cobra-type robotic arm into metal as the originally designed size. In addition, we are going to control the triangulation segment to get various angles. Then, additional control strategy for redundant joint is required. Also, the input devices will be modified for the ergonomics with feedback from users. After that ex-vivo and in-vivo experiments will be conducted with physicians to verify a feasibility in clinical environment.

ACKNOWLEGMENT

Research supported by National Research Foundation (NRF) of Korea. (Grant # NRF-2017H1A2A1043159)

REFERENCES

[1] B. P. Yeung and P. W. Chiu, Application of robotics in gastrointestinal endoscopy: A review. World J. Gastroenterol. 2016 Feb;22:1811–1825

[2] Lee D.-H., Cheon B., Hwang M., Kwon D.-S., Attachable Robotic Handler to Endoscope and Instrument for Solo-Endoscopy. Hamlyn Symposium 2017

[3] Lee D.-H., Cheon B., Hwang M., Kwon D.-S., “Robotic endoscopy system (EasyEndo) for solo procedure and its efficient manipulation for workload reduction.” Surg Endosc (In the review progress)

[4] Spaun GO, Zheng B, Swanstrom LL, A multitasking platform for natural orifice translumenal endoscopic surgery (NOTES): a benchtop comparison of a new device for flexible endoscopic surgery and a standard dual-channel endoscope. Surg Endosc. 2009, 23(12):2720–2727

Translational and Rotational Arrow Cues (TRAC) Outperforms Triplanar Display for use in 6-DOF IGS Navigation Tasks

David E. Usevitch and Jake J. Abbott

Department of Mechanical Engineering and the Robotics Center, University of Utah

{*david.usevitch, jake.abbott*}*@utah.edu*

INTRODUCTION

Many image-guided surgery (IGS) tasks require a human to manually position an object in space with 6 degrees-of-freedom (6-DOF). We are particularly interested in positioning robotic [1] and magnetic [2] devices during robot-assisted cochlear-implant surgery.[1] Displaying the current and desired pose of the object on a 2D display is straightforward, however, providing guidance to accurately and rapidly navigate the object in 6-DOF is challenging [3]. Visual guidance is typically accomplished using a triplanar display (Fig. 1) that shows three orthogonal views of the workspace [1,3–5]. This method is quite unintuitive, particularly before training.

We propose an intuitive method of visually communicating navigation instructions using a single principal view that approximates the human's egocentric view of the actual object, using translational and rotational arrow cues (TRAC) defined in an object-centric frame (Fig. 2). We show the arrow corresponding to the single DOF with the largest error until convergence in that DOF, at which point we switch to the new arrow corresponding to the largest error, alternating between rotation and translation. Copies of the moving virtual object and the respective arrow cues, which have small rotational offsets from the central virtual object but fixed positions on the screen, ensure that the arrow cues do not become occluded. With the TRAC method, the target pose is not actually required, and is useful to quickly perform the initial gross alignment. We show that the TRAC method outperforms the state-of-the-art triplanar method in terms of time to complete 6-DOF navigation tasks. Preliminary results also suggest this method enables improved accuracy.

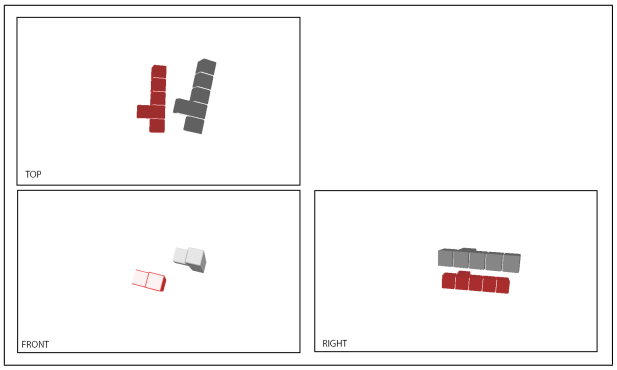

Fig. 1: Triplanar display showing three orthogonal views. The red stationary object is the target pose, and the gray object moves with the hand-held object.

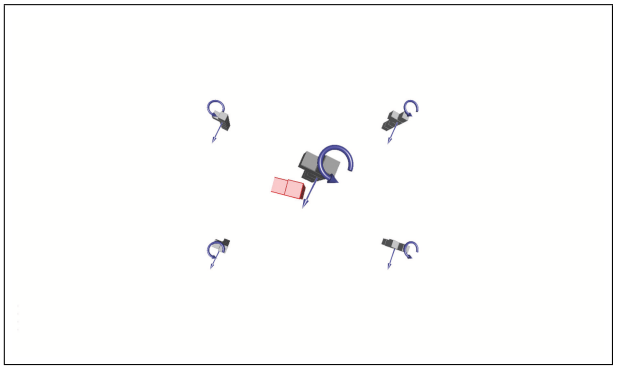

Fig. 2: Proposed TRAC method. The red stationary object is the target pose, and the gray objects move with the hand-held object. We show both translational and rotational arrows here for display purposes, but in practice only one arrow cue (either translational or rotational) is displayed at a time during navigation. Note that we maintained object sizes consistent with the triplanar display to avoid potential biases due to the increased object sizes enabled by the TRAC method (i.e., a single view filling the entire screen).

MATERIALS AND METHODS

To quantify the benefits of TRAC relative to a triplanar display, we conducted a human-subject study with IRB approval, comprising 4 males and 4 females, aged 21–31 years, from the engineering-student population at the University of Utah. The completion time (T) of 6-DOF pose matching was measured in two sessions, separated by 2 days to mitigate effects of learning and fatigue. Session A measured T using the triplanar display. There is no standard arrangement used in prior work, so we chose an arrangement that correlates closely with [1], in which we position a front view at the lower left corner, a side view at the lower right, and a top view at the upper left (Fig.1). This arrangement is also consistent with common mechanical-drawing techniques. Session B measured T using the TRAC method. In this method a single translational (straight) or rotational

[1]Research reported in this publication was supported in part by the National Institute of Deafness and Other Communication Disorders of the National Institutes of Health under Award Number R01DC013168.

(circular) arrow is displayed along one object-centric axis of the moving virtual object (Fig. 2). The object is first rotated to be within rotation thresholds for all three axes; translation is then performed until the position is within positioning thresholds for all three axes; during rotation and translation, the arrow corresponding with the maximum rotational or translational distance to the goal is displayed; the display alternates between these two cues until the pose is within all specified thresholds. Half of the subjects (balanced by gender) performed Session A first, and the other half performed Session B first.

A set of 30 poses was randomly generated from a uniform distribution with translational offsets along each of the three principal axes within ± 40 mm of the home position, and with each pose having a rotational offset of 15° (using the angle-axis formulation). These offsets were designed to represent the precision-alignment stage of pose matching. The same 30 poses were used in both sessions for all subjects, but the order of the 30 poses was randomized each time.

A 1.02 m LCD monitor was positioned above a Polaris Spectra optical tracker, both located 1.83 m in front of a subject seated at a table. The subject manually manipulated an unconstrained hand-held object with three distinct axes, which was equipped with motion-tracking markers. For each of the 30 poses in each session, the subject homed the object to a specified homing position, and then moved the object to match the target pose as quickly as possible. When the object was within 5° and 3 mm of the target (see Discussion), the object changed colors to signal a match, and the subject was required to maintain the object within this threshold for 1.5 sec, at which point the T was recorded and the 1.5 sec hold time was subtracted. The object was then homed in preparation for the next target pose.

A generalized linear regression analysis is used to determine statistical significance of treatment factor *navigation method* (treated as a fixed-effect variable) on response T, using blocking factors *subject* (treated as random-effect variable) and *session order* (treated as fixed-effect variable). The conventional significance for the entire analysis was determined at $\alpha = 0.05$.

RESULTS

In Fig. 3 we present the results of our study. The T data was skewed, and a gamma distribution was used to represent the data. We find that 6-DOF alignment is significantly faster using the TRAC method than using the triplanar method. With the triplanar method, the median T was 78% longer than the median T of the TRAC method. The worst-case T when using the triplanar method was more than six times longer than the worst-case T using the TRAC method. Additionally, subjects declared a unanimous preference for the TRAC method.

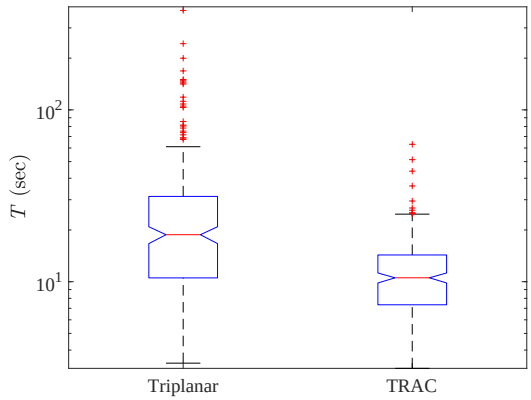

Fig. 3: Notched box-whisker plot comparing the completion time T for both methods, using a logarithmic scale. The red line represents the medium datum, the lower and upper edges of the box represent the first and third quartiles of the data, respectively, the lower/upper whisker represents the smallest/largest datum within 1.5 IQR, the notches represent the confidence interval of the median, and the red crosses represent outliers.

DISCUSSION

We chose a quite large convergence tolerance for our study because in pilot testing we found many subjects struggled with completing pose alignment in a reasonable amount of time when using the triplanar display if we used a tighter tolerance. Consequently, we believe our results under-represent the true relative benefit of TRAC. Anecdotally, we have been able to rapidly achieve 6-DOF alignment with sub-mm and sub-degree accuracy using TRAC. Quantifying the accuracy of TRAC is left as future work.

REFERENCES

[1] T. L. Bruns and R. J. Webster III, An image guidance system for positioning robotic cochlear implant insertion tools, *SPIE Medical Imaging*. 10135:1-6, 2017.

[2] L. Leon, F. M. Warren, and J. J. Abbott. Optimizing the magnetic dipole-field source for magnetically guided cochlear-implant electrode-array insertions, *J. Med. Robot. Res.* 3(1):1-15, 2018.

[3] R. F. Labadie and J. M. Fitzpatrick. What Does the Future Hold? *Image-guided Surgery : Fundamentals and Clinical Applications in Otolaryngology*. San Diego: Plural Publishing, 185–188, 2016.

[4] G. Dagnino, I. Georgilas, S. Morad, P. Gibbons, P. Tarassoli, R. Atkins, and S. Dogramadzi. Intra-operative fiducial-based CT/fluoroscope image registration framework for image-guided robot-assisted joint fracture surgery. *Int. J. Comput. Assist. Radiol. Surg.*, 12:1383-1397, 2017.

[5] L. Adams, W. Krybus, D. Meyer-Ebrecht, R. Rueger, J. M. Gilsbach, R. Moesges, and G. Schloendor. Computer-assisted surgery. *IEEE Comput. Graphics Appl.*, 10:43–51, 1990.

An Ergonomic Interaction Workspace Analysis Method for the Optimal Design of a Surgical Master Manipulator

D.-D. Zhang[1], J. Liu[1], G.-Z. Yang[1]

[1]The Hamlyn Centre for Robotic Surgery, IGHI, Imperial College London, UK
d.zhang17@imperial.ac.uk

INTRODUCTION

The master manipulator of a master control console, is used to interact and capture the gestures from an operator, and control the slave robot remotely. Several fundamental aspects for designing a master manipulator should be taken into account, such as safety, maneuverability and accuracy. Master control console is a place where robots collaborate with humans in a shared environment. Therefore, ergonomics is also an important aspect. With ergonomic consideration, the operator can feel more comfortable and confident to conduct the surgical tasks with higher efficiency, and the quality of the tele-operational robotic surgery can be improved.

Human reference model of the Master Motor Map (MMM) framework has been proposed for human arm workspace modelling and analysis [1]. However, for robotic surgery application, the effective workspace can be more specific based on the characteristics of master-slave operational mode. Ergonomic body posture of the surgeon during robot-assisted surgery was analyzed for the da Vinci console [2]. But its main focus was on geometric data and ergonomic instructions for an optimal console setting without considering the master manipulators. In this paper, an Ergonomic Interaction Workspace Analysis method is proposed to optimize master manipulators and fulfill ergonomics consideration for remote robotic surgery.

MATERIALS AND METHODS

As shown in Fig.1-(a), a pair of six Degrees of Freedom (DoF) master manipulators are taken for the calculation in this paper as an example. To control the master manipulators, operators normally rest their arm on the arm rest and hold the end-effectors of the manipulators via fingers. General motions include moving along the edge of the desk, moving arms forward and backward, pitch and roll motions on the fulcrum of the arm rest, and three dimensional wrist motions. Based on the general movements mentioned above, a pre-defined Equivalent Human Ergonomic Model (EHEM) can be built up for analysis of human comfortable workspace (Fig.1-(b)), with ergonomics consideration.

Reachable workspace of the master manipulators is analyzed at first, while Master Manipulator Dexterous Workspace (MMDW) is calculated based on the manipulability measurement index (see Fig.1-(c)), which was introduced by Yoshikawa [3].

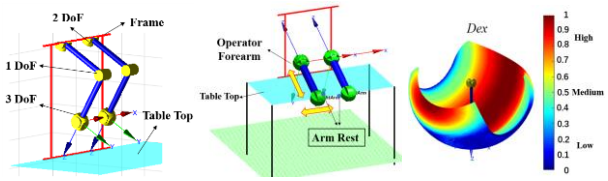

Fig. 1 (a) Master Manipulators; (b) Equivalent Human Ergonomic Model (EHEM). (c) Master Robot Dexterous Workspace (single arm).

It describes the distance of a given pose of the manipulator to a singular configuration. Joint limits have significant impacts on the end effector's maneuverability in workspace, and the influence can be addressed by adding a penalization term to augment the Jacobian matrix of the master manipulator [4][5]. The maneuverability can be written as follows:

$$Dex = \sqrt{\det(JJ^T)}[1-\exp(-K\prod_{j=1}^{N}\frac{(\theta_j-\theta_{j,down})(\theta_{j,up}-\theta_j)}{(\theta_{j,up}-\theta_{j,down})^2})] \quad (1)$$

where J is the Jacobian matrix, K is a scaling factor, N is the number of joints, θ_j is the joint angle, $\theta_{j,up}$ and $\theta_{j,down}$ are the upper and lower boundary of joint limitation respectively.

It is difficult to build a precise model for dexterity calculation, so Monte Carlo based technique is used for estimation. A large set of random master robot arm configurations are generated, and the position and orientation of the end-effector are computed via forward kinematics with corresponding dexterity value *Dex* after normalization of the calculation results from equation (1).

The scatter data of the calculation results are written as $Dex = S(x,y,z) \in \mathbb{R}_s(p_{Lx} \le x \le p_{Ux}, p_{Ly} \le y \le p_{Ly}, p_{Lz} \le z \le p_{Uz})$,where $\mathbb{R}_s$ is a 3D space with scatter data.

Some points of low dexterity value are abandoned based on a threshold value. Fig.2-(a) demonstrates the isosurface with isovalue of 0.3, which is a segmentation surface of low and high dexterity. As for workspace representation, the workspace can be divided into equally sized cubes called voxels, with a predefined desired resolution [6]. The voxel value can be represented as reachability by filling with dexterity measurement information describing the capabilities of the robot. The corresponding dexterity value *Dex* is mapped to a discretized workspace with cubic voxel, and can be represented as $Dex' = V(i,j,k) \in \mathbb{R}_v$, $(1 \le i \le (p_{Ux}-p_{Lx})/r, 1 \le j \le (p_{Uy}-p_{Ly})/r, 1 \le k \le (p_{Uz}-p_{Lz})/r)$,

where $\mathbb{R}_v$ is a 3D space with voxel data, r is the minimum distance between two scattered points. The corresponding relationship of the volume data and the scatter data is described as follows:

$$V(i,j,k) = S((x - p_{x\min})/r, (y - p_{y\min})/r, (z - p_{z\min})/r) \quad (2)$$

After calculating the MMDW, the shared volume between the right and the left arm and the overall dexterous workspace volume data can be generated, as shown in Fig.2 -(b) based on the following equation.

$$V_{dual}(i',j',k') = \gamma[V(i - r_x, j - r_y, k - r_z) + V(i + D - r_x, j - r_y, k - r_z)] \quad (3)$$

where $R = (r_x, r_y, r_z)$ is the translation vector of the frame of the operator and the master robot, D is the distance between the two master manipulator along the fixed frame and γ is the standardization factor used to ensure that the overall dexterous workspace volume data span the interval [0,1].

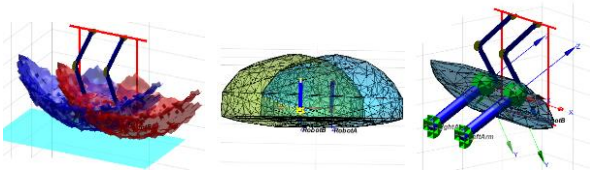

(a) (b) (c)

Fig. 2 (a) Isosurface of Dual Arms Dexterous Workspace with isovalue of 0.3; (b) Visualization of Overlap Volume of Dual Arm Dexterous Workspace; (c) Ergonomic Interaction Workspace.

The Equivalent Human Ergonomic Index in the 3-D workspace is represented as $E(i',j',k') = 0.5 \in \mathbb{R}_v$. The master manipulator's workspace should have the maximize intersection of the human arms' comfortable moving space. Therefore, the Ergonomic Interaction Workspace can be evaluated based on the following equation:

$$\sum_{i'=1}^{i'\max} \sum_{j'=1}^{j'\max} \sum_{k'=1}^{k'\max} [(E_{Left}(i',j',k') + E_{Right}(i',j',k'))] \cdot V_{dual}(i',j',k') \quad (4)$$

RESULTS

The optimized solution can be obtained by changing parameters of the manipulators' link length and the distance of the base of the two master manipulators along the mounting frame. Fig.2-(c) is the visualization result of the Ergonomic Interaction Workspace. Optimization method is used to maximize the volume of the Ergonomic Interaction Workspace, and the final D-H parameters of the master manipulator can be obtained (Table 1), while D=0.20 m. The optimization index can be represented as the percentage of the volume of Ergonomic Interaction Workspace V_I to the volume of Human Ergonomic Workspace V_R as $F = V_I / V_R$. V_R is calculated based on the EHEM model. The original result is $F = 0.0057$ with initial link length is 0.15m for both the first and second link of the manipulator, while the optimized result is $F = 0.2732$.

Table 1 Optimized Master Manipulator DH Parameters

	1	2	3	4	5	6
α	0	pi/2	-pi/2	0	-pi/2	pi/2
a	0	0	(0.15)0.26m	(0.15)0.18m	0	0
d	0	0	0	0	0	0
θ	θ_1	θ_2	θ_3	θ_4	θ_5	θ_5

DISCUSSION

An Equivalent Human Ergonomic Model (EHEM) is defined in this paper, which represents a simplified model for surgeon to realize remote control of surgical robots with armrests in the confined environment. The dexterity of the master manipulator is calculated, which is known as the Master Manipulator Dexterous Workspace (MMDW). The Ergonomic Interaction Workspace is formed by the intersection between the MMDW and EHEM. Optimization method is used to determine the suitable link length of the master manipulators for human-robot interaction tasks, which plays an important role in maximizing the interaction dexterous workspace volume in a predefined environment to improve the outcomes of master-slave remote control during robotic surgery. After optimization, the percentage of volume of Ergonomic Interaction Workspace is improved by 50 times. Future work will include building up a prototype and conducting user study to test the ergonomics and discover how much operational efficiency can be improved by the optimized design using Ergonomic Interaction Workspace Analysis method.

ACKNOWLEDGEMENT

The authors would like to thank Dr. Konrad Leibrandt for the advice of accelerating dexterous workspace calculation, and Dr. Lin Zhang, Yang Hu for discussion.

REFERENCES

[1] Ochiai T. Master Motor Map (MMM) - Framework and Toolkit for Capturing, Representing, and Reproducing Human Motion on Humanoid Robots[C]// Ieee-Ras International Conference on Humanoid Robots. IEEE, 2014:894-901.

[2] Hullenaar C D P V, Hermans B, Broeders I A M J. Ergonomic assessment of the da Vinci console in robot-assisted surgery[J]. Innovative Surgical Sciences, 2017, 2(2).

[3] Yoshikawa T. Manipulability of Robotic Mechanisms[J]. Int.j.robot.res, 1985, 4(2):3-9..

[4] Yoshikawa T. Foundations of Robotics:Analysis and Control[M]. The MIT Press, 1990.

[5] Leibrandt K, Wisanuvej P, Gras G, et al. Effective Manipulation in Confined Spaces of Highly Articulated Robotic Instruments for Single Access Surgery[J]. IEEE Robotics & Automation Letters, 2017, PP(99):1-1.

[6] Zacharias F, Borst C, Hirzinger G. Capturing robot workspace structure: representing robot capabilities[C]// Ieee/rsj International Conference on Intelligent Robots and Systems. IEEE, 2007:3229-3236.

Affordable Mobile-based Simulator for Robotic Surgery

Piyamate Wisanuvej[1,3], Petros Giataganas[1], Paul Riordan[1], Jean Nehme[1], and Danail Stoyanov[1,2]

[1]Digital Surgery Limited
London, UK
piyamate@touchsurgery.com

[2]University College London
London, UK
danail.stoyanov@ucl.ac.uk

[3]Kasetsart University
Bangkok, Thailand
fengpmw@ku.ac.th

INTRODUCTION

Robotic surgery presents great potentials towards safer, more accurate and consistent minimally invasive surgery (MIS) [1]. However, their adoption is fundamentally dependent on the access to training facilities and extensive surgical training [2, 3]. Robotic instruments require different dexterity skills compared to open or laparoscopic surgery as well as across different robotic systems. Surgeons, therefore, are required to invest significant time by attending extensive robotic training programs. Hands-on experiences, also, represent an additional operational cost for hospitals as the availability of robotic systems for training purposes is limited. All these technological and financial barriers for surgeons and hospitals hinder the adoption of robotic surgery technology.

Currently, the robotic surgery scene is represented by the state-of-the-art robotic MIS (RMIS) system, the da Vinci® surgical system (Intuitive Surgical, CA). Due to the increased interest for the system, various surgical simulators for the system have been developed over the years. They offer a computer-generated reproduction of real-world surgical procedures and surgical tasks for different levels of expertise. These platforms are mainly stand-alone and do not compromise patient's safety for training. However, they cost tens of thousands of dollars as they are based on either expensive, but accurate, electromagnetic systems or room-based visual tracking systems or high-end robotic manipulators. They are non-portable and often require dedicated training spaces, and are developed exclusively for the da Vinci systems. Similar limitations existed in laparoscopic surgical training but with technological advances, nowadays, low cost alternatives exist for basic surgical tasks with full performance analytics and support of generic laparoscopic instruments with cost of less than $1000. These simulators are often called 'take-home' simulators that surgeons can use to train anywhere and are potentially significant for countries where surgical training tools are limited.

In this work, we present a low-cost, fully wireless, and portable solution to train basic dexterity skills for introductory-level robotic surgery. The platform can facilitate the training of basic gestures and improve the users familiarity with the hand-motor axis control and ergonomics needed for manipulating robotic instruments. It is intended for surgeons without robotic surgery training to become familiarised with new dexterity skills required. To our knowledge, this is the first attempt to demonstrate such a system for RMIS.

Fig. 1: Prototype demonstration of the mobile surgical simulator presenting all the elements of the system.

MATERIALS AND METHODS

The proposed portable system consists of three core components as shown in Fig. 1: a pair of wireless hand-held master controllers with haptic and tactile feedback, a mobile dock, and a smartphone or tablet that run the simulation software. The smartphone can also housed inside a virtual reality (VR) headset for 3D visualisation. An overview of all the system components along with the communication links is presented in Fig. 2. Unlike many VR headsets, the system is self-contained and requires no external host computer. The material cost to build this system is approximately $500, which is significantly lower than existing commercial solutions.

The platform combines an inertial measurement unit (IMU) and an infrared (IR) tracking system to provide a low cost alternative to expensive commercial tracking solutions, *e.g.* electromagnetic tracking. The IMU is used only for the orientation tracking as the integration errors hinder its use for position estimation. The position of each wireless hand-held controller is tracked externally using a low cost IR stereo tracker (Leap Motion, USA) that is situated in the front of a docking station and an IR LED attached at the bottom of each controller. Active trackers were

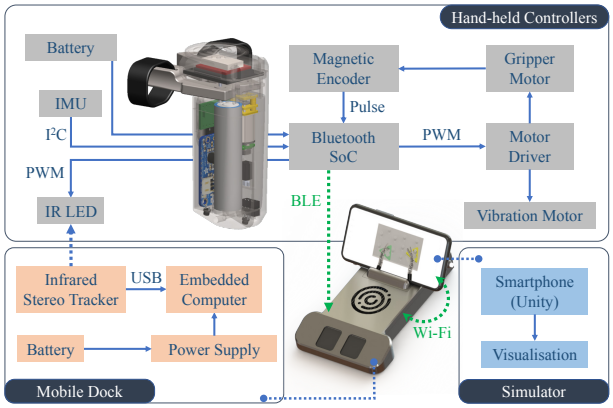

Fig. 2: Overview of the system architecture along the various communications between the components.

preferred due to their higher contrast and robustness in detection; passive markers are more prone to false positives due to flood illumination. A simple binary thresholding scheme is adopted to detect each marker. Then, the pair of corresponding markers in the stereo images are triangulated using the calibrated cameras and the triangulated points are smoothed over time using a moving average filter. Each controller is equipped with only one LED to reduce the computational load on the embedded computer. The position data from the cameras is complemented by the orientation data from the IMU to obtain full 6-DoF tracking.

Every hand-held controller has a multifunctional button. When pressed, then the user can activate the clutch of each surgical instrument. If the buttons on both controllers are pressed, then the user can adjust the camera view by moving both controllers in relative to each other for rotation and translation.

The simulation environment used with the smartphone or tablet is built using the Unity engine (Unity Technologies, USA), while the physical interactions are simulated using the built-in physics engine (Nvidia PhysX). The articulated instruments' joint angles are calculated using a commercially available inverse kinematics (IK) solver (Rootmotion). In the presented work, a simple but well-established pick and place surgical task is demonstrated,depicted in Fig. 3, which is an adaptation of the Fundamentals of Laparoscopic Surgery (FLS) model training task.

RESULTS

A preliminary study was conducted with five novice users to evaluate the usability of the mobile simulator. They were asked to perform a standard peg transfer task using the platform. Each user had five minutes to get familiarised with the task, then, the actual experiment commences. The task is to perform bi-manual peg transfers from one side to the other and repeated the steps until three minutes have passed. The experiment repeated three times for each user with a minute of break in between.

The metrics measured during the experiment include: number of success transfers, number of accidental drops, time spent per transfer, and the total distance moved. Fig. 4 summarises the results.

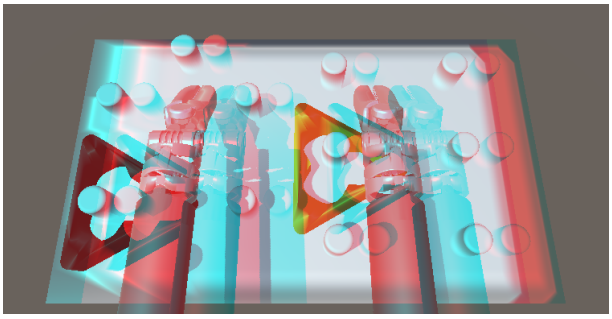

Fig. 3: Stereoscopic scene of the peg transfer task for the usability experiment in anaglyph 3D format.

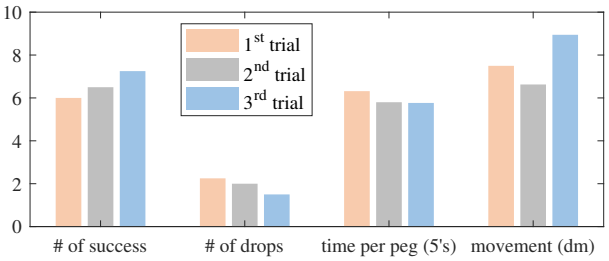

Fig. 4: Results from the user experiment, showing mean values of four performance metrics among all users.

DISCUSSION

The preliminary user study presents improvement in performance over time as indicated by the increasing number of successful transfers and the decreasing number of drops. The performance improvement of the second and the third trial over the first one is 8% and 21% for the number of successful transfers, and 11% and 33% for the number of accidental drops respectively. This suggests that the users could learn and improve their dexterity skills with the robotic simulator over a short period of time.

One common user feedback is the lack of depth perception, which can affect the fidelity of the simulation as well as the performance. To address this limitation, future studies will incorporate a virtual reality headset (Fig. 1), providing 3D visualisation. The studies will also include expert robotic surgeons, which can validate the metrics being used.

REFERENCES

[1] R. H. Taylor *et al.*, "Medical Robotics and Computer-Integrated Surgery," in *Springer Handbook of Robotics*, 2016, pp. 1657–1684.

[2] D. Alimisis, M. Vicentini, and P. Fiorini, "Towards a problem-based training curriculum for surgical robotics: the SAFROS project," in *Proc. of EdMedia: World Conference on Educational Media and Technology*, 2011, pp. 297–302.

[3] A. N. Sridhar *et al.*, "Training in Robotic Surgery-an Overview." *Current urology reports*, vol. 18, 2017.

Gravity Compensation Control for Magnetic Capsule Colonoscopy

L. Barducci[1], G. Pittiglio[1], J. W. Martin[1], J. Norton[1], K. L. Obstain[2], C. A. Avizzano[3], and P. Valdastri[1]

[1]STORM Lab UK, University of Leeds

[2]STORM Lab, Vanderbilt University

[3]PERCRO, Scuola Superiore Sant'Anna

{l.barducci, g.pittiglio}@leeds.ac.uk

INTRODUCTION

In the present paper, we discuss a novel approach to force control for the Magnetic Air Capsule (MAC) [1]. This magnetically actuated robotic system was introduced for painless colonoscopy, since able to reduce tissue stress. In fact, as the guidance is performed by magnetically actuating the capsule tip, tissue deformation is limited.

The advantages of using permanent magnets, one external (External Permanent magnet (EPM)) and one inside the capsule, over electromagnetic actuated systems (e.g. [2, 3, 4]), are the limited size of the platform and energy consumption. This is paid by some lack of controllability, to be balanced with accurate and effective control techniques.

The limitations of previous works, concerning the control of the MAC, are related to the absence of a closed-loop control of the force and control in the z direction [5]. Therefore, force is not ensured to converge to the required value and the imposed coupling force leads the capsule to exert excessive force on the colon wall. The latter turns into being more invasive and reduces smoothness of motion due to an increase in friction, presence of folds and deformation of the wall.

We instead propose an innovative control method for smooth guidance of the tethered capsule through the colon which, by counteracting gravity, achieves levitation of the capsule itself. Compared to the previous solutions, this achieves smooth and almost contact-free driving of the capsule. Moreover, we avoid complex actuation systems, in contrast with [4], and simplifications given by navigating in a fluid medium [6].

In the following we discuss the proposed control technique and report preliminary experimental results. The latter show the promise of the proposed technique in terms of navigating in a colon phantom.

MATERIALS AND METHODS

In the following we describe a backstepping control [7] approach for gravity compensation.

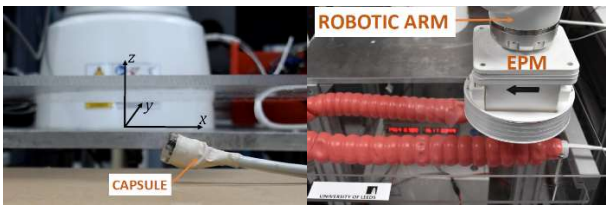

(a)Free-space Levitation (b) Experimental setup

Fig. 1 Experimental Analysis.

We assume the EPM and capsule to be modelled as magnetic dipoles whose interaction force can be computed as $\tau = f(x, q)$ [5]. Here, x is referred to as the capsule pose and q as the robot joint configuration. We consider the overall dynamics of the system as being composed by the capsule dynamic equilibrium and force dynamics, i.e.

$$\begin{cases} \tau = M(x)\ddot{x} + C(x, \dot{x})\dot{x} + G(x) \\ \dot{\tau} = J_x \dot{x} + J_q \dot{q} \end{cases}$$

where $M(x)$ is the capsule inertia, $C(x, \dot{x})$ Coriolis matrix and $G(x)$ gravity; $J_x = \frac{\partial f}{\partial x}$ and $J_q = \frac{\partial f}{\partial q}$.

The control technique is divided into two steps. First, we compute the required torque for the capsule to approach a desired configuration x_d

$$\tau_d = G(x) + K_p e_x + K_d \dot{e}_x$$

where $e_x = x - x_d$ and x is derived from magnetic localization [8], while K_p and K_d are the controller design parameters. We infer that this control law achieves stability of the equilibrium $(e_x, \dot{e}_x = 0)$ as long as[1] $\dot{x}_d = 0$.

Given the required force τ_d, the robot joint trajectory is computed as

$$\dot{q} = J_q^{+}(\dot{\tau}_d + K e_\tau - J_x \dot{x})$$

with $e_\tau = \tau_d - \tau$ and K is a design parameter.

This guarantees the capsule to approach the desired configuration.

RESULTS

Experiments were performed on the setup in Fig. 1 The Kuka LBR Med robot [2] was employed for the manipulation of the EPM. A cylindrical permanent magnet with diameter and length of 10.16 cm was used. The magnet has axial magnetization with residual flux

[1] This can be achieved by designing a constant piecewise trajectory.

[2] https://www.kuka.com/en-de/industries/healthcare/kuka-edical-robotics

density of 1.48 T. A synthetic phantom of a colon was posed on a bench and a first tract of 300 mm kept straight. Experiments were performed in this section of the colon only.

In order to prove the strength of the proposed approach,

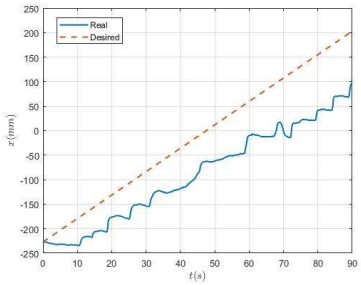

Fig. 2 Position on the x axis.

20 trials of 90 s each were performed. For each of them, the distance travelled was computed to demonstrate the colon can be navigated at a reasonable speed.

Fig. 2 and 3 report the results of one of the trials, presenting the position of the capsule along the x and z axis[3], as measured by the localization system [8] with accuracy of approximately 4 mm. In Fig. 2 the comparison between the desired and the real position along the x axis can be appreciated. Overall the mean absolute error was found to be 140 mm with standard deviation 67 mm. However, accuracy is not the main focus of the present work. In Fig. 3 the capsule oscillation along the z axis is observed: this is due to the capsule attempting to levitate.

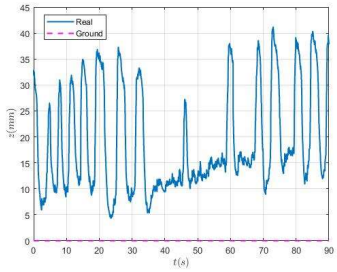

Fig. 3 Position on the z axis.

The mean value of the distance travelled was found to be 214 mm, with a standard deviation of 71 mm. Therefore, the mean velocity can be inferred to be around 2.4 mm/s with a standard deviation of 0.8 mm/s. The velocity of the proposed approach is comparable to the one obtained in open loop and lower than standard colonoscopy [1].

Fig. 4 compares the desired force on the z axis with the gravity acting on the employed capsule, whose weight is 0.016 Kg. Fig. 3 and 4 underline that levitation leads to marginally stable equilibria. Therefore, future work will focus on more robust control design.

DISCUSSION

In the present paper a novel technique for control of a magnetic capsule for robotic assisted colonoscopy was presented. Our main aim was to prove that compensating gravity, would reflect into a smoother navigation through the colon.

In fact, levitating the capsule reduces friction, tissue deformation and achieves obstacle avoidance.

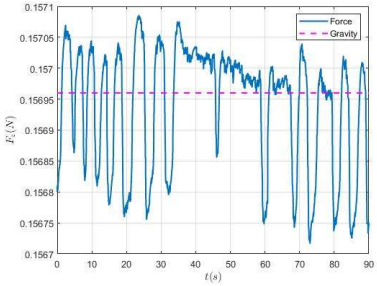

Fig. 4 Force on the z axis.

The experimental results reported prove that straight trajectories can be followed as fast as applying a non-autonomous open-loop control. This is due to the fact that low amount of force is exerted on the colon wall, compared to previous closed-loop solutions. Nevertheless, more effective and faster guidance is to be investigated.

Future work will be focused on reducing oscillations and performing a completely autonomous trajectory in the whole colon.

REFERENCES

[1] A. Arezzo, A. Menciassi. Experimental assessment of a novel robotically-driven endoscopic capsule compared to traditional colonoscopy. Digestive and Liver Disease. 2013;45 (8):657-662.

[2] J. Edelman, A. Petruska. Estimation-Based Control of a Magnetic Endoscope without Device Localization. Journal of Medical Robotics Research. 2017 Dec, 1-10.

[3] C. Chautems, B. J. Nelson. The tethered magnet: Force and 5-DOF pose control for cardiac ablation. IEEE International Conference on Robotics and Automation. 2017, 4837-4842.

[4] M. Miyasaka, P. Berkelman. Magnetic levitation with unlimited omnidirectional rotation range. Mechatronics. 2014, 24 (3):252-264.

[5] A. Z. Taddese, P. R. Slawinski. Nonholonomic closed-loop velocity control of a soft-tethered magnetic capsule endoscope. International Conference on Intelligent Robots and Systems (IROS). 2016 Oct, 1139-1144.

[6] A. W. Mahoney, J. J. Abbot. Five-degree-of-freedom manipulation of an untethered magnetic device in fluid using a single permanent magnet with application in stomach capsule endoscopy. The International Journal of Robotics Research. 2016, 35 (1-3):129-147.

[7] A. J. Koshkoue, A. S. I. Zinober. Adaptive backstepping control of nonlinear systems with unmatched uncertainty. IEEE Conference on Decision and Control. 2000, 5: 4765-4770.

[9] A. Z. Taddese, P. R. Slawinski. Enhanced Real-Time Pose Estimation for Closed Loop Robotic Manipulation of Magnetically Actuated Capsule Endoscopes. International Journal of Robotics Research. 2018, in press, available on line.

[3] The capsule moves orthogonal to the y axis, so no information is embedded in its plot.

DATA MINING USING A SOFT ROBOTIC BALLOON CATHETER: SIZING IDEALISED AORTIC ANNULAR PHANTOMS

Andrea Palombi[1], Giorgia M Bosi[1], Sara Di Giuseppe[2], Elena De Momi[2], Shervanthi Homer-Vanniasinkam[1], Gaetano Burriesci[1,3], Helge A Wurdemann[1]

[1]*UCL Mechanical Engineering, University College London, London WC1E 7JE, UK.*

[2]*Electronic Information and Bioengineering Department, Politecnico di Milano, Italy.*

[3]*Bioengineering Group at Ri.MED Foundation, 90133 Palermo, Italy.*

INTRODUCTION

Despite its evolution over the past decade, transcatheter aortic valve implantation (TAVI) is still affected by some major intra-operative complications like aortic regurgitation and atrioventricular blocks. Residual mild paravalvular leaks, associated with higher mortalities at two years, are reported in up to 61% of patients after TAVI [1]. The rate of permanent pacemaker implantation, due to atrioventricular blocks, varies between 12% and 33%, depending on the type of prosthetic valve [1]. Choosing the right valve size is crucial to prevent these complications. According to current recommendations, the prosthetic valve is selected based on pre-operative data, acquired with transesophageal or transthoracic echocardiography [2]. However, it has been demonstrated that measurements taken on echocardiographic images lead to an underestimation of the annular diameter of up to 3mm [2]. Multidetector computer tomography (MDCT) has been used to obtain a more accurate 3D reconstruction of the aortic root [3]. Nevertheless, MDCT has some procedural limitations. The risk of contrast nephropathy is very high in patients with renal morbidity, which is quite common in elderly people affected by AS [2]. Furthermore, both approaches do not consider potential changes in the annular geometry introduced by valvuloplasty, which is often undertaken immediately prior to deployment of the prosthetic device [4]. In this work, we propose a new approach to determine the diameter of the aortic annulus, exploiting intra-balloon pressure and volume data, acquired from a robotised valvuloplasty balloon catheter.

MATERIALS AND METHODS

A commercially available non-compliant valvuloplasty balloon catheter (Edwards 9350BC23, Lifesciences, Irvine, CA, US) was interfaced with a robotic system (Fig. 1), composed of a motorised rapid-prototyped syringe pump, a pressure transducer (PXM319-007A10V, Omega Engineering Inc., US) and an Arduino Uno microcontroller. The platform is entirely managed by a program developed in Processing, an open-source Java-based programming language and integrated development environment. The program relies on the Firmata protocol, which is implemented in the firmware uploaded on the Arduino, to communicate with the microcontroller via USB cable. The modality of operation (Inflation/Deflation) and the amount of fluid to be injected/retrieved are specified through a graphical user interface (GUI). Inputs from the GUI are fed to an automated routine, which drives the stepper motor and regulates data acquisition. At the end of the routine, a text file, containing an absolute pressure value and a volume value, for each step executed by the motor, is exported.

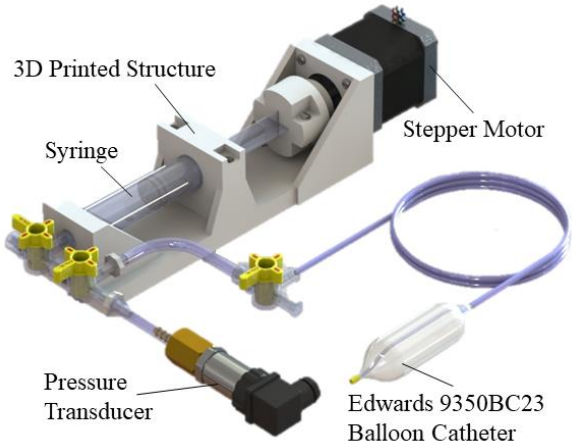

Fig. 1 Soft Robotic Balloon Catheter: the valvuloplasty balloon catheter is interfaced with a motorised inflation device, equipped with a pressure transducer.

The balloon was modelled as a pressurised cylindrical thin-walled vessel with hemispherical ends, to retrieve an analytical expression of its pressure-volume (p-v) free inflation curve and establish a direct mathematical relationship between its diameter and the intra-balloon pressure. The parameters of the model were adjusted, according to measurements on the actual device and experimental free inflation data.

The sizing algorithm was implemented in Matlab (MathWorks, Natick, MA, US). The algorithm is built upon the assumption that the diameter of the balloon, measured at the time when full contact with the annular walls is first attained, equals the annular diameter. Therefore, sizing can be performed indirectly by identi-

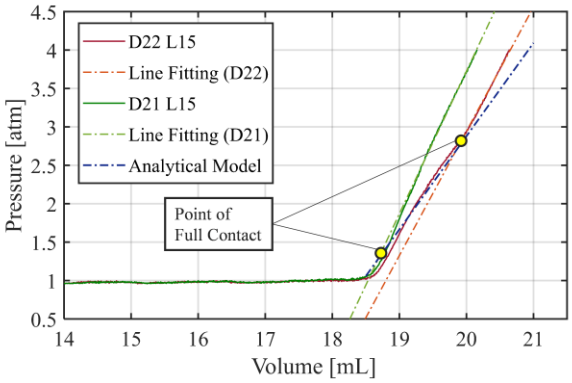

Fig. 2 Example of iterative linear regression performed on *p-v* curves, obtained from experimental valvuloplasty on idealised annuli with diameters of 22 and 21 mm (and 15 mm length).

fying the point within the acquired dataset, at which the *p-v* curve deviates from the analytical free inflation curve, and estimating the corresponding balloon diameter. This is achieved by iteratively performing linear regression on the *p-v* dataset. In each iteration, the data point with the lowest volume value is removed, a line is fitted to the updated dataset and the associated root-mean-square-error (RMSE) is extracted. The process stops when the RMSE is smaller than an empirically set threshold. Thus, the equation of a line, which approximates the portion of the processed *p-v* curve deviating from the free inflation curve, is obtained (Fig. 2). The symbolic mathematical capabilities of Matlab can then be exploited to find the desired point as the intersection between the fitted line and the analytical free inflation curve. The corresponding pressure can be used to estimate the diameter from the balloon mathematical model.

The proposed approach was tested on idealised rigid circular phantoms, made of stackable acrylic plates. Five different diameters (18, 19, 20, 21 and 22 mm) and two different lengths (15 and 20 mm) were investigated, to consider typical balloon-annulus sizing ratios and reported annular length variability in adult human aortic valves. During a series of experimental tests, the balloon was inflated at a constant flow rate of 0.076 ml/s until the intra-balloon absolute pressure reached 4 atm.

RESULTS

Our experimental results show that *p-v* data can be used to determine annular diameters, if the unstretched diameter of the balloon catheter (20.75mm for the Edwards 9350BC23) is smaller than the annular diameter. For these cases, the proposed approach exhibits good repeatability and high accuracy (Tab. 1).

For annular diameters smaller than the unstretched diameter of the balloon catheter, the point at which the *p-v* curve departs from the free inflation curve highly depends on both the annular diameter and length. Therefore, it is impossible to obtain a direct and unbiased estimation of the annular diameter from basic considerations on *p-v* data.

Nominal Diameter [mm]	Annular Length [mm]	Measured Diameter [mm]	Error [%]
22	20	22.002±0.03	0.01
22	15	22.204±0.11	0.93
21	20	20.908±0.05	0.44
21	15	21.133±0.10	0.63

Tab. 1 Nominal Annular Diameters vs Experimental Measurements (five tests for each phantom configuration).

DISCUSSION

The proposed solution can be integrated with standard balloon catheters, already used in routine clinical practice, to obtain a precise estimate of the annular diameter. This could be employed, alongside traditional sizing methods, to potentially make the TAVI device selection more accurate and prevent major complications, like aortic regurgitation and atrioventricular blocks.

In real application, rapid ventricular pacing (RVP) is applied during valvuloplasty, to decrease the cardiac output and stabilise the balloon positioning. The average duration of RVP is 30-40 seconds, hence the balloon needs to be inflated within a relatively short time. In future work, tests at higher injection flow rates will be performed and the impact of dynamics effects on the proposed method will be assessed. We will also investigate a mathematical model of the balloon which considers non-linearities of the balloon material and large deformations. An accurate finite element model of the balloon is currently under development. Further, the proposed approach will be tested on compliant aortic annular phantoms connected to a system capable of mimicking the pulsatile blood circulation. In principle, the proposed approach would work on compliant phantoms as well, given that their stiffness produces a detectable deviation in the p-v curve from the free inflation curve. Intra-balloon pressure and volume data will then be used to assess the mechanical properties of the aortic annulus. This will provide the operator with supplementary helpful information for TAVI device selection.

REFERENCES

[1] Helge Möllmann et al., *Heart*, 2015; 101: 900-908.
[2] Daniel Kretzschmar et al., *Clinical physiology and functional imaging*, 2016; 36(2): 99-105.
[3] David Messika-Zeitoun et al., *Journal of the American College of Cardiology*, 2010; 55(3):186–194.
[4] D. T. Murphy et al., *Journal of cardiovascular computed tomography*, 2016; 10(1): 37-43.

ACKNOWLEDGEMENTS

This work was supported by the Engineering and Physical Sciences Research Council (grant number: EP/N509577/1).

Comparison of Master-Slave Mapping Strategies for Efficient Robotic Endoscopy

J. Ahn[1], M. Hwang[1], D. Baek[1], H. Kim[1], D.S. Kwon[1]

[1]*Department of Mechanical Engineering, Korea Advanced Institute of Science and Technology (KAIST)*

wjdehwwkd@kaist.ac.kr

INTRODUCTION

With introduction of robotic technology, there have been noticeable improvements in endoscopic surgery. In robot surgery, surgeon manipulates master device to manipulate robotic surgical end effector equipped with endoscope. Master-slave mapping can be defined as kinematic correlation between master device and slave robot. It is considered to be very important in tele-operated robotic surgery because it has large impacts in terms of surgeon's workload, usability, and performances. Currently, the position mapping method of robotic surgical tools is well-established in most of the commercialized surgery robots such as da Vinci or ZEUS [1,2]. However, operation method of endoscope has not been established yet. In particular, it is necessary to study the operation control method of flexible endoscope which can pass through bending organs of human body such as gastroscopy or colonoscopy. Waseda university conducted a quantitative analysis for the control method using a graphic simulator of endoscopic manipulator which has three degrees of freedom at the end of a rigid overtube [3]. As an extension of the existing studies, we aim to conduct in-depth analysis using our developed flexible endoscopic platform. We believe that this study will improve the efficiency and precision of endoscopic manipulation, and have a great effect on outcome of surgery.

MATERIALS AND METHODS

This study was conducted using K-FLEX, a flexible endoscopic surgery robot for Natural Orifice Transluminal Endoscopic Surgery (NOTES) [4]. It consists of a bendable overtube, surgical instruments, and a master device (Figure 1). In this study, we compared the performance using two representative methods of master and slave mapping strategy. 1) "P mode" controls the position of slave corresponding to the position of master. 2) "V mode" controls the velocity of slave corresponding to the position of master. As shown in Fig. 2, we performed a marking test which simulates marking of ESD in endoscopic surgery. Subjects was commanded to touch the dots on a test board with the surgical tool of overtube using the master device following each mapping strategy. The efficiency and precision of the endoscopioc control were measured quantitatively by measuring time taken for a given test. The dimension of the test board used in the experiment is shown in Fig. 3. The test for measuring the efficiecy of each mode is to measure the time required to touch eight points of 2.5 mm diameter arranged in the circumference of a diameter of 30 mm and 150 mm using the surgical tool inserted in the channel of the overtube. The test for measuring the

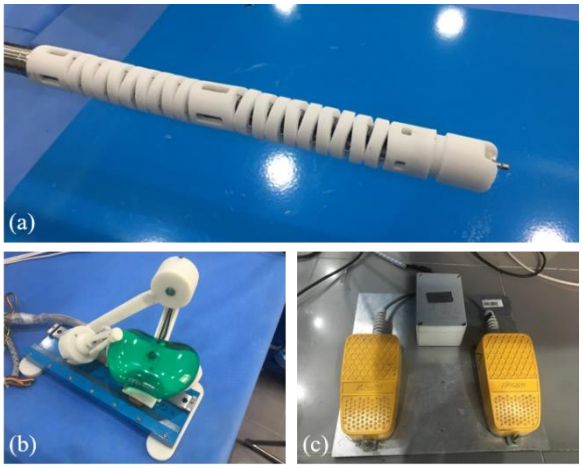

Fig. 1 System components of K-FLEX. (a) The overtube has four degrees of freedom (DOF), one translation movement and three rotation movements(roll, pitch, yaw). (b) The master device has the same kinematic structure with overtube except grasping. (c) Foot clutch is used to extend the master device's working space.

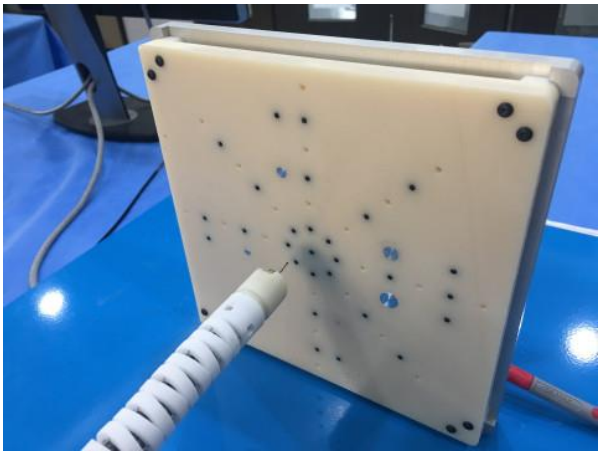

Fig. 2 Experimental set up for marking test. Efficiency and precision of endoscopic control can be measured using the benchtop test board.

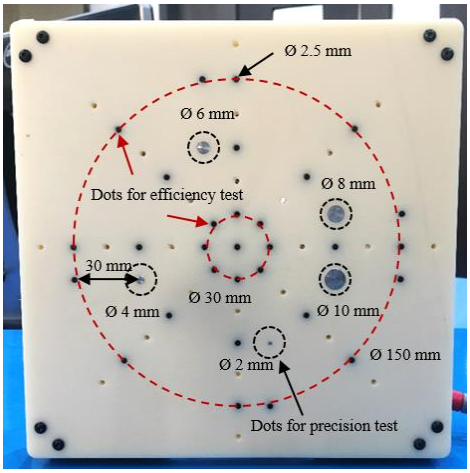

Fig. 3 Dimension of test board. Red dashed line circles represent the 8 dots for efficiecy test. Black dashed line circles represent the dots for precision test.

precision of each mode is to measure the time required to touch the points 2, 4, 6, 8, and 10 mm diameter at a distance of 30 mm from the point 2.5 mm diameter using the surgical tool inserted in the overtube. In position mode, the distance that an overtube can be moved at a time without a clutch operation is 40 mm. Four subjects participated in each test and a sufficient number of exercises were conducted before the test to eliminate errors due to unskilled operation.

RESULTS & DISCUSSION

- Efficiency test

Figure 4 shows the results of the efficiency test. In an experiment that touches 8 dots on a circle with a diameter of 30 mm, "P mode" took about 2.7 times less than "V mode" on average.If the diameter become larger to 150mm, "P-mode" took about 2.2 times less than "V mode" on average.

- Precision test

It was shown in the Fig. 5 that The task time was measured lower in "P mode" than "V mode" regardless of diameter of the dot. In particular, the test time required for precise operation(touching the small diameter dot) was significantly different between the two modes, and the difference in operation time between the two modes decreased with the test of touching the large diameter dot.

Through the efficiency test and the precision test, the "P mode" is suitable for precise moving work for the image of the surgical site, and the "V mode" which does not use the clutch could be expected to be a suitable mode for rough operation such as rapid movement to the approximate position of the surgical site after inserting the overtube into the body.

CONCLUSION

In this study, we quantitatively tested the efficiency and precision of the mapping strategy between the flexible overtube and the master device. It was confirmed from the tests that "P mode" is superior in terms of efficiency

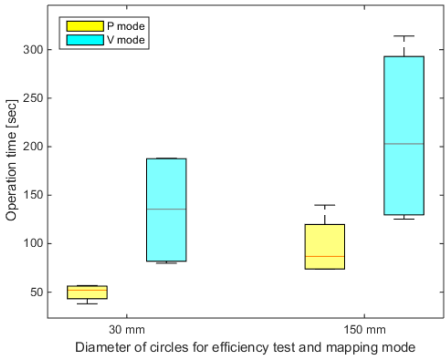

Fig. 4 Operation time for each control mode to verify the efficiency performance.

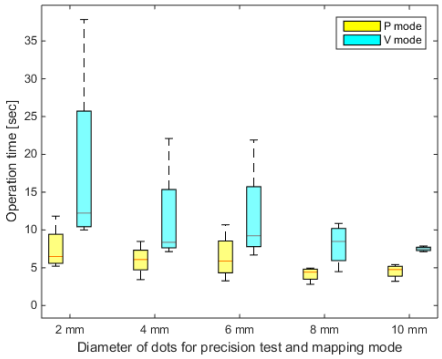

Fig. 5 Operation time for each control mode to verify the precision performance.

and precision by completing the given test at a time faster than "V mode". However, in the "P mode", the workload of the subject tended to increase because of the repetitive use of the clutch when moving a long distance. This can increase the workload of the surgeon performing the long operation. As a further work, we will study a new mapping strategy which combines the operability of "P mode" and the advantage of "V mode" which does not need to use clutch. Also, other metrics such as robot tip path length, and positioning accuracy will be applyied for reliable evaluation.

REFERENCES

[1] GUTHART, Gary S.; SALISBURY, J. Kenneth. The Intuitive/sup TM/telesurgery system: overview and application. In: Robotics and Automation, 2000. Proceedings. ICRA'00. IEEE International Conference on. IEEE, 2000. p. 618-621.

[2] REICHENSPURNER, Hermann, et al. Use of the voice-controlled and computer-assisted surgical system ZEUS for endoscopic coronary artery bypass grafting. The Journal of thoracic and cardiovascular surgery, 1999, 118.1: 11-16.

[3] NOGUCHI, Takehiko, et al. Application of control modes of a master manipulator for a robotic system to assist with single port endoscopic surgery. In: Intelligent Robots and Systems (IROS), 2012 IEEE/RSJ International Conference on. IEEE, 2012. p. 1270-1276.

[4] Minho Hwang, Dong-soo Kwon, Surgical joint with enhanced payload capability with its application to flexible endoscopic surgery robot, Ph.D. Dissertion, 2017

Image-based Estimation of Contact Forces on Catheters for Robot-assisted Cardiovascular Intervention

Amir Hooshiar[1,3], Naghmeh M. Bandari[1,2,3], and Javad Dargahi[1]

[1]*Robotic Surgery Lab., Concordia University, Montreal, Canada*
[2]*Optical Bio-Microsystems Lab., Concordia University, Montreal, Canada*
[3]*Surgical Innovation Program, McGill University, Montreal, Canada*
{*s_hooshi, nag_moha, dargahi*}*@encs.concordia.ca*

INTRODUCTION

Clinicians have reported the loss of haptic feedback during robot-assisted cardiovascular intervention (RCI) as the most challenging limitation of the state-of-the-art. It is also a risk factor of vascular perforation. To alleviate this problem, researchers have postulated using embedded force/torque sensors at distal or proximal end of catheters. However, this integration is impossible for the coronary catheters due to the small diameter. Another alternative is model-based haptic force estimation. Current literature show that the model-based estimation of contact forces on intravascular catheters has been used merely for simulation purposes, e.g. virtual reality. In such models, contact forces on the catheter are estimated using a contact treatment algorithm upon contact detection. The main limitation of model-based techniques is being computationally expensive and depending on a preoperative CT or MR scan. In this study, a novel image-based algorithm is proposed for fast and accurate contact detection and contact force estimation on catheter.

MATERIALS AND METHODS

Summary of the proposed framework for provision of image-based haptic feedback is presented in Fig.1. This study was a preliminary study on the feasibility of using image-based catheter contact detection and force estimation. To this end, the real-time image processing was implemented using OpenCV 3.2 in C++. A C920 camera (Logitec, Switzerland) was used for image acquisition (600 × 800 pixels resolution). Camera was calibrated using a 19 × 12, chessboard with 10mm edge size. Each frame was converted to greyscale and the boundary edge of the catheter was extracted using a KNN background remover. KNN background removal is a subtractive method applicable to greyscale images. Similar method for catheter extraction is reported in [2, 3]. To parameterize the shape of catheter, horizontal (H) and vertical (V) coordinates of each point on the boundary was interpolated using Eq.1. Furthermore, due to high slenderness of catheter, the curvature κ along the catheter was calculated using Eq. 2.

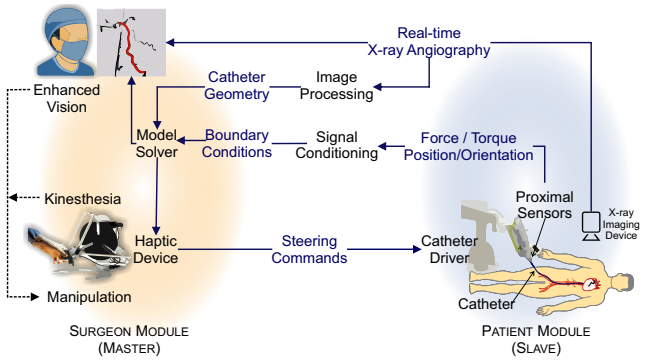

Fig. 1: Conceptual representation of the poroposed framework for provision of image-based haptic feedback.

$$\phi_{H,V}(s) = \sum_{i=0}^{5} C_i^{H,V} s^i, \tag{1}$$

$$\kappa = \frac{\phi_H^{''}(s)}{\phi_V^{''}(s)} = \frac{20C_5^H s^3 + 12C_4^H s^2 + 6C_3^H s + 2C_2^H}{20C_5^V s^3 + 12C_4^V s^2 + 6C_3^V s + 2C_2^V}, \tag{2}$$

where $(.^{''})$ denotes the second derivative with respect to s. In this study, for the first time and based on the beam theory, the locii of contact points were identified as where the second derivative of curvature κ was singular. To obtain the unknown contact forces, the catheter was modeled as an Euler-Bernoulli beam. Problem was formulated as a 2D finite element model, clamped at $s = 0$, subjected to N unknown shear forces. Beam model was discretized with 50 linear beam elements. Given the location s of contact points from Eq. 2, magnitude of unknown contact force were optimized by solving constrained minimization problem defined by (Eq. 3-4). Eq. 3 ensured FEM would converge to a catheter deformation (u_{FEM}) matching the image-extracted deformation u_{img}, while constraint Eq. 4 enforced the contact forcea being zero at points without contact (F_{NC}). Problem was solved using a particle swarm optimization technique with initial points of 50, inertia, cognitive and social coefficients set as 0.5. The solution was implemented using GPU-accelerated Armadillo linear algebra library in C++.

$$argmin(||u_{FEM} - u_{img}||), \tag{3}$$

$$||F_{NC}|| = 0 \quad (4)$$

Flexural rigidity, EI of 5 identical 6Fr. catheters (Runway^{TM}, Boston Scientific, MA, US) were calculated through three-point bending (3PB) tests. To replicate an RCI, a PID-controlled motorized (Faulhaber Group, Stuttgart, Germany) catheter introducer was built. Using System Identification toolbox of Matlab R2018a, PID coefficients were optimized for 5% overshoot and 1% steady-state error in position control ($K_P = 20, K_I = 0.5, K_D = 5$). A simple planar vascular phantom was prototyped and equipped with four calibrated force-sensing linear potentiometers (FSLP) (Pololu Corp., NV, US) for simultaneous measurement of contact position and force. The contact detection and force estimation was performed during catheter insertion with rate of $20mm.sec^{-1}$ (RCI experiment). RCI experiment was repeated 5 times. The hypotheses of difference between measured and estimated contact points and forces were tested using a Wilcoxon's signed-rank test ($p < 0.05$). Fig. 2 depicts the setup used in RCI experiment.

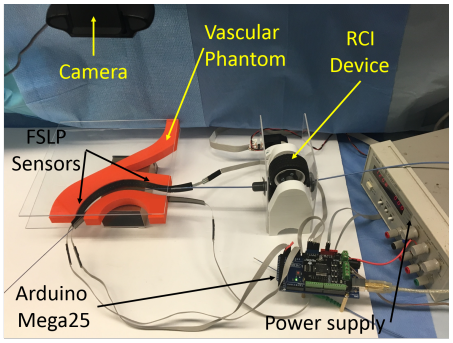

Fig. 2: Setup for RCI experiments.

RESULTS

Results from 3PB test indicated the flexural rigidity of catheters($n = 5$), EI as $723.69 \pm 31.66 N.mm^2$. Computation time of shape extraction and optimization was $23msec$ per frame (refresh rate: 43Hz). Range of contact force measured by sensors in 3PB and RCI was $0 - 0.45N$ and $0 - 0.36N$, respectively and average Euclidean norm of F_{NC} was $0.013 \pm 0.007N$, and $0.016 \pm 0.004N$ for 3PB and RCI, respectively. Range of variation and root-mean-square of error (E_{rms}) for contact location and force estimation are reported in Table 1. Fig. 3 depicts a snapshot of the results for contact detection.

Table 1: Error of model estimations vs. sensor measurements for five repetition of each test (n=5).

	Criterion	$\mathbf{E}_{min}$-$\mathbf{E}_{max}$	$\mathbf{E}_{rms}\pm$**SD**
3PB	Contact locations (mm)*	$0.7 - 9.4$	4.1 ± 0.74
	Contact force (N)*	$0.00 - 0.08$	0.04 ± 0.02
RCI	Contact locations (mm)*	$0.5 - 13.2$	6.7 ± 0.46
	Contact force (N)*	$0.00 - 0.06$	0.02 ± 0.09

*:significant difference wan not observed with $p < 0.05$

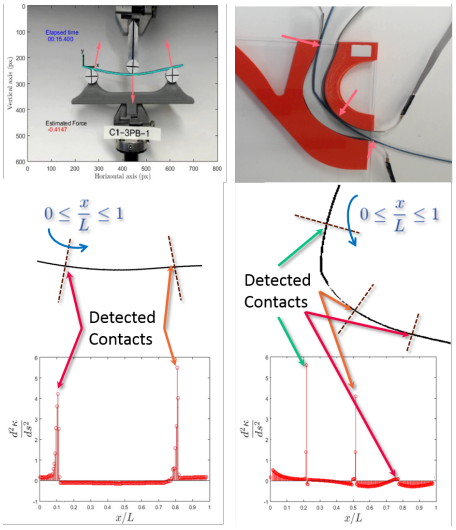

Fig. 3: Snapshot of catheter segmentation, contact point detection, and force estimation results: (left) 3PB, (right) RCI.

DISCUSSION

The proposed curvature-based contact detection was fairly successful and small Euclidean norm of F_{NC} showed fair accuracy of the FEM model. However, its diversion from measurements increased as catheter curvature increased. The reason might be due to non-captured geometric non-linearities. Based on descriptive statistics in Table 1, the observed error in this study was less than that of [1] and [4]. Also, accuracy of deformation extraction was comparable to that of [3]. Similarly, both measured and estimated contact forces were in fair agreement with experimental data in [1][3]. Wilcoxon's signed rank test confirmed no significant difference between estimations and measurements ($p < 0.05$). In conclusions, this study primarily showed the success and feasibility of using the proposed novel image-based haptic force estimation. Also, independency from prior knowledge of vascular geometry and ability to incorporate available x-ray images are the most prominent advantages of the postulated method. Future direction of this study is to use more realistic vascular phantom, consider the geometric non-linearity, and utilization of a computationally cheap multi-body catheter models.

REFERENCES

[1] Hasanzadeh S, Janabi-Sharifi F. Model-based force estimation for intracardiac catheters, IEEE/ASME Trans. on Mechat. 2016;21:154-162.

[2] Khoshnam M, Skanes AC, Patel RV. Modeling and estimation of tip contact force for steerable ablation catheters IEEE Trans. on Biomed. Eng. 2015; 62:1404-1415.

[3] Dalvand MM, Nahavandi S, Howe RD. Fast vision-based catheter 3D reconstruction, Phys. in med. and biol. 2016;61:5128-5148.

[4] Thakur Y, Holdsworth D, Drangova M. Design and performance evaluation of a remote catheter navigation system, IEEE Trans. on Biomed. Eng. 2009; 56:2140-214

A Simulation Study of Robotic In Utero Repair of Myelomeningocele

Thomas Looi[1,2], Francis Lebouthillier[3], Tim Van Mieghem[4], Greg Ryan[4], James M. Drake[1,2]

[1]The Hospital for Sick Children, Canada [2] University of Toronto, Canada [3]Ontario College of Art and Design, Canada [4]Mount Sinai Hospital, Canada

thomas.looi@sickkids.ca

INTRODUCTION

Myelomeningocele (MMC) is a type of neural tube defect where a portion of a baby's spinal cord presents on the skin usually in the lumbar region. The incidence rate of neural tube defects range from 0.17 to 6.39 per 1000 live births. [1] Babies born with MMC often develop hydrocephalus, lower limb motor dysfunction, and bladder, bowel and sexual dysfunction. Standard post natal treatment includes surgical repair of the lesion by replacing the spinal cord into the spinal canal and closing the soft tissues over top. Cerebrospinal fluid (CSF) shunting is required in 80-90% of patients, exposing them to the life long risk of shunt complications including shunt infection and failure which are common.

Open prenatal repair, via hysterotomy, was shown to significantly reduce CSF shunt inseration rate (40% vs 80%) and to increase independent ambulation in a large NIH funded trial [2] This procedure however requires opening the uterus surgically (hyserotomy) and is associated with preterm delivery and significant maternal morbidity. This has motivated surgeons to perform fetoscopic surgery as a minimally invasive approach. These procedures however, are technically very complex. Some groups have developed a method in which they facilitate the procedure by covering the defect with a patch, rather than performing a full resection and coverage. More recently, a group has shown that full dissection and repair can be perfomed with a 2-port technique, be it at the cost of very lengthy operation times (average 246 mins). [3]

The use of straight rigid instruments in both a single and dual port approach is a challenge for surgeons to operate and in particular perform the suturing task. While possible, the current fetoscopic procedure is very time consuming and technically demanding. Hence, the goal of this pilot study is to investigate the potential of using a DaVinci SI system to perform an in-utero repair of MMC in a pregnant phantom model.

MATERIALS AND METHODS

A Davinci SI (Intuitive Surgical, Sunnyvale) is used as the surgical platform with an 8.5mm 30 degree endoscope and 2 – 8mm trocar ports. For the procedure, the maternal and neurosurgeon used a combination of large needle driver, forceps and curved scissors. The phantom model is the Universal Maternal Abdomen (UMA by Surgical Touch Simulators, Toronto) which is used for fetoscopic procedure training. The model simulates a 23 week gestation period with 3 pre-existing ports for inserting tools. The silicone belly also allows for creating customized ports while the cavity can be filled with fluid and sealed to simulate the amniotic sac. See figure 1 for the phantom model.

Fig 1 - Universal Maternal Model

A raw chicken breast with skin is used to represent the MCC and it inserted in to the fetus where it has an opening in the lumbar spine. The fetus is placed into the abdomen and UMA is centered about the DaVinci SI. The endoscope is inserted through the centre belly button port and adjusted to provide the required viewing angle. Two 8mm trocars are inserted laterally approximately 6.8 cm on either side of the camera. An 3-4 cm skin elipse was excised from the chicken breast to emulate the MCC. The camera view was evaluated by materanal and neurosurgical staff.

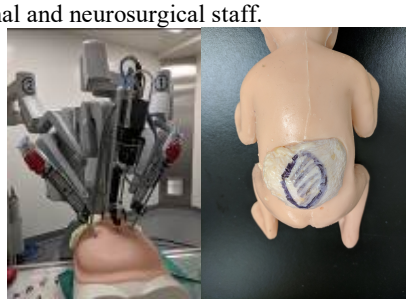

Fig 2 - Left: DaVinci Setup, Right: MCC Pathology

For the repair timing, a neurosurgeon mobilized the skin widely along the defect from the underlying subcutaneous tissue and muscle, akin to the procedure in a human patient. A 5-0 PDS suture through one of the trocars in to the abdominal cavity. A running stitch was used to re-approximate the skin edges under reasonable tension. The suturing and skin-to-skin time was recorded. After the procedure was completed, the fetus was removed and visually inspected for closure. Timing studies were done for each section of the procedure (skin elipse, mobilization and suturing). The procedure was also repeated with the 5mm diameter tools to determine if the smaller tools assisted in reducing collisions and providing more space in the

abdominal cavity. Smaller diameter tools and trochars would also be an advantage in terms of minimizing disruption of the uterine wall, and amniotic membranes.

RESULTS

The DaVinci endoscope provided sufficient depth and viewing angle for the maternal and neurosurgeon to view and examine the MCC lesion. See Figure 3 for a typical cross section camera, endoscope and completed result.

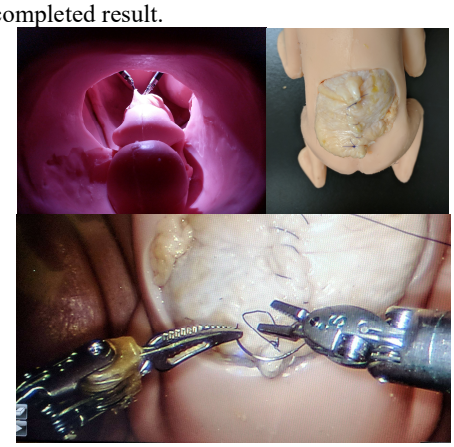

Fig 3 – Top left: Internal cross section, Top right: Resultant repair, Bottom: Endoscope view

Using the 8mm diameter tools, the neurosurgeon was able to reach and manipulate the tissue. The surgeon successfully sutured and closed the MCC. The tasks were repeated 4 times. Table 1 shows the average duration for each task.

Task	Duration (min)
Skin elipse (placode)	2.0
Mobilization	2.0
Suturing	11.3

Table 1 – Timing study of surgical tasks

The duration for the first time conducting the task was the longest where subsequent testing had a noted decrease (20-25 mins vs 15 mins). The total skin to skin time was less than 50 minutes. A visual inspection of the repair site revealed tight apposition of the suture line, without any tears, openings, or other unintended injury to surrounding areas.

With the 5mm diameter tools, the neurosurgeon was also able to successfully close the MCC with similar procedure duration and efficacy from visual inspection. There appeared to be no difference in the duration between the 5mm vs 8mm tools. In terms of internal and external collisions, there was no reported issues with either set of tools.

DISCUSSION

The DaVinci SI can be successfully used for minimally invasive in-utero repair of a simulated MCC in a phantom and may be a candidate technology for human patients. The feedback from clinicians indicated that the increased dexterity of the robotic wrists made the tissue manipulation and suturing much simpler and faster. In comparison to the current straight rigid fetoscopic tools, the dexterous tools significantly reduced the operation time as applied to the three specified tasks. This appears to be a significant improvement over a standard technique. However, the downside of using the DaVinci SI tools is the increased number and size of the trocars required. Previous clinical procedures used smaller diameter tools with fewer ports. As with any fetoscopic procedures, the higher number and large size could increase the trauma to the uterine wall and membranes, potentially predisposing to preterm birth. These effects may be mitigated by the DaVinci remote center of motion which prevents the axial translation and it keeps the tool centered about the MMC. This could also be a potential opportunity to investigate the use of the DaVinci Single Site system which requires one incision. It was also interesting that there was no perceived difference between the 8mm vs 5mm tool. The 5mm diameter tool has a larger bending radius which was not be an issue given the large workspace in the intra-uterine cavity.

It is important to note that this is a pilot study so there will be limitations to the realism of the model and similarity to the procedure. Limited position and orientation of the fetus inside the abdomen was studied and the positioning of the trocars in an optimal location with respect to the MCC was not completed.

For future work, we will compare laparoscopic to robotic repair, improve the realism of the procedure by floating the fetus in simulated amniotic fluid, and replace the chicken breast with an anesthetized rat for dissection and suturing of live tissues. For translation, a detailed workflow analysis will be completed. In general, it appears that the DaVinci SI provides desirable increased dexterity that would enable surgeon to complete the same tasks in a much shorter time. Robotic surgery could provide a positive impact to treating other in-utero conditions that would facilitate improved patient outcomes.

REFERENCES

[1] R. M. Bowman, V. Boshnjaku, and D. G. McLone, "The changing incidence of myelomeningocele and its impact on pediatric neurosurgery: A review from the children's memorial hospital," *Child's Nervous System*, vol. 25, no. 7. pp. 801–806, 2009.

[2] N. S. Adzick, E. A. Thom, C. Y. Spong, J. W. Brock, P. K. Burrows, M. P. Johnson, L. J. Howell, J. A. Farrell, M. E. Dabrowiak, L. N. Sutton, N. Gupta, N. B. Tulipan, M. E. Dalton, and D. L. Farmer, "A randomized trial of prenatal versus postnatal repair of myelomeningocele," *Obstetrical and Gynecological Survey*, vol. 66, no. 6. pp. 340–341, 2011.

[3] M. A. Belfort, W. E. Whitehead, A. A. Shamshirsaz, Z. H. Bateni, O. O. Olutoye, O. A. Olutoye, D. G. Mann, J. Espinoza, E. Williams, T. C. Lee, S. G. Keswani, N. Ayres, C. I. Cassady, A. R. Mehollin-Ray, M. S. Cortes, E. Carreras, J. L. Peiro, R. Ruano, and D. L. Cass, "Fetoscopic open neural tube defect repair: Development and refinement of a two-port, carbon dioxide insufflation technique," *Obstet. Gynecol.*, vol. 129, no. 4, pp. 734–743, 2017.

An Innovate Robot-Assisted Endoscope Holder for Sinus, Skull Base and Otoendoscopic Surgery – From Preclinical Evaluation to First Clinical Use

D.T. Friedrich, R. Grässlin, A. Leichtle, M.O. Scheithauer, T.K. Hoffmann, P.J. Schuler

Department of Otorhinolaryngology, Head and Neck Surgery
Ulm University Medical Center, Frauensteige 12, 89075 Ulm, Germany
daniel.friedrich@uniklinik-ulm.de

ABSTRACT

Introduction An increased number of scientific studies confirm that robot-assisted surgery facilitates the therapy of less accessible pathologies. In addition to surgical manipulation, robot-assisted visualization supports the surgeon by enabling bimanual instrumentation. For head and neck surgeons, this applies especially to endoscopic surgery of the sinuses, the skull base and the middle ear. In this study, we present an innovate robot-assisted endoscope holder and report our findings from preclinical evaluation to first clinical application. **Methods** The multidirectional active endoscope holding system (Medineering GmbH, Munich, Germany) consists of a manually adjustable mechatronic arm with 7 DOF and a load capacity of 2kg, and the actual endoscope robot with 5 DOF actuated by servomotors. The system was tested on human cadaver heads (2) without apparent pathologies, and sought to investigate applicability, controlling, visualization and patient safety in a simulated clinical setup. Endoscope guidance is controlled via foot pedal, leaving the surgeon with both hands free to operate instrumentation. Standard FESS interventions including visualization and manipulation of the frontal skull base were performed, as well as robot-assisted otoendoscopic interventions on the middle ear. After CE-Clearence for transnasal application in March 2018, we could perform a first clinical case. **Results** The system visualizes the interventions with adequate quality and stability, leaving both hands free for instrumentation. Control of the endoscope is effectively precise and enables a sufficient workflow. We successfully performed ethmoidectomy, maxillary antrostomy and sphenoidectomy with preparation of the anterior skull base, as well as transmeatal tympanoscopy, cochleostomy, insertion of a cochlea electrode, transmeatal tympanoplasty and mastoidectomy on both cadaver heads. Furthermore, bilateral ethmoidectomy and maxillary antrostomy were also performed in our first clinical case. **Conclusion** The system enables bimanual instrumentation without additional assistance. Usability has been proven for several interventions in transnasal and otoendoscopic surgery, both basic and advanced procedures. As all manipulation is performed on sight, the risk of accidental damage does not appear to exceed that of conventional endoscope guidance. The workflow in clinical application is satisfactory for basic interventions, with room for improvement. Here, especially the setup time and preparation for surgery is extended. Future investigations will demonstrate, whether the system will prevail in daily routine with potential severe bleeding and a higher demand for dynamic instrumentation. We assume, that the system might be beneficial especially for applications with a rather static perspective and advanced instrumentation, such as skull base interventions and transnasal surgery of the lacrimal ducts. CE-clearence is now obtained for all ENT endoscopic interventions, and an extension of possible indications, including other specialities like Neurosurgery, is another desirable development. To objectify these first impressions, a controlled clinical trial is the next step towards further implementation of the system.

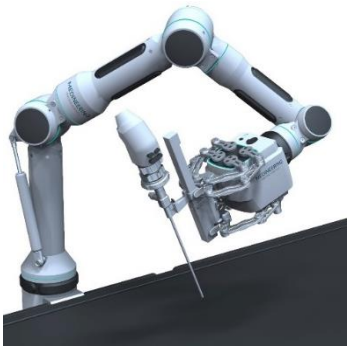

Fig. 1 System overview. The robotic guidance system consists of an intelligent mechatronic holding arm with four segments and seven degrees of freedom. Soft touchpads on each segment enable releasing and alignment of the robotic arm. LED light rings on each joint visualize the status of the system. A robotic hand with five active degrees of freedom is attached to the tip, realizing movement of the endoscope via foot pedal.

Fig. 2 System application. The system allows for bimanual instrumentation in transnasal surgery. This picture shows the first clinical application for sinus surgery. Note that both hands are free for instrumentation, while the endoscopic view is held steadily by the endoscope holding system.

Sand Blasting Inside a Patient: A CRISP Robot for Spraying Powder inside the Chest Cavity to Preclude Lung Collapse

P. L. Anderson[1,3], T. E. Ertop[1,3], A. Kuntz[4],

F. Maldonado[2,3], R. Alterovitz[4], and R. J. Webster III[1,3]

[1]*Department of Mechanical Engineering, Vanderbilt University*
[2]*Division of Pulmonary Medicine, Vanderbilt University Medical Center*
[3]*Vanderbilt Institute for Surgery and Engineering*
[4]*Department of Computer Science, University of North Carolina at Chapel Hill*
patrick.l.anderson@vanderbilt.edu

INTRODUCTION

We present a novel clinical application for a new kind of robot that self-assembles inside the patient. It is made of multiple needles that capture one another with snares at their tips. Each needle bends continuously, making the entire system a continuum, reconfigurable, incisionless surgical parallel (CRISP) robot, as shown in Fig. 1. It is incisionless because its needle-diameter (<3mm) tools are so small that no sutures are required after surgery.

The CRISP robot moves as robot arms outside the patient apply movements to the base of each needle. The robot motions are coordinated using mechanics-based models of the needles and the constraints imposed on one another when coupled [1] [2]. This enables the system to achieve tool tip motions specified by the physician.

In this paper, we explore using the CRISP system for pleurodesis, a medical procedure to which surgical robots have never previously been applied. Pleurodesis prevents lung collapse by intentionally introducing an irritant (e.g. talc powder) that causes the visceral pleura and parietal pleura to adhere to one another through scar formation. It is used for patients with recurrent lung collapse, buildup of fluid around their lungs (e.g., due to cancer), or who have had a first lung collapse and work in jobs in which subsequent collapses could be catastrophic (e.g., as an airplane pilot). Without pleurodesis, patients suffering a spontaneous lung collapse have a 20% chance of recurrence after their first episode, 60% after the second, and 80% after the third [3].

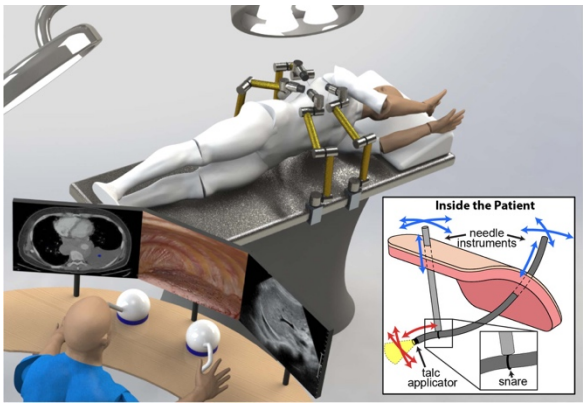

Fig. 1: The CRISP robot gives the surgeon percutaneous access to the pleural space. Robot manipulators outside the patient control each needle in a coordinated manner.

Pleurodesis is improved by an even distribution of powder applied to the surface of the pleurae (see Fig. 2). Pleurodesis can fail if there is a "patchy distribution of talc" [4], and fails up to 57% of the time when attempted using an indwelling pleural catheter that cannot be actively aimed inside the body [5]. The alternative, if the physician wishes to aim the powder delivery tube, is currently thoracoscopic surgery, which requires larger incisions to admit endoscopes and other tools [6].

In this paper, we propose the CRISP robot as a new and less invasive way to deliver the powder to the pleura. We hypothesize that the CRISP robot approach will enable surgeons to more thoroughly cover the pleural surfaces with powder during pleurodesis and do so solely through needle-sized openings that produce no scarring and do not even require sutures after surgery. This promises to enable better pleural adhesion and a lower recurrence rates of lung collapse for patients.

MATERIALS AND METHODS

Our CRISP robot prototype system is shown in Fig. 3a. To enable the needles to attach to one another within the patient, a snare made of a Nitinol wire basket is inserted through a needle made of superelastic Nitinol tubing (OD: 1.17 mm, ID: 0.85 mm). This needle is used to grasp the powder deployment tube inside the chest cavity, which is made from PEEK (OD: 1.70 mm, ID: 1.00 mm). The base of each needle is controlled by a robot manipulator (AUBO Robotics). The insertion length of each needle is controlled by a linear actuator consisting of a motor driving a lead screw.

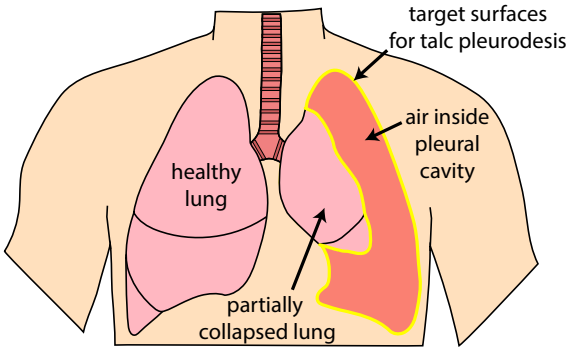

Fig. 2: Pleurodesis prevents recurrent pneumothorax (collapsed lung) by using chemical agents (e.g., talc powder) to irritate and adhere the pleural surfaces outlined in yellow.

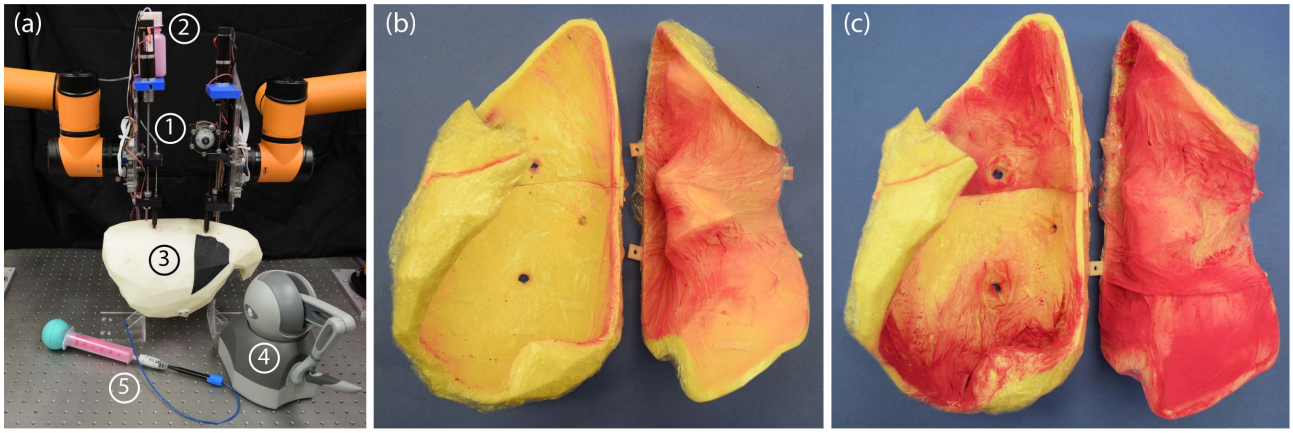

Fig. 3: (a) Experimental setup showing (1) CRISP robot, (2) powder container, (3) phantom model, (4) haptic control device, and (5) manual powder applicator. (b) Powder spraying results using manual method. (c) Powder spraying results using CRISP robot.

Our CRISP robot prototype is teleoperated with a 3D Systems Touch haptic device. The user controls the pose of the distal end of the powder spray tube using resolved rates control. The points along the needle shafts that coincide with the chest wall are programmed to remain at remote center of motion points, as described in [2].

Experiment Design: To evaluate the surface coverage improvement enabled by our robot, we compared it to the current manual approach. The manual approach consists of deploying the powder applicator through or attached to a rigid endoscope and tilting it to aim the powder. We simulated this by tilting the powder delivery tube through all possible angles through the entry port while spraying powder. To perform these experiments, we created a phantom model of the lung cavity by segmenting a CT scan of a patient with a partially collapsed left lung. We segmented the air in the pleural space and 3D printed an anatomically accurate volume. The phantom interior was lined with a transparent film layer covered with slow tacking spray adhesive to enable powder to adhere to the film. To facilitate these experiments, the phantom was made in two halves, so that the top half of the cavity could be sprayed while viewing through the bottom, and vice versa. Both the robotic and manual experiments were conducted in this manner.

The powder was colored red to enable easy visualization of surface coverage. After spraying the powder onto the surface, the film covering the interior of the lung cavity was removed and photographed. Coverage percentages were computed in MATLAB by thresholding HSV images to segment colored regions and converting pixel dimensions to physical dimensions using a ruler that was included in each image.

RESULTS

The results of the manual spraying are shown in Fig. 3b. Since the tube could only be tilted, and not bent to aim at all surfaces, it could achieve good coverage only on the side of the cavity opposite to the one where it entered the chest (i.e., the right-hand side of Fig. 3b). In contrast, the CRISP robot enabled the tube to be aimed in many directions, as shown by the greater coverage visible in Fig. 3c. In particular, notice the improved coverage of the surface of the cavity through which the spray tube was introduced. Quantitatively, image processing revealed that the robotic method covered 860 cm^2 of the interior area, while the manual method achieved 513 cm^2.

DISCUSSION

As seen in Fig. 3, more complete coverage of the pleural surface was achieved with the CRISP robot, due to its ability to aim the powder applicator within the chest cavity. This illustrates the feasibility of delivering better coverage less invasively than can be done by current manual techniques, which seems likely to improve the success rate of the procedure. We believe this is just one of many potential interventions that may be enabled in the future by the CRISP approach. The ability to access the lung cavity with a teleoperated system through needle-size openings that do not scar and require only a simple band-aid to close after surgery opens up new possibilities in less invasive lung biopsy and intervention, that may one day improve outcomes for many patients.

REFERENCES

[1] Mahoney, et al., "Reconfigurable Parallel Continuum Robots for Incisionless Surgery," in *IEEE/RSJ IROS*, 2016.

[2] Kuntz, et al., "Motion Planning for Continuum Reconfigurable Incisionless Surgical Parallel Robots," in *IEEE/RSJ IROS*, 2017.

[3] Chan, et al., "Efficacy study of video-assisted thoracoscopic surgery pleurodesis for spontaneous pneumothorax," *Annals of Thoracic Surgery,* 71(2):452-454, 2001.

[4] Massard, et al., "Minimally Invasive Management for First and Recurrent Pneumothorax," *Annals of Thoracic Surgery,* 66(2):592-599, 1998.

[5] Bhatnagar, et al., "Outpatient Talc Administration by Indwelling Pleural Catheter for Malignant Effusion" *N. Eng. J. Med.* 378(14):1313-1322, 2018.

[6] Viallat, et al., "Thoracoscopic talc poudrage pleurodesis for malignant effusions: a review of 360 cases," *Chest,*110(6):1387-1393, 1996.

Automation of the "Big Bubble" Hydro-Dissection Method for DALK Cornea Transplant Surgery

N.R. Sarfaraz[1], S Guo[2], T Schroeder[1], W Gensheimer[3], J Kang[2], A Krieger[1]

[1] *Department of Mechanical Engineering, University of Maryland, College Park*

[2] *Department of Electrical and Computer Engineering, Johns Hopkins University, Baltimore*

[3] *Warfighter Eye Center, Malcolm Grow Medical Clinics and Surgery Center, Joint Base Andrews*

nrsarfaraz@gmail.com, axel@umd.edu

INTRODUCTION

The purpose of this research is to automate the "Big Bubble" hydro-dissection method for deep anterior lamellar keratoplasty (DALK) cornea transplant surgery. When done manually, this surgery involves the surgeon trephinating and debulking the cornea to remove the majority of the stromal tissue [1]-[2]. After, a needle is inserted down to Descemet's Membrane and a fluid is injected to separate the remaining stroma from the membrane [1]-[2]. Finally, the cornea is removed and replaced with the donor cornea [1]-[2]. Compared to traditional penetrating keratoplasty (PK), which involves a full thickness graft, this method significantly reduces the risk of rejection of the donor cornea by keeping Descemet's Membrane intact [3]. The primary drawback of this method is the difficulty of manually inserting the needle to the correct depth, as penetrating too far requires a transition to the traditional PK method [1], [2], [4]. This paper reports the preliminary design of a robotic system that could autonomously drive the needle to the appropriate depth with the help of an integrated common-path swept source optical coherence tomography (CP-SSOCT or OCT) depth sensor. Unlike certain existing approaches, this system aims to fully automate the needle insertion step rather than relying on joint manipulation [4]. The feasibility of this approach is demonstrated in cadaver cow eyes.

MATERIALS AND METHODS

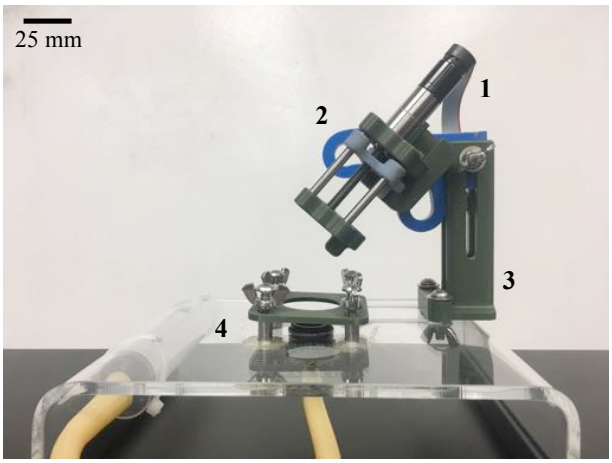

Fig. 1 Labeled image of the motorized needle drive system, showing the four major components.

The method of automation involves motorizing the needle, allowing it to be precisely advanced to the proper depth with the help of the OCT sensor.

The motorized needle drive consists of four parts. The first is a linear step that uses a lead screw to advance the needle with a precision of more than a micron (Fig. 1 - 1). The second is an angular slide that allows tests to be done using different angles of attack (Fig. 1 - 2). The third consists of three other slides that allow the device to be manually adjusted to the correct starting point (Fig 1 - 3). The fourth is a suction baseplate to hold the eye in place during testing (Fig. 1 - 4).

To sense the depth to which the needle has penetrated relative to Descemet's Membrane, the robot integrates a CP-SSOCT sensor, which uses near-infrared light swept source to perform highly accurate depth detection [5]-[6]. Unlike typical B-scan/C-scan OCT applications, the system measures the depth by acquiring A-scan data and obtaining the reference from the edge of the fiber. The fiber also implements an elliptical lens to enhance the OCT signal sensitivity in the cornea (Fig. 2). The OCT sensor consists of a swept source OEM engine (AXSUN, central wavelength: 1060 nm, sweeping rate: 100kHz), a balanced photo-detector, and a digitizer with a sampling rate of up to 500 MSPS with 12-bit resolution, and a Camera Link frame grabber (PCIe-1433, National Instruments).

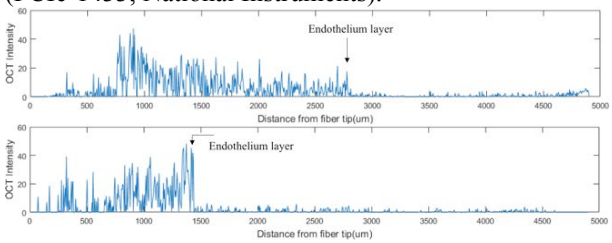

Fig. 2 OCT signal indicating the distance to the endothelium in microns from both outside (top), and inside (bottom) of the cornea.

RESULTS

The first tests of the needle drive involved penetrating an un-trephinated cow eye at 0°, 45°, and 75° from vertical (60° being the current clinical standard [1]-[2]). These tests confirmed that the linear stage had sufficient precision to reach Descemet's Membrane without

penetrating into the anterior chamber. Through a microscope (250x magnification), the deformation of the endothelial layer as the needle pushed against it was visible, without using the OCT sensor (Fig 3). Subsequent tests revealed however that the current setup cannot penetrate successfully into a trephinated cow eye, either debulked or not, without penetrating too far. Trephination is necessary in order to properly remove the cornea [1]-[2]. This led to the order of operations being reversed in later tests, separating the layers first before trephinating and removing the cornea.

Fig. 3 Deformation of the endothelial layer as the needle pushes against it before penetrating into the anterior chamber. Test performed with 25 gauge needle in fresh cow eye at 75°.

The next round of testing was done with the integration of the OCT fiber. The fiber was glued into a separate needle, which itself was glued alongside the needle used to inject the fluid for dissection (Fig. 4). A small gap of approximately 500 microns was left between the two tips so that the needle is inserted ahead of the fiber.

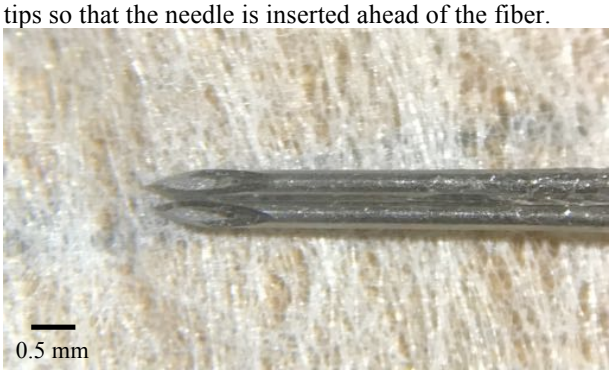

Fig. 4 Image showing the layout of the two 30 gauge needles glued side-by-side with the injection needle (bottom), slightly leading the needle carrying the OCT fiber (top).

Using this setup made it possible to determine the depth to which the needle had penetrated the cornea, relative to Descemet's membrane, far more precisely than a microscope or by hand, with little surgical training. These tests resulted in many partial successes (Fig. 5), demonstrating the feasibility of the use of an OCT fiber to automate the surgery. Although we were able to penetrate to the right depth, the injected fluid did not evenly disperse, resulting in some separation of stromal layers before Descemet's Membrane. This problem will need to be addressed in future iterations.

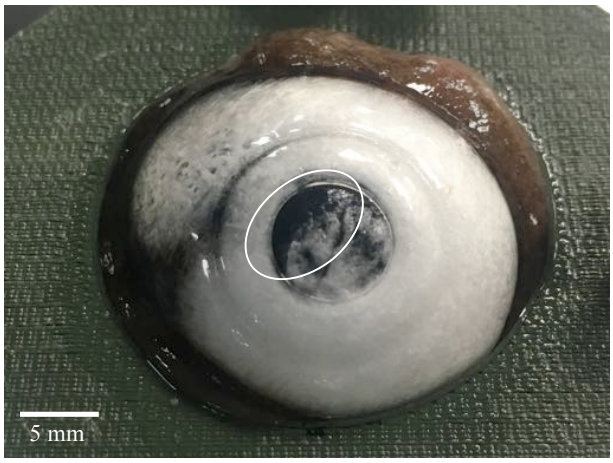

Fig. 5 Image of a cow eye with cornea removed. Eye was injected with air through 30 gauge needle inserted with motorized stage, then trephined. The clear area of the trephined region indicates partial successful separation.

DISCUSSION

The tests thus far stand as a proof of concept that "Big Bubble" DALK surgery can be automated using an OCT sensor to advance the needle to the appropriate depth more reliably than by hand.

There exist two main obstacles to the further success of this method. First, it can be difficult to receive a strong, clear signal from the OCT sensor when penetrating the eye at shallower angles (more than 45° from vertical). Second, the deformation of the eye upon insertion of the needle can be quite pronounced at steeper angles (less than 45° from vertical). In order to reconcile these two opposing constraints, our next steps will be to separate the needle and sensor fiber. The sensor will be mounted vertically above the eye, and the needle will be inserted at an angle closer to the current clinical standard of 60° [1]-[2]. Some other method of retention of the eye to increase the positioning accuracy of the needle may also be needed.

REFERENCES

[1] Anwar M, Teichmann KD. Big-bubble technique to bare Descemet's membrane in anterior lamellar keratoplasty. *J Cataract Refract Surg*. 2002;28(3):398-403.

[2] Fogla R, Padmanabhan P. Results of Deep Lamellar Keratoplasty Using the Big-bubble Technique in Patients With Keratoconus. *Am J Ophthalmol*. 2006;141(2):254-259.

[3] Liu H, Chen Y, Wang P, Li B, Wang W, Su Y, Sheng M. Efficacy and safety of deep anterior lamellar keratoplasty vs. penetrating keratoplasty for keratoconus: a meta-analysis. *PLoS One*. 2015;10(1):e0113332.

[4] Draelos M, Keller B, Tang G, Kuo A, Hauser K, Izatt J. Real-Time Image-Guided Cooperative Robotic Assist Device for Deep Anterior Lamellar Keratoplasty. 2018.

[5] Cheon GW, Huang Y, Cha J, Gehlbach PL, Kang JU. Accurate real-time depth control for CP-SSOCT distal sensor based handheld microsurgery tools. *Biomed Optics Express*. 2015;6(5):1942-1953.

[6] Song C, Park DY, Gehlbach PL, Park SJ, Kang JU. Fiber-optic OCT sensor guided "SMART" micro-forceps for microsurgery. *Biomed Optics Express*. 2013;4(7):1045-1050.

Robotic-arm assisted total knee arthroplasty improves early functional recovery and time to hospital discharge compared to conventional jig-based total knee arthroplasty: A prospective cohort study

B Kayani, S Konan, J Tahmassebi, FS Haddad

University College London Hospital, 235 Euston Road London, NW12BU
babar.kayani@gmail.com

ABSTRACT

Background:
Total knee arthroplasty (TKA) is an established and highly effective procedure that is performed in over 90,000 patients per year within the United Kingdom. Robotic-arm assisted TKA has been developed to improve the accuracy of implant positioing but the impact of this technology on early functional recovery remains unknown[1-2].

The objective of this study was to compare early postoperative functional outcomes and time to hospital discharge between conventional jig-based total knee arthroplasty and robotic-arm assisted total knee arthroplasty.

Methods:
This prospective cohort study included 40 consecutive patients undergoing conventional jig-based TKA followed by 40 consecutive patients receiving robotic-arm assisted TKA. All surgical procedures were performed by a single-surgeon using the medial parapatellar approach with identical implant designs and standardised postoperative inpatient rehabilitation. Inpatient functional outcomes and time to hospital discharge were collected in all study patients.

Results:
There were no systemic differences in baseline characteristics between the conventional jig-based TKA and robotic-guided TKA treatment groups with respect to age (p=0-32), gender (p=0.50), body mass index (p=0.17), ASA score (p=0.88), and preoperative haemoglobin level (p=0.82).

Robotic-arm assisted total knee arthroplasty was associated with reduced postoperative pain (P<0.001) (figure 1), decreased analgesia requirements (p<0.001) (Figure 2), reduced intraoperative blood loss (p<0.001), shorter time to straight leg raise (p<0.001), decreased number of physiotherapy sessions (p<0.001), and improved maximum knee flexion at discharge (p<0.001) compared to conventional jig-based TKA.

Median time to hospital discharge in robotic-arm assisted TKA was 77 hours (IQR, 74-81) compared to 105 hours (IQR, 98-126 hours) in conventional jig-based TKA (p<0.001).

Conclusion:
Robotic-arm assisted TKA is associated with decreased pain, improved early functional recovery, and reduced time to hospital discharge compared to conventional jig-based TKA.

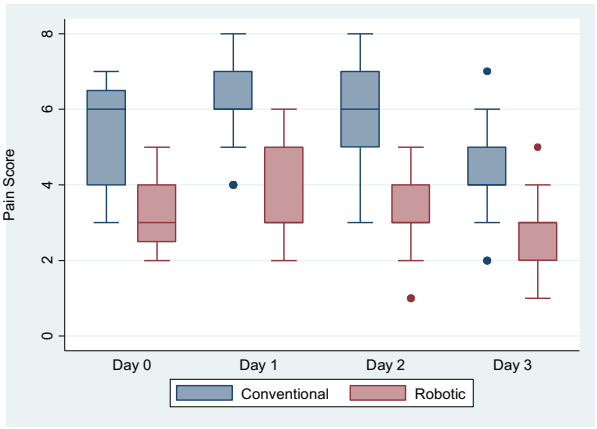

Fig. 1 Boxplot showing pain score as measured using the numerical rating scale in conventional jig-based TKA versus robotic-arm assisted TKA

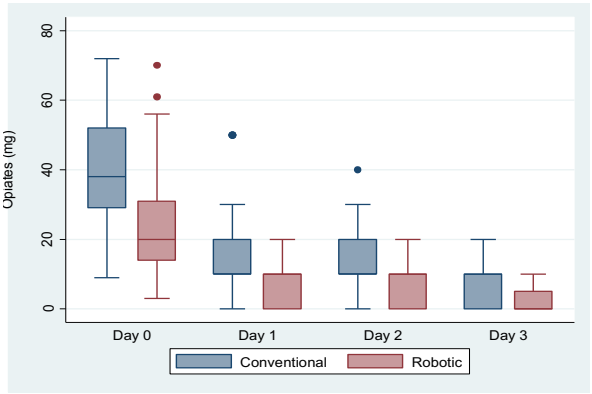

Fig. 2 Boxplot showing opiate analgesia consumption in conventional jig-based TKA versus robotic-arm assisted TKA

REFERENCES

1. Khlopas A, Chughtai M, Hampp EL, et al. Robotic-arm assisted total knee arthroplasty demonstrated soft tissue protection. Surg Technol Int. 2017;30:441–446.
2. Park SE, Lee CT. Comparison of robotic-assisted and conventional manual implantation of a primary total knee arthroplasty. J Arthroplasty 2007;22:1054–1059.

Expertise Related Disparity in Prefrontal-Motor Brain Connectivity

F. Deligianni[1*], H. Singh[2*], H.N. Modi[2], Darzi A, D.R. Leff[2], G.Z Yang[1]

[1]Hamlyn Centre for Robotic Surgery, Imperial College London

[2]Department of Surgery and Cancer, Imperial College London
fani.deligianni@imperial.ac.uk

INTRODUCTION

Surgery requires both dexterious motor skills as well as the ability to maintain cognitive control under stressful and time-pressurised conditions (e.g. control bleeding). Several factors can affect operative performance which depend on the mental demands of the task as well as surgical proficiency. Neuroimaging using functional Near Infrared Spectroscopy (fNIRS) to quantify changes in brain oxygenation that reflect neuronal activation demonstrate prefrontal cortex attenuation under stress is associated with performance degradation, whereas prefrontal engagement accompanies task success [1, 2]. However, technical skill relies not only on prefrontal or executive control but rather interactions between these areas and the motor cortex (M1). In this context, it remains unknown whether patterns of prefrontal-motor connectivity change under temporal demand and if these changes are expertise-dependent.

Therefore, this paper builds upon prior work based soley on activation analyses to better understand the interplay between motor skills (M1) and cognitive (prefrontal) performance under stress, which is important in human-robot interaction. We contrast brain networks based on partial connectivity derived based on shrinkage algorithms for covariance estimation. Subsequently, reliable connectivity differences between junior and senior surgeons are identified based on Network Based Statistics (NBS).

MATERIALS AND METHODS

Connectivity estimation in brain networks: Typically, large scale functional connectivity derived from fNIRS data is modelled as a network or a graph. The nodes of the graph represent brain regions and in this case, each region or *"node"* is associated with an fNIRS measurement channel.

We characterize brain connectivity based on partial correlation. Partial correlation is an undirected measure of synchrony that disentangles the influence of indirect connections on the connectivity between each pair of brain regions. In other words, it provides a measure of the signal transmitted directly between two regions [3]. Since, it is estimated based on the inverse covariance matrix, it is important to be well conditioned.

We estimate the covariance matrix of the fNIRS signal based on the Oracle Approximating Shrinkage (OAS) estimator [4]. In high dimensional problems of small sample number, shrinkage methods aim to better condition the covariance matrix and in general result in improved performance. This approach builds upon the Ledoit-Wolf (LW) estimator which minimizes the mean-squared error [5, 6]. For small sample sizes OAS outperforms LW significantly under the assumption of Gaussian distribution.

Comparing brain networks: We exploit Network Based Statistics (NBS) to identify "*edges"* that are statistically different between brain networks [7]. This method alleviates the problem of false discovery rate which arises in a large number of univariate edge-wise hypothesis tests. Instead, NBS uses clustering to identify subgraphs and associates the hypothesis test with a global network measure. In particular, an F-test is estimated for each graph edge and thus a suprathresholded graph is constructed. Subsequently, connected edges are identified as component and a p-value is associated by comparing with the null distribution. In this way, NBS provides greater power to detect differences between networks.

RESULTS

Subjects: Twenty-nine surgeons enrolled in the study (median age 33 (range), 9 females) and were sub-classified based on their prior training into 'junior', 'intermediate', and 'senior' residents. Technical skill was objectively assessed using four performance parameters: Task Progression Score (TPS; arbitrary units, au), Error Score (mm), Leak Volume (ml), and Knot Tensile Strength (KTS; Newtons, N).

Experimental Design: Participants were instructed to perform a laparoscopic suturing (LS) task using an intracorporeal technique on a laparoscopic box trainer (iSim2, iSurgicals, UK). The task involved inserting a 2-0 Vicryl® suture (Ethicon, Somerville, NJ) as close to pre-marked entry and exit points on either side of a defect in a Penrose drain. To tie a knot laparoscopically, participants were instructed to formulate one double throw followed by two single throws of the suture.

All subjects performed the task under two experimental conditions: (1) *'self-paced'* (SP), in which residents were permitted to take as long as required to tie each knot, (2) *'time pressure'* (TP), in which, a two-minute per knot time restriction was applied. Participants performed the LS task five times under each experimental condition with 30 second inter-trial rest periods between each knot. The order in which the subjects experienced the conditions was randomized.

Data Acquisition: The ETG-4000 Optical Topography System (Hitachi Medical Co, Japan) was used to measure activation across 24 prefrontal and 22 motor cortical locations ('channels'), based on the international 10-20 system of probe placement.

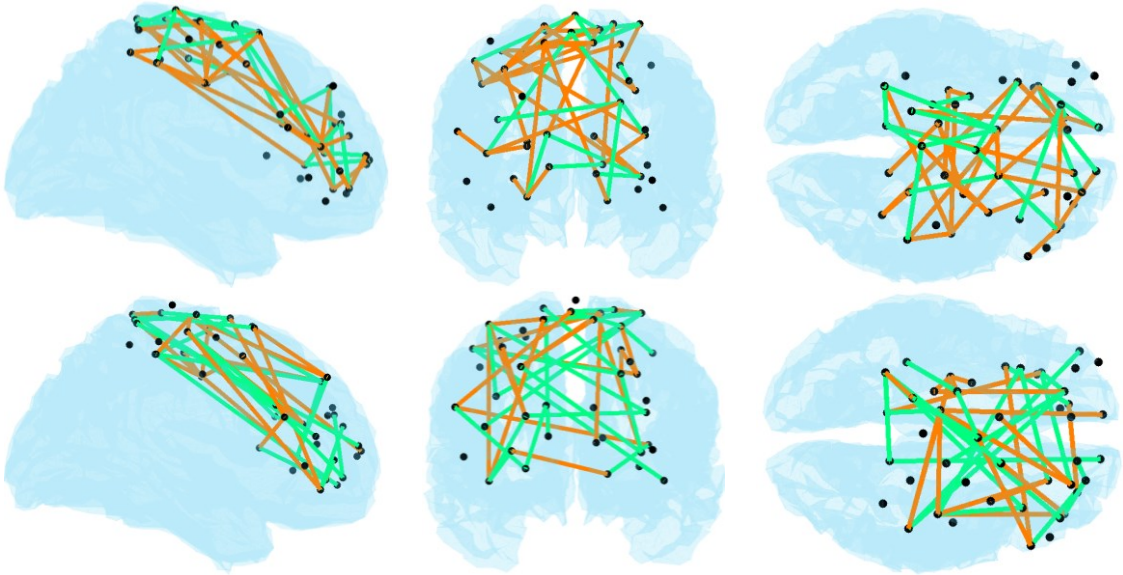

Fig. 1: Between-group differences in pre-frontal M1 connectivity amongst junior and senior surgeons visualised in sagittal, coronal and axial views, respectively. Significantly stronger connectivity amongst expert group (green line) versus greater connectivity amongst juniors (orange line). The top row illustrates results of self-paced' (SP), and bottom row the results of 'time-pressure' (TP) conditions respectively.

Preprocessing: Optical data was pre-processed using a customized MATLAB-based toolbox (HOMER2). A low-pass filter (0.5Hz) was applied to minimise high frequency noise and electrocardiographic effects on the data. Data was de-trended, baseline corrected and averaged across blocks to increase the signal-to-noise ratio. Raw mean intensity values were converted to changes in optical density relative to the mean of each channel across the whole task period. Channel-wise motion detection and spline correction were performed. Relative changes in light intensities were converted into changes in HbO_2 and HHb concentration using the modified Beer-Lambert Law.

Brain Connectivity Results: We used NBS to compare between conditions based on one-way ANOVA. Fig. 1 illustrates significantly different brain networks amongst junior and senior surgeons ($p\text{-val}<0.001$). Striking between-group differences in connectivity are observed. Junior residents demonstrate enhanced connectivity under self-paced conditions and attenuation under stress, Table 1. Conversely, more expert surgeons depict sparse inter-hemispheric connectivity during self-paced conditions and upregulation of connectivity strength under stress.

DISCUSSION

We observe that strengthening of prefontal-M1 connectivity amongst senior surgeons compared to junior surgeons emerges under 'time-pressure' conditions. This may reflect significant cross-talk between motor and prefrontal cortex regions related to the advanced training and ability to better cope with stress. Similarly, relative connectivity attenuation under calm conditions is understood as a "small-world" network optimised for maximum efficiency when cognitive demands are low.

Table 1: Comparison of connectivity strength between juniors (JS) and senior (SS) surgeons.

	SP	TP
Total Number of Edges	46	42
Edges with higher strength in SS	37%	55%

REFERENCES

[1] H. N. Modi, H. Singh, G. Z. Yang, A. Darzi, and D. R. Leff, "A decade of imaging surgeons' brain function (part II): A systematic review of applications for technical and nontechnical skills assessment," *Surgery,* vol. 162, pp. 1130-1139, Nov 2017.

[2] H. N. Modi, H. Singh, F. Orihuela-Espina, T. Athanasiou, F. Fiorentino, G.-Z. Yang*, et al.*, "Temporal Stress in the Operating Room: Brain Engagement Promotes "Coping" and Disengagement Prompts "Choking"," *Annals of Surgery,* vol. 267, pp. 683-691, 2018.

[3] F. Deligiannia, E. Robinson, C. F. Beckmann, D. Sharp, A. D. Edwards, and D. Rueckert, "Inference of Functional Connectivity from Direct and Indirect Structural Brain Connections," *2011 8th Ieee International Symposium on Biomedical Imaging: From Nano to Macro,* pp. 849-852, 2011.

[4] Y. L. Chen, A. Wiesel, and A. O. Hero, "Shrinkage Estimation of High Dimensional Covariance Matrices," *2009 Ieee International Conference on Acoustics, Speech, and Signal Processing, Vols 1- 8, Proceedings,* pp. 2937-2940, 2009.

[5] Y. L. Chen, A. Wiesel, Y. C. Eldar, and A. O. Hero, "Shrinkage Algorithms for MMSE Covariance Estimation," *Ieee Transactions on Signal Processing,* vol. 58, pp. 5016-5029, Oct 2010.

[6] F. Deligianni, G. Varoquaux, B. Thirion, E. Robinson, D. J. Sharp, A. D. Edwards*, et al.*, "A Probabilistic Framework to Infer Brain Functional Connectivity from Anatomical Connections," *Information Processing in Medical Imaging,* vol. 6801, pp. 296-307, 2011.

[7] A. Zalesky, A. Fornito, and E. T. Bullmore, "Network-based statistic: Identifying differences in brain networks," *Neuroimage,* vol. 53, pp. 1197-1207, Dec 2010.

Response Times of a Tactile Motion Intent Recognition System

T. Stefanou[1], G. Chance[2], T. Assaf[2], S. Dogramadzi[2]

[1]*Bristol Robotics Laboratory, University of Bristol, UWE*

[2]*Bristol Robotics Laboratory, UWE*
thekla.stefanou@bristol.ac.uk

INTRODUCTION

In the quest for high performance and consistency in motion intent recognition systems we experiment with tactile sensing. We investigate the potential of a tactile motion intent recognition system for use in autonomous rehabilitative and assistive devices. The focus of this work is on the latency of its motion detection.

Looking at upper limb motion intent recognition we aim to capture and interpret the tactile cues that arise. We used a tactile arm brace, the TAB, placed on the forearm to detect muscle activity while performing gripping motions using a bespoke 3D printed and sensorised gripping device. Analysis of the data showed that the TAB detects gripping instances, on average, 0.26s before gripping device.

METHODOLOGY

Tactile Sensing

The muscle contraction that takes place during gripping can be captured on the skin surface using tactile sensing. Our aim to mimic the recognition of movement intent as done in a therapist-patient setting; the therapist lightly touches the arm to sense the contraction of the muscles before guiding the limb through the exercise.

Prior studies have shown that weak forearm muscle contractions can be detected using inexpensive force sensors (Stefanou et al. 2017). The potential of force myography, or tactile imaging, is still being explored to determine whether it can be an alternative to the conventional electromyography techniques (Ravindra&Castellini 2014). For the purposes of these studies, the TAB and a gripping device have been designed and built.

The TAB

The TAB is made up of 8 force sensitive resistive (FSR) sensors uniformly distributed around a flexible, adjustable arm band. In all the user experiments performed, the TAB was placed on the right forearm and the gripping device was held as shown in Figure 1. The gripping device uses two button load cells to measure the force experienced as two rods, attached to the handle of the device, press vertically against each one. During gripping, the strength being was proportional to the individual FSR sensor readings, Figure 2. The data used in this study included experiments that incorporated power, precision, tripod and pinch gripping motions.

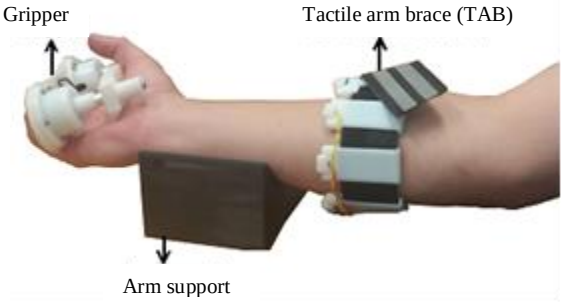

Figure 1 Participant performing gripping motions with the gripping device while wearing the TAB (tactile arm brace).

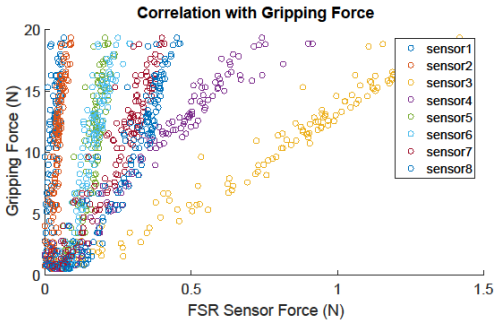

Figure 2 Grip force against TAB sensors contact forces during power gripping.

Detecting Intent

Since there is correlation between the TAB sensor forces and the grip strength being used, the gradient changes in the waveforms will be identified in order to determine whether a gripping motion has been initiated.

The faster it gets detected the quicker a rehabilitative device can assist the hand movement. In order to calculate how quickly the TAB can detect the intent of motion during gripping, a comparison is made between the TAB and the gripping device data.

The eight TAB sensor waveforms and the grip strength waveform were analysed and the instances where change was detected were compared. The cumulative sum algorithm (*cusum*) was slightly modified to detect only positive changes in the data. On both the gripping device data and the TAB data a threshold of 1.5 times the maximum noise amplitude was used in the implementation. The drift parameter was set to half of the threshold.

The *cusum* algorithm can detect the changing points in a waveform and the time where the change had actually

began. Thus a threshold was put in place to filter out changes that had occurred at a grip strength of over 0.3kg. This ensured that any positive gradient changes taking place post-gripping were not taken into account.
Furthermore, an algorithm was created to form clusters of the data where possible; finding the instances where both the TAB and the grip strength device detect a gripping action. Iterating through each of the eight TAB sensors' detection points the closest gripping indication within 50 samples (0.25s) as indicated by the grip strength waveform was found. Thus, that TAB detection point was assigned to a cluster.

RESULTS

The algorithms used indicated that 92% of the grip detection instances detected by the gripping device were also detected by the TAB. As evident in Figure 3, there were cases where the TAB sensors detected a change but the gripping device did not, or the other way around. Some of those may have been false positives but the high percentage of clustering indicates that overall the algorithm used performs well on the waveforms.
There were 438 gripping instances detected on the gripping device data waveform and for 35 of those there were no TAB sensor change indicators. On the other hand, there were 314 (7.5%) change indications amongst the eight FSR waveforms that could not be clustered with the grip strength device detection points. Within those, only 1.8% could not be clustered together at all.

Visualisation of the distribution of the TAB detection times with respect to the gripping device's respective times, Figure 4, confirms that the TAB detects changes that arise with the initiation of gripping faster than the gripping device. On average the arm brace achieves detection 0.26s (13 data samples) prior to the gripping device. On 2.73% of all 403 common detections the gripping device detected the change before the TAB.

We hypothesise that the proximities of the 8 TAB sensors to certain muscles may affect their individual sensitivities to the various movements as well as the types of gripping. We thus ran the same analysis using only one TAB sensor's data at a time. The results indicated that each sensor detects the changes faster than the gripping device. Nonetheless, there was on average 14% less common detections between with the gripping device and the individual sensors; with three of the sensors in particular indicating a lack of response to gripping, with 22% less common gripping detection instances.

DISCUSSION

The data analysis performed showed that the TAB is slightly more sensitive to muscle contractions than the gripping device used. The faster motion detection by the arm brace suggests that tactile sensing has good potential to recognise motion intent. This may also vary with the speed of the motion.

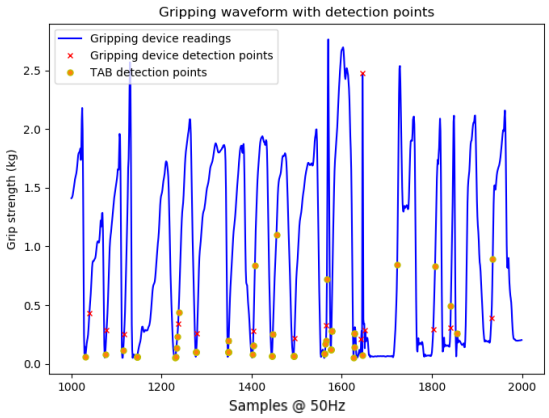

Figure 3 Gripping strength waveform and the detection points of both the gripping device and the TAB sensors.

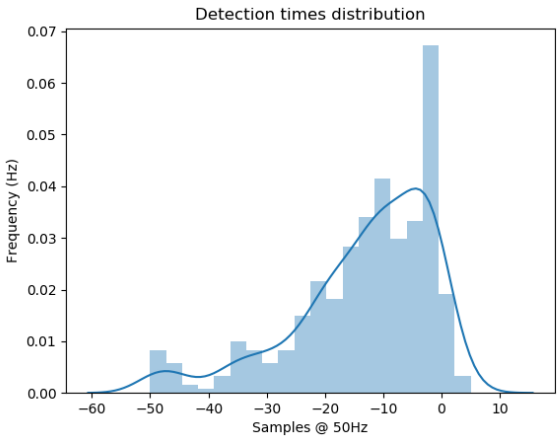

Figure 4 The distribution of the TAB detection points wrt the gripping device detection points (0).

Additionally, the results indicate that the combination of sensing data from all around the forearm is necessary to achieve higher consistency and quicker detection.
Future work will incorporate sonographic imaging which will act as a ground truth. Comparison of the TAB readings to the ultrasound imaging data, will allow for a more accurate evaluation of the TAB response time. In these experiments a variety of motions, and thus muscle contractions, will be looked at. Additionally, the experiments will be repeated using electromyography sensors, thus constructing a good basis from the results for future motion intent recognition systems.

REFERENCES

[1] Ravindra, V. & Castellini, C., 2014. A comparative analysis of three non-invasive human-machine interfaces for the disabled. *Frontiers in Neurorobotic*.

[2] Stefanou, T. et al., 2017. Upper limb motion intent recognition using tactile sensing. In *2017 IEEE/RSJ International Conference on Intelligent Robots and Systems (IROS)*. IEEE, pp. 6601–6608.

Evaluation of High-Speed Dynamic Motions for Robotic Guidewire Crossing Techniques

Young-Ho Kim, Ankur Kapoor, Rodolfo Finocchi, and Erin Girard
Siemens Healthineers, Medical Imaging Technologies, Princeton, NJ, USA
(young-ho.kim|ankur.kapoor|rodolfo.finocchi|erin.girard)@siemens-healthineers.com

INTRODUCTION

Percutaneous Coronary Intervention (PCI) is a non-surgical approach used to open narrowed coronary arteries and restore arterial blood flow to heart tissue. During a PCI procedure, the clinician places a guiding catheter in the ostium of the relevant coronary and then manipulates a guidewire through the catheter, into the coronary, and across the stenosis or blockage. The clinician uses X-ray fluoroscopy to visualize and guide the catheter, guidewire, and other devices (*e.g.* angioplasty balloons and stents). Robot-assisted PCI could potentially reduce the radiation exposure of operators and provide a more ergonomic work-flow.

Currently, several commercial robotic-assisted catheter systems (*e.g.,* the Magellan of Hansen Medical, the CorPath of Corindus Vascular Robotics) are available. The common features of robotic-assisted systems are to offer positional control of devices with reduced radiation exposure to the primary operator (but not necessarily the laboratory staff). However, they are still passively controlled by human operators at the cockpit [1]. Recently, Madder et al. [2] modified CorPath, and then proposed automatic guidewire retraction motions with a rotation of 180° to cannulate a coronary artery bifurcation. This is the first known automatic motion used for PCI and is important in reducing the overall execution time.

The fundamental motions that a clinician can use to control the movement and direction of the guidewire are rotation and pushing/retracting, from the proximal end of the guidewire outside the insertion point on the patient's body. Chronic total occlusion (CTO) presents the greatest challenge for recanulizing a vessel and, as demonstrated in one study, after attempting for 30 minutes, only 48.2% of lesions were successfully wired. In this paper, we focus on the common task of controlling guidewires to cross stenosed lesions referred to as *wiring a vessel* and introduce methods to generate distal guidewire motions that may be difficult to generate by a human hand.

We begin by constructing behavior-based motions designed to cross stenosed lesions. We then demonstrate both autonomous and collaborative control modes that can manipulate the guidewire from proximal to distal end in a phantom. The latter control mode allows the operator to give a preferred motion to the robot when transitions among behaviors are needed. Finally, we analyze our methods with regards to success rate and execution time in different environmental settings.

MATERIALS AND METHODS

Figure 1 shows an overview of a PCI workflow including the concept of our proposed idea. The operator identifies

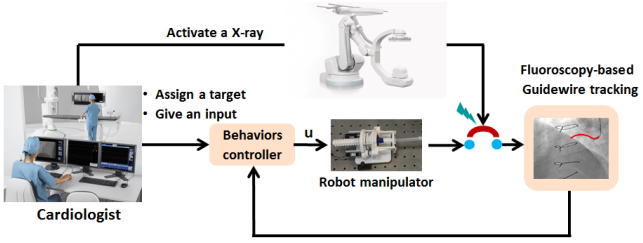

Fig. 1: An overview of the proposed robotic-assisted system.

the target stenosis that is to be crossed, which activates our proposed behavior controller for the guidewire. The behavior controller provides outputs, $\mathbf{u}$, to the low-level positional controller of the robot manipulator. In the collaborative control mode, the user can provide additional input to our controller based on the visual cues observed in the image.

The experimental setup shown in Fig. 2 was built to demonstrate our conceptual idea of *wiring a vessel* during PCI. The robot was fixed to a table along with a camera tracking system to simulate a X-ray system. We use two geared motors (850 rpm, 86 mNm) to provide high-speed motions. We used a JL4 catheter and an angled tip guidewire (.014 inch diameter Journey, Boston Scientific). As in typical PCI, the catheter is positioned at the ostium of the target vessel. The guidewire is threaded through the catheter such that its tip just extends beyond the distal end of the catheter. The proximal end of the guidewire is held by a small plastic device commonly called the *torquer* which in turn is rigidly attached to the robot.

At the torquer's attachment point to the robot, the guidewire's state, X_k, has a translation d and rotation ψ. At the tip of the guidewire, the state X_t is defined by the position and orientation in $SE(3)$. We consider p as the physical parameters of the guidewire including tip style, diameter, length, and tip coating type. Then our manipulation system can be treated as a transition function F. Using control $u \in U$, F makes the transition from $X(t)$ to another state $X(t+1)$:

$$X(t+1) = F(X(t), u(t); p), \tag{1}$$

where X consists of states X_k and X_t.

We design u as a special case of the discrete-time model [3]

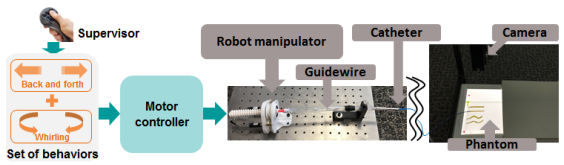

Fig. 2: Experimental setup: The rotation/translation motors manipulate a guidewire to cross stenosed lesions. The user can also advise and apply preferred behaviors into the controller for collaborative manipulation. The camera provides image feedback of guidewire tip postion in real-time.

referred to as "motion behaviors". In this paper we demonstrate two such behavior motions each consisting of velocity, acceleration, and time as $\{(v_0, a_0, t_0), \ldots, (v_m, a_m, t_m)\}$, where d (or ψ) = $v \cdot t + \frac{1}{2} \cdot a \cdot t^2$.

For *translational motion* the robot generates a forward motion ($2i$ distance at j velocity), and then a backward motion (i distance with j velocity), whereas, a *rotational motion* comprises a clock-wise rotation (n cycles with k velocity), and then an equal counter clock-wise rotation. Using these two primitives, we define two behavior-based control methods and compare the experimental results.

In the $naive$ control, which is operated in a open-loop control, a fixed cycle translation motion ($i = 1\ mm$ and $j = 5\ cm/s$) is combined with a fixed cycle rotation motion ($n = 2$ and $k = 5\ cycle/s$). The $collaborative$ control extends the $naive$ control by allowing the user to stop the the operation of the current motions when the user visualizes unsuccessful guidewire progress or safety concerns. At this point the controller executes the retraction operation once (the backward motion only with $1\ mm$ and $5\ cm/s$) before re-executing the previous motion set.

To validate our approach, we used 2D vessel phantoms constructed with flexible vinyl tubes ($6\ cm$ distance, $4\ mm$ outer diameter, $3\ mm$ internal diameter[1]). The variable inner diameter was constructed by applying Polyvinyl alcohol to the interior surface to provide different obstructive conditions with an internal diameter ranging $0.5\ mm$ to $2.5\ mm$, simulating 25-75% stenosis. We generated straight and tortuous shaped polycarbonate frames and inserted constructed tubes.

We have four scenarios of straight (25% and 75% stenosis) and tortuous vessels (25% and 75% stenosis), called *straight-25*, *straight-75*, *tortuous-25*, and *tortuous-75*. We consructed three randomly generated vessels for each scenario (approximately $\pm\ 10\%$ of the target stenosis).

RESULTS

Figure 3(a) shows the phantom with two types of exemplary vessel scenarios and the progress of the guidewire through the straight (Fig. 3(b)) and the tortuous (Fig. 3(c)) vessels, with tip tracking over time. We tested for 15 trials for each scenarios (5 trials for each phantom). A detailed analysis of all the results appears in Table. 1: The $naive$ control shows a good success rate for easy tasks: *straight-25* (93.3%) and *tortuous-25* (86.6%) while low success rate for hard tasks: *straight-75* (53.3%) and *tortuous-75* (40%). For the hard tasks under $naive$ control, if the guidewire buckled, the task could not be completed using this open-loop control.

However, $collaborative$ control shows improved the success rates for both easy and hard tasks. Note that the times reported for the $collaborative$ control include retraction time ($1\ sec.$). The easy tasks rarely need supervision to retract the guidewire, while the hard tasks need repeated retraction motions, thus spending greater time and deviation value than the $naive$ control.

[1]The average luminal diameter of the mid left anterior descending coronary is $4.6\ mm$.

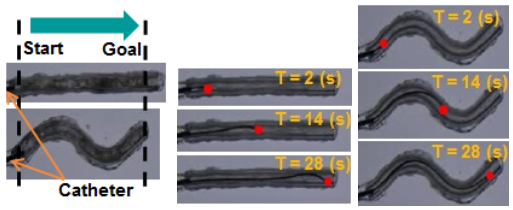

(a) (b) (c)

Fig. 3: Close up of the phantom: (a) start and goal lines for the phantom (b-c) progression of guidewire in straight and tortuous vessels, respectively. The red dot indicates the tracking of the guidewire tip.

	Naive	*Collaborative*
straight-25	$(29.8, 2.1)$, 93.3%	$(30.6, 1.8)$, 100%
straight-75	$(31.4, 1.7)$, 53.3%	$(36.0, 3.0)$, 86.6%
tortuous-25	$(29.0, 1.3)$, 86.6%	$(30.7, 1.5)$, 100%
tortuous-75	$(30.6, 1.5)$, 40.0%	$(35.4, 6.4)$, 93.3%

Table 1: The results are mean and standard deviation of execution times (seconds) for 15 trials. The latter shows the success rate of each controller (Note that the execution time only considers the successful tasks).

DISCUSSION

To our knowledge the present study is the first to study the effects of high-speed dynamic motions in robotic PCI. The use of high-frequency motions could be safe and efficient when integrated with user feedback. Robotic motions of the guidewire could provide another set of tools for lesion crossing, delivering motions that a human operator could not. This could be useful in CTO PCI to support crossing a difficult lesion and used in combination with new guidewire technology that applies energy at the distal tip.

Motion primitives need to be characterized by parameters. It might be difficult to estimate parameters for each guidewire and each case. However, the workspace of guidewires is very small in terms of the length of stenosis. Thus, we can use a data-driven approach whereby sub-optimal parameters can be updated with repeated motion trials based on previous motion feedback.

ACKNOWLEDGEMENT

This feature is based on research, and is not commercially available. Due to regulatory reasons its future availability cannot be guaranteed.

REFERENCES

[1] E. Maor, M. F. Eleid, R. Gulati, A. Lerman, and G. S. Sandhu, "Current and Future Use of Robotic Devices to Perform Percutaneous Coronary Interventions: A Review," *Journal of the American Heart Association*, vol. 6, no. 7, 2017.

[2] R. Madder, W. Lombardi, M. Parikh, D. Kandzari, J. A. Grantham, and S. Rao, "Impact of a Novel Advanced Robotic Wiring Algorithm on Time to Wire a Coronary Artery Bifurcation in a Porcine Model." *Journal of the American College of Cardiology, Supplement B*, vol. 70, no. 80, p. B223, 2017.

[3] S. M. LaValle, *Planning Algorithms*. New York, NY, USA: Cambridge University Press, 2006.

A hand-held robot for safe and automatic PIVC

Zhuoqi Cheng[1], Brian L. Davies[1,2], Darwin Caldwell[1], Leonardo S. Mattos[1]

[1]*Department of Advanced Robotics, Istituto Italiano di Tecnologia, Genova, Italy,*

[2]*Department of Mechanical Engineering, Imperial College London, UK*

zhuoqi.cheng@iit.it

INTRODUCTION

Peripheral IntraVenous Catheterization (PIVC) is a frequent operation in hospital. However, it suffers from a very low success rate. Especially for pediatric patients, over half of the first insertions were reported as failed since their veins are small and fragile. Given the levels of precision and controllability needed for pediatric PIVC, robotic systems have the potential to greatly assist and improve this operation. Previous developments of fully autonomous robots (e.g. HaemoBot [1]) are expensive, complex and not suitable for pediatric PIVC. Two hand-held robotic devices for assisting the PIVC insertion process were proposed in our previous studies [2, 3]. However, these 2 devices were developed to address only the difficult procedure of venipuncture detection and insertion control, while the subsequent steps after venipuncture can also be difficult and critical for the success of PIVC.

In this study we describe a new hand-held robot called CathBot, which extends the capabilities of our previous systems with automatic venous access control, cannula insertion and needle withdrawal. Being hand-held, the device also allows intra-operative control by the operating clinician over the whole PIVC operation.

MATERIALS AND METHODS

CathBot exploits a venous entry detection system based on electrical impedance sensing [2,3]. The device measures electrical bio-impedance of the tissue contacting the needle tip through the central core and the outer shaft of a concentric electrode needle. The venous entry can be detected when the measured value is found within the range of blood. Then the solenoid of the CathBot will automatically activate a crank-slider and brake.

The CathBot uses a crank-slider mechanism to convert the complicated and dexterous catheterization procedure to a simple forward motion. During a conventional PIVC operation, the operator picks up a catheter, aligns it with the vein, and starts the insertion. The insertion should stop immediately once the operator perceives venipuncture has occurred. Subsequently, the needle is kept still while the cannula is pushed forward to slide off the needle and enter the vein. Finally, the needle is removed from the cannula, and the PIVC insertion is completed. Using CathBot, the operator needs only to push its handle forwards along the insertion direction during the PIVC insertion, and the device can automatically complete the PIVC by inserting the cannula into the vein accurately and then retracting the needle.

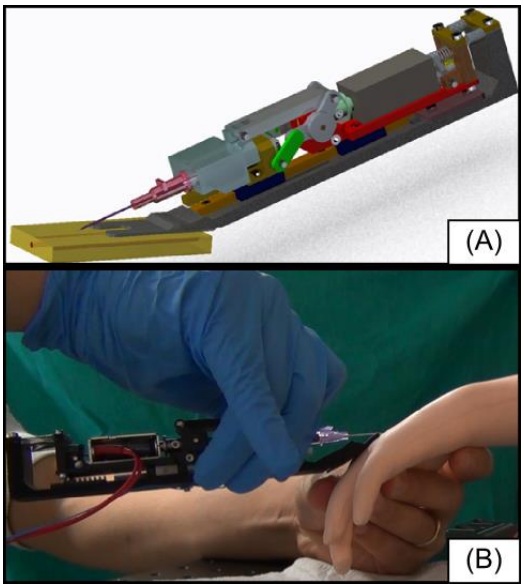

Fig. 1 3D modelling and the prototype of CathBot.

Fig. 1(A) shows the 3D modeling of CathBot. The device is designed with a symmetric structure. A linear guide is used and fixed on the base for guiding the insertion direction. Before every use, a new Concentric Electrode Needle (CEN) is plugged into the device. The original shape of the CEN and the adaptor are slightly modified in order to generate a sliding pair between them. The adaptor is also used as a handle for the user to grip the CathBot. A solenoid actuator is fixed on the main body and is used to control both the rotation of the crank-slider mechanism and the brake assembly. The crank-slider mechanism is integrated to the system for advancing the cannula and retracting the CEN. After the brake assembly is activated by the solenoid, the main body is stopped from moving forwards. For initializing the position of the device, a pair of return springs connects the top surface of the main body to the base. A shoe is designed to buckle onto the base to assist the operator to control the insertion angle to 20°. As shown in Fig. 1(B), a prototype of CathBot was made using aluminum and it is light weight (85g) and comfortable for manipulation.

Fig. 2 shows the workflow of CathBot. Initially (Fig. 2(a)), the solenoid is deactivated and the brake unlocks the main body from the base, allowing the main body to slide along the linear guide. Meanwhile, a small latch mounted onto the head of the solenoid plunger locks the cranks. Therefore, pushing of handle does not rotate the

crank, but moves the main body forwards. In this case, the catheter can be inserting into the site. During this procedure, the detection system continues sensing the electrical impedance at the CEN tip and checking the measurements. Once the venipuncture is detected (Fig. 2(b)), the solenoid would be activated immediately and automatically to pull back its plunger. Hence, the brake assembly is activated to lock the main body to the base, and the cranks are able to rotate. Afterwards, continuously pushing the handle forwards would start to rotate the crank via its connecting linkage. The crank-slider mechanism then retracts the CEN out of the skin (Fig. 2(c)), whilst the cannula is simultaneously advanced into the vein.

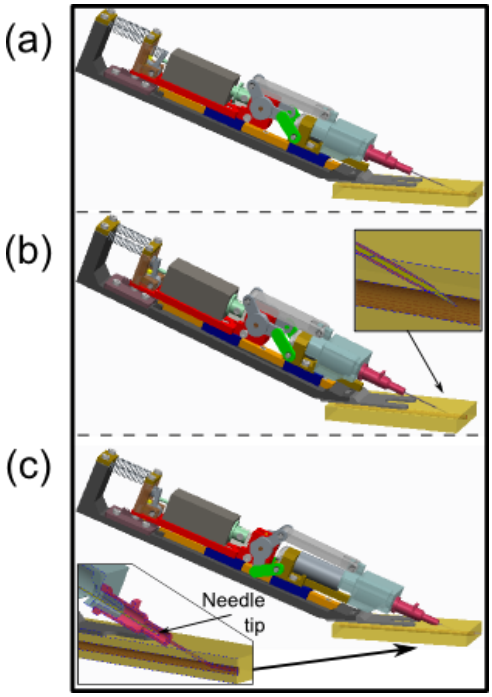

Fig. 2 The workflow of CathBot shows that after venipuncture, the device automatically inserts the cannula precisely into the vein and retracts the CEN.

RESULTS

As shown in Fig. 3, CathBot was firstly characterized by mounting it on a motion stage (Siskiyou Corp., USA) to create a repeatable and controllable assessment setup. A realistic baby arm phantom (M95, Kyoto Kagaku Co., Ltd., Japan) was used, and it was firmly locked on a stand. Saline solution with similar electrical impedance properties to blood, was used as blood substitute. Then the shoe of the device was laid onto the baby arm, and another stand was used to support the device at its bottom. The handle of the CathBot was mounted on a linear motion stage, which simulates the user's hand motion pushing the handle of the CathBot to advance 18 mm at 1 mm/s. After the device finished the stroke, CathBot was removed and the cannula stayed in the phantom. In total, 5 trials were conducted and all were successful as blood flowed out through the cannula in all 5 cases. This was a clear demonstration of the efficacy of the device.

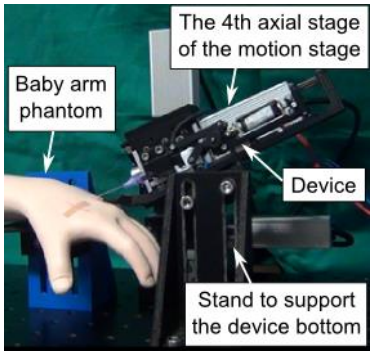

Fig. 3 Characterization of CathBot using a linear motion stage.

Subsequently, a user trial experiment was conducted to evaluate the hand-held CathBot. This experiment involved 5 subjects who had no prior PIVC experience. Before the experiments, all subjects received verbal and written information describing the experiments and its goal. Then a 5 min video tutorial about the PIVC process and an introductory document about CathBot were provided. Subsequently, the subjects were asked to perform 10 attempts on catheterizing the baby arm phantom with CathBot. In total, we collected 50 trials and a very high average success rate (84% ± 8%) was found. Also, 4 out of 5 subjects succeeded in their very first PIVC attempts. Most failed cases were caused by misaligning the insertion direction to the vein direction due to subjects' carelessness.

DISCUSSION

This paper describes the development and assessment of a hand-held robotic device for automating PIVC in pediatric patients. The device uses a crank-slider mechanism and a solenoid actuator to convert the complicated intravenous catheterization manipulations to a simple linear forward motion of the operator's hand. The user just needs to push the device's handle forwards and the device completes the whole PIVC insertion procedure automatically. The evaluation results demonstrate CathBot can significantly deskill the PIVC procedure and improve the PIVC performance on small veins. Hence, this device shows great potential to significantly improve the total PIVC process and to allow even non-expert clinicians to successfully perform these delicate operations. Since CathBot can deskill the error-prone post operation after venipuncture, the PIVC performance with CathBot was found to be better than the performances with its peer designs (80% average success rate with SAID and 78% with SDOP) as reported in our previous studies [2, 3].

REFERENCES

[1] R. Brewer. Improving peripheral iv catheterization through robotics: From simple assistive devices to a fully-autonomous system. Doctoral dissertation (2015).

[2] Z. Cheng, *et al*. A hand-held robotic device for peripheral intravenous catheterization. Journal of Engineering in Medicine (2017).

[3] Z. Cheng, *et al*. SDOP: A Smart handheld Device for Over puncture Prevention during pediatric peripheral intravenous catheterization. IEEE ISMR (2018).

A Preliminary Study on Customizable Origami Grippers with Elastic Hinges for Minimally Invasive Surgery

Jongwoo Kim[1], Sun-Pill Jung[1], Chunwoo Kim[2], Kyu-Jin Cho[1]

[1]Biorobotics Laboratory, Department of Mechanical and Aerospace Engineering, Seoul National University,

[2]Center for Medical Robotics, Korea Institute of Science and Technology (KIST)
kimjongwoo1988@gmail.com

INTRODUCTION

Minimally invasive surgery (MIS) has provided reduced recovery time, scar reduction, and traumas compared to traditional open surgery. To minimize incisions and tissue damage and expand their vesatlility, the current surgical devices are required to have scalability, lower cost, and easy-cutomization.

Origami-inspired design can be a solution to the MIS issues, as a foldable mechanism has been an effective solution for space-saving problems in both natural and artificial systems [1]. The design enables a foldable structure to be compact, lightweight, and scalable while maintaining kinematic behavior replacing mechanical components with flexure hinges and stiff facets. These characteristics make origami design widely applied as a method to manufacture robots at various scales for stent [2], locking mechanism [3], [4], forceps [5], etc.

This study demonstrates a customized origami gripper that allows access to narrow spaces. We replaced pin joints and mechanical links with compliant flexure or elastic hinges, allowing scalable mechansim for MIS. Moreover, we implemented a lightweight and compact operating system driven by a single tendon. The tendon actuates the grippers to be folded when pulled. The bent polyethyleneterephthalate (PET) that used as the elastic hinges restores the grippers unfolded when the tendon is released.

Unlike the joints with precisely determined movement in conventional mechanisms, the hinges of origami structures are made of flexible or elastic materials that allow undesirable movement [6]. Thus, we granted folding patterns with multi-layer structure to prevent unexpected motions. Adjacent layers have different stiffnesses to form folding lines so that it determines the shape of deployable structure. Additionally, the layer-based manufacturing eases the customization of the grippers design. For example, we vary the length of the gripper arm or the shape and dimension of the grippers by changing the design parameters in the planar diagram. Moreover, compared to the molding or CNC methods, the layer-based manufacturing reduces production cycle and expenses to customize products. Therefore, the origami-inspired design enhances the design flexilbity of grippers and enables the deployable structure for confined space without complex or bulky accessories.

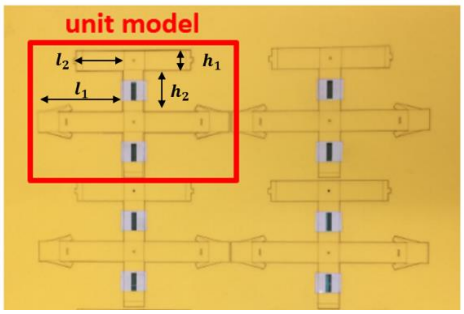

Fig. 1 Planar diagram for a unit model of the grippers and their design parameters.

MATERIALS AND METHODS

The structure of the grippers is composed of multi-layers with different stiffness. The design parameters of planar diagram are chosen to determine the dimension and the shape of grippers. Noting grippers inherently have symmetric structure, Fig.1. demonstrates the design parameters (l_1, l_2, h_1, h_2, t). l_1 determines the length of the gripper arms; l_2 for the length of supporter to fold the grippers; h_1 for the dimesion of the elastic hinges; h_2 for the minimum size of the base when folded; t for the thickness of the elastic layer. In this design, we set (l_1, l_2, h_1, h_2, t)=(13mm, 7mm, 6mm, 3mm, 0.2mm) as Fig.3 and Fig.4. Moreover, the manufacturing method has benefits to produce multiple models at once as Fig.1.

To manufacture the grippers, the layers with different material properties give stiffness difference between facets and folding lines. At first, the layers were laser-cut with desired patterns, and then were laminated together

Table I Fabrication steps to make the grippers.

1)	Desired folding patterns were laser-cut (VLS 3.5, Universal Laser System) and excess material was removed (Fig.3a).
2)	Laminating the elastic PET layer and the paper layers to give stiffness difference between facets and fold lines (Fig.3b).
3)	The sandwiched structure was pressed in the heat presser (QM900A, QME-SYS) for 4 min at 70℃ and 0.5MPa to melt the thermal adhesive so that the layers were bonded together.
4)	Laser-cutting the edges of the sandwiched structure (Fig.3c).
5)	Folding along the fold lines to complete the grippers (Fig.3d).

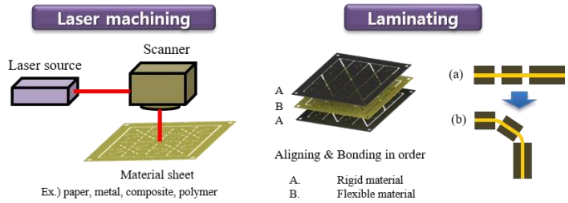

Fig. 2 Laminating the patterned layers to make facets and folding lines for the origami grippers.

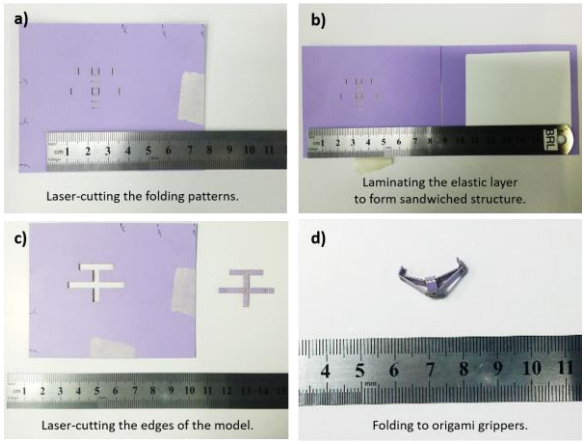

Fig. 3 Layer-based manufacturing process to make the grippers.

to form the sandwiched structure (Fig.2). In this study, a paper layer with thermal adhesive on one side (0.35 mm) was chosen for the facets, and the elastic PET film (0.2 mm) was chosen as elastic layer for the folding lines. The gap between folding lines determines the range of folding angle as Fig.2. Table I describes the details to manufacture the grippers.

As Fig.4, the grippers are attached to the distal end of the pre-curved stainless steel tubes with 2mm in diameter. A single tendon is connected to the center of the structure to actuate the grippers. Through the rotational and translational movements of the tubes, the grippers address target sites. We performed pick and place test of various objects with the grippers.

RESULTS

The single tendon and the elastic components actuate the folding mechanism of the grippers. Pulling the tendon folds the grippers, and stores elastic energy in the elastic components. On the other hand, when the tendon is released, the elastic components release the stored energy to unfold the grippers. Fig. 4b and 4c compare the folded and unfolded states of the grippers. The released elastic energy restores the grippers from Fig. 4c to Fig. 4b when the tendon is released. The thickness of the elastic layer and slits on the layer control the elastic force to restore its original shape when the tendon is released.

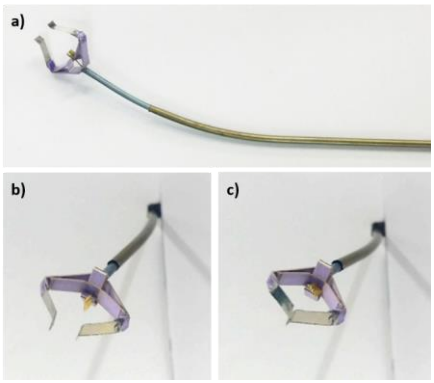

Fig. 4 a) The assembled grippers, b) the unfolded state, c) the folded state.

In tests, we manufactured the grippers from 12mm to 40mm in width. We varied the design parameters (l_1, l_2, h_1, h_2, t) to determine the length of the arms and the shape and dimension of the deployable structure according to surgical targets. The grippers successfully relocated various objects by holding and releasing them by the gripper arms. Additionally, the trained person can customize the design and manufacture the gripper within 15 minutes, significantly shortening the production cycle.

DISCUSSION

The origami grippers demonstrate the scalability, the ease of customization, and the feasibility for fast prototyping. We replace mechanical links with the patterns of facets and flexures. Especially, the elastic hinges of PET enable a single tendon actuation system for the folding mechanism of the grippers. The thickness of the elastic layer determines the elastic force to unfold the grippers. It makes compact grippers to be suitable for the restricted environment of inner body. Moreover, thanks to the layer-based manufacturing, one easily modifies the shape and dimension of the grippers and manufactures them rapidly. It does not require laborious works to assemble joint or bearings. Thus, it provides time-saving as well as cost-saving benefits compared to conventional CNC or molding manufacturing.

In future work, we will employ other materials such as fortified PET or metals to endure higher loads during operation. Also, we plan to design fully foldable grippers so that they remain inside of delivering tubes while invading toward targets, and then deploy with extended gripping arms at target sites. In other words, it can be needlescopic instrument during invasion, and then utilize longer moment arms at surgical sites. We consider bistable origami patterns as one solution to fully foldable grippers. We will optimize the design parameters to make the deployable structure efficiently space-saving. It brings that the grippers perform versatile tasks in a anatomically confined space.

REFERENCES

[1] E. Morris, D. A. McAdams, and R. Malak, “The State of the Art of Origami-Inspired Products: A Review,” p. V05BT07A014, Aug. 2016.

[2] K. Kuribayashi *et al.*, “Self-deployable origami stent grafts as a biomedical application of Ni-rich TiNi shape memory alloy foil,” *Mater. Sci. Eng. A*, vol. 419, no. 1, pp. 131–137, Mar. 2006.

[3] S.-J. Kim, D.-Y. Lee, G.-P. Jung, and K.-J. Cho, “An origami-inspired, self-locking robotic arm that can be folded flat,” *Sci. Robot.*, vol. 3, no. 16, p. eaar2915, Mar. 2018.

[4] J. Kim, *et al.*, “A self-deployable origami structure with locking mechanism induced by buckling effect,” in *Robotics and Automation (ICRA), 2015 IEEE International Conference on*, 2015, pp. 3166–3171.

[5] B. J. Edmondson, L. A. Bowen, C. L. Grames, S. P. Magleby, L. L. Howell, and T. C. Bateman, “Oriceps: Origami-Inspired Forceps,” 2013, p. V001T01A027.

[6] S.-P. Jung, *et al.*, “Fabrication of Composite and Sheet Metal Laminated Bistable Jumping Mechanism,” *J. Mech. Robot.*, vol. 7, no. 2, p. 021010, May 2015.

Index of Authors

The Hamlyn Symposium on Medical Robotics

24-27 June 2018, Imperial College London, UK